UNIVERSITÄT
BERN

Graduate School for Cellular and Biomedical Sciences
University of Bern

Dynamics of Red Blood Cell Partitioning and Flow in *In Vitro* Microvascular Networks: The Roles of Lingering Red Blood Cells and Pericyte Activation

PhD Thesis submitted by

Aurelia Lucilla Bucciarelli

for the degree of

PhD in Biomedical Engineering

Supervisor

Prof. Dr. Dominik Obrist
ARTORG Center for Biomedical Engineering
Faculty of Medicine of the University of Bern

Co-advisor

Prof. Dr. Robert Rieben
Department for BioMedical Research
Faculty of Medicine of the University of Bern

Copyright notice

Accepted by the Faculty of Medicine, the Faculty of Science and the Vetsuisse Faculty of the University of Bern at the request of the Graduate School for Cellular and Biomedical Sciences.

Bern, Dean of the Faculty of Medicine

Bern, Dean of the Faculty of Science

Bern, Dean of the Vetsuisse Faculty Bern

Abstract

The microcirculation consists of intricate capillary networks, measuring 5 to 10 μm in diameter, responsible for efficient oxygen delivery and nutrient exchange. Red blood cell (RBC) distribution within these networks is shaped by spatial and temporal dynamics at microvascular bifurcations, including the Zweifach-Fung effect, where RBCs preferentially enter daughter vessels with higher blood flow. However, in larger networks, deviations such as reduced or reversed partitioning occur due to complex RBC behaviors influenced by skewed hematocrit profiles, low feeding hematocrit, and increased flow velocities. Lingering RBCs (LRBCs), which temporarily pause at bifurcation apexes, have been identified as another key factor altering local hematocrit profiles and flow dynamics, yet this phenomenon remains insufficiently studied.

Beyond passive RBC flow, neurovascular coupling ensures adequate oxygen delivery during heightened neuronal activity, with pericytes playing a central role in modulating capillary diameter in response to neural signals. While pericytes are suspected to enable localized and rapid blood flow regulation, their contributions in time and space remain debated. Using an *in vitro* microfluidic model, this study investigates the impact of LRBCs and pericyte activation on RBC distribution and flow dynamics.

The first study investigates RBC dynamics at bifurcations using a microfluidic chip with a single diverging bifurcation. After developing a robust classification method for LRBCs, we observed that these cells travel along the centerline in parent vessels but tend to marginate toward the distal wall in daughter vessels. While lingering events did not directly affect local hematocrit partitioning, LRBCs influenced downstream bifurcations by skewing hematocrit distribution. This skewness, linked to the network history effect, highlights the long-range impact of LRBC behavior on reverse hematocrit partitioning.

The second study explores the impact of capillary cross-sectional area changes induced by pericyte activation, a mechanism associated with functional hyperemia. By employing a programmable pressure pump to simulate gradual variations in capillary cross-sectional area, we observed that short-term activation increased RBC velocity and hematocrit near the activation site, enhancing localized perfusion. In contrast, prolonged activation caused a network-wide redistribution of RBCs to minimize resistance, ultimately leading to hematocrit depletion due to the Fåhræus effect. These findings highlight the dynamic and adaptive nature of blood flow in capillary vessels, where sustained localized changes can propagate into systemic effects over time. These results suggest that coordinated activation of multiple pericytes and descending arterioles is required to sustain long-time RBC perfusion and prevent systemic imbalances.

Together, these studies provide new insights into the interplay between localized flow regulation and systemic capillary network dynamics. They reveal how geometric and dynamic factors influence RBC behavior and perfusion, offering a comprehensive framework for understanding capillary function in both physiological and pathological contexts.

Acknowledgments

During my time at ARTORG, I had the privilege of collaborating with and learning from many exceptional researchers who supported my work in numerous ways.

First, I would like to express my sincere gratitude to Prof. Dr. Dominik Obrist for giving me the opportunity to pursue a PhD in the Cardiovascular Engineering (CVE) group at the ARTORG Center for Biomedical Engineering Research, working on such an exciting research topic. I greatly appreciated his guidance, passion, and the invaluable scientific insights and support he provided, especially during challenging moments when I felt stuck.

I wish to thank Prof. Dr. Robert Rieben for co-advising this research project and offering insights into the biological aspects of the work. My gratitude extends to Prof. Dr. Andreas Heaberlin for his mentorship, assistance with statistical analyses, and support in securing the animal license. Additionally, I would like to thank Prof. Dr. Timm Krüger (Edinburgh University) for serving as an external co-referee and for his assessment of this thesis.

A special thanks goes to Dr. Alberto Mantegazza, who introduced me to the fascinating world of red blood cell microfluidics and guided me in producing the microfluidic chip. His collaboration was instrumental in shaping the first part of this dissertation. I would also like to thank my former master's student, Alice della Casa, for her contributions to my research.

I am deeply grateful to the CVE group for their support, camaraderie, and lively atmosphere. Your help, laughter, and lunch discussions made this journey enjoyable. Keep up the wonderful spirit that makes the CVE group special!

This project would not have been possible without the assistance of many colleagues from various labs with whom I had the privilege to work. I would like to thank the members of the Organs-on-Chip Technologies group for answering my many questions about microfluidic chip production. My thanks also go to PD Dr. Fabian Blank and Dr. Yury Belyaev for their help with my microscopy questions. I am especially grateful to Dr. Anastasia Milusev and Neda Salimi Afjani for their assistance with the endothelialization of the microfluidic chips. Pethö Laszlo (EMPA Thun) introduced me to the Nanoscribe 3D printer for producing rounded microchannels, and Dr. Michael Gerlt (Lund University) created the new microfluidics mask used for the endothelialization-thank you both for your invaluable contributions.

Lastly, I would like to express my heartfelt gratitude to my family, Nino, and my friends for their unwavering support. Your encouragement and belief in me shaped who I am today. Thank you from the bottom of my heart!

Bern, January 08, 2025 Aurelia Lucilla Bucciarelli

Dedication

To my Mother, who taught me patience and perseverance;
To my Father, who introduced me to the world of engineering and taught me the value of being hands-on;
To my Grandfather, who through his life demonstrated the importance of not judging and speaking kindly to everyone;
To all my family and friends supported me unconditionally and without hesitation.

Contents

Nomenclature

Symbols used throughout the thesis and their description are listed alphabetically in the first and the second columns, respectively. The third column specifies the unit of measurement. The international systems of units have been adopted (meter m, second s, kilogram kg, Newton N, Pascal Pa, pixel px, degree °). For pressure, both Pascal and Bar (bar = 10^5 Pa) will be used.

Roman Upper Case

A	Apex	-
D	Diameter	m
D_h	Hydraulic diameter	m
G	Green's function	-
G_s	Surface elastic shear modulus	N m^{-1}
L	Path of length (Chapter 3)	m
L	Length of porous media(Chapter 4)	m
L_ref	Characteristic length scale	m
H	Height	m
H_d	Discharge hematocrit	-
H_f	Feeding hematocrit	-
H_H	Homogenized hematocrit	-
H_r	Reservoir hematocrit	-
H_t	Tube hematocrit	-
K	Porous media permeability	-
N_frames	Number of frames	-
N_RBC	Number of RBC	-
Q	Volumentry flow rate	m^3 s^{-1}
Q_blood	Blood flow rate	m^3 s^{-1}
Q_RBC	RBC flux	m^3 s^{-1}
R	Hydraulic resistance (Chapter 1)	Pa s m^{-3}
R	Cross-correlation coefficient (Chapter 2)	-
U	Characteristic velocity	m s^{-1}
V	Volume	m^3
W	Width	m

Roman Lower Case

a	Radius	m
f	Frequency	s^{-1}
g	Gravitational acceleration	m s^{-2}
p	Pressure	bar
r_{RBC}	Radius RBC	m
t_{ref}	Reference time	s
$t_{\mathrm{r,RBC}}$	Residence time	s
$\mathbf{u}$	Velocity vector	m s^{-1}
u_{blood}	Velocity of blood	m s^{-1}
u_{H}	Homogenized velocity of RBC	m s^{-1}
u_{RBC}	Velocity of RBC	m s^{-1}
y^*	Normalized lateral coordinate	-

Greek Upper Case

Δh	Hight difference	m
Δp	Perfusion pressure	Pa
Δs	Distance between RBC centroid and apex	m
Φ	Fractional blood flow rate	-
Ψ	Fractional RBC flux	-

Greek Lower Case

β	Orientation	$^\circ$
γ	Weighting factor	-
$\dot{\gamma}$	Shear rate	s^{-1}
δ	Thickness of the CFL (Chapter 1)	-
δ	Dirac delta function (Chapter 4)	-
ϵ	Circularity (Chapter 3)	-
ϵ	Small perturbation (Chapter 4)	-
η	Relative apparent viscosity	-
κ	core to tube ration	
λ	Confinement ratio	-
μ	Dynamic Viscosity	Pa s
ρ	Density	kg m^{-3}
σ	Standard deviation	-
τ	Shear stress	N m^{-2}
τ_{RBC}	Relative residence time	-
χ	Ratio between RBC and plasma velocity	-

ω	Angular frequency	rad s^{-1}

Subscripts

act	Active	-
app	Apparent	-
del	Delay	-
inact	Inactive	-
meas	Measured	-

Chemical Symbols

Ca^{2+}	Calcium ion	-
Cl^{-}	Chloride ion	
H_2O	Water	-
K^{+}	Potassium ion	-
Na^{+}	Sodium ion	-
NO	Nitric Oxide	-

Dimensionless Variables

Ca	Capillary number	-
Re	Reynolds number	-
Wo	Womersley number	-

Abbreviations

α-SMA	α-Smooth Muscle Actin	-
BF	Balance Factor	-
BSA	Bovine Serum Albumin	-
CBF	Celebral Blood Flow	-
CFL	Cell-Free Layer	-
CL	Channel Length	m
DA	Data Analysis	-
EP	Experimental Protocol	-
GASP	Glucose-Albumin-Sodium-Phosphate	-
GM	Gaussian kernel Mask	-
IPP	Image PreProcessing	-
LDF	Lateral Distribution Function	-
LIF	Light Intensity Filter	-
LR	Lateral Resolution	m px^{-1}

LRBC	Lingering Red Blood Cell	-
MCV_{RBC}	Mean Corpuscular Volume of RBC	m^3
NA	Numerical Aperture	-
NLRBC	Non-Lingering Red Blood Cell	-
nNOS	Neuronal Nitric Oxide Syntheas	-
PBS	Phosphate-Buffered Saline	-
PDMS	Polydimethylsiloxane	-
PEG_2	Prostaglandin E_2	-
PTV	Particle Tracking Velocimetry	-
RBC	Erythrocyte/Red Blood Cell	-
RCF	Relative Centrifugal Force	-
ROI	Region Of Interest	-
SA	Symmetry Axis	-
Sk	Skewness index	-
S/V	Surface-to-Volume	m^{-1}
TTL	Transistor-Transistor Logic signal	-
VSMC	Vascular Smooth Muscle Cell	-
WBC	Leukocyte/White Blood Cell	-
WG	Weighted Gaussian function	-
WT	Wall Thickness	m

Chapter 1

Background

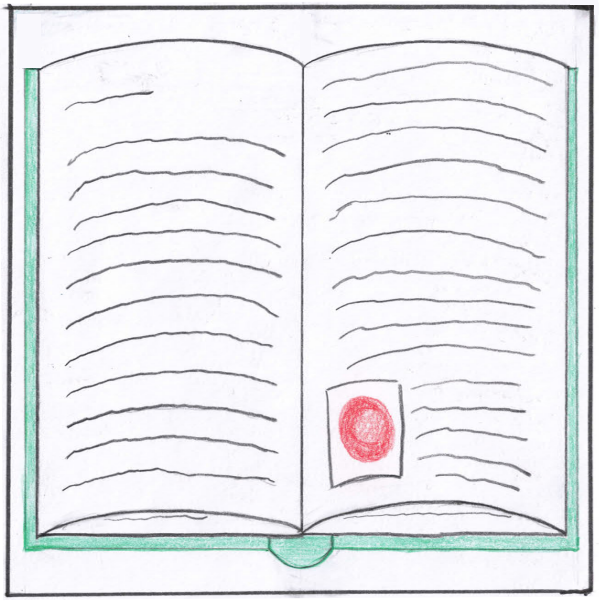

1.1 Introduction

The microcirculation is composed of intricate networks of capillaries, measuring 5 to 10 μm in diameter (Pappano and Wier, 2013a), which ensure efficient local oxygen delivery and nutrient exchange. These networks exhibit nonuniform red blood cell (RBC) distribution, influenced by spatial and temporal dynamics at microvascular bifurcations (Schulte et al., 2003; Kleinfeld et al., 1998; Mantegazza et al., 2020a,b; Balogh and Bagchi, 2017a). RBCs preferentially enter daughter vessels with higher blood flow, a process known as the Zweifach-Fung effect, which governs classical hematocrit partitioning (Pries et al., 1990; Fung, 1973). In larger networks, deviations such as reduced or reversed partitioning arise due to more complex RBC behaviors. These behaviors are influenced by factors such as skewed hematocrit profiles, low feeding hematocrit, and increased flow velocities (Shen et al., 2016; Clavica et al., 2016; Mantegazza et al., 2020a,b; Balogh and Bagchi, 2017b). Balogh and Bagchi (2017b, 2018) identified RBC lingering, where cells temporarily pause at bifurcation apex before continuing downstream, as a contributor to these effects by altering local hematocrit profiles and flow dynamics. Although lingering has been recognized as an important phenomenon for the RBC dynamics in the microcirculation, the number of studies remains limited (Balogh and Bagchi, 2017b; Kihm et al., 2021; Rashidi et al., 2023; Pskowski et al., 2021).

Additionally to the RBC dynamics the adequate oxygen supply during heightened neuronal activity in the brain is ensured by the regulation of blood flow through neurovascular coupling, interactions between neurons, astrocytes, and vascular cells. Pericytes, contractile cells surrounding capillaries, play a key role in modulating capillary diameter in response to neural activity, facilitating localized blood flow control. Research by Hall et al. (2014) highlights that capillary dilation occurs more rapidly than arteriole dilation, suggesting that pericytes provide a faster and more precise mechanism for regulating local blood flow. However, other studies, such as Hill et al. (2015), propose that vascular smooth muscle cells (VSMC) are the primary regulators of cerebral blood flow (CBF), with pericytes having a secondary role. Therefore the relative contributions of arterioles and capillaries to neurovascular coupling remain an area of ongoing investigation.

This study investigates the impact of lingering RBCs and pericyte activity on RBC distribution within a capillary network using an *in vitro* model. Two microfluidic devices were designed to replicate both a single bifurcation and a complex honeycomb-like vascular network. The single bifurcation model was used to examine the effects of lingering RBCs on hematocrit partitioning at bifurcations. The complex honeycomb device incorporated a pneumatic valve system to simulate pericyte-mediated capillary dilation and constriction, enabling the analysis of downstream effects of pericyte activity. This research provides valuable insights into how pericytes influence hematocrit distribution and velocity changes in the microcirculation, while the study of lingering RBCs offers a deeper understanding of RBC partitioning dynamics at bifurcations.

1.1.1 Thesis Outline

Chapter 1 Background This chapter provides an overview of the circulatory system, with a focus on cerebral circulation. It introduces blood and its components, particularly red blood cells, and explains fluid dynamics and blood rheology in the capillary network.

Chapter 2 Materials and Methods In this chapter, the methodologies used and developed during this project are presented. This entails the fabrication methods of the microfluidics chips, the experiment set-up and protocols, and the processing techniques for the acquired data.

Chapter 3 Relation Between Hematocrit Partitioning and RBC Lingering Here, we examine RBC dynamics at a bifurcation, focusing on lingering red blood cells. We analyze their role in hematocrit partitioning at a specific bifurcation and its impact on subsequent bifurcations.

Chapter 4 Influence of Pericyte Activation on RBC Flux and Partitioning In this study, we investigate the impact of pericyte activation on red blood cell dynamics within a capillary network. Specifically, we analyze how pericyte activation temporally influences the velocity and hematocrit distribution across the different capillaries in the network.

Chapter 5 Conclusion and Outlook In this chapter, the main findings of this research project are summarized, a conclusion is drawn, and suggestions for further research are offered.

1.2 Cardiovascular System

The anatomy and physiology of the cardiovascular system are extensively detailed in various textbooks (Hall, 2015a; Pappano and Wier, 2013b). This chapter introduces the key features of the cardiovascular system, with a particular focus on microcirculation, which forms the foundation for understanding the experimental investigations presented in this thesis.

The cardiovascular system serves three primary roles: i) delivering oxygen and nutrients to tissues, ii) removing waste products from cellular metabolism, and iii) maintaining homeostasis, such as pH balance and body temperature regulation. To fulfill these roles, the system comprises the heart, blood vessels (arteries, arterioles, capillaries, venules, veins), and lymphatic vessels. Within these structures, two fluids circulate: blood (through blood vessels and capillaries) and lymph (through lymphatic vessels). This thesis focuses on the heart and blood vessels.

From both functional and topological perspectives, the cardiovascular system can be divided into three main subsystems: i) systemic circulation, ii) pulmonary circulation, and iii) coronary circulation (Fig. 1.1a). Systemic circulation transports oxygen-rich blood from the heart to the rest of the body and returns oxygen-depleted blood back to the heart. Pulmonary circulation carries deoxygenated blood to the lungs for oxygenation, while coronary circulation supplies blood to the heart muscle itself. These subsystems form closed loops, with blood beginning and ending its journey in the heart.

For the purposes of this thesis, it is useful to emphasize the functional organization of the circulatory system. The macrocirculation, comprising the heart, arteries, and veins, is responsible for the advection and distribution of blood throughout the body. In contrast, microcirculation, composed of arterioles, capillaries, and venules, is the site of gas exchange, nutrient delivery, and waste removal between the blood and tissues. As illustrated in Fig. 1.1a, the microcirculation serves as a critical intermediary in the larger circulatory pathways, forming a bridge between the smallest arteries and the smallest

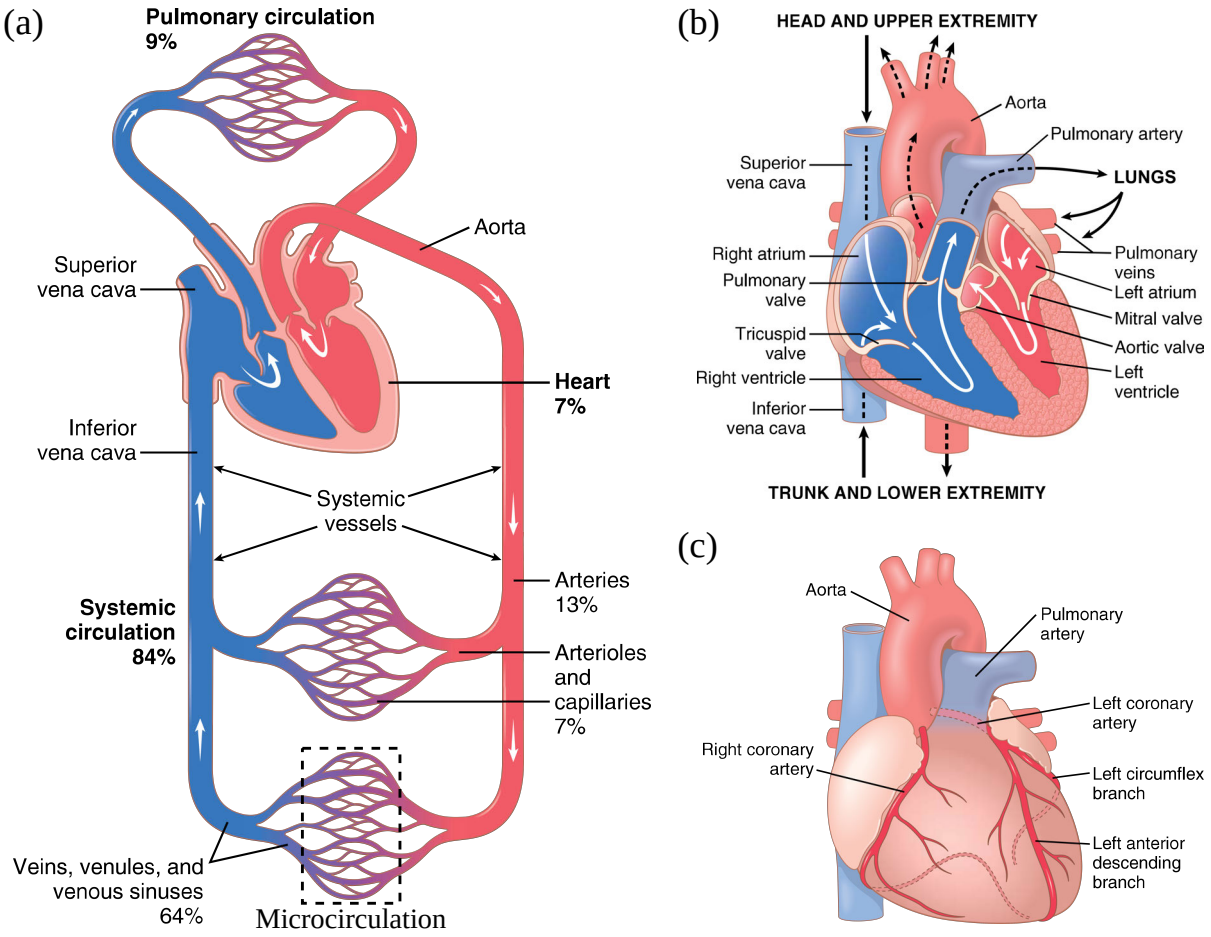

Figure 1.1: Cardiovascular system. **a)** Overview of the cardiovascular system, highlighting its components and blood distribution. **b)** Diagram of the heart illustrating its structure, blood flow through the chambers, and the function of heart valves. **c)** Detailed view of the coronary artery structure.[1]

veins. It ensures a continuous and seamless flow of blood by connecting the blood that is delivered from the heart to the blood returning to the heart.

1.2.1 Macrocirculation

As described above, the macrocirculation consists of the heart, arteries, and veins. On the arterial side, the typical diameter of blood vessels ranges from 3 cm for the aorta to 100 μm for the smaller arteries. Similarly, on the venous side, the diameter of blood vessels varies from 8 cm for the vena cava to 200 μm for the smaller veins.

The heart is the central organ of the macrocirculation, comprising four chambers (atriums and ventricles, Fig. 1.1b) separated by four valves, which ensure unidirectional blood flow. The tricuspid valve separates the right atrium from the right ventricle, while the mitral valve separates the left atrium from the left ventricle. The pulmonary valve controls blood flow from the right ventricle to the pulmonary artery, and the aortic valve

[1]Figures 14-1, 9-1 and 21-3 in Hall (2015a). Reproduced with the publisher's permission.

regulates blood flow from the left ventricle to the aorta.

Starting in the left ventricle, during heart contraction, oxygenated blood is pumped through the aortic valve into the aorta. From the aorta, the blood flows into the arterial tree, branching into progressively smaller arteries until it reaches the capillary networks where the exchange of gases, nutrients, and waste products occurs with surrounding tissues. Then, deoxygenated blood, enriched with carbon dioxide, exits the capillary networks and enters the venous system. It travels through progressively larger veins, eventually reaching the vena cava, which delivers the blood back to the heart's right atrium, completing the systemic circulation.

Then, during the heart contraction, the deoxygenated blood in the right ventricle is pumped through the pulmonary valve into the pulmonary artery. This blood is transported to the capillary networks of the lungs, where it undergoes oxygenation. Oxygen-rich blood then returns to the heart's left atrium via the pulmonary veins, completing pulmonary circulation.

Coronary circulation ensures that the heart muscle (myocardium) receives the oxygen and nutrients necessary for its function (Fig. 1.1c). Oxygenated blood enters the coronary arteries, which branch off from the aorta just after the base of the aortic valve. These arteries deliver blood to the capillary networks surrounding the myocardium. After oxygen and nutrients are delivered, the deoxygenated blood is drained by the cardiac veins and returned directly to the right atrium.

1.2.2 Microcirculation

As previously described, the microcirculation consists of arterioles, capillaries, and venules (Fig. 1.1).

Arterioles have an average diameter ranging from 10 μm to 150 μm and are responsible for transporting oxygenated blood from the larger arteries to the capillaries. Capillaries, with diameters less than 10 μm, form highly interconnected networks known as capillary beds. Unlike the tree-like branching structure of arteries and veins, capillary beds exhibit a dense, three-dimensional organization. These networks are the primary sites for the exchange of molecules and gases between the blood and surrounding tissues. Venules have diameters ranging from 10 μm to 100 μm and serve to collect deoxygenated blood from the capillaries. They channel this blood back toward the veins.

Arterioles, capillaries, and venules are structurally distinct to support their specific functions in the microcirculation.

Artery and arterioles are composed of three layers:

Tunica intima: the inner layer, which comprises endothelial cells in direct contact with the blood, providing a smooth surface for blood flow.

Tunica media: the middle layer, which consists of two layers of vascular smooth muscle cells (VSMCs) arranged spirally around the endothelium. This layer plays a crucial role in regulating blood flow and pressure through contraction and relaxation.

Tunica adventitia: the outer layer, which consists of connective tissue (collagen and elastin), which provides structural support and shape to the blood vessel.

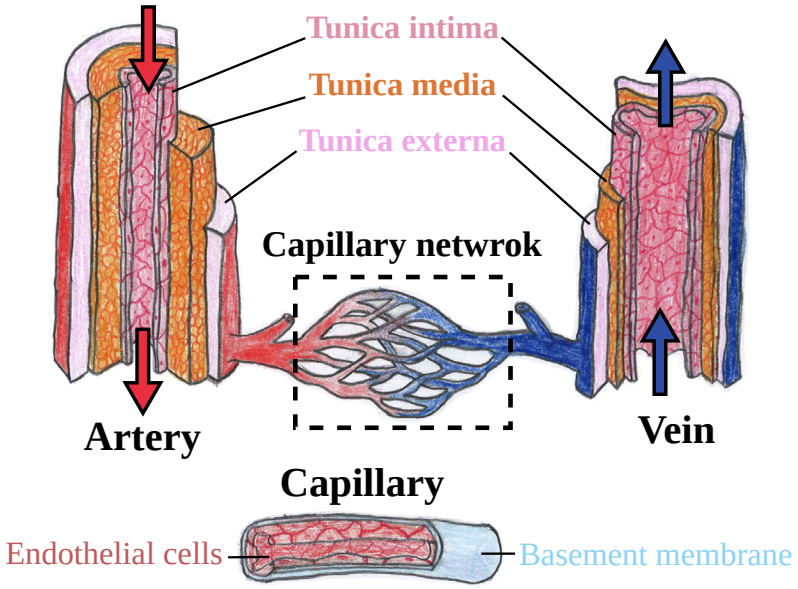

Figure 1.2: Schematic illustrating the structural differences between artery, capillary, and vein.

Veins and venules share a similar structure to arterioles but also have valves that prevent blood from flowing backward, ensuring unidirectional movement toward the heart. These structures can be seen in Fig. 1.2.

Capillaries, in contrast, are much simpler in structure. They consist of only a single layer of endothelial cells and a thin basement membrane, facilitating the efficient exchange of gases, nutrients, and waste products. Capillaries can be classified into three types based on their structure and permeability (Fig. 1.3).

Continuous capillaries are the most common type and are found predominantly in connective tissues, muscles, and lungs. They provide a relatively selective barrier and are often surrounded by pericytes.

Fenestrated capillaries are found in tissues with high levels of molecular exchange, such as the intestines and kidneys, these capillaries have small pores (100 nm in diameter) that significantly increase their permeability to certain molecules.

Discontinuous capillaries are found in organs like the liver, spleen, and bone marrow; these capillaries have larger openings to allow the passage of cells and large molecules.

Capillaries are highly suited for the exchange of gases and nutrients due to their unique structural properties. Their walls are extremely thin, with a thickness of approximately 0.5 μm, which minimizes the diffusion distance for molecules and gases. Additionally, the dense spatial arrangement of capillaries creates a large surface area, ensuring efficient oxygen delivery to surrounding tissues.

The small diameter of capillaries often causes RBCs to deform as they pass through. This deformation increases the effective surface area of the RBCs in contact with the

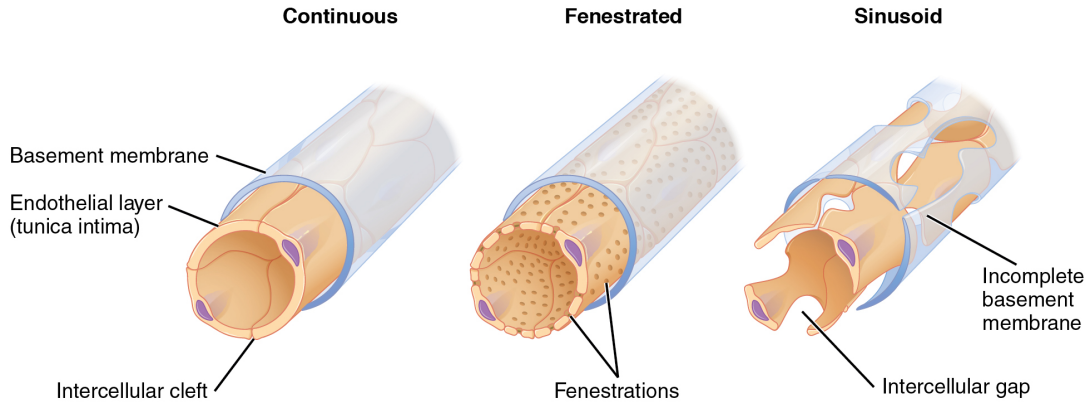

Figure 1.3: Illustration of the three capillary types: continuous, fenestrated, and sinusoid, highlighting their structural features.[2]

endothelium, further reducing the diffusion path and enhancing the exchange of oxygen and carbon dioxide between the blood and tissues.

Moreover, the geometric confinement of capillaries results in very low blood flow velocities compared to other parts of the circulatory system. This reduced velocity increases the residence time of RBCs within the capillary networks, allowing sufficient time for RBCs to sense oxygen gradients and facilitate diffusion. These combined factors make capillaries the ideal site for efficient molecular exchange essential for tissue health and function.

1.2.3 Blood Regulation in the Brain

The human brain, despite constituting only 2% of the body's mass, consumes about 20% of the energy produced when the body is at rest. This high energy demand is essential for normal brain function, as most of it is used to reverse ion influxes associated with synaptic and action potentials (Attwell et al., 2010). When inadequate blood glucose and oxygen are supplied to specific brain regions, neurons and glial cells (astrocytes) can become damaged or die.

Therefore, understanding the regulation of blood flow in the brain is very important. According to reviews by Attwell et al. (2010) and Hillman (2014), functional hyperemia, the increase in blood flow to regions with sustained neuronal activity, is a key aspect of neurovascular coupling mechanisms and ensures a normal brain function.

As depicted in Fig. 1.4, blood reaches the deeper layers of the brain through pial arteries which run along the brain's surface. These arteries branch into smaller descending arterioles, which penetrate the cortical tissue to supply the underlying regions. The arterioles connect to an extensive capillary network, facilitating gas exchange and nutrient delivery. The capillaries then transition into post-capillary venules, which merge into larger veins, ultimately returning deoxygenated blood to the pial veins on the surface.

Experimental evidence shows that this blood flow increase can result in local hyperoxygenation, where oxygen supply exceeds metabolic demands, while glucose supply remains sufficient (Hillman, 2014). As a result, many studies have concluded that increased blood

[2]Copyright by Wikipedia user CFCF. CC BY-SA 4.0.

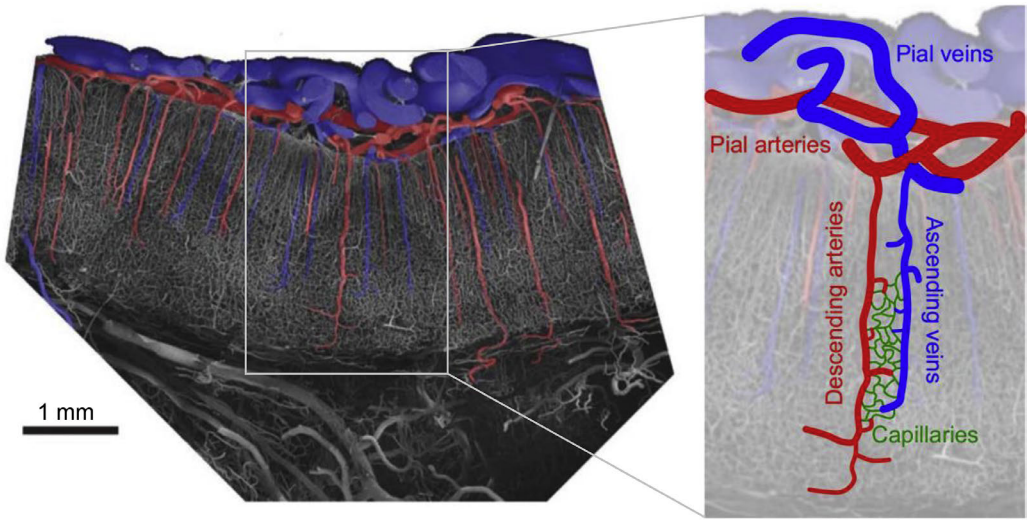

Figure 1.4: Structure of the cortical vasculature. Scanning electron micrograph of a vascular corrosion cast from a monkey primary visual cortex. Arteries are highlighted in red, veins are highlighted in blue, and capillaries are highlighted in green.[3]

flow primarily supports glucose transport rather than oxygen delivery. Furthermore, Lindauer et al. (2010) and Wolf et al. (1997) demonstrated that functional hyperemia persists in animals with excess oxygen and glucose in the brain, suggesting that the response is not driven by nutrient deficits.

The delay of approximately one second between neuronal stimulation and the onset of increased cerebral blood flow indicates that neurons do not rely on functional hyperemia to meet their immediate glucose and oxygen needs. Instead, this suggests that neurons possess sufficient energy reserves for initial metabolic demands, and the increased blood supply during functional activation supports the prolonged neuronal activity (Hillman, 2014).

In vivo, optical imaging, and two-photon microscopy studies reveal that the functional hyperemia originates at a depth of 0.6 to 0.9 mm in the cerebral cortex and spreads towards the surface at about 0.9 mm/s. Within one second of neuronal stimulation, hemoglobin levels increase in the deep capillary network, likely due to capillary lumen expansion, though whether this process is active or passive remains unclear. Within two seconds, a retrograde signal induces dilation of the penetrating arterioles, delayed by about 1.4 s relative to the capillaries. This signal can propagate over 1 mm, reaching pial arteries up to 2 mm from the activation center. Between 2 to 6 s, hyperemia also affects the venous side (Hillman, 2014).

The return to the basal condition occurs in reverse order: pial arteries return to baseline first (> 4 s), followed by other vessels, typically restoring basal conditions within 10 s. The increase in blood flow results from the increase in the diameter of the pial arteries, penetrating arterioles, and capillaries. The change in diameter in the arterioles is a result of dilatation or constriction of the VSMCs, which are in the tunica media of the arterioles. Through the expression of α-smooth muscle actin (α-SMA), VSMCs can contract to regulate arteriolar resistance (Lacolley et al., 2012). However, key questions

[3]Figure 1 in Schmid et al. (2019a). Reproduced with the publisher's permission.

remain, including the active or passive nature of capillary dilation, the primary roles of capillaries and arterioles in flow regulation, the presence of layer-specific mechanisms in the cortex, and the spatial extent of hyperemia (Hillman, 2014). To better understand functional hyperemia, in the next paragraph, we will explain the different signaling pathways forming the neurovascular coupling mechanisms, which can be identified as neuron-arteriole smooth muscle cells, astrocyte-arteriole smooth muscle cells, neuron-pericyte, and astrocyte-pericyte signaling.

Signaling Pathways to Arteriole Smooth Muscle Cells

Signaling to the VSMCs of arterioles occurs via two primary pathways: one directly from neurons and the other mediated by astrocytes. Neuronal signaling begins with the synaptic release of glutamate, which activates NMDA receptors, leading to calcium ion (Ca^{2+}) influx and the activation of neuronal nitric oxide synthase (nNOS). This enzyme produces nitric oxide (NO), which diffuses into the extracellular matrix and penetrates the surrounding VSMC. Within these cells, NO induces vasodilation, a process observed in both *in vitro* and *in vivo* (Attwell and Iadecola, 2002). In the cortex, inhibition of nNOS significantly reduces the blood flow increase typically associated with neural activity, but this effect can be reversed by administering NO donors. This suggests that NO is essential for neurovascular coupling, though it does not act as a dynamic signaling molecule. However, in the cerebellum, NO directly mediates aspects of the vascular response. Peptidergic interneurons and the neurotransmitter GABA also contribute to vascular regulation, though it remains unclear whether these effects occur directly or involve astrocytes (Attwell et al., 2010).

Astrocytes, strategically positioned at the interface between neurons and blood vessels (surrounding synapses and touching the blood vessels via their endfeet), regulate cerebral blood flow through various mechanisms. Activated by neuronal signals, astrocytes release potassium ions (K^+) and arachidonic acid metabolites, such as prostaglandins (PGE_2) and epoxyeicosatrienoic acids. These molecules reduce Ca^{2+} entry into smooth muscle cells, promoting vasodilation. Under specific conditions, however, astrocytes can trigger vasoconstriction by enhancing the production of 20-HETE within VSMC (Attwell et al., 2010).

In vivo, studies have shown changes in arteriolar diameter, dilation, or constriction, corresponding to neuronal activity during functional hyperemia (Hall et al., 2014; Hill et al., 2015; Mishra et al., 2016). While activation of VSMCs has long been recognized as central to blood flow regulation during functional hyperemia, whether it alone ensures precise flow distribution within the capillary network remains an open question.

Signaling Pathways to Pericyte

As discussed in Section 1.2.2, capillaries are composed of only an endothelial layer and a basal lamina membrane, traditionally thought to lack the ability to actively alter their diameter. Early hypotheses suggested that any observed diameter changes were passive responses to increased blood flow from descending arterioles. However, recent studies challenge this view, showing that capillaries may actively regulate blood flow (Hall et al., 2014; Peppiatt et al., 2006; Mishra et al., 2016). These active changes are mediated by

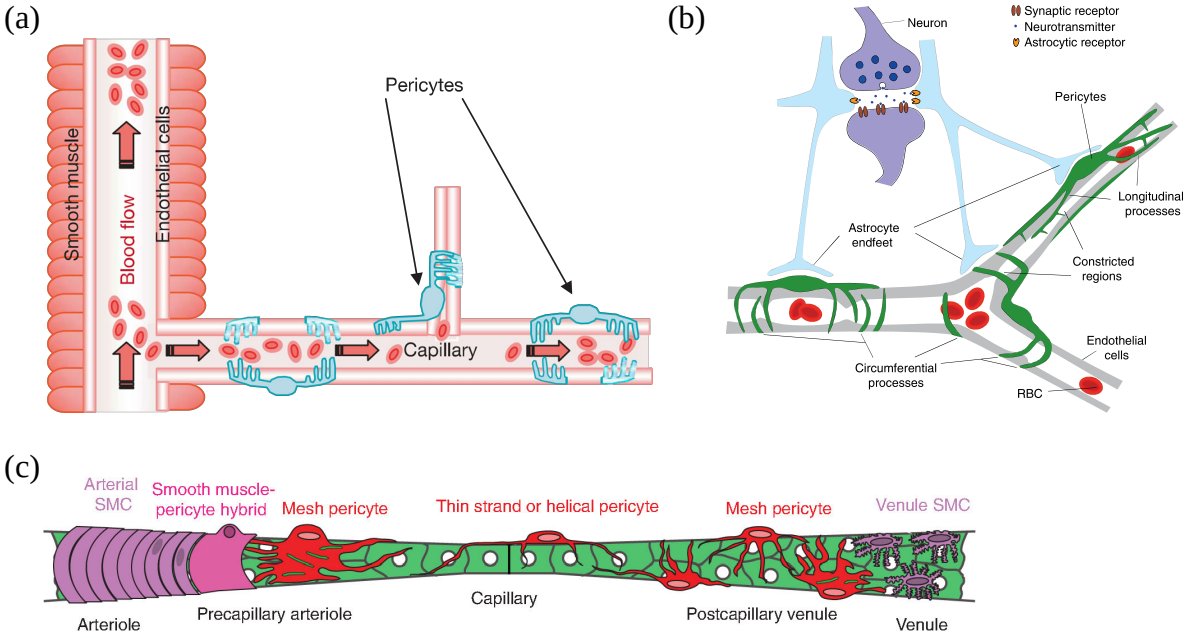

Figure 1.5: Schematic representations of blood flow control cells, neurovascular connections, and pericyte morphology in the cerebral vasculature. **a)** Schematic representation of potential blood flow control cells in the cerebral vasculature: arteriolar smooth muscle cells and pericytes. **b)** Schematic illustrating the connection between neurons, astrocytes, and pericytes. **c)** Schematic depicting the diversity of pericyte morphologies, based on imaging of brain microvasculature in mice expressing fluorescent proteins under NG2 and PDGFRβ promoter control.[4]

pericytes, contractile cells distributed along the capillary network (Fig. 1.5a).

Pericytes were first described in the 1870s by Eberth (1871) and Rouget (1873) as spatially isolated cells with elongated extensions of their membrane and cytoskeleton. The term "pericyte" was later introduced by Zimmermann (1923) in 1923. These cells are located between the endothelial cells and the basal lamina membrane of capillaries. Their morphology varies along the capillary network: near arterioles, they exhibit circumferential extensions; in mid-capillary regions, they show longitudinal extensions; and near venules, they adopt a stellate morphology. Pericytes are identified by their expression of the growth factor receptor PDGFRβ and the proteoglycan NG2 (Fig. 1.5c).

In addition to morphological diversity, pericytes display variation in protein expression. Pericytes with circumferential extensions near arterioles express higher levels of smooth muscle α-SMA (Hill et al., 2015), which suggests a role in cerebral blood flow regulation (Attwell et al., 2016). Mid-capillary pericytes also express α-SMA, but at lower levels (Bandopadhyay et al., 2001); these cells play a critical role in maintaining the blood-brain barrier (Attwell et al., 2016). Pericytes near venules may regulate immune cell entry into the brain parenchyma (Attwell et al., 2016). This thesis focuses on blood flow regulation and, therefore, we concentrate only on pericytes near arterioles, which

[4]Combination of Figure 1a in Peppiatt et al. (2006), Figure 1 in Mishra et al. (2014) and Figure 10 in Hartmann et al. (2015). Reproduced with the publishers's permissions.

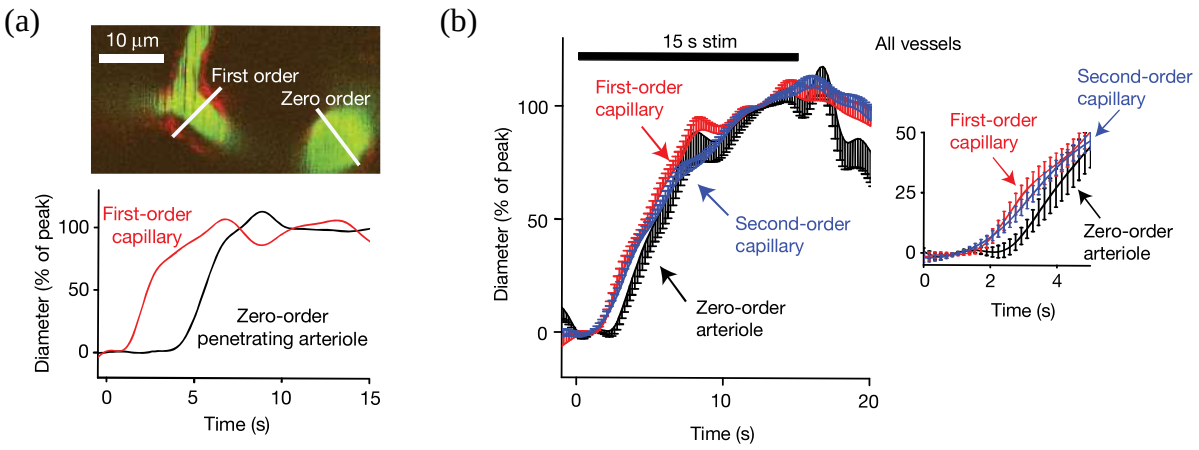

Figure 1.6: Diameter changes and dilation dynamics in penetrating arterioles and capillaries during stimulation. **a)** Example of diameter changes in a simultaneously imaged penetrating arteriole and first-order capillary, with top lines indicating measurement loci, during stimulation. **b)** Dilatation dynamics observed across all responding (>5%) penetrating arterioles and first- and second-order capillaries.[5]

express α-SMA.

As shown in Fig. 1.5b, pericytes are situated in close proximity to the endfeet of astrocytes, which wrap around blood vessels and are positioned near neuronal cell bodies. This spatial organization creates a direct and highly efficient pathway for communication and signaling between neurons, astrocytes, and pericytes.

Pericytes on isolated retinal capillaries have been shown to constrict or dilate in response to neurotransmitters via intracellular Ca^{2+} signaling. Calcium influx depolarizes the pericyte membrane, initiating a cascade of events that align actin filaments within cytoplasmic extensions, ultimately leading to contraction. This mechanism was also demonstrated by Peppiatt et al. (2006), who showed that cerebral pericyte constriction could be inhibited by increasing glutamate levels or reducing extracellular calcium in retina and cerebellar slices. Other stimuli, such as angiotensin II, serotonin, histamine, and noradrenaline, also induce pericyte constriction (Hamilton, 2010). Whereas the Ca^{2+} in astrocytes promotes the generation of arachidonic acid, which is then metabolized in PEG_2 (Sweeney et al., 2016). PEG_2 will then bind to EP_4 receptors, which open the K^+ channels, hyperpolarizing the pericyte and lowering the intercellular calcium Ca^{2+} which inhibits Ca^{2+}-gated chloride ione (Cl^-) channels and induce pericyte relaxation i.e., dilatation (Attwell et al., 2010; Hamilton, 2010; Hall et al., 2014; Sweeney et al., 2016).

Therefore, it is evident that pericytes can influence blood flow, but the extent of this influence relative to that of arterioles remains uncertain. A study by Hall et al. (2014) demonstrated that capillary dilation occurs more rapidly (cr. 1 s) in response to neural activity compared to arteriole dilation, suggesting that pericytes offer a faster and more precise mechanism for regulating local blood flow (Fig. 1.6). However, studies such as Hill et al. (2015) argue that VSMCs are the primary regulators of cerebral blood flow, with

[5]Figure 3d,g in Hall et al. (2014). Reproduced with the publishers's permissions.

pericytes playing a secondary role. Consequently, the respective contributions of arterioles and capillaries to neurovascular coupling continue to be an area of active research.

1.3 Blood Composition

As explained in Section 1.2, blood plays a critical role in transporting oxygen and nutrients to the tissues while removing carbon dioxide and waste products. It maintains homeostasis by regulating body temperature and solute concentrations (e.g., ions, proteins, and hormones) and supports the immune response. In an average adult human, the total circulating blood volume is approximately 5 L, accounting for about 7% of body weight (Alberts, 2017). During the cardiac cycle, $\approx$ 9% of the blood volume is in the pulmonary circulation, $\approx$ 7% in the heart, and $\approx$ 84% in the systemic circulation. If we divide the systemic circulation, we will find $\approx$ 13% of the total blood volume in the arteries, $\approx$ 7% in the capillaries, and the remainder $\approx$ 64% in the venis and venules (Hall, 2015a).

Blood is a complex fluid and is composed of plasma (the liquid part $\approx$ 54%) and suspended blood cells. The blood cells are composed of erythrocytes (red blood cells, RBC, $\approx$ 45%), leukocytes (white blood cells, WBC, $< 1\%$), and thrombocytes (platelets, $< 1\%$).

Plasma is considered a Newtonian fluid with a viscosity of about 1.5 mPa s in healthy individuals (Rand et al., 1964). It is an aqueous solution primarily composed of ions such as Na^+, K^+, Ca^{2+}, and Cl^- (95% of plasma) (Hall, 2015b). Additionally, plasma contains macromolecules, including fibrinogen (5%), albumin (50%), and globulin (45%) (Hall, 2015c).

All blood cells have different lifetimes (about 120 days for RBC, from hours to years for WBC, and around 10 days for plates); therefore, they need to be produced throughout the lifetime of a human. They all originate from hematopoietic stem cells located in the bone marrow.

Leukocytes (WBC) are nucleated cells that are key players in the immune system. Although they make up less than $< 1\%$ of the blood volume, they are larger than RBCs and can adhere to endothelial walls, potentially obstructing small vessels and influencing RBC distribution.

Thrombocytes (Platelets) are cell fragments that are essential for coagulation. They participate in the conversion of soluble fibrinogen into insoluble fibrin, forming a solid matrix that prevents blood flow in cases of injury.

Erythrocytes (RBC) are nucleus-free cells that are primarily responsible for oxygen and carbon dioxide transport. Their detailed properties are discussed in Section 1.3.1.

Since RBCs occupy the majority of the non-liquid volume, they significantly contribute to blood's rheological behavior. The fraction of blood volume occupied by RBCs, known as the hematocrit, ranges from 37% and 52% in healthy individuals. Systemic hematocrit levels deviate in pathological conditions, such as polycythemia (elevated hematocrit) or anemia (reduced hematocrit).

Table 1.1: Values of density, concentration, mean corpuscular volume (MCV) and diameter of the blood cells. [a] Data from Randaelli and Montevecchi (2012). [b] Data from Alberts (2017). [c] Mean from Amin and Sirs (1985), Lewis (1996a), Salvioli et al. (1993) and Tomaiuolo et al. (2012). [d] Data from Lewis (1996b).

Cell type	Density $[\mathrm{kg\,m^{-3}}]$[a]	Concentration $[\mathrm{cells\,L^{-1}}]$ [b]	MCV $[\mu\mathrm{m}^3]$	Diameter $[\mu\mathrm{m}]$
Erythrocytes (RBC)	1090	$5 \cdot 10^{12}$	87.6[c]	7.3 [d]
Leukocytes (WBC)	1070			
Neurophils		$5 \cdot 10^{9}$	440[a]	$12 - 14$[a]
Eosinophils		$2 \cdot 10^{8}$	440[a]	$12 - 17$[a]
Basophils		$4 \cdot 10^{7}$	440[a]	$14 - 16$[a]
Monocytes		$4 \cdot 10^{8}$	400[a]	20[a]
B cells		$\approx 0.3 \cdot 10^{9}$		
T cells		$\approx 2 \cdot 10^{9}$		
Natural killer cells		$1 \cdot 10^{8}$		
Platelets	1030	$3 \cdot 10^{11}$	15[a]	3[a]

Table 1.1 provides a summary of numerical values for blood cells: density, concentration, mean corpuscular volume (MCV) and diameter.

1.3.1 Red Blood Cell (RBC)

The formation of an RBC, known as erythropoiesis, begins with a nearly spherical cell measuring approximately $20 - 25\,\mu$m in diameter, referred to as a proerythroblast (Peter Klinken, 2002). This cell contains a nucleus and a cytoplasm rich in ribonucleic acid (RNA). At this stage, hemoglobin is absent; its synthesis commences only after the proerythroblast differentiates into an erythroblast. During its development, the erythroblast undergoes multiple stages, during which its diameter decreases progressively to around $10\,\mu$m, while hemoglobin concentration in the cytoplasm steadily increases. Eventually, the erythroblast expels its nucleus and transforms into a reticulocyte, acquiring the characteristic biconcave shape of a mature RBC, as illustrated in Fig. 1.7a.

From the bone marrow, reticulocytes migrate into the circulatory system, where they complete their maturation within two to three days, becoming fully developed erythrocytes (Peter Klinken, 2002). The fine mean corpuscular volume (MCV_{RBC}) of a human RBC is $87.6\,\mu\mathrm{m}^3$ (Amin and Sirs, 1985; Lewis, 1996a; Salvioli et al., 1993; Tomaiuolo et al., 2012) and has a mean diameter of $7.3\,\mu$m (Lewis, 1996b). Remarkably, approximately two million reticulocytes are produced every second in the human body.

The erythrocyte membrane comprises three primary layers: the glycocalyx, the lipid bilayer, and the cytoskeleton (Fig. 1.7b).

The glycocalyx is located on the external surface of the RBC. It primarily consists of glycoproteins and glycolipids, which are responsible for interactions between the RBCs and other cells, such as blood cells and endothelial wall cells.

The lipid bilayer is composed mainly of cholesterol and phospholipids. Embedded within this bilayer are proteins essential for the transport of solutes, including gases and

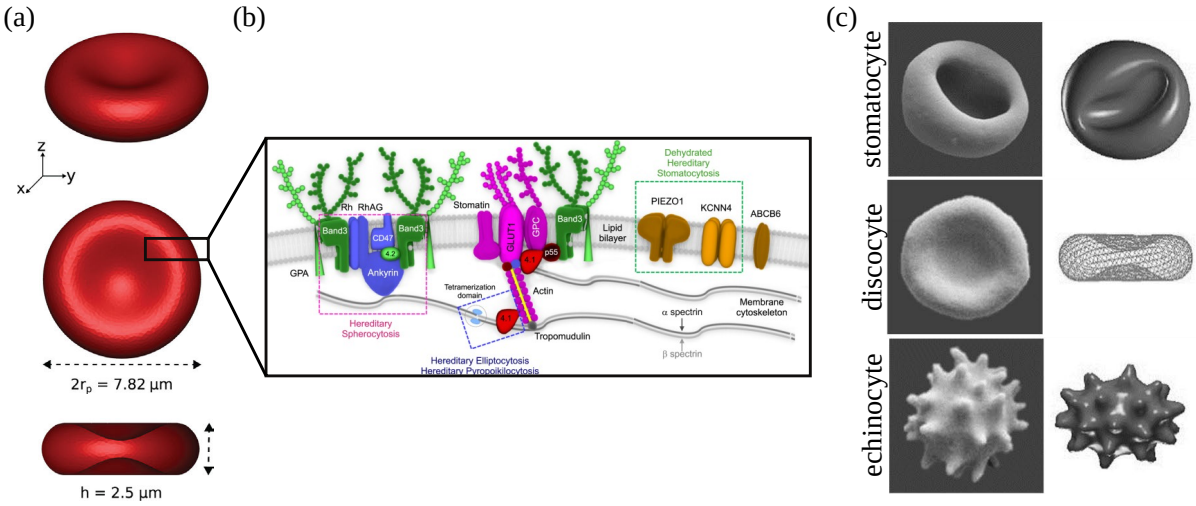

Figure 1.7: Red blood cell geometry, membrane structure and shape. **a)** Red blood cell geometry. **b)** Schematic representation of RBC membrane structure with major functional components. **c)** Comparison of shape of different RBCs seen with scanning electron microscopy (first column) and numerical simulation (second column). The first row is a stomatocyte, the second row is a healthy RBC (discocyte), and the last row is an echinocyte.[6]

ions, between the RBC and its surrounding environment. The bilayer is linked to the cytoskeleton through the protein actin. Cholesterol is evenly distributed between the two sides of the bilayer, whereas phospholipids are asymmetrically arranged.

Proteins within the lipid bilayer extend from the inner surface to the outer surface of the membrane, making them transmembrane proteins. These proteins have two distinct domains: a hydrophilic region exposed to plasma and a hydrophobic region interacting with the cytoplasm. Transmembrane proteins fulfill critical roles, such as transporting ions and molecules, facilitating adhesion between RBCs and endothelial cells, and maintaining structural integrity by anchoring the membrane to the cytoskeleton. Given the unique role of RBCs in gas exchange, transmembrane proteins involved in molecular transport are indispensable to their function.

The cytoskeleton is a structural network primarily composed of actin and spectrin, which provides the RBC membrane with mechanical stability and flexibility. The protein actin links the lipid bilayer to the cytoskeleton, enabling RBCs to traverse even the narrowest capillaries. Protein 4.1 plays a critical role in maintaining membrane integrity; without it, the characteristic discoid shape of RBCs is compromised, leading to ellipsoidal or spherical shapes. α- and β-spectrin are the predominant cytoskeletal proteins, forming long, flexible structures that assemble into heterodimers or tetramers. When structural proteins are absent due to hereditary conditions, the membrane becomes unstable, lipids are not retained, and the RBC exhibit increased susceptibility to shape changes or fusion (Dalal et al., 2024).

The fluid inside an erythrocyte (cytoplasm) is an aqueous solution (80%) rich in

[6]Figure 2 in Mantegazza et al. (2024), Figure 1 in Kim et al. (2017) and part of Figure 3 in Geekiyanage et al. (2019). All reproduced under CC BY 4.0.

proteins, with hemoglobin as the most abundant, accounting for approximately 90% of all cytoplasmic proteins. Hemoglobin concentration ranges from 12-18 g/dL (Lewis, 1996a), with an average of 13.9 g/dL in women and 15.3 g/dL in men (Peter Klinken, 2002). Each hemoglobin molecule can bind four oxygen molecules, and when oxygen is bound, the complex is referred to as oxyhemoglobin. On average, 98% of the oxygen circulating in the human body is carried by hemoglobin.

Healthy erythrocytes typically exhibit their iconic discoid shape. However, under certain conditions, they can undergo morphological changes, resulting in stomatocytes or echinocytes (Fig. 1.7c). Stomatocytes are swollen, cup-shaped cells caused by altered membrane permeability or exposure to acidic solutions with a pH lower than plasma. Conversely, echinocytes are irregularly spiky cells that form in response to high-pH solutions, elevated intracellular calcium levels, or adenosine triphosphate (ATP) deficiency (Geekiyanage et al., 2019).

The fundamental properties of erythrocytes remain largely consistent across mammalian species, unlike non-mammalian species, such as birds, whose erythrocytes retain nuclei. Among mammals, the primary differences are in erythrocyte size and count. In this thesis, we use both human and rabbit erythrocytes. Rabbit erythrocytes have a smaller MCV ($MCV_{\mathrm{RBC,rabbit}} = 68.6\,\mu\mathrm{m}^3$ (Kim et al., 2002; Lewis, 1996c; Windberger et al., 2003)) and diameter compared to human erythrocytes. The hemoglobin content in rabbit erythrocytes is slightly lower (12.8 g/dL (Lewis, 1996c)), suggesting they may carry less oxygen. Despite these differences, no significant variation in cell shape or rheological properties under flow conditions was observed.

1.4 Fluid Dynamics in the Capillary System

In fluid dynamic analysis, various dimensionless numbers are employed to characterize flow regimes in fluids. Two key parameters for blood flow in the circulatory system are the Reynolds number (Re) and the Womersley number (Wo).

The Reynolds number represents the ratio of inertial forces to viscous forces in a fluid, calculated as:

$$Re = \frac{\text{inertial forces}}{\text{viscous forces}} = \frac{U\rho L_{\mathrm{ref}}}{\mu}\,, \tag{1.1}$$

where U is the characteristic velocity, ρ is the fluid density, L_{ref} is the characteristic length scale (e.g., pipe diameter), and μ is the dynamic viscosity. At low Reynolds numbers ($Re \ll 1$), flow is laminar, and viscous forces dominate over inertial forces. When $Re > 1$, inertial forces become significant, and above a critical Reynolds number (e.g., $Re > 2300$ for pipe flow), the flow transitions to turbulence.

The Womersley number quantifies the ratio of transient inertial forces to viscous forces, particularly relevant for pulsatile flows like blood circulation:

$$Wo = L_{\mathrm{ref}}\sqrt{\frac{2\pi f\rho}{\mu}} = L_{\mathrm{ref}}\sqrt{\frac{\omega\rho}{\mu}}\,, \tag{1.2}$$

where $\omega = 2\pi f$ is the angular frequency of oscillations, f is the oscillation frequency, ρ is the fluid density, L_{ref} is the characteristic length, and μ is the dynamic viscosity. When

Table 1.2: Characteristic dimensions, Re number, and Wo number of blood vessels in the human body.[7]

Vessel type	**Diameter** [mm]	**Length** [cm]	**Re**	**Wo**
Ascending aorta	30	4	4000	10.5
Thoracic aorta	20	15	2500	7.7
Iliac artery	5	20	1000	3.5
Femoral artery	7	45	800	2.8
Small artery	2	10	100	1.4
Arteriole	0.02	0.4	0.5	0.014
Capillary	0.01	0.002-0.1	0.003	0.007
Venule	0.02	0.4	0.5	0.014
Small vein	2	10	100	1.4
Large vein	8	50	1700	5.6

$Wo > 1$, pulsatility significantly influences the flow; for $Wo < 1$, viscous effects dominate, and pulsatility can be neglected.

Table 1.2 illustrates the variation in flow parameters across different blood vessels. For instance, flow in the aorta is pulsatile and turbulent ($Re > 2300$ and $Wo > 1$), while flow in the microcirculation is laminar and non-pulsatile ($Re \ll 1$ and $Wo < 1$).

In blood flow, the conservation of mass and momentum govern its behavior. Since blood can be considered incompressible in physiological flow regimes, the governing equations are the incompressible continuity equation and the Navier-Stokes equations:

$$\nabla \cdot \mathbf{u} = 0\,, \tag{1.3}$$

$$\rho \frac{\partial}{\partial t}\mathbf{u} + \rho(\mathbf{u} \cdot \nabla)\mathbf{u} = -\nabla p + \mu \nabla^2 \mathbf{u}\,, \tag{1.4}$$

where $\mathbf{u}$ is the velocity vector, ρ is fluid density, p is pressure, and μ is dynamic viscosity.

The Navier-Stokes equations can be expressed in a dimensionless form as follows:

$$\nabla' \cdot \mathbf{u}' = 0\,, \tag{1.5}$$

$$Wo^2 \frac{\partial}{\partial t'}\mathbf{u}' + Re(\mathbf{u}' \cdot \nabla')\mathbf{u}' = -Re\nabla' p' + \nabla'^2 \mathbf{u}'\,, \tag{1.6}$$

where the prime ($'$) denotes dimensionless quantities: coordinates, velocity, and pressure.

In large blood vessels, blood can be approximated as a Newtonian fluid with constant density and dynamic viscosity. Under normal physiological conditions and a hematocrit level of 45%, the density of blood is $\rho_{\text{blood}} = 1060\,\text{kg}\,\text{m}^{-3}$ and the dynamic viscosity varies between $\mu_{\text{blood}} = 3.2\,\text{Pa}\,\text{s}$ and $\mu_{\text{blood}} = 4.2\,\text{Pa}\,\text{s}$.

In the microcirculation, however, the assumptions of constant viscosity and density no longer hold. Instead, the blood density depends on the volumetric hematocrit (H_t) within a given capillary and can be calculated as:

$$\rho_{\text{blood,micro}} = (1 - H_\text{t})\rho_{\text{plasma}} + H_\text{t}\rho_{\text{RBC}}\,, \tag{1.7}$$

[7] Adapted Table 1.1 in Frey (2018). Reproduced with permission.

where $\rho_{\text{plasma}} = 1028\,\text{kg}\,\text{m}^{-3}$ is the density of plasma, and $\rho_{\text{RBC}} = 1090\,\text{kg}\,\text{m}^{-3}$ is the density of RBCs.

The viscosity of blood is influenced by multiple factors, including plasma viscosity, protein concentration, hematocrit, temperature, shear rate, and the diameter of the capillary. This variability makes it challenging to define general values for density and viscosity. In particular, the dependence of blood viscosity on capillary diameter is described by the Fåhræus-Lindqvist effect, which will be discussed in Section 1.6.2.

Since in this thesis, we are interested in the microcirculation, the low Reynolds and Womersley numbers ($Re = 0.003$ and the $Wo = 0.007$) simplify Equation 1.4 to the Stokes equations:

$$\nabla \cdot \mathbf{u} = 0\,, \tag{1.8}$$

$$\nabla p = \mu \nabla^2 \mathbf{u}\,. \tag{1.9}$$

Here, the convective term (due to the low Re) and the time derivative are negligible (due to the low Wo), resulting in laminar flow.

1.4.1 Poiseuille Flow

The Stokes equations 1.8 and 1.9 have an analytical solution for flow in a straight pipe with a constant cross-sectional area, known as Poiseuille flow. This solution applies under steady-state conditions for an incompressible Newtonian fluid in a rigid pipe with negligible gravity and no-slip boundary conditions (zero velocity at the walls). Since capillaries can be modeled as straight pipes with constant cross-sectional areas, we can adopt this solution:

$$u_z(r) = -\frac{\Delta p}{4\mu L} r^2 + C_1 ln(r) + C_2\,, \tag{1.10}$$

where L is the length of the pipe, r is the radial coordinate and $\Delta p = p_2 - p_1$ is the pressure difference between the ends of the pipe (Fig. 1.8). The logarithmic term, $C_1 ln(r)$, introduces a singularity at $r = 0$, which is physically unrealistic since the velocity exists at $r = 0$. Therefore, $C_1 = 0$. Applying the no-slip boundary condition, $u_z(a) = 0$ (where a is the pipe radius), we find $C_2 = \frac{\Delta p}{4\mu L} a^2$. Substituting these conditions into the original equation simplifies it to:

$$u_z(r) = \frac{\Delta p}{4\mu L}(a^2 - r^2)\,. \tag{1.11}$$

This equation describes a parabolic velocity profile, with the maximum velocity at the pipe center ($r = 0$), where it is twice the mean velocity. From here, to calculate the volumetric flow rate Q, we integrate the velocity profile over the cross-sectional area of the pipe. For an infinitesimal cross-section:

$$dQ = u_z(r) dA\,. \tag{1.12}$$

Performing the integration yields:

$$Q = \int_A v_z(r) dA \quad \rightarrow \quad Q = \frac{a^4 \pi}{8\mu L} \Delta p\,, \tag{1.13}$$

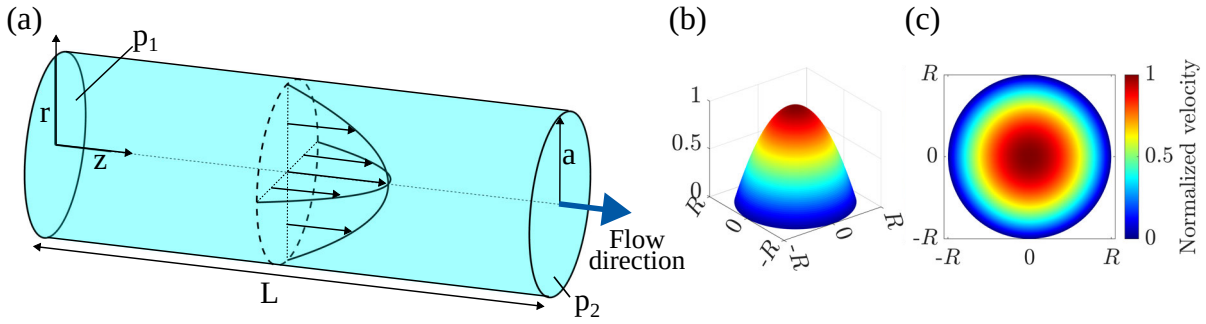

Figure 1.8: Schematic of Poiseuille flow. **a)** Schematic illustrating Poiseuille flow in a cylindrical pipe with radius a and length L, driven by a pressure difference $\Delta p = p_2 - p_1$. **b)** 3D representation of the normalized velocity profile within the pipe. **c)** 2D cross-sectional view of the normalized velocity distribution.

where Q is the volumetric flow rate, μ is the dynamic viscosity, L is the pipe length, a is the pipe radius, and Δp is the pressure difference.

From the flow rate equation, we can derive the hydraulic resistance R, defined as the ratio of the pressure difference to the flow rate:

$$R = \frac{\Delta p}{Q} = \frac{8\mu L}{\pi a^4}\,. \tag{1.14}$$

1.4.2 Flow in Rectangular Channels

In this thesis, the microfluidic chip channels have a rectangular cross-section due to fabrication limitations, as discussed in Section 2.2. Therefore, understanding flow behavior in rectangular channels relative to circular channels is essential.

Starting with the dimensionless form of the Stokes equations 1.8-1.9, and assuming steady-state conditions, an incompressible Newtonian fluid, rigid walls, negligible gravity, and no-slip boundary conditions, we arrive at the simplified equation:

$$\frac{\partial^2 u'}{\partial y'^2} + \frac{\partial^2 u'}{\partial z'^2} = Re\frac{\partial p'}{\partial x'} \tag{1.15}$$

However, as demonstrated by Spiga and Morino (1994) and Oosterbroek (1999), obtaining an exact analytical solution for the momentum equation in rectangular ducts is impossible. Instead, solutions are expressed as Fourier series expansions:

$$u'(y,z) = \frac{16\beta^2}{\pi^4}\sum_{n\,odd}^{\infty}\sum_{m\,odd}^{\infty}\frac{sin(n\pi\frac{y}{W})sin(m\pi\frac{z}{H})}{nm(\beta^2 n^2 + m^2)}\,, \tag{1.16}$$

where $\beta = H/W$ is the aspect ratio of the rectangle, W is the width, and H is the height of the channel.

For a first-order approximation, the velocity profile simplifies to:

$$u'(y,z) = -\frac{5}{8}\left[\frac{(y^2 - (0.5W)^2))(z^2 - (0.5H)^2)}{(0.5W)^2 + (0.5H)^2}\right]\,. \tag{1.17}$$

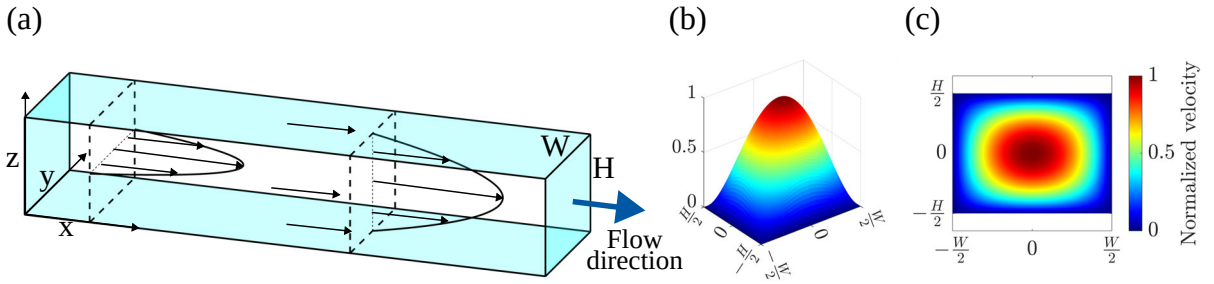

Figure 1.9: Schematic of flow in a rectangular channel. **a)** Schematic illustrating flow in a rectangular channel with a width W and height H. **b)** 3D representation of the normalized velocity profile within the channel. **c)** 2D cross-sectional view of the normalized velocity distribution.

This results in a paraboloid velocity profile, where the shape depends on the aspect ratio of the rectangular duct. An example of this profile is illustrated in Fig. 1.9. The hydraulic resistance for flow in a rectangular duct can be approximated as:

$$R = \frac{64\mu L}{WH^3}\left[\frac{16}{3} - 3.36\frac{H}{W}\left(1 - \frac{H^4}{12W^4}\right)\right]^{-1} . \tag{1.18}$$

To calculate the Re number and Wo number for rectangular channels, the characteristic length is the hydraulic diameter D_h, defined as:

$$D_\mathrm{h} = \frac{2 \cdot (W \cdot H)}{H + W} . \tag{1.19}$$

This parameter accounts for the geometry of the rectangular channel and allows comparison with circular channels.

1.5 Red Blood Cell Dynamics

The dynamics of RBCs are fundamental to microcirculation and significantly impact various physiological processes. These dynamics are shaped by their physical and mechanical properties, as well as their behavior in flow conditions. In this context, RBC dynamics refers to the motion of RBCs as they flow through capillaries. Describing these dynamics is highly complex, even in simple shear flow, as it involves mechanisms at the scale of a single cell.

Key aspects of RBC dynamics include their deformability, motion as single cells, tendency to aggregate, and their axial concentration in flow. Investigating these dynamics requires consideration of numerous aspects, such as cell-to-fluid and cell-to-cell interactions, the fluid's and RBC's rheological properties (e.g., the cytoplasm's ratio to plasma viscosity), and shear stress distribution. While a complete discussion on this topic is beyond the scope of this work, this section highlights the essential RBC dynamics.

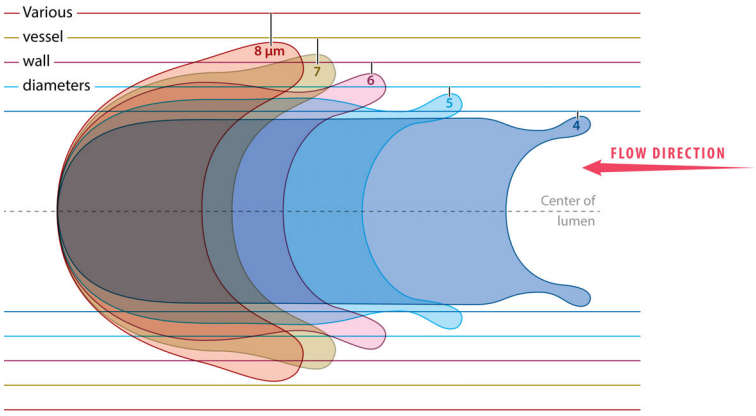

Figure 1.10: Axisymmetric RBC shapes in vessels with diameters ranging from 4 μm to 8 μm. The corresponding three-dimensional cell shapes were derived by rotating the computed axisymmetric profiles around the central axis (Secomb et al., 1986). The RBC velocity was set to 0.1 mm/s for these calculations.[8]

1.5.1 Deformability of Red Blood Cells

As discussed in Sections 1.2.2 and 1.3.1, capillary vessel diameters range from 5 to 10 μm, while RBCs have an average diameter of approximately 7.3 μm. Consequently, RBCs must deform to flow in these narrow vessels. One of the earliest models to explore RBC deformation in vessels of varying dimensions was developed by Secomb et al. (1986). The relationship between vessel diameter and RBC deformation is illustrated in Fig. 1.10. RBCs adopt a parachute-like shape when they flow in a vessel with a diameter of 8 μm, forming a cell-free layer between the vessel wall and the RBC. In narrower vessels, the cells deform further into a bullet-like shape. This simulation was based on two key assumptions: an axisymmetric cell shape and the application of lubrication theory to describe plasma flow between the RBC and the vessel wall. These simulation results were later validated by *in vitro* experiments (Tomaiuolo and Guido, 2011; Tomaiuolo et al., 2016).

The deformability of RBCs arises from the properties of their membranes and cytoskeleton structure. The RBC cytoskeleton's surface area exceeds the inner surface area it covers, and theoretical estimates suggest that the spectrin chains are approximately three times longer than required to connect adjacent actin molecules (Smith, 1987). This configuration imparts significant tensile strength and deformability to the RBC membrane.

The geometric characteristics of the RBC membrane, particularly the surface-to-volume (S/V) ratio, also play an important role in maintaining deformability. For example, with a MCV of 87.6 μm^3 and a surface area of approximately 142 μm^2 (Salvioli et al., 1993), the S/V ratio is calculated to be 1.62 μm^{-1}. A high S/V ratio is critical for RBC deformability as demonstrated by Viallat and Abkarian (2014) where the reduced surface area in malaria-affected RBC was correlated with cell stiffening.

Aging also impacts RBC properties. Over time, the volume, surface area, and cytoplasmic content of RBC decreases, with cytoplasmic content decreasing by approximately

[8] Figure 2 in Secomb (2017). Reproduced with the publisher's permission.

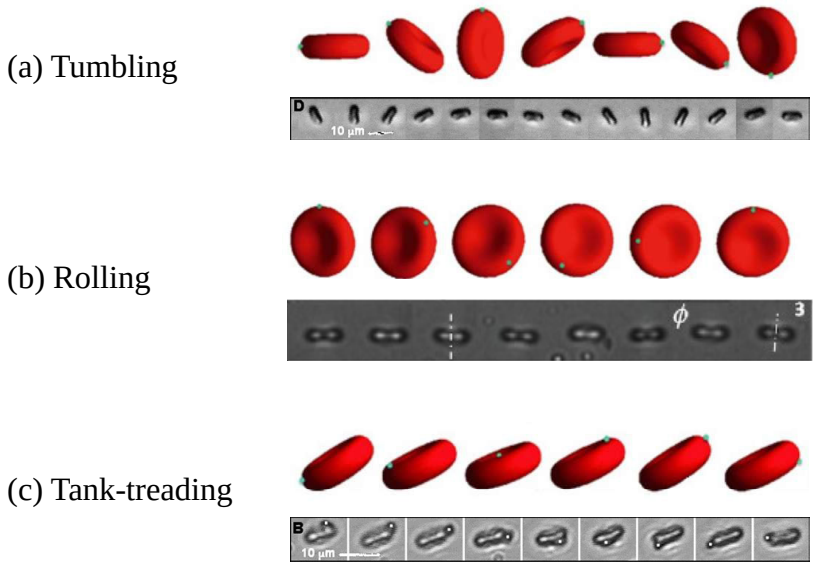

Figure 1.11: Red blood cells in shear flow: schematic and *in vitro* visualization. **a)** Schematic representation of a tumbling RBC alongside an *in vitro* image depicting the same motion. **b)** Schematic representation of a rolling RBC accompanied by an *in vitro* top view illustrating the same rolling motion. **c)** Schematic representation of a tank-treading RBC, alongside an *in vitro* image depicting the same motion with the rotation of a bead (diameter 1 μm) adhered to the RBC membrane.[9]

20% (Corrons et al., 2021). This reduction results in increased hemoglobin concentration, which alters cytoplasmic viscosity and further affects deformability.

In summary, RBC deformability is governed by three primary factors: the rheological and structural properties of the membrane, the S/V ratio, and the cytoplasmic viscosity.

1.5.2 Motion of a Single Red Blood Cell

When examining the motion of a single RBC in an unconfined vessel, distinctive dynamic motions are observed, enabling the cell to minimize energetically unfavorable deformations (Dupire et al., 2012; Viallat and Abkarian, 2014). Various types of RBC motion have been identified, including tumbling, tank-treading, rolling, swinging, and chaotic motion. These behaviors are influenced by specific shear rates, viscosity differences between the cytoplasm and plasma, and the initial orientation of the RBC.

Tumbling resembles an unstable flipping motion, much like a coin flipping through the air, where the RBC does not deform and maintains a biconcave shape (Dupire et al., 2012). The axis of symmetry for this motion aligns with the velocity vector. Tumbling typically occurs at low shear rates and when the cytoplasmic viscosity is higher than the plasma viscosity. Fig. 1.11a illustrates this behavior. As the shear rate increases, tumbling transitions into rolling. During rolling, the RBC continuously rotates, like a coin rolling on a table, with the axis of symmetry perpendicular to the shear plane (Abkarian and

[9]Combination of Figure 1 and 2 in Viallat and Abkarian (2014) and Figure 1 in Abkarian and Viallat (2008). Reproduced with the publisher's permissions.

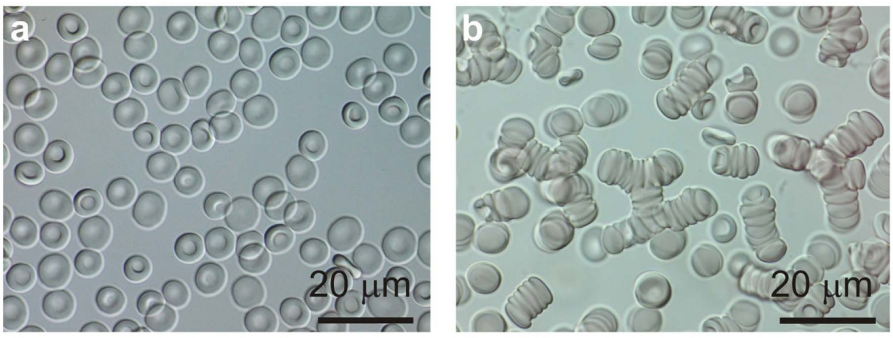

Figure 1.12: Image of single RBCs and aggregated RBCs in a solution. **a)** Single RBCs in a buffer solution. **b)** Aggregated RBCs (rouleaux) in a 20 mg/mL dextran solution within a Petri dish.[10]

Viallat, 2008) (Fig. 1.11b). This motion allows the cell to minimize energy consumption to do membrane deformations.

As the shear rate further increases and the cytoplasmic viscosity becomes significantly lower than the plasma viscosity, rolling transitions into tank-treading. In this motion, the RBC membrane rotates around the cell's center of mass while maintaining a stable cell orientation (Fig. 1.11c). This phenomenon arises from the unique structure of the RBC, where the cytoskeleton and plasma membrane form a tightly coupled layer near the cell surface, and the absence of cytoskeletal elements within the cytoplasm allows the membrane and cytoskeleton to move independently (Basu et al., 2011).

Abkarian et al. (2007) explored RBC dynamics at moderate shear rates near the tumbling-to-tank-treading transition and observed a phenomenon called swinging. In this state, the RBC undergo tank-treading motion, but its orientation relative to the main flow direction oscillates over time. Interestingly, under oscillatory or pulsatile flow conditions, tumbling and tank-treading can coexist, resulting in chaotic RBC dynamics with irregular yet sometimes stable and synchronized orientations.

These motion patterns highlight the adaptability of RBCs in various flow conditions, contributing to their remarkable ability to navigate complex vascular environments.

1.5.3 Aggregation of Red Blood Cells

Aggregability is another fundamental property of RBCs that influences their behavior in both physiological and pathological contexts. This phenomenon is due to the presence of macromolecules dissolved in plasma, such as fibrinogen, which encourage RBC aggregation and lead to the formation of large structures known as rouleaux (Fig. 1.12).

Currently, there is no consensus on whether small RBC aggregation has a negative impact. Similarly, the mechanisms driving this phenomenon remain under debate. Two primary hypotheses, both centered on the role of fibrinogen, have been proposed to explain the origins of RBC aggregation (Wagner et al., 2013).

The first hypothesis suggests that fibrinogen, being positively charged, is adsorbed onto the negatively charged RBC surface, creating molecular bridges between neighboring

[10]Part of Figure 3 in Brust et al. (2014). CC BY-NC-ND 3.0.

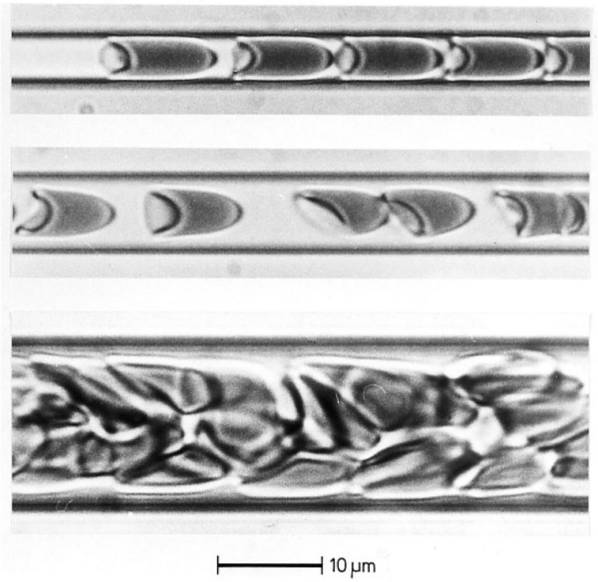

Figure 1.13: Single-file and multi-file flow of human RBC. RBCs flow in glass tubes of approximate diameters 4.5 μm, 7 μm, and 15 μm top to bottom. The flow direction is from left to right.[11]

RBCs. These bridges are strong enough to overcome the electrostatic repulsion between the RBCs. The second hypothesis suggests that aggregation results from localized fibrinogen depletion in the space between adjacent RBCs. This depletion generates attractive forces due to the concentration gradients of fibrinogen, which intensify as the cells move closer together (Neu and Meiselman, 2002).

RBC aggregation is reversible: rouleaux formation occurs at low shear rates or in static conditions, but as the shear rate increases, the RBCs start to detach from each other. This reversibility supports the hypothesis that rouleaux formation is most prevalent on the venous side of the cardiovascular system, where blood flow velocity is lowest. However, under physiological conditions, rouleaux are not observed in the microcirculation because the shear rates in these regions are sufficiently high to prevent aggregation. Athletic mammals, such as horses, are known to exhibit greater RBC aggregability than humans. This distinctive feature raises intriguing questions about whether aggregation might serve functional advantages, such as optimizing RBC transport within the circulatory system (Brust et al., 2014). The study of RBC aggregation remains an open field, with many unanswered questions surrounding its biological significance.

1.5.4 Axial Concentration of Red Blood Cells

In the capillary vessels, we can observe two different RBC configurations of flow: a single-file and a multi-file flow (Fig 1.13). Multi-file flow is present when the cell-to-tube diameter (confinement ratio λ) is bigger than 1, where the RBC has enough space for a radial distribution of the RBC in the vessel. This is normally the case at $D \geq 8\,\mu$m. If the diameter of the vessel is between 6 μm and 8 μm, a multi-file flow is observed if high

[11] Figure 4.1.1 in Secomb and Pozrikidis (2003). Reproduced with the publisher's permission.

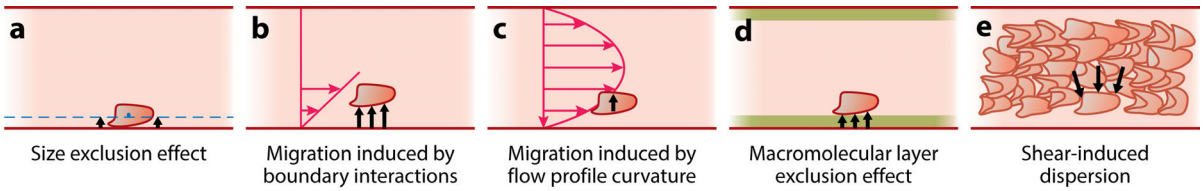

Figure 1.14: Mechanisms causing lateral migration of RBCs flowing in microvessels. **a)** Size exclusion effect. **b)** Migration induced by boundary interaction. **c)** Migration induced by flow profile curvature. **d)** Macromolecular layer exclusion effect. **e)** Shear-induced dispersion.[12]

hematocrit is present, whereas a single-file flow is observed if low hematocrit is present. For lower vessel diameter ($D \leq 6\,\mu$m), only single-file flow is present, and due to their high confinement ratio, they deform in a bullet shape and low along the vessel centerline.

Interestingly, both for the single-file and the multi-file flows, a thin cell-free layer (CFL) close to the walls is observed. This CFL has a thickness of a few microns with the local viscosity of blood plasma, and it has fundamental implications for the dynamics of blood flow in the capillary vessels (Section 1.6).

There are different phenomena promoting the radial distribution of RBCs leading to the formation of the CFL:

a) Size exclusion effect. The margination of the cells due to their finite size limits the radial position the cell center can occupy. The center of the cell can not be closer than $1\,\mu$m to the wall since the cell min thickness is $2\,\mu$m (Fig. 1.14a).

b) Migration induced by boundary interaction. Deformable particles and RBCs tend to migrate away from the solid boundaries (Fig. 1.14b). A comprehensive mechanistic understanding of the phenomenon remains unknown. In all reported experiments (Grandchamp et al., 2013; Secomb and Pozrikidis, 2003) and simulations (Coupier et al., 2008; Doddi and Bagchi, 2009), deformable RBCs and vesicles near the wall appear to migrate away from it. However, no definitive proof has been provided to establish that this behavior is universally true for such particles.

c) Migration induce by flow profile curvature. The parabolic flow profile in the vessel creates a non-uniform shear stress distribution, which exerts a force on RBCs, causing them to migrate radially toward the center of the vessel (Fig. 1.14c).

d) Macromolecular layer exclusion effect. Endothelial cells have glycolipids, glycoproteins, and proteoglycans on their surfaces (endothelial surface layer). This layer is a porous medium, making the flow of RBCs in this layer impossible (Fig. 1.14d).

e) Shear-induced dispersion. This effect acts opposite to the others, where frequent interactions between particles result in a net migration away from regions of higher concentration, moving the RBCs toward the wall (Fig. 1.14e).

[12]Figure 3 in Secomb (2017). Reproduced with the publisher's permission.

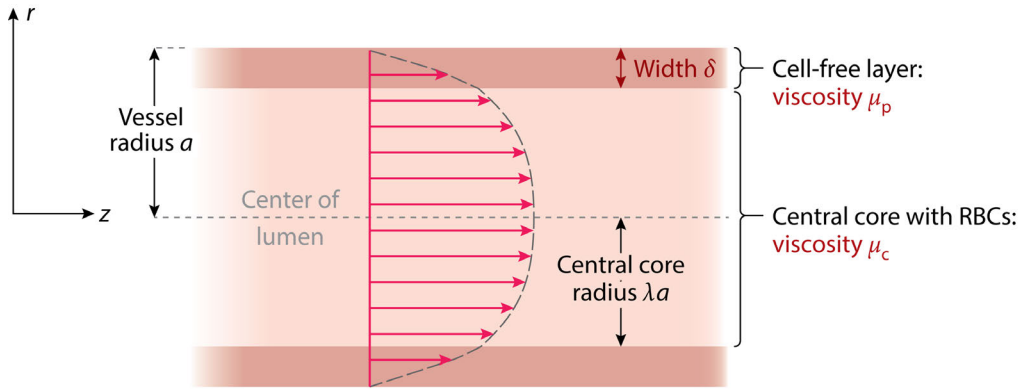

Figure 1.15: Two-phase model of the blood flow in a microvessel with a typical resulting velocity profile.[13]

If we consider the flow in the vessel, we can split the flow field into two sections: the center (core), which contains all the RBCs, and near the CFL (Fig. 1.15). Here, the flow profile is not a Poiseuille flow (parabolic profile, Section 1.4.1), but a plug flow where, in the core, we have an almost constant velocity, and in the CFL is where we have the velocity gradient from zero at the wall to the core velocity at the interface between the two. We can describe the velocity profile using a two-phase model derived by Vand (1948) derived from Poiseuille's velocity profile:

$$u_z(r) = \begin{cases} \frac{\Delta p\, a^2}{4L}\left[\frac{\kappa^2 - r^2/a^2}{\mu_{\text{RBC}}} + \frac{1-\kappa^2}{\mu_{\text{plasma}}}\right], & \text{if } r < \kappa a\,, \\ \frac{\Delta p\, a^2}{4L}\frac{1-r^2/a^2}{\mu_{\text{plasma}}}, & \text{if } r \geq \kappa a\,, \end{cases} \tag{1.20}$$

where $\kappa = 1 - \delta/a$ is the core to the tube radius ratio, δ is the thickness of the CFL, and a id the tube radius. And the blood flow rate is:

$$Q(r) = \begin{cases} \frac{\Delta p\, \pi\, a^2}{4\mu_{\text{plasma}} L}\left[a^2 - \left(1 - \frac{\mu_{\text{plasma}}}{2\mu_{\text{RBC}}}\right)\frac{(a-\delta)^4}{a^2}\right], & \text{if } r < \kappa a\,, \\ \frac{\Delta p\, \pi}{8\mu_{\text{plasma}} L}\left[a^2 - (a-\delta)^2\right]^2, & \text{if } r \geq \kappa a\,. \end{cases} \tag{1.21}$$

And the total blood flow rate is the sum of the two:

$$Q = \frac{\Delta p\, \pi\, a^4}{8\mu_{\text{plasma}} L}\left(1 - \kappa^4 \frac{\mu_{\text{plasma}}}{\mu_{\text{RBC}}}\right). \tag{1.22}$$

As will be demonstrated later in this thesis, the distribution of RBC at the capillary level plays a critical role in their partitioning behavior at bifurcations, which will significantly influence RBC flow and the overall perfusion dynamics within larger capillary networks.

1.6 Blood Rheology in the Capillary System

Blood rheology, or hemorheology, is the study of the properties of blood as it flows. In large blood vessels, blood can be considered as a homogeneous and Newtonian fluid.

[13] Figure 4 in Secomb (2017). Reproduced with the publisher's permission.

However, in vessels smaller than $1000\,\mu$m, the heterogeneity nature of blood becomes significant. Specifically, the deformability of RBCs, as well as their interactions with each other and with the vessel walls, introduces non-linear effects that influence both the density and viscosity of blood. In smaller vessels, the viscosity becomes dependent on the shear rate. This behavior categorizes blood as a non-Newtonian fluid in microcirculation.

The shear rate ($\dot{\gamma}$) is defined as the ratio of shear stress to the dynamic viscosity (μ) of the fluid. Viscosity, an intrinsic fluid property, measures resistance to flow and is associated with the internal friction between fluid layers as they slide past one another. The shear stress (τ) is given by:

$$\tau = \mu \frac{\partial u}{\partial y} = \mu \dot{\gamma}\,, \tag{1.23}$$

where u is the longitudinal velocity component.

Non-Newtonian fluids are defined by the way their viscosity changes with shear rate. In shear-thickening fluids, viscosity increases as the shear rate rises, while in shear-thinning fluids, viscosity decreases as the shear rate increases. Blood exhibits shear-thinning behavior at the microscale. As discussed in Section 1.5.3, RBCs tend to aggregate when the shear rate is low ($\dot{\gamma} < 100\,\mathrm{s}^{-1}$), which causes an increase in viscosity. This increase in viscosity leads to a rise in the shear rate, which helps break up the aggregates, thereby reducing the viscosity again. Additional factors contributing to blood's shear-thinning behavior include the axial concentration of RBCs (Section 1.5.4), the Fåhræus effect (Section 1.6.1) and the Fåhræus-Lindqvist effect (Section 1.6.2).

Given that blood viscosity depends on the specific flow conditions, an apparent viscosity, μ_{app}, is often defined. The apparent viscosity of blood in the microcirculation refers to a specific property. It is the viscosity that a Newtonian fluid would exhibit if it flowed in the same vessel under the same pressure gradient. It can be expressed as:

$$\mu_{\mathrm{app}} = \frac{\pi a^4 \Delta p}{8 L Q}\,. \tag{1.24}$$

where a is the vessel radius, Δp is the pressure difference, L is the vessel length, and Q is the flow rate. Under these assumptions, Poiseuille's theory is applicable for modeling blood flow in the microcirculation.

Plasma, on the other hand, is considered a Newtonian fluid with a dynamic viscosity of $\mu_{\mathrm{plasma}} = 1 - 1.5\,\mathrm{mPa\,s}$ at 37° C. Typically, the apparent viscosity is normalized with respect to plasma viscosity using the parameter $\eta = \mu_{\mathrm{app}}/\mu_{\mathrm{plasma}}$.

1.6.1 Fåhræus Effect

Fåhraeus (1929) observed a reduction in RBC concentration, or hematocrit, between blood flowing in a small tube and the reservoir feeding the tube. This reduction results from a non-uniform radial distribution of RBCs within the tubes, leading to differences in travel speed between the RBCs and the suspending fluid. The non-uniform distribution is caused by the formation of a cell-depleted layer near the tube walls, as RBCs migrate toward the centerline where the velocity is higher due to the parabolic velocity profile (Sec. 1.4.1). Consequently, the RBCs exhibit a higher volumetric flow rate than the

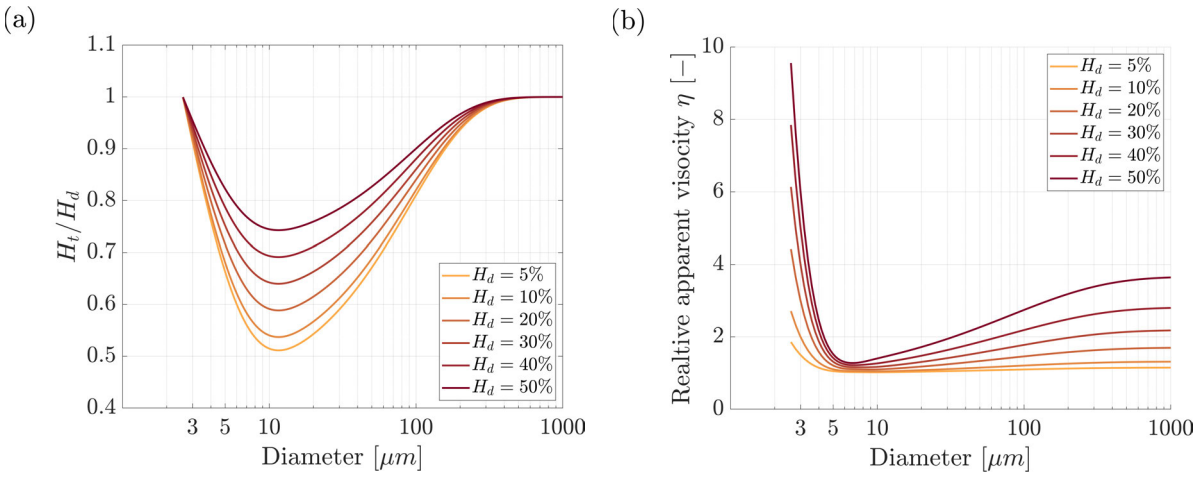

Figure 1.16: Fåhræus and Fåhræus-Lindqvist effects. **a)** Variation of the ratio $H_\mathrm{t}/H_\mathrm{d}$ with respect to the vessel diameter, illustrating the Fåhræus effect. The discharge hematocrit $H_\mathrm{t}/H_\mathrm{d}$ is calculated using equation 1.27. **b)** Relationship between relative apparent viscosity η and vessel diameter, demonstrating the Fåhræus-Lindqvist effect calculated according to equation 1.28.

overall fluid, reducing the hematocrit inside the tube (H_t) compared to the reservoir's feeding hematocrit.

The hematocrit within the channel can be calculated as:

$$H_\mathrm{t} = \frac{V_\mathrm{RBC}}{V_\mathrm{channel}} = \frac{N_\mathrm{RBC} MCV_\mathrm{RBC}}{V_\mathrm{channel}}\,, \tag{1.25}$$

where N_RBC is the number of RBCs in the channel, MCV_RBC is the mean corpuscular volume of an RBC, and V_channel is the channel volume.

When the RBCs exit the tube and enter the reservoir, the discharge hematocrit (H_d) matches the feeding hematocrit, as mass conservation applies, and, therefore, is higher than the tube hematocrit. The ratio $\chi = H_\mathrm{t}/H_\mathrm{d}$ deviates significantly from unity for tube diameters below $300\,\mu$m. This effect intensifies as the tube diameter decreases until approximately $D = 8\,\mu$m, where the tube diameter is similar to the diameter of an RBC. Beyond this point, the effect diminishes as RBCs must deform to pass through the tube, reducing the cell-free layer thickness. This relationship can be expressed as:

$$u_\mathrm{RBC} H_\mathrm{t} = u_\mathrm{bulk} H_\mathrm{d} \quad \rightarrow \quad \frac{H_\mathrm{t}}{H_\mathrm{d}} = \frac{u_\mathrm{bulk}}{u_\mathrm{RBC}} < 1\,, \tag{1.26}$$

where u_RBC is the velocity of RBCs, and u_bulk is the bulk fluid velocity. The relationship between the Fåhræus effect and tube diameter is shown in Fig. 1.16a, where we can observe that at lower feeding hematocrit, the Fåhræus effect amplifies.

Pries et al. (1990) proposed an empirical equation to describe the Fåhræus effect in tubes:

$$\frac{H_\mathrm{t}}{H_\mathrm{d}} = H_\mathrm{d} + (1 - H_\mathrm{d})(1 + 1.7e^{-0.415D} - 0.6e^{-0.11D})\,, \tag{1.27}$$

where D is the tube diameter (in μm), this equation assumes human RBCs with a mean corpuscular volume ($MCV_{\mathrm{RBC,human}}$) of $92\,\mu\mathrm{m}^3$. For RBCs from other species, the tube diameter should be adjusted using the factor $(MCV_{\mathrm{RBC,human}}/MCV_{\mathrm{RBC,animal}})^{1/3}$.

1.6.2 Fåhræus-Lindqvist Effect

In the microcirculation, in addition to the Fåhræus effect, a second phenomenon, known as the Fåhræus-Lindqvist effect, was observed by Fåhræus and Lindqvist (1931). This effect describes a decrease in the apparent viscosity of blood in smaller channels. The decrease becomes noticeable in channels with diameters below $300\,\mu$m, reaching its minimum at approximately $8\,\mu$m. For channels smaller than $8\,\mu$m, the apparent viscosity increases again.

This behavior is explained by the presence of the cell-free layer, a region near the vessel walls devoid of RBCs. The cell-free layer is present in most vessels as long as the RBCs do not need to squeeze through the channel. As the channel diameter decreases, the relative proportion of the cell-free layer increases. Since the cell-free layer has a lower viscosity (equal to the plasma viscosity) compared to the viscosity of blood, the overall apparent viscosity decreases as the cell-free layer becomes more prominent. However, when the channel diameter becomes smaller than $8\,\mu$m, RBCs must deform to pass through, reducing or eliminating the cell-free layer and thereby increasing the apparent viscosity.

Pries et al. (1990) proposed an empirical equation to describe the Fåhræus-Lindqvist effect:

$$\eta = 1 + (\eta_{0.45} - 1) \cdot \frac{(1 - H_{\mathrm{d}})^C - 1}{(1 - 0.45)^C - 14}\,, \tag{1.28}$$

where $\eta_{0.45}$ is the relative apparent viscosity for a fixed discharge hematocrit of 0.45, defined as:

$$\eta_{0.45} = 220 \cdot e^{-1.3D} + 3.2 - 2.44 \cdot e^{-0.06D^{0.645}}\,, \tag{1.29}$$

and D is the vessel diameter (in μm). The coefficient C is calculated as:

$$C = (0.8 + e^{-0.075D}) \cdot \left(-1 + \frac{1}{1 + 10^{-11} \cdot D^{12}}\right) + \frac{1}{1 + 10^{-11} \cdot D^{12}}\,. \tag{1.30}$$

The relationship between relative apparent viscosity and tube diameter is illustrated in Fig. 1.16b, showing how the viscosity decreases with decreasing tube diameter until $8\,\mu$m, which increases due to the decrease in dimension of the CFL.

An analytical expression for the Fåhræus-Lindqvist effect can be derived from the two-phase model presented in Section 1.5.4. From equation 1.24 and equation 1.22:

$$\mu_{\mathrm{app}} = \frac{\mu_{\mathrm{plasma}}}{1 - \kappa^4(\mu_{\mathrm{plasma}}/\mu_{\mathrm{RBC}})}\,, \tag{1.31}$$

where $\kappa = 1 - \delta/a$ is the core to the tube radius ratio, δ is the thickness of the CFL, and a is the tube radius.

1.6.3 Blood Phase Separation

Numerous studies in microcirculation have documented the non-uniform phase separation of blood at bifurcations, where the distribution of blood between daughter vessels is uneven (Krogh (1921); Svanes and Zweifach (1968); Fung (1973); Schmid-Schönbein et al. (1980); Pries et al. (2003); Balogh and Bagchi (2018)). This phenomenon is called *phase separation*.

The phenomenon was first described by Krogh (1921), who observed that capillaries emerging laterally from arterioles received fewer RBCs. This occurs because the plasma-rich region near the vessel wall, with fewer RBCs, preferentially flows into these capillaries, a phenomenon known as *plasma skimming*. Krogh (1921) also noted that the daughter vessel with the lower flow rate tends to have a significantly reduced hematocrit, with the difference increasing as the flow rates diverge between daughter vessels.

Another mechanism called *cell screening*, influences phase separation. This refers to the tendency of RBCs to deviate from fluid streamlines and enter vessels they otherwise would not have entered due to their inertia, dynamics, and interactions with other cells. Numerical simulations by Balogh and Bagchi (2018) on realistic capillary networks revealed that smaller capillary diameters amplify the cell screening effect and that one of the causes is RBCs stuck at the bifurcation, which temporarily partially closes one of the two daughter cells.

Phase separation has been observed in *in vivo* vessels by Svanes and Zweifach (1968) and in *in vitro* experiments by Fung (1973). Both studies showed that the daughter branch with the higher flow rate receives a disproportionately larger share of RBCs, a phenomenon now referred to as the Zweifach-Fung effect. For instance, if the blood flow in the daughter vessel ($Q_{\text{blood,D}}$) is 80% of the flow in the parent vessel ($Q_{\text{blood,P}}$), the daughter vessel will receive more than 80% of the RBCs from the parent vessel ($Q_{\text{RBC,D}} > 0.8 \cdot Q_{\text{RBC,P}}$).

Furthermore, Fung (1973) described a *self-regulation* mechanism at bifurcations. As RBCs preferentially enter the daughter vessel with the higher blood flow rate, the increased concentration of RBCs raises the vessel's resistance. This increased resistance leads to a pressure drop, reducing the flow rate in that vessel over time. Eventually, with its now higher flow rate, the other daughter vessel begins attracting more RBCs, initiating a similar cycle. This alternation continues, creating a self-regulating dynamic that, when averaged over time, reduces long-term disparities in flow rates between the branches (Schmid et al., 2015).

To quantify RBC partitioning, Pries et al. (1990) developed empirical equations to compute the RBC flux fraction in daughter vessel ($\Psi = Q_{\text{RBC,D1}}/Q_{\text{RBC,P}}$), These equations are based on the blood flow fraction in each vessel ($\Phi = Q_{\text{blood,D1}}/Q_{\text{blood,P}}$), the diameters of the vessels, and the hematocrit in the parent vessel. Later, Pries et al. (2003) refined these equations. The general equation uses a logit function as follows:

$$\text{logit}(\Psi_{\text{Pries}}) = A + B \times \text{logit}\left(\frac{\Phi - X_0}{1 - 2X_0}\right) , \tag{1.32}$$

where $\text{logit}(x) = \ln(x/(1-x))$. Solving the logit function yields the following expression

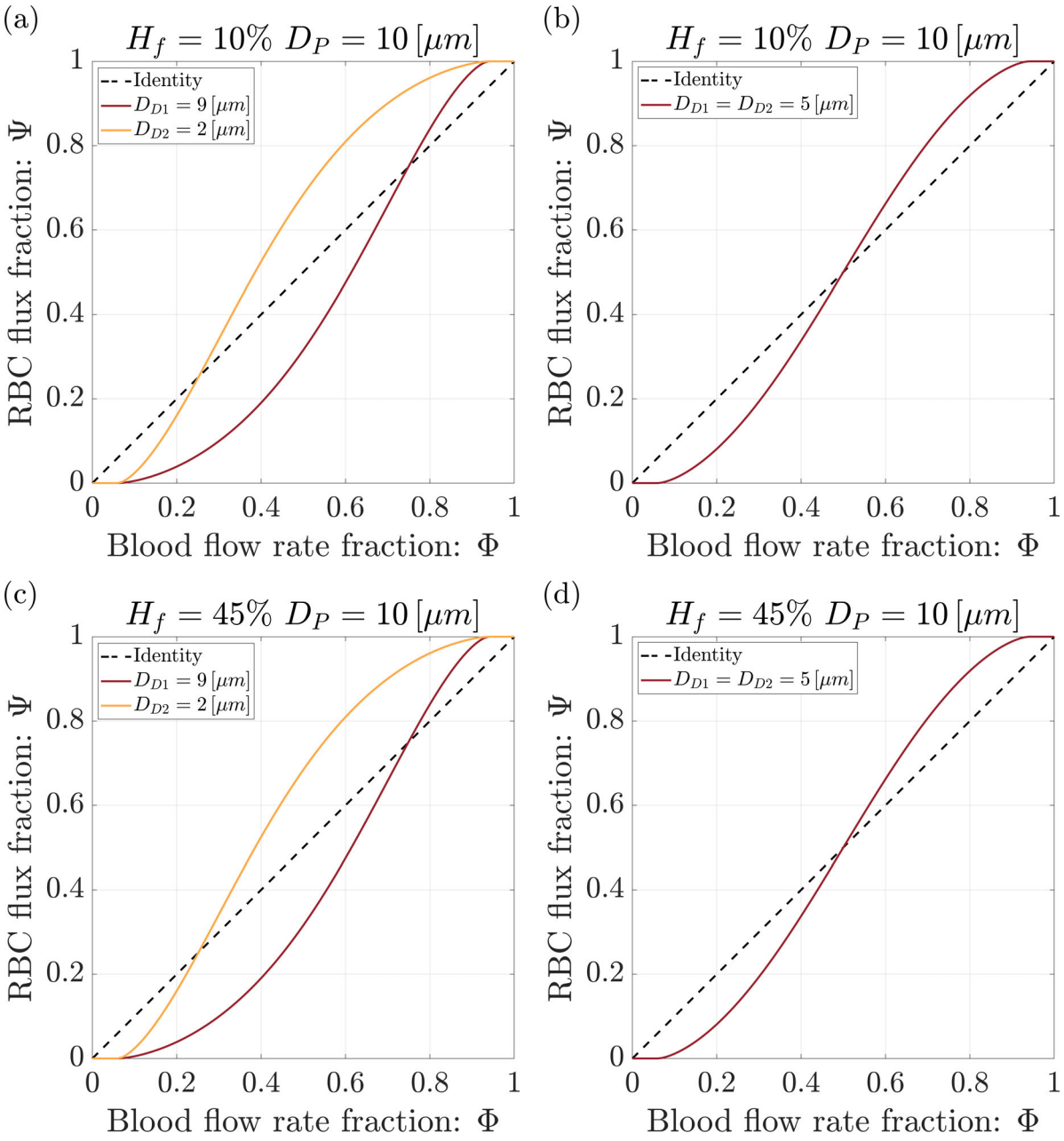

Figure 1.17: Phase separation law for $D_\mathrm{P} = 10\,\mu\mathrm{m}$ with two daughter configurations at different feeding hematocrit H_f. The dashed line indicates the identity line, representing no phase separation. Calculations are based on Equation 1.33. **a)** Configuration with $D_1 = 9\,\mu\mathrm{m}$, $D_2 = 2\,\mu\mathrm{m}$, and $H_\mathrm{f} = 10\%$. **b)** Configuration with $D_1 = D_2 = 5\,\mu\mathrm{m}$ and $H_\mathrm{f} = 10\%$. **c)** Configuration with $D_1 = 9\,\mu\mathrm{m}$, $D_2 = 2\,\mu\mathrm{m}$ and $H_\mathrm{f} = 45\%$. **d)** Configuration with $D_1 = D_2 = 5\,\mu\mathrm{m}$ and $H_\mathrm{f} = 45\%$.

for Ψ_{Pries}:

$$\Psi_{\mathrm{Pries}} = \begin{cases} 0 & \text{if } \Phi^\alpha < X_0\,, \\ 1 & \text{if } \Phi^\alpha > 1 - X_0\,, \\ \frac{1}{1+e^{-\left(A+B\cdot\mathrm{logit}\left(\frac{\Phi - X_0}{1-2X_0}\right)\right)}} & \text{else,} \end{cases} \tag{1.33}$$

Here, A, B, X_0 define the phase separation characteristics of the bifurcation. These parameters, derived from experiments with rat RBCs, are given by:

$$A = -13.29[(D_{\mathrm{D1}}^2/D_{\mathrm{D2}}^2 - 1)/(D_{\mathrm{D1}}^2/D_{\mathrm{D2}}^2 + 1)](1 - H_{\mathrm{f}})/D_{\mathrm{P}} \ , \tag{1.34}$$

$$B = 1 + 6.98(1 - H_{\mathrm{f}})/D_{\mathrm{P}} \ , \tag{1.35}$$

$$X_0 = 0.964(1 - H_{\mathrm{f}})/D_{\mathrm{P}} \ . \tag{1.36}$$

where D_{P}, D_{D1}, and D_{D2} are the diameters of the parent and daughter vessels, and H_{f} is the feeding hematocrit. These equations assume rat RBCs with a mean corpuscular volume ($MCV_{\mathrm{RBC,rat}}$) of $55\,\mu\mathrm{m}^3$. For other species, the tube diameter should be scaled by $(MCV_{\mathrm{RBC,rat}}/MCV_{\mathrm{RBC,animal}})^{1/3}$. A describes the asymmetry between the daughter vessels. B controls the sigmoidal shape of the fitting function, and X_0 represents the minimum blood flow fraction at which no RBCs enter the daughter vessel. Fig. 1.17 shows multiple examples of this phase separation.

In vitro studies by Fenton et al. (1985) and Roman et al. (2016) corroborated these models; additionally, they showed a reduced phase separation effect as feeding hematocrit increased. At high hematocrit levels, experimental data approached the identity line.

In more complex networks with more complex RBC dynamics, deviations from the classic Zweifach-Fung partitioning have been observed (Balogh and Bagchi, 2017b,a; Mantegazza et al., 2020b,a; Shen et al., 2016; Clavica et al., 2016). Reductions or inversions of this effect are more pronounced at low feeding hematocrit (Shen et al., 2016), increased inlet velocities (Mantegazza et al., 2020a; Clavica et al., 2016), and skewed hematocrit profiles before the bifurcation (Mantegazza et al., 2020b; Balogh and Bagchi, 2017b).

1.7 Hypothesis and Objective

This doctoral project focuses on understanding the fluid dynamics and partitioning of RBCs in an *in vitro* capillary network and at microvascular bifurcations. The primary aim is to gain a deeper understanding of the local mechanisms driving the heterogeneous distribution of RBCs in capillary networks and their relationship to the regulation of cerebral blood flow during functional hyperemia.

Hypotheses

H1 Lingering RBCs influence the partitioning of RBCs at a bifurcation even in a less confined environment ($\lambda > 1$).

H2 The modulation of blood flow and RBC distribution begins locally near the pericyte if a pericyte is activated (i.e., local capillary dilation) for a short period of time but extends throughout the capillary network with prolonged activation.

H3 The capillary network behaves as a homogeneous porous medium, where pericyte activation can be interpreted as a localized increase in porosity if observed shortly after activation. However, over a prolonged period, the rearrangement of RBCs negates this interpretation.

Objectives

To test these hypotheses, the following objectives were defined:

O1 Develop a robust classification method to differentiate lingering and non-lingering RBCs at a bifurcation.

O2 Analyze the influence of lingering and non-lingering RBC dynamics on partitioning at diverging bifurcations.

O3 Adapt and refine the experimental set-up previously established in the lab to enable repeatable dynamic activation of pressure chambers (i.e., channel dilation) as a simulation of pericyte activation.

O4 Investigate the impact of dynamic pericyte activation on capillary network perfusion and RBC distribution.

O5 Compare the effects of pericyte activation with those of a localized increase in porosity within a porous medium.

Chapter 2

Materials and Methods

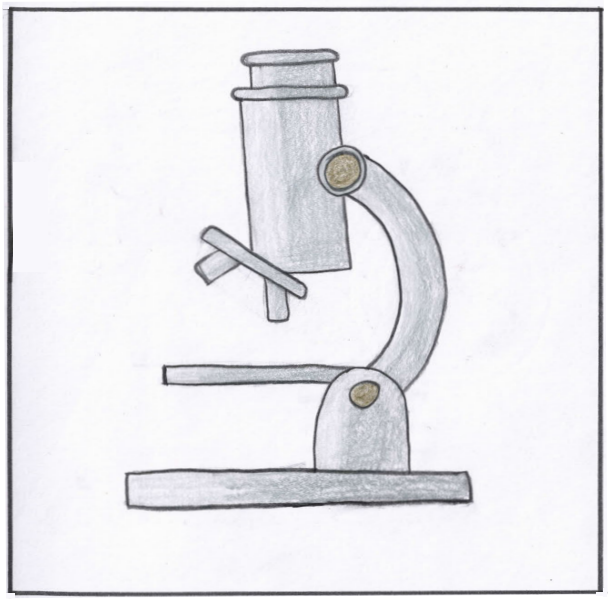

This chapter outlines the general materials and methods used throughout the project. Any specific variations or details relevant to individual experiments are provided in the *Materials and Methods* sections of the relevant chapters.

The microfluidic chip, experimental setup, and data analysis methods used here have been used in previously published works by Clavica et al. (2016); Mantegazza et al. (2020a,b) and Bucciarelli et al. (2024). As a result, certain sections of this chapter may overlap with those publications.

2.1 Microfluidic Chip Production

The experiments were performed using a microfluidic device made of polydimethylsiloxane (PDMS), fabricated via conventional soft lithography techniques. Soft lithography, originally developed by Xia and Whitesides (1998), combines photolithography, which creates a mold with the negative design of the microfluidic chip (the channels protrude from the mold), and replica molding, which enables repeated chip fabrication.

Photolithography is a well-established technique for creating small patterns (nanometer-sized) on a photosensitive material through light exposure using a photomask (Karimi et al., 2024; Scott and Ali, 2021). Replica molding is also well-established, allowing for the repeated production of microfluidic devices by pouring silicone-based elastomers onto a mold. Once the elastomer hardens, it is peeled off the mold and bonded to a base layer, forming the desired microfluidic chip (Xia and Whitesides, 1998). In our case, PDMS was selected for its numerous advantages: it is easy to cast, optically transparent (essential for observing RBC under a microscope), gas-permeable, biocompatible (Bélanger and Marois, 2001) and tunable mechanics (Khanafer et al., 2009; Johnston et al., 2014).

A. Manteganzza carried out the photolithography process in a clean room at the University of Applied Sciences in La Chaux-de-Fonds, Switzerland, while the replica molding was performed in-house prior to each experiment.

2.1.1 Photolithography Procedure

Before outlining the photolithography process, it is crucial to determine the type of photoresist to be used, either negative or positive, as this decision impacts the fabrication of the photomask. Negative photoresists polymerize only when exposed to light, making those areas resistant to the developer, while positive photoresists behave oppositely, with light-exposed areas becoming soluble to the developer. For our process, we used a negative SU-8 photoresist (Gersteltec, Pully, Switzerland), which required a photomask with transparent channels, as shown in Fig. 2.1b. A dark chrome-coated photomask (JD Photodata, Hitchin, UK) was utilized. The schematic of the photolithography process is depicted in Fig. 2.1, and the following paragraphs describe the protocol used to produce our mold.

The procedure begins by cleaning a silicon wafer in an oxygen plasma cleaner and then heating it on a hot plate to remove any residual moisture. A thin layer of negative SU-8 photoresist is spin-coated onto the silicon wafer (spinning at 250 rpm for 40 seconds, followed by 3000 rpm for 1 second, and then a 5-minute relaxation period) to achieve a uniform thickness of 8 μm, as shown in Fig. 2.1a. The silicon wafer is pre-baked (1 minute

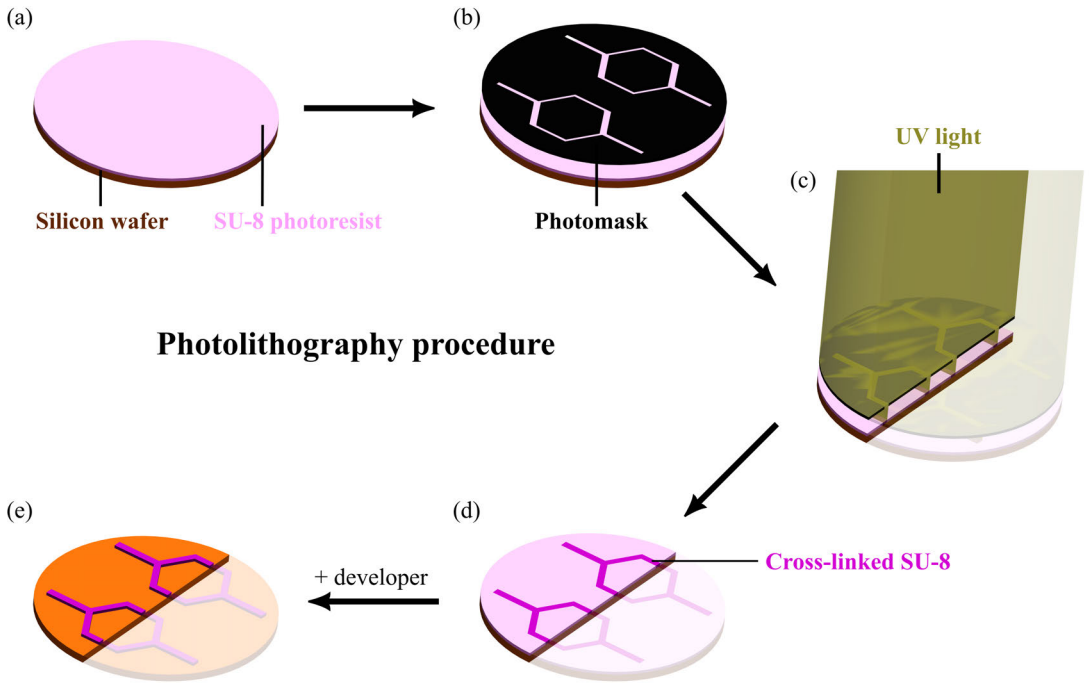

Figure 2.1: Photolithography procedure. **a)**A silicon wafer coated with an 8 μm thick layer of SU-8 photoresist. **b)**Photomask alleged with the silicon wafer. **c)** Exposure of the photomask to ultraviolet light. **d)** Cross-linked and unpolymerized SU-8 on the silicon wafer after exposure. **e)** Final silicon wafer, which is used as a mold in the replica molding process.

at 60° C, followed by 2 minutes at 95° C, then cooled on the hot plate) to evaporate excess solvent from the photoresist.

The silicon wafer and the photomask are then aligned, without touching, in a mask aligner, after which the mask is exposed to high-intensity ultraviolet light (158 mJ cm^{-2}, Fig. 2.1c). Only the exposed SU-8 (where the mask is transparent) polymerizes (Fig. 2.1d). After a 10-minute relaxation period, the silicon wafer is immersed in a developer (propylene glycol methyl ether acetate) for 1 minute, followed by a 1 minute rinse in isopropanol. A hard bake (2 hours at 135° C, Fig. 2.1e) is then performed to harden the photoresist further and improve adhesion to the silicon wafer. Finally, a silanization procedure is applied to reduce the stickiness of the PDMS to the silicon wafer (for in-house silanization protocol, Appendix A.1). The mold is ready to be used.

2.1.2 Replica Molding Procedure

The PDMS microfluidic chip consists of two parts: the top layer, which contains the channels, and the base layer, which is flat and serves to form the channels. Most microfluidics devices bound the PDMS layer to a microscope glass slide to close the channels. Instead, as written before, we will use a base PDMS layer for two reasons. First, if a glass slide had been used, a coating step for the glass would have been needed since RBCs could become activated when in contact with the glass. Second, as described

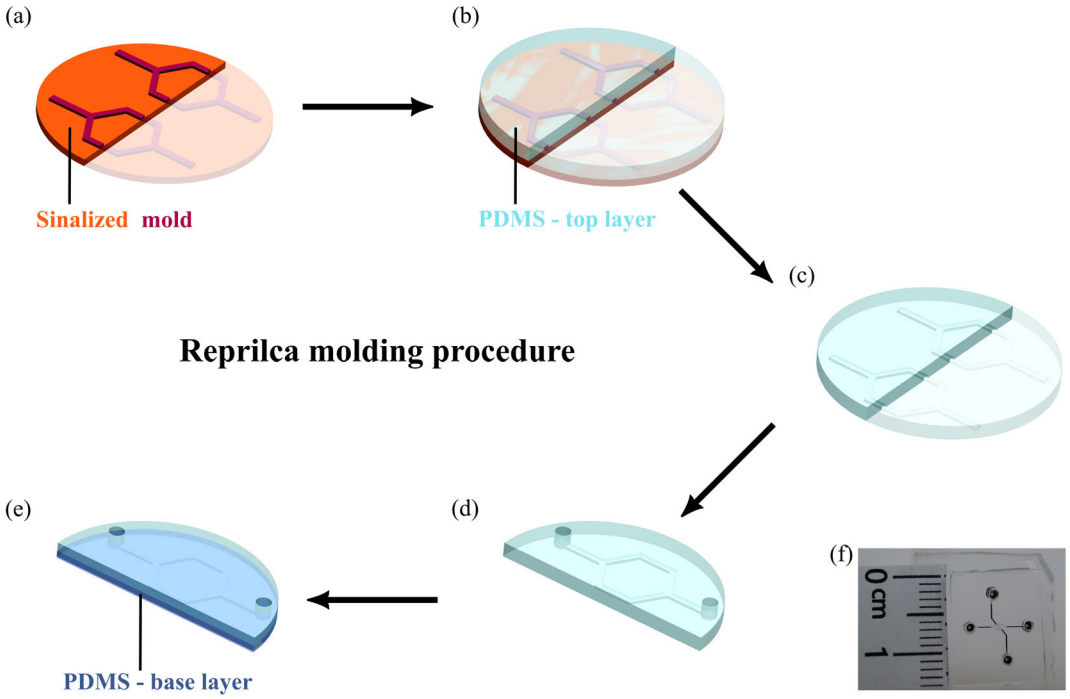

Figure 2.2: Replica molding procedure. **a)** Silanized mold. **b)** PDMS poured on the mold. **c)** Top layer after overnight curing and peeling off, with visible channels. **d)** Single chip with biopsy punches used to create inlets. **e)** Final chip after plasma bounding to the base layer and curing overnight. **f)** Example of the microfluidics chip with colored microchannels.

in Section 2.2.2, one of the microfluidic chip designs has a pneumatic valve. Which performs better if all the channel walls are made from the same material.

Fig. 2.2 shows a schematic of the replica molding process. To ensure a microfluidic chip is produced with minimal impurities, the production is always done in a flow-hood and using gloves.

The first step in fabricating the chip involves preparing two batches of PDMS (Sylgard 184, Dow Corning, Midland, MI, USA) with different mixing ratios: one with a 12:1 ratio and the other with a 10:1 ratio, followed by a degassing step. The 12:1 PDMS to curing agent ratio is used for the top layer to provide the necessary softness for proper pneumatic valve function (see design details in Section 2.2.2). The 10:1 ratio is used for the base layer to ensure the chip's structural stability.

Next, the mold is cleaned using pressurized air and deionized water. After ensuring the mold is dry and clean, the PDMS with a 12:1 ratio is poured onto the mold to form a layer approximately 5 mm thick (Fig. 2.2b), this will be the top layer. For the base layer, PDMS with a 10:1 ratio is poured into an empty Petri dish to form a $1-2$ mm thick layer. Both layers are degassed for about 20 minutes, then cured overnight in an oven at 60° C. Once cured, the PDMS is peeled off the mold (Fig. 2.2c), and individual microfluidic chip designs are separated using a scalpel. A 1.5 mm biopsy punch (pfm medical, 48115) is used to create inlets, outlets, and connections for the pneumatic valves, completing the

top layer (Fig. 2.2d). The base layer is also removed from the Petri dish and cut into squares of approximately 2 cm × 2 cm.

Finally, the top layer is bonded to the base layer using oxygen plasma bonding (Henniker plasma HPT-200) (power: 100 W, time: 60 s, pressure: 0.65 mbar). During this process, hydrocarbon groups (CH_3) are removed from the exposed PDMS surface, leaving behind silanol groups (Si−OH). Strong covalent Si−O−Si bonds are formed when the two layers come into contact, making the PDMS layers inseparable. The assembled microfluidic chip is then placed in an oven at 60° C overnight to strengthen the bond further. After checking under a microscope to ensure successful production, confirming no collapsed channels and intact walls, the microfluidic chip is ready for use (Fig. 2.2e). The step-by-step protocol can be found in Appendix A.2.

2.2 Microfluidic Chip Designs

In this thesis, two different microfluidic chip designs were utilized. The first, a simpler design (Section 2.2.1), was dedicated to studying the behavior of single RBCs at a bifurcation (Chapter 3). The second, more complex design (Section 2.2.2), was used to investigate the influence of pericyte activation on RBC flow and distribution (Chapter 4). Both designs were initially developed by A. Mantegazza, who used them in a previous study within our research group (Mantegazza et al., 2020a).

The chip designs are intended to replicate an idealized capillary network, with a hexagonal structure as the basis for the geometry. Due to manufacturing constraints, the channels have a rectangular cross-section and a uniform height throughout. This uniformity results from the photolithography process, which utilizes only a single layer of photoresist. Additionally, the rectangular cross-section is an inherent limitation of standard photolithographic techniques. Recent advances in photolithography have made it possible to fabricate semi-circular molds (Fenech et al., 2019; Huang et al., 2012), which, by producing two top layers and bonding them together, can form round channels. However, achieving this precise alignment becomes challenging with channel dimensions below 10 μm, as needed in our designs to simulate capillary vessel dimensions.

Some preliminary tests using 3D printing were conducted to produce round channels, but these attempts were unsuccessful. As this was not the primary objective of the thesis, further development of the round channel design was postponed. The results of these 3D printing trials are provided in Appendix B.

2.2.1 Single Honeycomb

To study single RBC behavior at a bifurcation, a simple hexagonal loop design was used, connected upstream and downstream to wider inlet and outlet microchannels (width 100 μm) as shown in Fig. 2.3 (left top panel). The microchannels have a rectangular cross-section with a width of $W = 9.6\,\mu$m and height of $H = 8\,\mu$m, while the length of each hexagonal edge is $CL = 120\,\mu$m. The bifurcation points, both diverging and converging, are symmetrical, each with a bifurcation angle of 120°. An image of the diverging bifurcation observed under the microscope is provided in Fig. 2.3 (right panel).

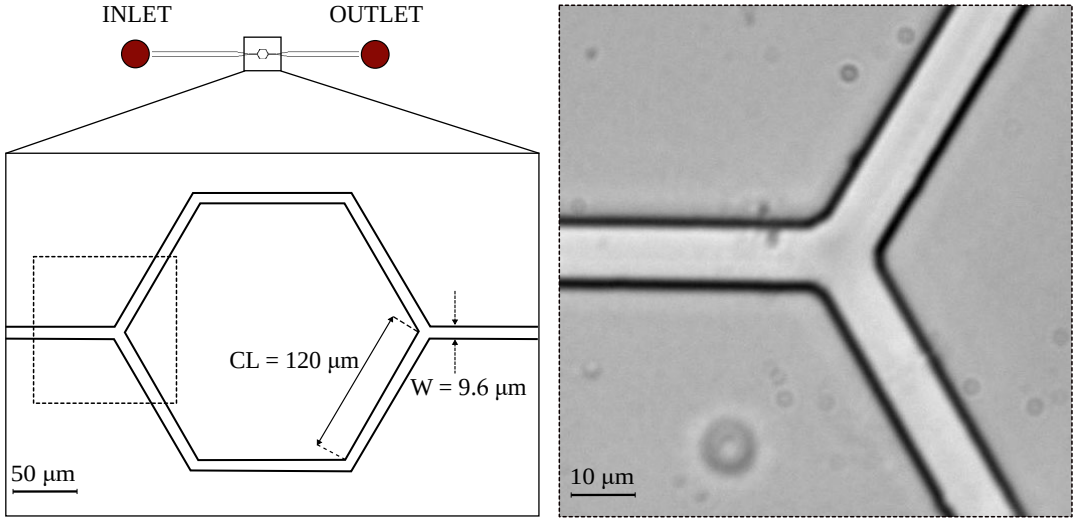

Figure 2.3: Schematic of the single honeycomb microfluidic chip. Microfluidic device with inlet and outlet (top left), a magnified version of the single-mesh network (bottom left), and a microscope image (512 px × 512 px) of the diverging bifurcation (right).[1]

2.2.2 Honeycomb Network

The second chip design features a more complex honeycomb-like network linked to larger inlet and outlet microchannels (width 100 μm; see Fig. 2.4, top left). Sixteen hexagonal structures connect to the inlet and outlet through three T-junctions each (Fig. 2.4, red channels top). All microchannels within this network have a rectangular cross-section of width $W = 9.6\,\mu$m, height $H = 8\,\mu$m, and a hexagonal edge length of $CL = 85\,\mu$m.

Additionally, two pressure chambers are positioned upstream and downstream of the honeycomb network (Fig. 2.4, blue channels), at a distance of $WT = 5\,\mu$m from one of the microchannels in the T-junctions (see enlarged view in Fig. 2.4, blue panel). This forms a thin wall of 5 μm between the pressure channel and the channel where the RBCs flow. When the pressure chamber is pressurized, the wall between the two is deformed, changing the adjacent microchannel cross-sectional area, a mechanism used here to simulate pericyte activation. As detailed in Section 1.2.3, pericyte activation alters the cross-sectional area of the underlying capillary. The blue panel in Fig. 2.4 shows the channels and pressure chamber when the simulated pericyte is inactive, while the orange panel shows the setup when the pericyte is active. Interestingly, the channel appears narrower in the active state if only the 2D view is considered, contrary to the expected behavior of increased cross-sectional area upon pericyte activation. This "contradiction" will be explained further in Section 4.4.1.

2.3 Red Blood Cell Sample Preparation

As outlined in Section 1.7, our goal is to analyze the dynamics of RBCs in microcirculation. To simulate conditions as close to *in vivo* as possible, we used real RBCs from

[1]Simplified Figure 1 in Bucciarelli et al. (2024). CC BY 4.0.

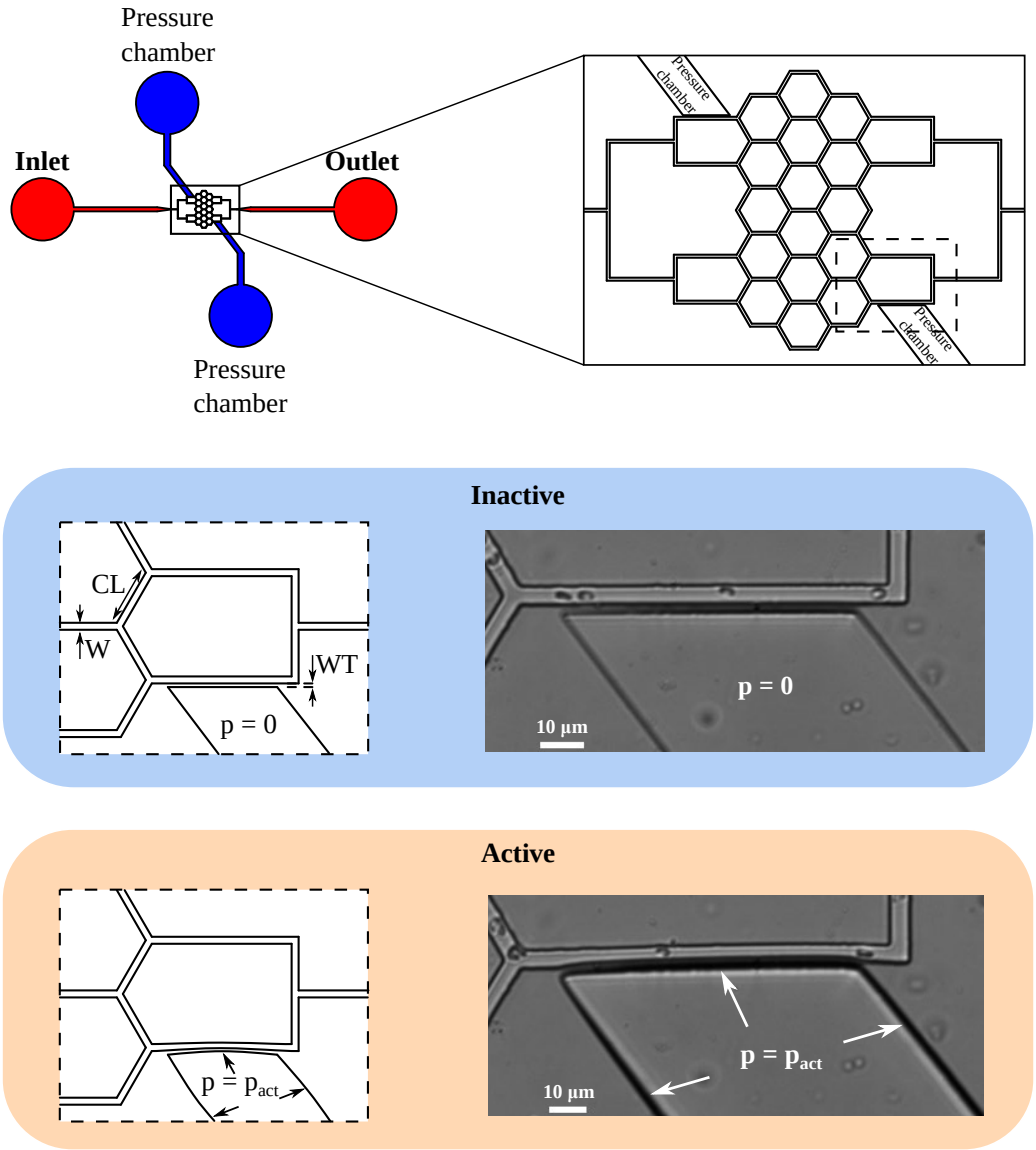

Figure 2.4: Schematic of the honeycomb network microfluidic chip. **Top left**: Overview of the microfluidics chip. In red are the channels where RBCs flow, and in blue are the pressure chambers. **Top right**: Enlargement of the honeycomb network where the T-junctions, honeycomb network, and pressure chamber can be observed. **Blue panel**: Enlargement of the bottom corner of the honeycomb network when the pericyte is inactive with an image of the same region seen under the microscope. $CL = 85\,\mu$m, $W = 9.6\,\mu$m, $WT = 5\,\mu$m. **Orange panel**: Enlargement of the bottom corner of the honeycomb network when the pericyte is active with an image of the same region seen under the microscope.

animals. In this thesis, we worked with both rabbit and human RBCs. Fresh, heparinized blood from New Zealand rabbits was supplied by the Experimental Surgery Facility at the University of Bern under the animal license BE 37/19, issued by the Canton of Bern's

veterinary authorities. Anonymized fresh human blood was obtained from healthy volunteers through the Swiss Red Cross (SRK, Bern, Switzerland) with informed consent, in accordance with the Declaration of Helsinki, Swiss Federal regulations, and the University of Bern guidelines.

Since we focus exclusively on RBC dynamics, we separated RBCs from platelets and WBC. This required the preparation of four solutions, labeled Solution 0, Solution 1, Solution 2 and Solution 3, as follows:

Solution 0: 2.5 mg/mL of Bovine Serum Albumin (BSA, Sigma A9418) in 1% Phosphate Buffered Saline (PBS, Sigma P4417).

Solution 1: GASP: 1% PBS with 1 mg/mL glucose (Sigma G7021) and 2.5 mg/mL BSA.

Solution 2: 90% Optiprep (Sigma D1556) and 10% GASP ten times concentrated.

Solution 3: 65% Solution 1 and 35% Solution 2.

Solution 0 was used to wash the RBCs and to pre-fill the microfluidic chip channels before the experiment. Solutions 1 and 2 served solely to produce the suspending medium, Solution 3, which was tuned to closely mimic plasma viscosity ($\mu = 1.96 \cdot 10^{-3}$ Pa s at 20° C) and match the RBC density ($\rho = 1090\,\mathrm{kg\,m^{-3}}$). Density matching is crucial to prevent RBC sedimentation or flotation during the experiment. Additionally, Solution 3 maintained ionic balance to preserve RBC shape, as a hypertonic medium induces echinocytosis while a hypotonic one favors stomatocytosis. To eliminate impurities or aggregated proteins that might clog the microfluidic chip, all solutions were filtered with a hydrophilic syringe filter with 0.2 μm porosity before use (ClearLine, Dominique Dutscher SAS, France).

Appendix A.3 shows a detailed, step-by-step protocol. Briefly, blood samples were divided into centrifuge tubes with 5 mL per tube and centrifuged for 10 minutes at 1.8 RCF (relative centrifugal force). After removing the supernatant, 0.6 mL of RBCs from the center of the RBC pellet was extracted. 1.2 mL of these RBCs were resuspended in 9 mL of Solution 0; this enabled us to wash the RBC and reduce echinocytosis, as described by Reinhart et al. (2015). After gentle mixing for 10 minutes, the samples were centrifuged again for another 10 minutes at 2.5 RCF. From each tube, 0.5 mL of RBCs from the center of the RBC pellet were then suspended in Solution 3. The final RBC concentration in Solution 3 was adjusted to achieve the desired reservoir hematocrit (H_r) for each experiment, typically between 10% and 30%, a physiological range for microcirculatory hematocrit. Before use, the RBCs in the suspension were visually inspected to confirm RBC shape integrity, ensuring no transformation into stomatocytes or echinocytes. The RBC suspension was used within the day for the experiment.

This RBC preparation protocol has been successfully implemented in prior studies using RBCs from various animals, as documented by Merlo (2018); Merlo et al. (2022); Roman et al. (2012, 2016); Clavica et al. (2016) and Mantegazza et al. (2020a,b).

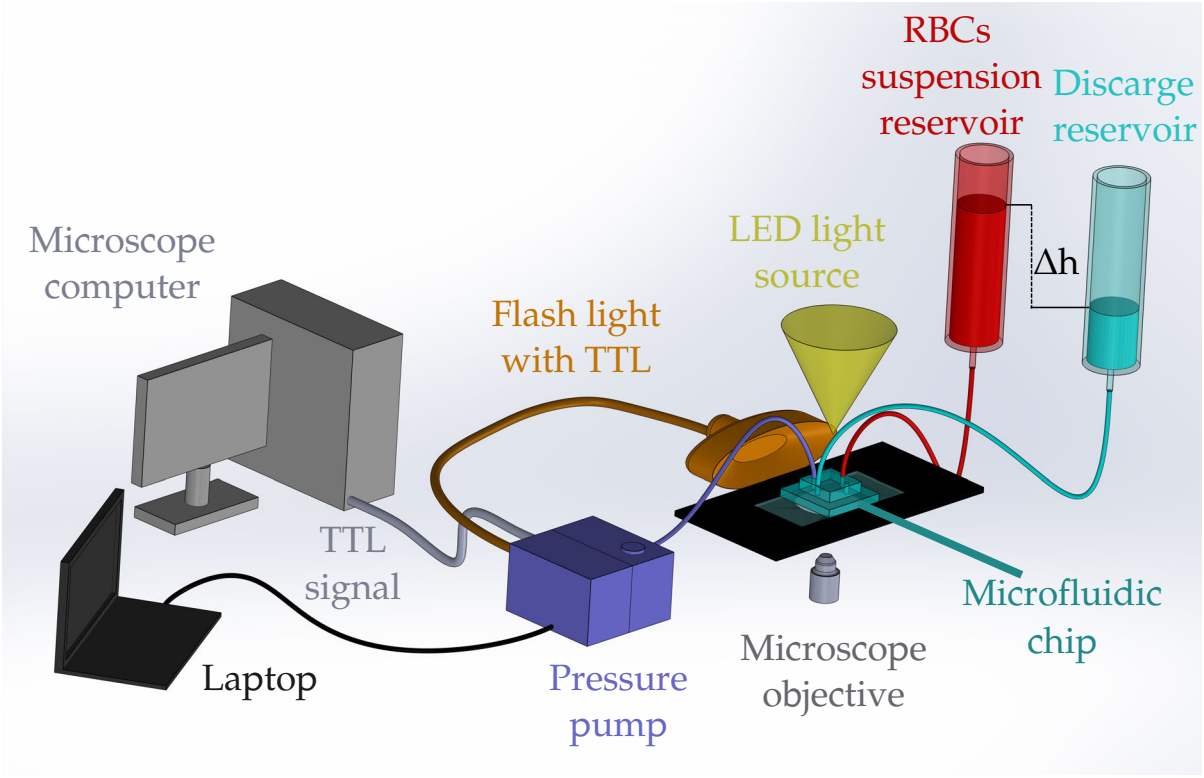

Figure 2.5: Schematic of the experimental set-up, displaying all components. The height difference, Δh, between the two reservoirs establishes the perfusion pressure driving the flow within the microfluidic chip.

2.4 Experimental Set-up

To perform the experiment and observe single RBCs flowing in the microfluidics chip, we required several components: a microscope for visualization, a pressure pump to control the pressure chamber, and a flashlight to synchronize the pump with the microscope. Additionally, two reservoirs were set up, one for the RBC suspension and another for discharge. These reservoirs were connected to the microfluidic chip's inlet and outlet. The height difference (Δh) between the reservoirs determined the perfusion pressure, given by $\Delta p = \rho \cdot g \cdot \Delta h$, which acted as the driving force for RBC movement through the microfluidic chip. The experimental setup is shown schematically in Fig. 2.5, with a corresponding image of the real set-up provided in Fig. 2.6.

2.4.1 Microscope

For all experiments, we used an inverted microscope with a spinning disk (Nikon Eclipse Ti-E, Nikon, Japan) positioned on a vibration-isolated table. The microscope setup included two cameras: a high-speed camera (ORCA-Flash 4.0, Hamamatsu, Photonics K.K., Japan) and a secondary camera used with the spinning disk (iXon Ultra 888 EMCCD, Andor, Oxford Instruments plc, UK). Four objective lenses were available from the CFI P-Apo line (Nikon, Japan): a 4x air objective (Numerical Aperture [NA] 0.20), a

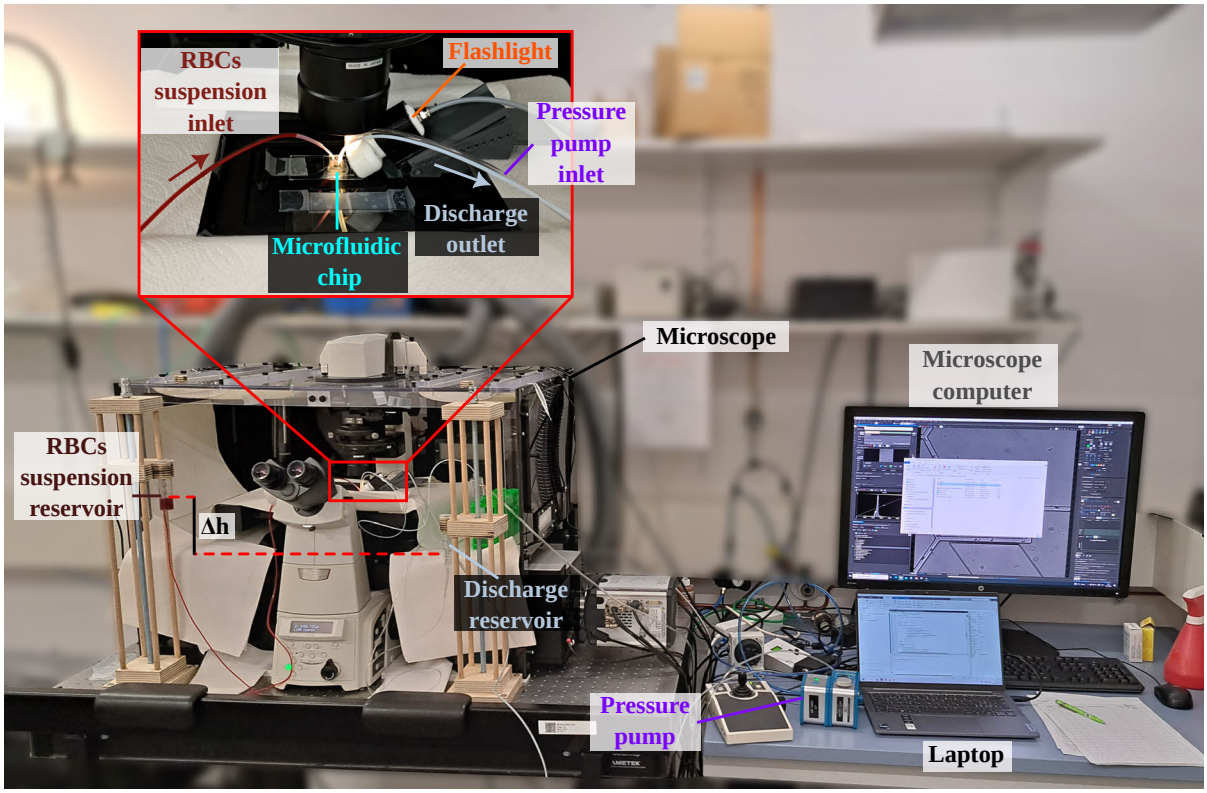

Figure 2.6: Real image of the experimental set-up, showing all components, with a close-up view of the microscope slide holder and the positioning of the flashlight.

10x air objective (NA 0.45, lateral resolution (LR) 0.65 μm/px with the high-speed camera), a 20x extra-long working distance air objective (NA 0.45, LR 0.51 μm/px, with the spinning disk camera), and a 40x extra-long working distance air objective (NA 0.60, LR 0.16 μm/px with the high-speed camera and 0.26 μm/px with the spinning disk camera).

For high-speed recordings, the microscope captured bright-field images with image dimensions of 512 px $\times$ 512 px with an acquisition frequency of 395 fps. Additionally, z-stack imaging of the microfluidic channels filled with fluorescent fluid was performed using the spinning disk, enabling 3D reconstruction by capturing fluorescence from specific z-planes. The NIS-Elements software and Jobs module were used to manage the microscope's operations and control the Transistor-Transistor Logic signal (TTL) output, which initiated the pressure pump as the microscope recording started.

2.4.2 Pressure Pump

We employed a Flow EZ™ LU-FEZ-7000 pressure pump (Fluigent, France) to control the pressure chamber, linked to a laptop, microscope, and flashlight through a Flow EZ™ LU-LINK-002 module. Custom MATLAB code was used to control pressure profiles, as shown in Fig. 2.7a. This code initiated the pressure sequence upon receiving a TTL signal from the microscope, setting an initial pressure p_{inact} for a delay period t_{delay} to account for the microscope's response time (Fig. 2.7b). The pressure then ramped to p_{act} over t_{up}, held for t_{act}, then decreased back to p_{inact} over t_{down} and held for t_{inactive}. This cycle

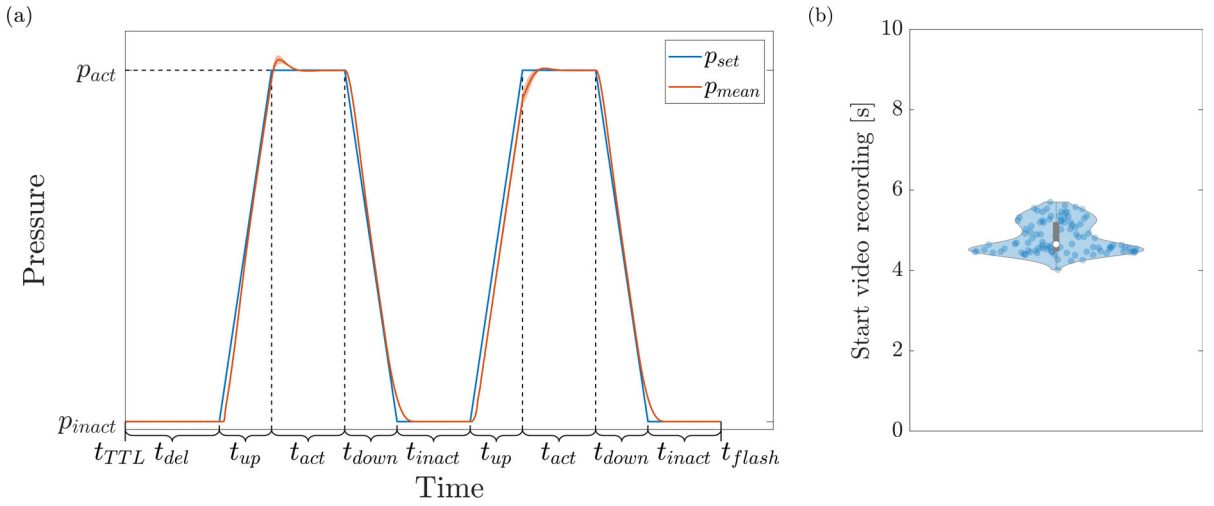

Figure 2.7: Pressure pump settings and recording initiation times. **a)** Pressure pump activation cycle transitioning between p_{inact} and p_{act}. The blue line represents the set pressure defined by the MATLAB script, while the orange line shows the mean measured pressure across 100 repetitions, with $p_{\text{inact}} = 0\,\text{mbar}$ and $p_{\text{act}} = 2250\,\text{mbar}$ (shaded area indicates standard deviation). **b)** Distribution of the recording start time of the microscope following initiation of the Jobs script.

repeated, and upon completion, the pressure pump sent a TTL signal to activate the flashlight.

To ensure consistency, we analyzed mean pressure and standard deviation across 100 double cycles. Fig. 2.7a displays the average pressure (orange line) and variation (orange shaded area around the orange line). The mean standard deviation was $\sigma_{\text{mean}} = 7\,\text{mbar}$, with values ranging from 0.3 mbar to 52.6 mbar. Notably, pressure overshoots occurred during the first increase phase, averaging 67.7 mbar, while subsequent phases showed a smoother approach due to the pump's self-regulation mechanism.

2.4.3 Flashlight

As seen in Fig. 2.7b, the microscope delayed its start after sending the TTL signal, which led us not to trust the synchronization with the pressure pump. To address this, we added a visual synchronization by developing an in-house flashlight that activates 5 μs after detecting the TTL signal from the pressure pump and remains on for 40 ms (Fig. 2.7a). Positioned beside the microfluidic chip (Fig. 2.6), the flashlight's flash increased image intensity, providing a clear synchronization point (orange cross in Fig. 2.7b). This increase was automatically detected and integrated into our imaging preprocessing script (Section 2.6.1 IPP-A).

2.5 Experimental Protocols (EP)

This thesis involved four distinct experiments. The first (Section 2.5.1) is used in Chapter 3, while the other three (Sections 2.5.2 to 2.5.4) are used in Chapter 4.

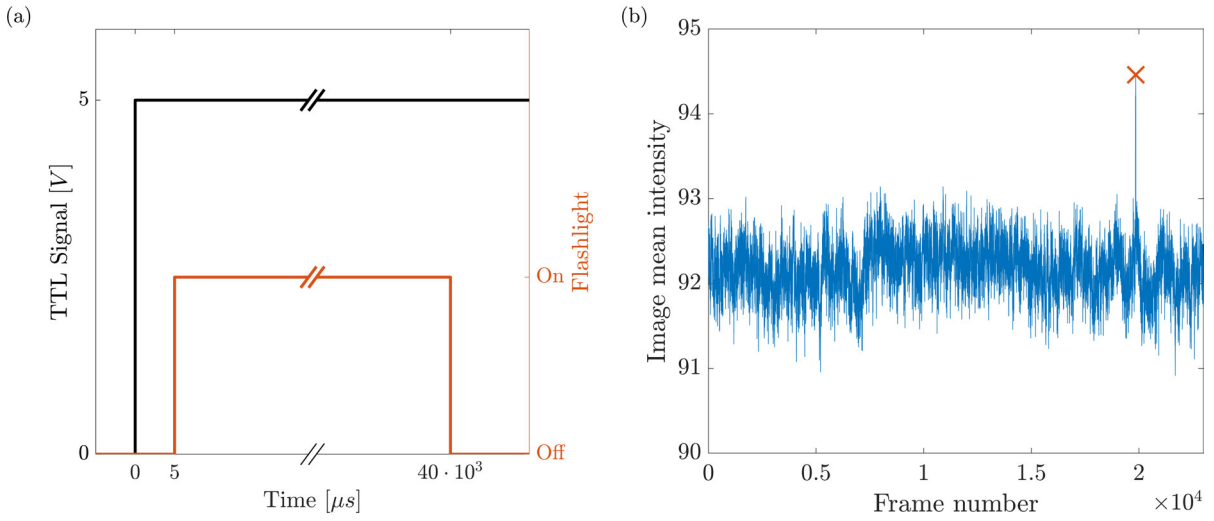

Figure 2.8: Flashlight activation and mean image intensity. **a)** Flashlight activation triggered by the TTL signal from the pressure pump (black line), lasting 40 ms (orange line). The time 0 μs aligns with t_{flash} in Fig. 2.7a. **b)** Mean image intensity within the LIF ROI (Section 2.6.1 and Fig. 2.9) for each frame. The orange cross denotes the peak intensity, which is the point where the flashlight is activated and it is automatically detectable in the images.

For all experiments, microfluidic chip preparation began three to four days prior. The RBC suspension is freshly prepared and used on the same day as blood delivery. Each setup started by placing the microfluidic chip onto a microscope slide and examining the channels and the wall between the pressure chamber and channel network to confirm structural integrity. We tried positioning the chip to align the horizontal channel with the microscope view. To pre-fill and coat the channels with albumin to prevent RBC adhesion, the chip was degassed. Solution 0 droplets were then placed on top of all the inlets and outlets and degassed for at least 20 minutes. After degassing, the chip was positioned on the microscope slide holder with the solution 0 droplets still on top to avoid air entering the microchannels during the reservoir connection to the inlets, and it was secured with tape.

2.5.1 EP for Single RBCs Dynamics Analysis

The protocol for analyzing single RBC dynamics used the single honeycomb design. Three different RBC suspensions hematocrit values (H_{r}) of 10%, 20%, and 30% were tested.

Once the chip was positioned on the microscope, a syringe containing Solution 0 was attached to the outlet as a discharge reservoir. A second reservoir containing the RBC suspension (initially at $H_{\text{r}} = 10\%$) was connected to the inlet. A height difference of $\Delta h = 20\,\text{mm}$ between the reservoirs resulted in a perfusion pressure of $\Delta p = 213.86\,\text{Pa}$ ($\Delta p = \Delta h \cdot \rho \cdot g$), generating RBC flow with an average velocity of 0.67 mm/s in ROI 0 (Fig. 3.1). After focusing the channels with the 4x objective, we used the 40x objective to zoom in on the diverging bifurcation (Fig. 2.3 right) and adjusted the focus to maximize

RBC contrast for easier image processing (dark RBC, light background).

Before recording, we allowed RBCs to reach a steady flow state, then captured 4000 frames (10.13 s) with the high-speed camera. The experiment was repeated with RBC suspensions at $H_r = 20\%$ and $H_r = 30\%$.

2.5.2 EP for RBC Dynamics Analysis During Static Pericyte Activation

The experiment for analyzing RBC dynamics during static pericyte activation used the honeycomb network design with an RBC suspension at $H_r = 10\%$.

Before starting the experiment, we prepared all the necessary equipment. The pressure pump was connected to the building's air supply and linked to the link module, which was then connected to the laptop, flashlight, and microscope. Although the microscope and flashlight were not required for this experiment, they were set up in advance for the subsequent experiment (Section 2.5.3) as both experiments were conducted in sequence.

After placing the chip on the microscope, we connected a discharge syringe filled with Solution 0 to the outlet and connected the pressure pump to the pressure chamber near the outlet. The RBC suspension reservoir was connected to the inlet, and a height difference of $\Delta h = 82\,\text{mm}$ established a perfusion pressure of $\Delta p = 876.82\,\text{Pa}$, resulting in an average flow velocity of 0.42 mm/s at the four inlet channels to the honeycomb network. After focusing the channels with the 4x objective, we switched to a 10x objective for closer examination of the network region adjacent to the pressure chamber.

The pressure pump was tested by setting it to $p_{act} = 2250\,\text{mbar}$, checking for leaks at the connection, and observing the movement in the wall between the chamber and channel (Fig. 2.4, orange panel). If no issues were detected, the pressure was reset to 0 mbar, and the experiment started. Focusing was adjusted to optimize RBC visibility for image processing (dark RBC, light background).

Due to the chip's size, we divided it into ten sections, which, if taken all together, covered all the visible channels in the top right Fig. 2.4. For each section, 10000 frames (25.32 s) were recorded at $p_{inact} = 0\,\text{mbar}$. The pressure was then set to $p_{act} = 2250\,\text{mbar}$, and a waiting period of approximately 5 min was allowed before again for each section 10000 frames (25.32 s) were recorded.

2.5.3 EP for RBC Dynamics Analysis During Dynamic Pericyte Activation

This experiment, conducted directly after the static pericyte activation analysis, used an RBC suspension at $H_r = 10\%$. The parameters for the pressure pump were set as follows: $p_{inact} = 0\,\text{mbar}$, $p_{act} = 2250\,\text{mbar}$, $t_{up} = t_{down} = 5\,s$, and $t_{act} = t_{inact} = 7\,s$, with a microscope response-dependent t_{del} between 4 and 5.5 seconds (Fig. 2.7a). To capture two pressure pump cycles, we recorded 24000 frames (60.75 s). The Δh was the same as before $\Delta h = 82\,\text{mm}$, resulting in a perfusion pressure $\Delta p = 876.82\,\text{Pa}$, resulting in an average flow velocity of 0.42 mm/s at the four inlet channels to the honeycomb network.

Following the previous experiment, the flashlight was positioned near the chip. A test run confirmed both the pump program's functionality and the flash's visibility in recorded

images, ensuring synchronization.

We divided the chip into ten sections, with each experiment repeated ten times per section, resulting in 100 recordings. A step-by-step protocol for this and the previous experiment is detailed in Appendix A.4.

2.5.4 EP for Characterizing Cross-sectional Area Changes Due to Pressure in the Pressure Chamber

To characterize the change in cross-sectional area with pressure changes in the pressure chamber, the inlet reservoir contained FITC-Dextran in PBS at 150 μg/mL (a fluorescent particle with a 490 nm excitation maximum and 520 nm emission maximum) instead of the RBC suspension.

Using the spinning disk for 3D geometry capture, we excited the FITC-Dextran with a 470 nm lightwave. A 535 nm filter cube was used to capture only the emitted light waves of FITC-Dextran. Z-stacks with a 0.1 μm step size were performed with the 20x objectives at both $p_{\text{inact}} = 0$ mbar and $p_{\text{act}} = 2250$ mbar.

2.6 Image Analysis

To analyze RBC dynamics, we need to track each RBC in recorded video frames to gather information on RBC velocity and concentration in the different channels. We decided to utilize particle tracking velocimetry (PTV), a technique often used to measure fluid velocity in a non-intrusive way. PTV involves suspending small tracer particles in the fluid, then capturing high-speed images to track the same particle across consecutive frames, extracting displacement and velocity at the particle's position. With our setup, we could perform a 2D PTV using a single high-speed camera, which provides velocity information in the x and y directions. This approach is suitable since the RBCs flow in a confined channel, making movement in the z direction negligible. Although typical PTV requires tracer particles that match the fluid density and do not influence flow (passive tracers), RBCs do not meet this criterion, as they have the same density as the medium but are not passive tracers and influence the flow. This distinction is important when deriving the overall flow velocity of the blood (equation 2.13).

The video analysis process consists of three primary steps: image preprocessing (IPP), PTV, and data analysis (DA). These steps were implemented in MATLAB (version R2023a, Natick, MA, USA) and Fiji (Schindelin et al., 2012) through a custom MATLAB script.

In the following sections, each step is described in detail, however, not all steps are required for every analysis. The specific steps applied for each analysis are outlined in the *Materials and Methods* sections of the individual chapters.

The preprocessing builds on an automated process developed by Mantegazza et al. (2020b), Clavica et al. (2016), and Schirinzi (2018). Additional preprocessing steps were added for the new experiment, and the code was optimized to handle larger and more numerous video files efficiently.

2.6.1 Image Preprocessing (IPP)

IPP prepares videos for PTV, which requires black-and-white images with RBCs in white and the background in black.

First, ND2 files are loaded into MATLAB as a $512 \times 512 \times N_{\text{frames}}$ matrix, where N_{frames} is the number of frames. We loaded video data using the open-source function *ND2 Reader* (MATLAB Central File Exchange, Jacob Zuo). We converted it into an *uint8* format (8-bit precision, max value 255) for efficient processing (1 video is 11.3 GB if it is not converted). This conversion does not affect results significantly, as the PTV algorithm requires binarized images.

IPP-A: Define and Retrieve Information

The initial step involves defining region and frames of interest for analysis ($I(:,:,:)$, typically the entire 512×512 image Fig. 2.9a blue square and all frames). A region without channels is also selected to serve as a reference for the light intensity filter (LIF) and synchronization (Fig. 2.9a yellow square). Given that horizontal channels may not be perfectly aligned, we calculate their angle by selecting a region with a single "horizontal" channel wall and applying both a manual method and a Hough transform to detect the wall and measure the angle.

For the manual method, we select two points along the wall and calculate the angle between the line connecting these points and the horizontal axis. The selected region is inverted for the Hough transform method, and an edge detection filter is applied to emphasize edges for easier line detection. A Hough transform then maps these edge points to a parameter space of distance and angle, where potential lines appear as clusters. We extract these lines by identifying peaks in the Hough accumulator matrix and calculating the average angle to the horizontal axis. If a single line is detected, its angle is used directly. If the angle obtained from the Hough transform falls between 0.7 and 1.3 times the manual angle, it is accepted as the rotation angle; otherwise, the manually calculated angle is retained.

Once calculated, regions of interest (ROIs) are defined. A main region (a horizontal channel, Fig. 2.9a red square MD_1) is selected, followed by additional regions, which vary from 2 to 16 in number (Fig. 2.9a pink polygons AD_X). The wanted IPP, PTV, DA steps, and the necessary settings for the image analysis are also selected at this stage.

IPP-B: Synchronization Information and Translation

Using the mean intensity of each frame within the LIF ROI and a peak detection function, we identify the first frame with highest intensity, marking the flashlight activation time (Fig 2.8b). This helps us correlate the frame with pressure pump activation and synchronize the video between repetitions.

During the experiment, we observed that activating the pressure pump caused a slight shift in the microfluidics chip within the microscope's visible ROI as the pressure increased and decreased. This shift complicates background detection and removal. To address this, we perform a translation detection for each frame relative to the first frame using the *imregtform* function (The MathWorks, Inc.), focusing only on x and y translations. We

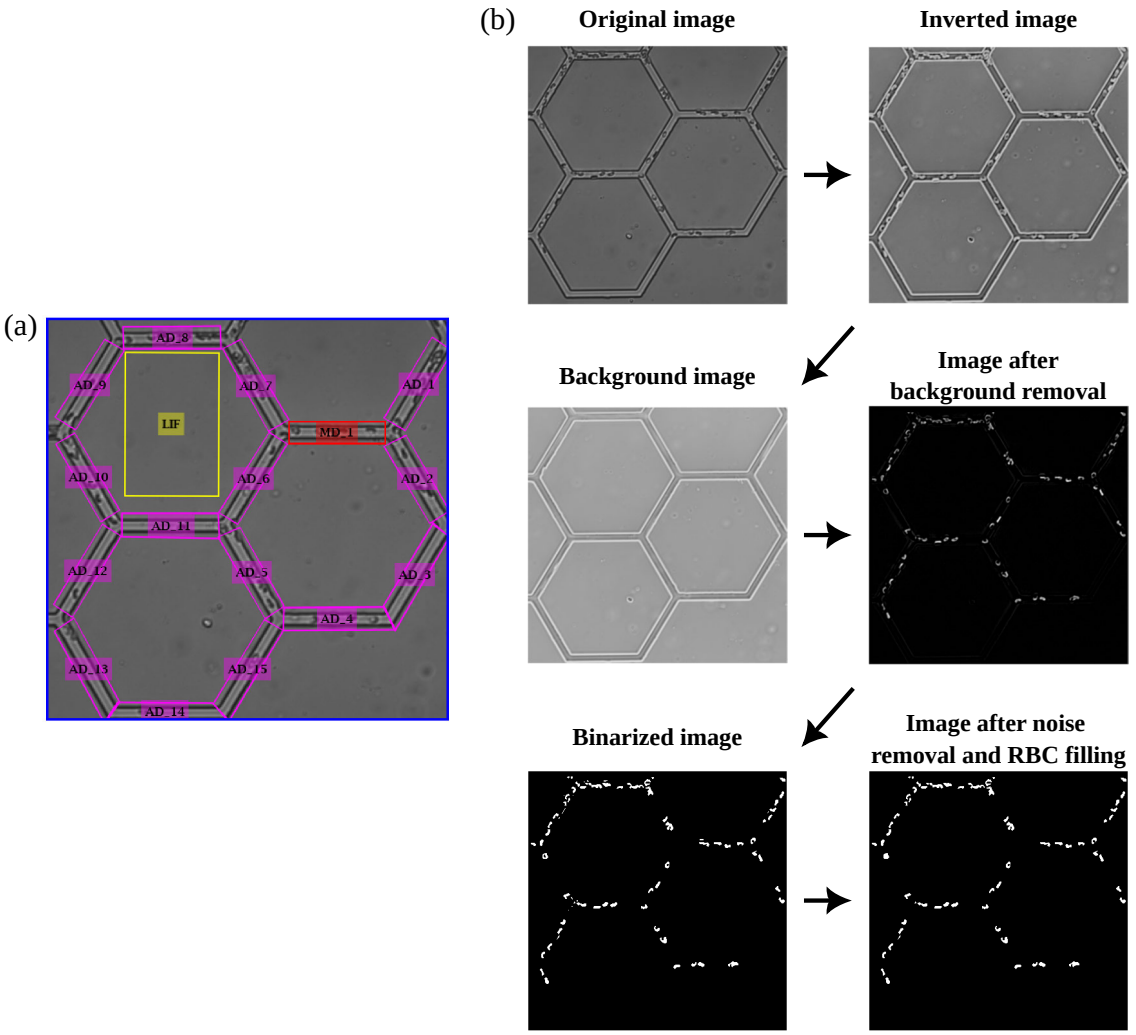

Figure 2.9: Illustration of regions of interest and example of image preprocessing steps. **a)** The blue square outlines the general area of interest. The yellow region denotes the area used for the light intensity filter (LIF). The primary region, labeled MD_1, is highlighted in red, with additional regions, AD_X, marked in pink. **b)** Example of the image preprocessing steps: original, inversion, detected background, background removal, binarization, noise removal and RBC filling.

then apply the inverse of the detected translation to each frame with the *imwarp* function (The MathWorks, Inc.), resulting in the adjusted matrix $I_{\text{trans}}(:,:,:)$.

IPP-C: Grayscale Inversion

Recorded images have a light-gray background and black RBCs. Since PTV requires RBCs in white, we invert the grayscale by subtracting each frame from a white image (255 values), yielding:

$$I_{\text{inv}}(:,:,j) = 255 \cdot \mathbf{1}(:,:) - I_{\text{trans}}(:,:,j)\,, \tag{2.1}$$

where $\mathbf{1}(:,:)$ is a matrix of ones matches the dimensions of $I_{\text{trans}}(:,:,1)$. Fig. 2.9b shows an example.

IPP-D: Background Detection

As previously explained, for PTV to function effectively, it requires a clear background with only the RBCs visible. Therefore, background detection and removal are needed. Two methods were used for background detection: a running average and a background image.

The running average calculates the background for each frame (Bg_j) by averaging each pixel's value over n frames as follows:

$$Bg(:,:,j) = \begin{cases} \frac{1}{n}\sum_{k=1}^{n} I_{\text{inv}}(:,:,k)\,, & \text{if } j \leq n\,, \\ \frac{1}{n}\sum_{k=j-n}^{j-1} I_{\text{inv}}(:,:,k)\,, & \text{if } j > n\,. \end{cases} \tag{2.2}$$

The effectiveness of this background calculation depends on the selection of n and the recording conditions. If n is too large, RBC streaks may appear, similar to light trails seen with long exposure photography. If n is too small, individual RBCs may still be visible in the background. When n is chosen appropriately, the method works well, but it has limitations. First, it fails if hematocrit levels are high and RBCs nearly fill the channels. Second, it does not work in areas with stagnation points where RBCs remain stationary. In Chapter 4, these issues were not a concern, so an $n = 100$ was chosen. Fig. 2.9b shows an example of the calculated background. However, in Chapter 3, lingering RBCs posed a problem, making this method ineffective. Therefore, we used an alternative approach by composing a background image from parts of 4 to 5 frames where no RBCs were present in the channels, resulting in a single frame displaying only the background.

IPP-E: Light Intensity Filter (LIF) and Background Removal

As shown in Fig 2.8b, light intensity varies between frames, even when the flashlight is off. To correct for this, we apply a light intensity filter (LIF). For each frame (j), we calculate the mean intensity within the LIF ROI, specified by coordinates $[a_1 : a_2, b_1 : b_2]$, in both the inverted image (I_{inv}) and the background (Bg). We then compute the intensity difference (ΔInt) between these two values and subtract it from I_{inv} as follows:

$$\Delta Int(j,1) = \frac{1}{c}\sum_{k_1=a_1}^{a_2}\sum_{k_2=b_1}^{b_2} I_{\text{inv}}(k_1,k_2,j) - \frac{1}{c}\sum_{k_1=a_1}^{a_2}\sum_{k_2=b_1}^{b_2} Bg(k_1,k_2,j)\,, \tag{2.3}$$

$$I_{\text{corr}}(:,:,j) = I_{\text{inv}}(:,:,j) - \Delta Int(j,1)\,, \tag{2.4}$$

where $c = (a_2 - a_1 + 1)\cdot(b_2 - b_1 + 1)$ is the number of pixels in the LIF ROI. If the background detection uses a static background image, Bg is constant and independent of j.

After applying this correction, we subtract the background from the corrected image, resulting in a grayscale image where only the RBCs are visible as white on a black background:

$$I_{\text{back}}(:,:,j) = I_{\text{corr}}(:,:,j) - Bg(:,:,j)\,. \tag{2.5}$$

Fig. 2.9b shows an example.

IPP-F: Rotation and Binarization

The frames were then rotated (I_{rot}) to horizontally align the channels using the *imrotate* function (The MathWorks, Inc.) and the previously calculated angle (*IPP-A*). Next, we applied binarization to convert the grayscale image to black and white, with RBCs appearing in white. The binarization process is defined as follows:

$$I_{\text{bin}}(a,b,j) = \begin{cases} 0\,, & \text{if } I_{\text{rot}}(a,b,j) \leq \kappa\,, \\ 1\,, & \text{if } I_{\text{rot}}(a,b,j) > \kappa\,, \end{cases} \tag{2.6}$$

where κ is a threshold the specific video determines, typically between 10 and 15. This low threshold is feasible because most of the background has already been removed, as seen in Fig. 2.9b.

IPP-G: Noise Filtering and RBC Filling

To remove false positive pixels mistakenly identified as RBCs after binarization, we applied a noise filter in two steps: erosion and reconstruction. First, we performed erosion using a circular filtering element to reduce noise pixels (I_{er}). The filter's size needed to be large enough to erode noise pixels while preserving RBCs, so we selected a radius of 1 px based on the smaller size of noise elements relative to RBCs. This erosion step reduced the size of all image elements, ideally eroding noise entirely.

To retain the original dimensions and restore RBC information, we then used the *imreconstruct* function (The MathWorks, Inc.) to reconstruct the filtered frame (I_{er}) using the pre-erosion frame (I_{bin}) as a reference, resulting in the final noise-filtered frame I_{nf}.

Additionally, we observed that the inner regions of some RBCs appeared similar in color to the background, which sometimes left holes in the center of RBCs after background removal. To address this, we applied the *imfill* function (The MathWorks, Inc.), which fills any dark pixel areas entirely surrounded by lighter pixels, restoring the RBCs to a solid appearance (I_{fill}).

The final frame after preprocessing can be observed in Fig. 2.9b.

2.6.2 Particle Tracking Velocimetry (PTV)

For our analysis, we used PTVlab, an open-source MATLAB software developed by Brevis et al. (2011) and further customized in this thesis to meet specific requirements. PTVlab's was validated for tracking RBCs by Mantegazza et al. (2020b). The software offers multiple algorithmic methods: cross-correlation (CC), relaxation, and hybrid approaches. The CC method was particularly effective given our flow type and typical particle (RBC) seeding density. This method uses binary intensity matrices (Hassan et al., 1992) to track individual particles by identifying the highest similarity between particle distribution patterns, known for its computational efficiency (Ruhnau et al., 2005; Ishikawa et al., 2000).

The PTV process consists of two main steps: first, detecting all RBCs within each frame, and second, tracking the movement of each detected RBC across frames.

PTV-A: RBC Detection

Before performing PTV, we need to detect all RBCs in the frames. If RBCs always flow without touching other RBCs, detection could be achieved using the *regionprops* function alone, which measures properties (e.g., area, centroid) of each object (connected component) in an image. However, since RBCs can cluster while flowing, *regionprops* alone is insufficient, as it may interpret multiple RBCs traveling together as a single RBC.

To address this, we applied two different detection methods. The first combines *regionprops*, *watershed* segmentation (in Fiji, ImageJ (Schindelin et al., 2012)), and manual verification in MATLAB. This approach was used in the experiment described in Chapter 3, where accurate RBC shape detection was essential. In Fig. 2.10a, the watershed method successfully separated some aggregated objects (e.g., dividing objects 6 and 7 (blues) from object 4 (green)) but could not fully separate all clusters, necessitating manual checks and corrections. From here, the centroid, circularity, and orientation are extracted.

The second method, used in the experiment described in Chapter 4, was focused on RBC tracking rather than precise shape, given the large number of frames. This method combines *regionprops* with a Gaussian Kernel mask approach (Takehara and Etoh, 1998). Before detecting RBCs with *regionprops*, we calculated their mean diameter and area by analyzing all objects in the MD_01 ROI across frames. We plotted the diameter and area distributions in a histogram (see Fig. 2.10b,c) to determine the mean diameter ($\overline{D}$), which ranged from 8 to 10 pixels, and the mean area ($\overline{A}$), which ranged from 50 to 70 pixels.

After identifying objects in each frame, we categorized them into two groups. Objects with $20\,\mathrm{px}^2 < A < 1.4\overline{A}$ were considered single RBCs, while those with $A > 1.4\overline{A}$ were processed using the Gaussian Kernel mask method. This method uses a binary, oval-shaped mask to scan the image, looking for similarly shaped objects. The correlation between the mask shape and detected objects is calculated, and objects are retained for analysis only if the correlation coefficient exceeds a set threshold. This process can distinguish clustered RBCs by matching them to the Gaussian Kernel mask (GM), which is defined as a two-dimensional Gaussian function centered at $n = 1.5 \cdot \overline{D}$ with a standard deviation influenced by $\overline{D}$ as follows:

$$GM = exp\left(-\frac{(x-\frac{n}{2})^2/B_1^2 + (y-\frac{n}{2})^2}{B_2^2 \cdot 2 \cdot \overline{D}}\right) \tag{2.7}$$

where B_1 and B_2 are scaling factors that shape the Gaussian distribution. We achieved optimal results with $B_1 = 1.35$, $B_2 = 0.4$, a correlation threshold of 0.4, and an intensity threshold of 70.

At the end of this step, we obtained a list of all detected objects along with their centroid positions for each frame.

PTV-B: RBC Tracking

In this algorithm, particle velocity is determined by identifying the highest cross-correlation coefficient, calculated by comparing a reference intensity matrix in the current

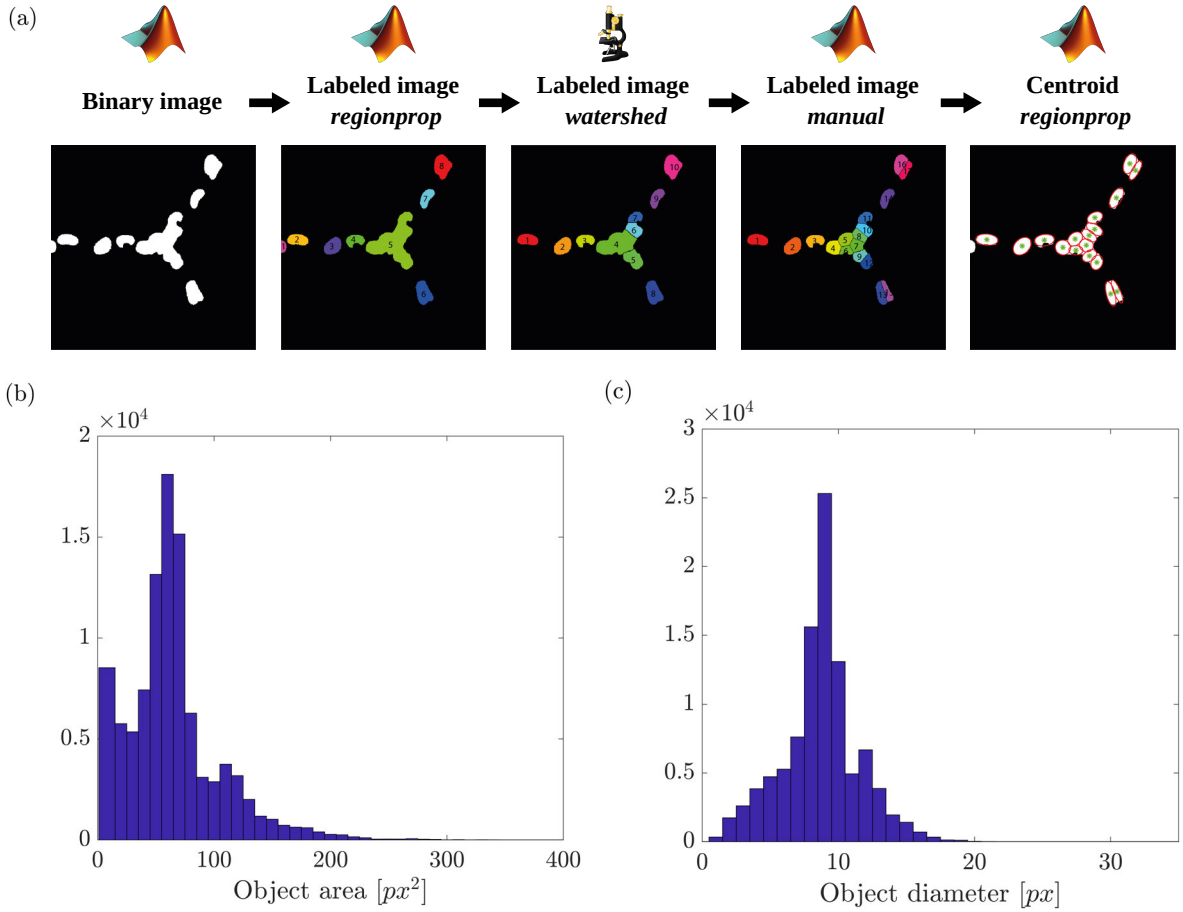

Figure 2.10: Example of the two particle detection methods. **a)** Combined approach using *regionprop* (MATLAB), *watershed* segmentation (Fiji), and manual correction (MATLAB). **b)** Histogram of object areas within the main domain. **c)** Histogram of object diameters within the main domain.

frame with a set of sub-matrices in the subsequent frame. The reference matrix is formed by extracting the image intensities within a square interrogation window of size $l_\mathrm{w} \times l_\mathrm{w}$ centered on the particle's position (Fig. 2.11 red particle p). A second set of matrices is generated from interrogation windows centered on each potential particle location in the following frame (Fig. 2.11 blue, yellow, orange and green particles). Potential matches in frame two are identified as particles within a distance l_1 from the particle of interest in the first frame (we used $l_\mathrm{w} = l_1 = 20\,\mathrm{px}$).

Cross-correlation coefficients between the reference matrix in the first frame and each particle-centered matrix in the second frame are calculated as follows:

$$R = \frac{\sum_{l_\mathrm{w}} \sum_{l_\mathrm{w}} (A_{l_\mathrm{w},l_\mathrm{w}} - \overline{A})(B_{l_\mathrm{w},l_\mathrm{w}} - \overline{B})}{\sqrt{\sum_{l_\mathrm{w}} \sum_{l_\mathrm{w}} (A_{l_\mathrm{w},l_\mathrm{w}} - \overline{A})^2 \sum_{l_\mathrm{w}} \sum_{l_\mathrm{w}} (B_{l_\mathrm{w},l_\mathrm{w}} - \overline{B})^2}} \tag{2.8}$$

where R is the cross-correlation coefficient, A and B are matrices of size $l_\mathrm{w} \times l_\mathrm{w}$, and $\overline{A}$ and $\overline{B}$ are the mean light intensities of the elements in matrices A and B, respectively. If only one possible particle has an R value exceeding a specified threshold (0.6 in our case), that

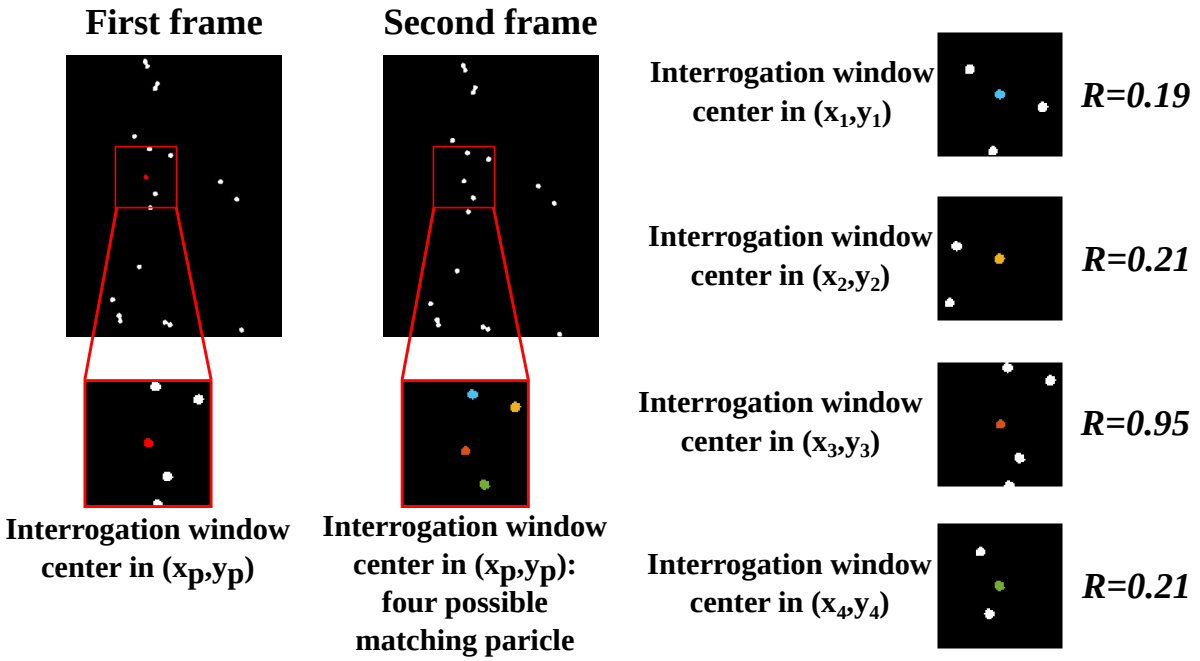

Figure 2.11: Example of PTV algorithm for tracking particle p. The particle is highlighted in red, with the interrogation window shown as a red square in the first frame (centered at (x_p, y_p)). In the second frame, four potential matching particles (blue, yellow, orange, and green) are detected within the same window. For each candidate, an interrogation window is generated, centered at their respective coordinates (x_x, y_x), used for a comparison matrix. Cross-correlation coefficients are then calculated for each particle, with the orange particle identified as the best match. The particle's velocity is determined as $u_x = (x_3 - x_p)/\Delta t$ and $u_y = (y_3 - y_p)/\Delta t$.

particle is considered the correct match. If multiple particles exceed the threshold, their displacements are compared with those of neighboring particles, and the displacement with the closest direction and magnitude to neighboring particles is selected as valid.

Using this matching process, we generate a data matrix for each video, recording each tracked RBC's position, velocity, frame number, and ID. Velocity ($\vec{u}_{p,j}$) is calculated as:

$$\vec{u}_{p,j} = \frac{\vec{d}_{p,j}}{\Delta t} \tag{2.9}$$

where p is the specific particle, $\vec{d}$ is its displacement between frames j and $j+1$, and Δt is the time interval between frames 1/fps.

2.6.3 Data Analysis (DA)

This section presents the general formula for the analysis of the information extracted from the PTV. This is for the case of most complex experiments, which include repetition.

By matching the channel and RBC positions, we could extract all the RBCs flowing in a specific channel ($p \in i$) for each frame. For each channel (i), frame (j), and experiment

repetition (k), the number of RBCs ($N_{\mathrm{RBC},ijk}$) inside the channel were calculated. Then, the mean velocity in the channel is calculated:

$$u_{\mathrm{RBC},ijk} = \frac{1}{N_{\mathrm{RBC},ijk}} \sum_{p \in i \text{ at } k} |\vec{u}_{p,jk}| \,. \tag{2.10}$$

From these values, the tube hematocrit ($H_{\mathrm{t},ijk}$), RBC flux ($Q_{\mathrm{RBC},ijk}$), and blood flow ($Q_{\mathrm{blood},ijk}$) for each channel, frame, and repetition were determined using the following equations:

$$H_{\mathrm{t},ijk} = \frac{N_{\mathrm{RBC},ijk} \cdot MCV_{\mathrm{RBC}}}{V_{ik}} \,, \tag{2.11}$$

$$Q_{\mathrm{RBC},ijk} = u_{\mathrm{RBC},ijk} \cdot H_{\mathrm{t},ijk} \cdot (W \cdot H) = u_{\mathrm{RBC},ijk} \cdot \frac{N_{\mathrm{RBC},ijk} \cdot MCV_{\mathrm{RBC}}}{L_{\mathrm{ROI},ik}} \,, \tag{2.12}$$

$$Q_{\mathrm{blood},ijk} = u_{\mathrm{blood},ijk} \cdot (W \cdot H) = \chi \ \cdot u_{\mathrm{RBC},ijk} \cdot (W \cdot H) \,. \tag{2.13}$$

Where MCV_{RBC} is the mean corpuscular volume of the RBCs and V_{ik} is the volume of the microchannel, calculated as $V_{ik} = W \cdot H \cdot L_{\mathrm{ROI},ik}$. $L_{\mathrm{ROI},ik}$ is the length of the ROI for each specific channel and repetition. Here, χ is the coefficient for the velocity difference between plasma and RBCs. Due to the Fåhræus effect (Fåhraeus, 1929), the RBC velocity is typically higher than the plasma velocity and is typically calculated as $\chi = H_{\mathrm{t}}/H_{\mathrm{d}}$. We set $\chi = 1$ based on the assumption that RBC velocity equals blood velocity (Sherwood et al., 2014). Since we use Q_{blood} only to compute fractional blood flow at bifurcations (see below), which is a division of the blood flow in the daughter vessel and the parent vessel, χ would be canceled out and therefore making Q_{blood} independent of χ. We should still consider that χ depends both on the channel size and on the tube hematocrit. Making $\chi_{\mathrm{D}}/\chi_{\mathrm{P}} \approx 1$ and approximation which is still legitimate.

Before calculating the fractional blood flow Φ and the fractional RBC flux Ψ at each diverging bifurcation, corrections were applied to ensure mass conservation at the bifurcations. These corrections were performed following the method proposed by Pries et al. (1989). In this setup, P represents the parent vessel, and D1 and D2 are the two daughter vessels.

The corrected blood flow ($\widehat{Q}$) for the parent and daughter vessels are computed using the following equations:

$$\widehat{Q}^{\mathrm{P}} = Q^{\mathrm{P}} \cdot \frac{1 + W_{\mathrm{D1}} + W_{\mathrm{D2}}}{W_{\mathrm{P}} + W_{\mathrm{D1}} + W_{\mathrm{D2}}} \,, \tag{2.14}$$

$$\widehat{Q}^{\mathrm{D1}} = Q^{\mathrm{D1}} \cdot \frac{W_{\mathrm{P}} + (Q^{\mathrm{P}} - Q^{\mathrm{D2}})/(Q^{\mathrm{P}} + Q^{\mathrm{D2}}) + W_{\mathrm{D2}}}{W_{\mathrm{P}} + W_{\mathrm{D1}} + W_{\mathrm{D2}}} \,, \tag{2.15}$$

$$\widehat{Q}^{\mathrm{D2}} = Q^{\mathrm{D2}} \cdot \frac{W_{\mathrm{P}} + W_{\mathrm{D1}} + (Q^{\mathrm{P}} - Q^{\mathrm{D1}})/(Q^{\mathrm{P}} + Q^{\mathrm{D1}})}{W_{\mathrm{P}} + W_{\mathrm{D1}} + W_{\mathrm{D2}}} \,, \tag{2.16}$$

where:

$$W_{\mathrm{P}} = \frac{Q^{\mathrm{P}}}{Q^{\mathrm{D1}} + Q^{\mathrm{D2}}} \,, \quad W_{\mathrm{D1}} = \frac{Q^{\mathrm{D1}}}{Q^{\mathrm{P}} + Q^{\mathrm{D2}}} \,, \quad W_{\mathrm{D2}} = \frac{Q^{\mathrm{D2}}}{Q^{\mathrm{D1}} + Q^{\mathrm{P}}} \,. \tag{2.17}$$

Finally, the fractional blood flow Φ and fractional RBC flux Ψ for each daughter vessel α at a bifurcation are calculated as:

$$\Phi^{\alpha} = \frac{\widehat{Q}^{D\alpha}_{\text{blood}}}{\widehat{Q}^{\text{P}}_{\text{blood}}} \ , \quad \Psi^{\alpha} = \frac{\widehat{Q}^{D\alpha}_{\text{RBC}}}{\widehat{Q}^{\text{P}}_{\text{RBC}}} \ . \tag{2.18}$$

The measured values of Φ^{α} and Ψ^{α} were then compared to the predictions provided by Pries et al. (2003). The model was already presented in Section 1.6.3 and equations equations (1.33) to (1.36). Since all the bifurcations in this experiment were symmetric, the coefficient A (equation 1.34) equals 0. For the coefficient B and X_0 (equations 1.35 and 1.36), a correction factor (C) needs to be applied since these derivations for that coefficient were obtained from experiments with rat RBCs, and our experiment involves human or rabbits RBCs. As suggested by Pries and Secomb (2008) and used by Roman et al. (2016), the hydraulic diameters were multiplied by the following factor:

$$C = \left(\frac{MCV_{\text{RBC,rat}}}{MCV_{\text{RBC,human/rabbit}}} \right)^{(1/3)} \ , \tag{2.19}$$

where $MCV_{\text{RBC,rat}} = 55\,\mu\text{m}^3$ (Pries and Secomb, 2008) and as stated before human RBCs have $MCV_{\text{RBC,human}} = 87.4\,\mu\text{m}^3$ (Amin and Sirs, 1985; Lewis, 1996a; Salvioli et al., 1993; Tomaiuolo et al., 2012) resulting in a factor of $C = 0.86$ and $MCV_{\text{RBC,rabbit}} = 68.5\,\mu\text{m}^3$ (Kim et al., 2002; Lewis, 1996c; Windberger et al., 2003) resulting in a factor of $C = 0.93$. To determine whether a diverging bifurcation can be considered well-balanced, we calculated the balance factor, BF, using the approach described by Schmid et al. (2015):

$$BF = 1 - \frac{|0.5 - \Phi^{\alpha}|}{0.5} \tag{2.20}$$

where Φ^{α} represents the blood flow fraction in one of the daughter branches. The balance factor BF ranges from 0 for a completely unbalanced network to 1 for a perfectly balanced network. According to Schmid et al. (2015), a network is considered well-balanced if $BF > 0.8$.

Chapter 3

Relation Between Hematocrit Partitioning and RBC Lingering

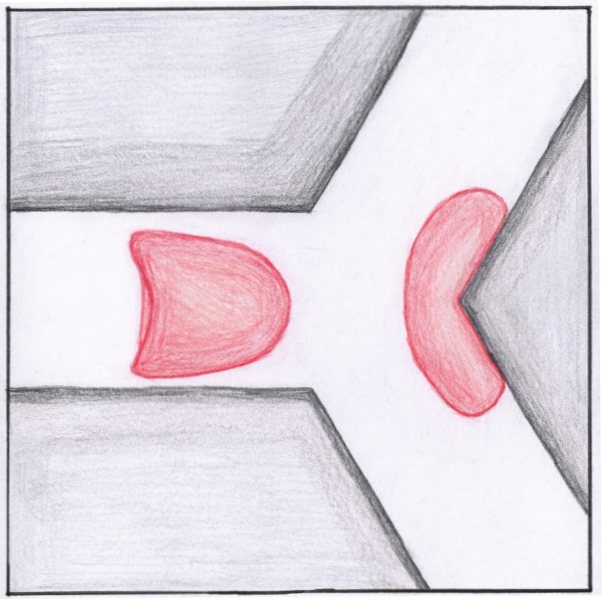

3.1 Preamble

This chapter is based on the author's publication *Relation between hematocrit partitioning and red blood cell lingering in a microfluidic network* which has been published in Biophysical Journal (2024) (Bucciarelli et al., 2024).

3.2 Introduction

As outlined in Chapter 1, the microcirculation consists of highly interconnected networks of small capillaries arranged in a mesh-like fashion, enabling efficient local oxygen transport carried by RBCs to surrounding tissues. Numerous studies have demonstrated that RBC distribution within microvascular networks is spatially and temporally heterogeneous, with this heterogeneity linked to RBC behavior at microvascular bifurcations (Schulte et al., 2003; Kleinfeld et al., 1998; Mantegazza et al., 2020a,b; Balogh and Bagchi, 2017a).

As discussed in Section 1.6.1, RBCs exhibit a nonuniform and time-dependent distribution at divergent bifurcations (Balogh and Bagchi, 2018), often following classical hematocrit partitioning, the Zweifach-Fung effect. However, in larger networks with more complex RBC dynamics, reductions or inversions of this classical partitioning have been observed (Balogh and Bagchi, 2017b,a; Mantegazza et al., 2020b,a; Shen et al., 2016; Hyakutake et al., 2022; Clavica et al., 2016). One cause of this reverse partitioning was identified in an *in vitro* network by Mantegazza et al. (2020b,a), who correlated it with skewed hematocrit profiles in the parent vessels. However, the fluid dynamics at the RBC scale that led to these skewed profiles were not investigated. Balogh and Bagchi (2017b, 2018) simulated a physiologically realistic microvascular network, identifying competing phenomena that give rise to transient events that cause RBC behavior to oscillate between classical and reverse partitioning, with RBC lingering at bifurcation apex being one factor in local hematocrit partitioning.

This study aims to determine whether RBC lingering at the bifurcation apex contributes to skewed hematocrit profiles, potentially driving reverse partitioning at downstream bifurcations.

Qualitatively, lingering RBCs (LRBCs) are cells that stay at the bifurcation apex rather than flowing directly from the parent vessel into the daughter vessels. These LRBCs often remain near the separation surface, the boundary dividing streamlines toward each daughter vessel. Approaching the apex with near-zero velocity, LRBCs interact with vessel walls and other RBCs, lingering there for a prolonged period of time before eventually entering a daughter vessel. This process is dominated by cell-cell and cell-wall interactions, not by the undisturbed streamlines that carry non-lingering RBCs (NLRBCs) and cannot be reduced to simple cell deceleration.

While lingering has been recognized as an important phenomenon of RBC dynamics in microcirculation, studies on the topic remain limited (Kihm et al., 2021; Rashidi et al., 2023; Balogh and Bagchi, 2017b; Pskowski et al., 2021). As such, a standardized mathematical definition of lingering has yet to be established. It is essential to compare the methods used to define lingering, as results vary significantly with the criteria for distinguishing LRBCs from NLRBCs. Prior studies identified LRBCs by minimum RBC

velocity (Kihm et al., 2021; Rashidi et al., 2023) and RBC residence time (Balogh and Bagchi, 2017b; Pskowski et al., 2021). This study will compare purely geometric and kinematic criteria (minimum RBC-apex distance and minimum RBC velocity) to relative residence time, which combines these criteria, demonstrating that the latter is the most effective for identifying LRBCs in our experimental data.

Previous studies (Balogh and Bagchi, 2017b, 2018; Rashidi et al., 2023) investigated the effects of LRBCs on hematocrit partitioning at the bifurcation where they linger, focusing on vessels with diameters similar to or smaller than RBC size. In these cases, where the confinement ratio (λ) is less than one (high confinement), LRBCs may partially block the entry of the daughter vessels, forcing incoming RBCs to cross the separation surface and enter low-flow vessels, facilitating reverse partitioning.

This study investigates whether RBC lingering can also impact the dynamics at downstream bifurcations. We hypothesize that lingering RBCs flowing into a daughter vessel may create skewed hematocrit profiles, favoring reverse partitioning at subsequent bifurcations and contributing to the network history effect (Merlo, 2018; Mantegazza et al., 2020b). To test this, we used a microfluidic device with a single symmetric diverging bifurcation to examine LRBC dynamics at low tube hematocrit. Unlike prior studies, these microchannels were larger than typical RBCs, resulting in a low confinement ratio ($\lambda > 1$), where local blockage due to lingering is expected to be minimal.

The results from this single diverging bifurcation were then compared to data from previous experiments in a complex network where reverse partitioning was observed (Mantegazza et al., 2020b). This comparison suggests that reverse partitioning may occur at subsequent bifurcations when sufficient numbers of RBCs linger at earlier bifurcations.

3.3 Materials and Methods

3.3.1 Microfluidic Device, RBC Suspension, Experimental Set-up, and Protocol

This study utilized the single honeycomb microfluidic chip, as detailed in Section 2.2.1, fabricated according to the methods described in Sections 2.1.1 and 2.1.2.

Heparinized blood from New Zealand rabbits was used to prepare RBC suspensions following the protocol outlined in Section 2.3. Three RBC suspension concentrations were produced: $H_\mathrm{r} = 10\%$, 20%, and 30%.

We used a simplified version described in Section 2.4 for the experimental set-up, where we excluded the pressure pump and flash lamp.

The experimental protocol, outlined in Section 2.5.1, involved applying a perfusion pressure of $\Delta p = 213.86\,\mathrm{Pa}$, generating an average RBC flow velocity of 0.67 mm/s in ROI 0 (Fig. 3.1), which is comparable to velocities observed in capillary networks under resting conditions (Hudetz, 1997; Schulte et al., 2003; Schmid et al., 2019b). For each hematocrit condition, 4000 frames were recorded using a 40x objective at 395 fps.

3.3.2 Image Processing

All recorded videos are available through a link in Appendix C.1 (Videos S1-S3).

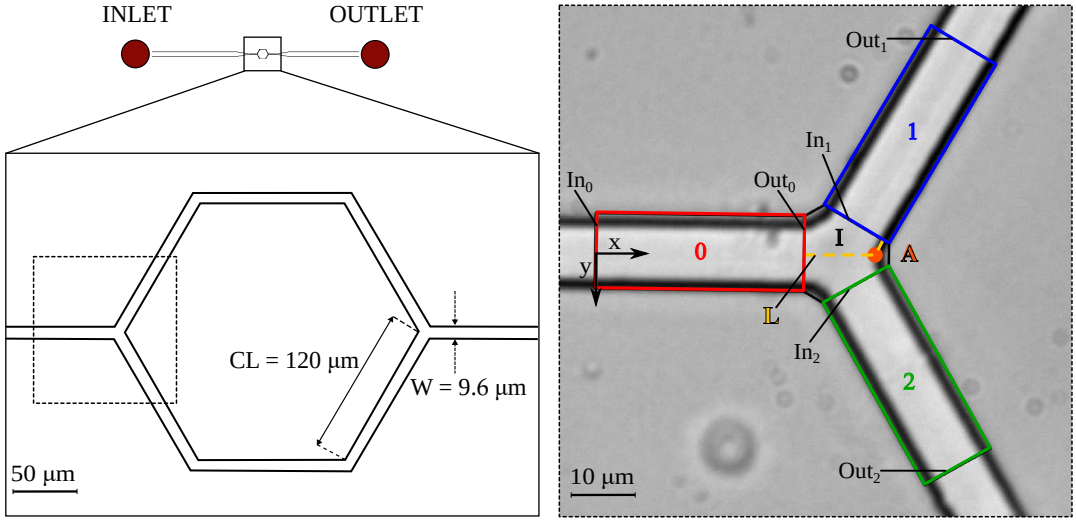

Figure 3.1: Schematic single honeycomb microfluidic chip. Microfluidic device with inlet and outlet (top left), a magnified version of the single-mesh network (bottom left), and a microscope image (512x512 pixels) of the diverging bifurcation (right) with regions of interest (ROIs) used for the image analysis: parent vessel (ROI 0) in red, daughter vessel 1 (ROI 1) in blue, daughter vessel 2 (ROI 2) in green, and the intersection (I) in the center where the apex (A, orange) is located. The dashed yellow path of length L is the reference length for the definition of relative residence time τ_{RBC}.[1]

The preprocessing procedure involved several steps as detailed in Section 2.6.1: defining and retrieving information (Section 2.6.1 IPP-A), grayscale inversion (Section 2.6.1 IPP-C), background detection (Section 2.6.1 IPP-D), LIF and background removal (Section 2.6.1 IPP-E), rotation and binarization (Section 2.6.1 IPP-F), and noise filtering with RBC filling (Section 2.6.1 IPP-G). For *IPP-A*, the main region of interest was defined as the parent channel (ROI 0), as shown on the right side in Fig. 3.1. The two daughter vessels were defined as ROI 1 and 2, with the area between these regions labeled as intersection (I). ROIs 0, 1, and 2 each had a length of 33.2 μm and were positioned 5.5 μm from the center of the intersection.

Following preprocessing, we perform the PTV as described in Section 2.6.2. RBC detection was performed using the *regionprops* and *watershed* method in Fiji, followed by a manual check, as outlined in Section 2.6.2 PTV-A. The tracking of detected RBCs was completed using the open-source software PTVlab (Brevis et al., 2011), with the tracking algorithm described in Section 2.6.2 PTV-B.

For each tracked RBC, we extracted not only position (mm) and velocity (u in mm/s) but also circularity (ϵ) and orientation (β in °). The position was converted to a normalized lateral coordinate, $y^* = y/W$, ranging from -0.5 to 0.5, with $y = 0$ at the center of the parent vessel (ROI 0). In the daughter vessels, we labeled the channel walls as proximal ($y^* = -0.5$) and distal ($y^* = 0.5$), based on flow direction. Inlets (In) and outlets (Out) were also defined according to flow direction. The bifurcation apex (A) was set at the intersection of the daughter vessels' distal walls. Finally, the distance Δs between the

[1]Figure 1 in Bucciarelli et al. (2024). CC BY 4.0.

RBC centroid and apex A was computed, decreasing to zero as an RBC approaches the intersection and increasing as the RBC enters a daughter vessel.

3.3.3 Classification of LRBCs

To distinguish LRBCs from NLRBCs, a relative residence time τ_{RBC} was defined as the normalized time spent by a RBC at the intersection I (Fig. 3.1):

$$\tau_{\mathrm{RBC}} = \frac{t_{\mathrm{r,RBC}}}{t_{\mathrm{ref}}}, \tag{3.1}$$

where $t_{\mathrm{r,RBC}}$ is the residence time of a specific RBC at the intersection and $t_{\mathrm{ref}} = L/\overline{u}_{\mathrm{Out},0}$ is the reference time a RBC needs to travel the reference length L (from the exit of the ROI of the parent vessel to the apex and then to the entry of the daughter vessel, Fig. 3.1) with a velocity equal to the mean velocity at the outlet of the parent vessel ($\overline{u}_{\mathrm{Out},0}$). The choice of this reference time scale defines a convective time scale for RBC transport in the bifurcation. This definition is similar to the lingering Péclet number defined by Rashidi et al. (2023), except that it is a cell-based definition instead of a statistical estimation based on the probability density function of the RBC velocity. For our experiments, a RBC was defined as a LRBC if $\tau_{\mathrm{RBC}} > 2.0$. A justification *a posteriori* for this choice is given in Section 3.4.1.

3.3.4 Hematocrit

The mean tube hematocrit $\overline{H}_{\mathrm{t},i}$ in ROI i was computed as

$$\overline{H}_{\mathrm{t},i} = \frac{1}{N_{\mathrm{frames}}} \sum_{j=1}^{N_{\mathrm{frames}}} \frac{N_{\mathrm{RBC},j} \times MCV_{\mathrm{RBC}}}{V_i}, \tag{3.2}$$

where N_{frames} is the number of frames, $N_{\mathrm{RBC},j}$ is the number of RBCs in ROI i at frame j, and V_i is the microchannel volume corresponding to ROI i. The mean corpuscular volume of New Zealand rabbit RBCs (Kim et al., 2002; Lewis, 1996c; Windberger et al., 2003) is $MCV_{\mathrm{RBC}} = 68.6\,\mu\mathrm{m}^3$. The mean tube hematocrit measured in the parent vessel was $\overline{H}_{\mathrm{t},0} \approx 5.2\%$, which was in good agreement with the theoretical value of $H_{\mathrm{t}} = 5.50\%$ for a reservoir hematocrit of $H_{\mathrm{r}} = 10\%$ and a hydraulic diameter of $D_{\mathrm{h}} = (2 \times W \times H)/(W + H) = 8.72\,\mu\mathrm{m}$ predicted by Pries and Secomb (2008) (equation 1.27).

Two experiments with different reservoir hematocrit ($H_{\mathrm{r}} = 20\%$ and $H_{\mathrm{r}} = 30\%$) were also carried out and the measured tube hematocrit was $\overline{H}_{\mathrm{t},0} \approx 6.3\%$ and $\overline{H}_{\mathrm{t},0} \approx 8.7\%$, respectively. Results for these hematocrits were not significantly different from the experiment with $\overline{H}_{\mathrm{t},0} \approx 5.2\%$ ($H_{\mathrm{r}} = 10\%$), thus detailed data from these experiments are only reported in the Appendix C.4.

3.3.5 Lateral RBC Distribution

The lateral distribution function $LDF_i(y^*)$ of RBCs in the ROI i (i.e. the hematocrit profile) was computed from the histogram of the lateral position of RBCs at the inlet

and outlet of the ROI i. The skewness index (Sherwood et al., 2014) for the RBC lateral distribution in the respective ROI i was then calculated according to

$$Sk_i = \left| \frac{\int_{-0.5}^{0} LDF_i(y^*)dy^*}{\int_{-0.5}^{0.5} LDF_i(y^*)dy^*} - 0.5 \right|. \tag{3.3}$$

For $Sk = 0$, the RBC lateral distribution is symmetrical with respect to the microchannel centerline. For $Sk = \pm 0.5$, the RBC lateral distribution is such that all RBCs are located on one side of the microchannel.

To evaluate the relation between RBC lingering and hematocrit partitioning, we compared lateral distribution functions $LDF(y^*)$, that we obtained in a different experimental setup in a previous study where we quantified the partitioning of RBCs in several consecutive bifurcations (Mantegazza et al., 2020b), to the present lateral distribution functions obtained in a single divergent bifurcation for lingering and non-lingering red blood cells (LDF_{LRBC} and LDF_{NLRBC}, respectively). To this end, a composite lateral distribution function (LDF_{C}) was defined as

$$LDF_{\mathrm{C}}(y^*, \gamma) = \gamma \cdot LDF_{\mathrm{LRBC}}(y^*) + (1 - \gamma) \cdot LDF_{\mathrm{NLRBC}}(y^*), \tag{3.4}$$

where LDF_{LRBC} and LDF_{NLRBC} were measured at the end of the daughter vessels and γ is a weighting factor that can be interpreted as the percentage of lingering RBCs (lingering frequency).

An optimal lingering frequency $\widehat{\gamma}$ was determined by minimizing the error $E(\gamma)$ between the the composite lateral distribution LDF_{C} and the previously reported lateral distribution $LDF(y^*)$:

$$E(\widehat{\gamma}) = \min_{\gamma} \; E(\gamma), \tag{3.5}$$

$$E(\gamma) = \int_0^{0.5} \left[LDF(y^*) - LDF_{\mathrm{C}}(y^*, \gamma) \right]^2 dy^*. \tag{3.6}$$

Note that the squared error is only integrated over the interval $[0, 0.5]$. This is due to the network topology used by Mantegazza et al. (2020b) which will be further explained in Section 3.4.5.

3.3.6 Blood Flow Rate and RBC Flux

The blood flow rate was calculated from the spatial and temporal mean of the RBC velocities $\overline{u}_{\mathrm{RBC},i}$ in the ROI i as (Mantegazza et al., 2020b,a):

$$Q_{\mathrm{blood},i} = \overline{u}_{\mathrm{blood},i} \times (W \times H) = \chi \; \times \overline{u}_{\mathrm{RBC},i} \times (W \times H), \tag{3.7}$$

where χ is the coefficient accounting for the velocity difference between plasma and RBCs. Due to the Fåhræus effect (Fåhraeus, 1929), the RBC velocity is typically higher than the plasma velocity. Following Sherwood et al. (2014), we assumed $\chi = 1$, implying that the mean RBC velocity is equal to the mean whole blood velocity. We will show later that the mean RBC velocity in the daughter vessels is biased by lingering RBCs which leads

to an underestimation of the blood flow rate. Similarly, the RBC flux in the different ROI was computed as:

$$Q_{\mathrm{RBC},i} = \overline{u}_{\mathrm{RBC},i} \times \overline{H}_{\mathrm{t},i} \times (W \times H). \tag{3.8}$$

The fluxes $\widehat{Q}_{\mathrm{blood},i}$ and $\widehat{Q}_{\mathrm{RBC},i}$ were corrected according to satisfy mass conservation at the bifurcation. To this end, we employed the procedure originally developed by Pries et al. (1989), detailed in Section 2.6.3, and previously utilized in our work (Mantegazza et al., 2020b).

The fractional blood flow rate Φ_i and fractional RBC flux Ψ_i in the daughter vessel i was calculated as:

$$\Phi_i = \frac{\widehat{Q}_{\mathrm{blood},i}}{\widehat{Q}_{\mathrm{blood},0}} \quad \text{and} \quad \Psi_i = \frac{\widehat{Q}_{\mathrm{RBC},i}}{\widehat{Q}_{\mathrm{RBC},0}}. \tag{3.9}$$

3.3.7 Statistical Analysis

For the statistical analysis of the RBC position, velocity, circularity, and orientation, we used a two-sample Kolmogorov-Smirnov test (K-S test). The K-S test was selected due to its higher sensitivity to differences in distribution shape rather than the distribution median. For the statistical analysis of $\widehat{\gamma}$, we used a Mann-Whitney-U test (M-W-U test), which is primarily sensitive to differences in the distribution median. All statistical tests were performed with a significance level of $p = 0.05$.

3.4 Results

3.4.1 Classification of Non-lingering and Lingering RBC

A total of 378 RBCs were tracked throughout the experiment with $\overline{H}_{\mathrm{t},0} \approx 5.2\%$ ($H_{\mathrm{r}} = 10\%$). The minimum distance to the apex (Δs_{min}) varied from $7.67\,\mu$m to $0.86\,\mu$m, whereas the minimum velocity in the intersection (u_{min}) varied from $0.52\,$mm/s to $0.004\,$mm/s (Fig. 3.2a).

In general, we found that the minimum RBC velocity was lower for RBCs that were closer to the apex (Fig. 3.2a). At the same time, we also observed some very slow RBCs far away from the apex of the bifurcation. These outliers were individually checked and turned out to be RBCs that changed their shape between two consecutive frames without sensibly advancing their centroid position, such that their velocity was very low. If only u_{min} was used to distinguish LRBCs from NLRBCs, those outliers would be classified as LRBCs (i.e., false positives).

If we considered only the minimum distance Δs_{min} for the RBC classification, some RBCs would be falsely classified as LRBCs as they may pass very close to the apex without lingering and enter directly one of the daughter vessels. Therefore, neither the minimum distance to the apex Δs_{min} nor the minimum velocity at the intersection u_{min} should be used alone to determine whether an RBC lingers.

Two other methods are used by other researchers to define LRBC, which are based on a combination of distance to apex and velocity. The first method, used by Rashidi et al.

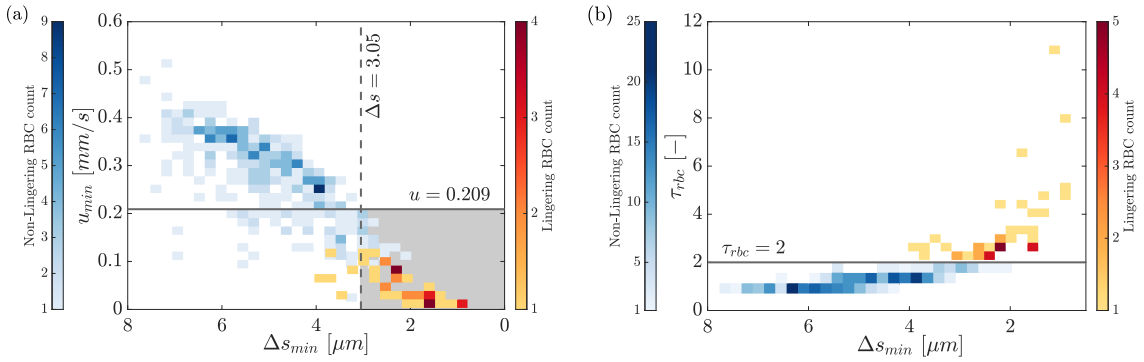

Figure 3.2: Classification of NLRBC and LRBC. **a)** Binscatter plot of the minimal velocity in the intersection $u_{\min}$ as function of the minimal distance to the apex Δs. The solid line refers to the local minimum in the PDF of all velocities in the intersection. The dashed line refers to the radius of a rabbit RBC. The grey shaded area represents the location where RBC would be considered lingering following the method of Rashidi et al. (2023). **b)** Binscatter plot of the reference time constant τ_{RBC} as function of the minimal distance to the apex $\Delta s_{\min}$. The solid line refers to $\tau_{\mathrm{RBC}} = 2.0$.[2]

(2023), defines a LRBC if the RBC is within a distance $\Delta s < r_{\mathrm{RBC}}$ from the apex and has a velocity lower than the local minimum detected in the probability density function (PDF) of a collective dataset of RBC velocities in the mother vessel and bifurcation area. The second method, used by Pskowski et al. (2021), calculates the relative residence time of each RBC, which is the normalized time spent by an RBC at the intersection, and defines LRBC as the RBCs with higher relative residence time.

We took inspiration from Pskowski et al. (2021) and used the relative residence time τ_{RBC} to classify LRBCs and NLRBCs. In our experiments, we observed that τ_{RBC} varied from 0.7 to 11.0 and increased strongly when $\Delta s_{\min}$ decreased (Fig. 3.2b), which is an illustration of the temporal heterogeneity of RBC flow at the microscale and of the variability of RBC behavior at bifurcations.

To find an appropriate threshold for the relative residence time beyond which an RBC is considered to be lingering, we compared the lingering frequency (number of LRBCs divided by the total number of RBCs) to *in vivo* observations by Kihm et al. (2021), who reported lingering frequencies between 0.1 and 0.2 for a capillary bifurcation with a blood flow fraction of $0.45 < \Phi_{1,2} < 0.55$. For a threshold of $\tau_{\mathrm{RBC}} = 2.0$, we obtained a lingering frequency of 0.11 while the blood flow fraction was $\Phi_{1,2} \approx 0.5$. This is also consistent with the results of the only other *in vitro* study on RBC lingering that reported a lingering frequency of $0.1 - 0.15$ for $\Phi_{1,2} = 0.5$ and a reservoir hematocrit of $H_{\mathrm{r}} < 20\%$ (Pskowski et al., 2021). Therefore, we fixed the threshold to $\tau_{\mathrm{RBC}} = 2.0$ which resulted in 43 LRBCs and 335 NLRBCs in our experiments.

A sensitivity analysis was performed to evaluate the impact of the threshold for τ_{RBC} on the major findings of the study. Lingering frequencies of 0.18 and 0.09 were obtained for thresholds of $\tau_{\mathrm{RBC,t}} = 1.7$ and 2.3, respectively. Despite this change in the lingering frequency, the major results and conclusions of the study were not affected qualitatively by the choice of the threshold (within the tested range). The sensitivity analysis is reported in

[2]Figure 2 in Bucciarelli et al. (2024). CC BY 4.0.

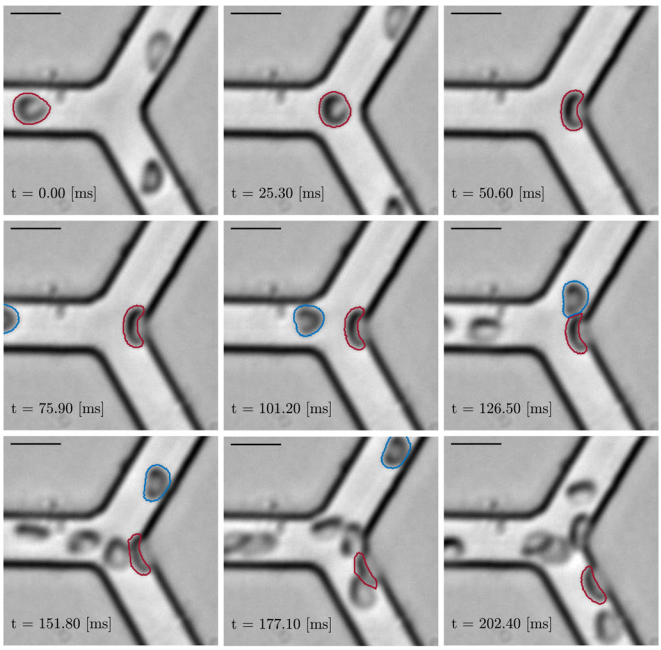

Figure 3.3: typical lingering event. Temporal evolution of a NLRBC (blue) and a LRBC (red) approaching a divergent bifurcation. Scale bar 10 μm.[3]

Appendix C.2. In the following, results are presented only for the threshold $\tau_{\mathrm{RBC,t}} = 2.0$.

Finally, we calculated the lingering frequency using the method proposed by Rashidi et al. (2023). For our experimental setup, the thresholds were $\Delta s < r_{\mathrm{RBC}} = 3.05\ \mu$m (Lewis, 1996b) for the distance to the apex and $u < 0.209$ mm/s, which is the local minimum in the PDF of all RBC velocities in the intersection. These two thresholds are depicted in Fig. 3.2a. With this method, the lingering frequency would increase slightly to 0.14.

3.4.2 Qualitative Lingering Analysis

A typical lingering event is shown in Fig. 3.3, in which the temporal behavior and deformation dynamics are displayed for a LRBC and an NLRBC (see also the supplementary videos for dynamic illustrations of lingering events). The LRBC flows along the symmetry axis of the parent vessel while maintaining the canonical discocyte shape. At the intersection, the LRBC does not immediately enter a daughter vessel but folds around the apex of the bifurcation, partially obstructing the passage to the daughter vessels. During this process, the LRBC is subjected to a large deformation, resulting in a C-like shape. This LRBC lingers at the apex for approximately 142 ms (range for all LRBCs: $45 - 238$ ms) before moving into the daughter vessel, where it leans on the distal wall of the microchannel while maintaining the deformed and elongated shape. The NLRBC also has a discoidal shape when it approaches the bifurcation, but is laterally shifted to the top half of the parent vessel. The NLRBC is slightly elongated when it approaches the intersection and it takes only 18 ms to cross the intersection I (i.e., 5 times less than the LRBC). The NLRBC has a brief cell-to-cell interaction with the lingering

[3]Figure 3 in Bucciarelli et al. (2024). CC BY 4.0.

LRBCs, but it manages to enter the daughter vessel without significant deformation. This qualitative analysis of a typical lingering event shows that position, velocity, circularity, and orientation are properties that could differ between LRBCs and NLRCs and should be investigated in more detail.

3.4.3 RBC Characteristics

In the parent vessel, LRBCs were statistically significantly faster than NLRBCs (quantitative data reported in Appendix C.3.1) due to their concentration along the centerline. In contrast, LRBCs were significantly slower in the daughter vessels as a consequence of lingering itself. The corrected average blood flow rates (equation 3.9) were $\widehat{Q}_{\text{blood},0} = 4.76 \cdot 10^{-5} \pm 2.8 \cdot 10^{-6}\,\text{mm}^3/\text{s}$, $\widehat{Q}_{\text{blood},1} = 2.35 \cdot 10^{-5} \pm 2.9 \cdot 10^{-6}\,\text{mm}^3/\text{s}$ and $\widehat{Q}_{\text{blood},2} = 2.41 \cdot 10^{-5} \pm 2.2 \cdot 10^{-6}\,\text{mm}^3/\text{s}$, resulting in average fractional blood flow rates $\Phi_1 = 0.494 \pm 0.046$ and $\Phi_2 = 0.506 \pm 0.046$. If only the mean velocity of NLRBCs is considered, the (uncorrected) blood flow rates increase to $Q_{\text{blood,NLRBC},0} = 5.16 \cdot 10^{-5}\text{mm}^3/\text{s}$ and $Q_{\text{blood,NLRBC},1+2} = 4.91 \cdot 10^{-5}\text{mm}^3/\text{s}$. This reduces the difference between the flow rate of the parent vessel and the sum of the flow rates of the daughter vessels by 52.1% compared to the (uncorrected) blood flow rate computed considering both the LRBC and NLRBC mean velocity. This highlights that there may be a significant error in blood flow rates determined from RBC velocities if there is a high percentage of LRBCs in the vessel of interest. In the present study, however, this error does not affect the results on lingering RBCs. The time-averaged fractional RBC flux in the two daughter vessels was $\Psi_1 = \Psi_2 = 0.50$.

The corrected time-averaged fractional blood flow rates and the RBC fluxes indicate that the blood flow partitioned symmetrically in the daughter vessels, which was expected due to the symmetric geometry of the channel network. Therefore, the following results will be reported collectively without discriminating between top and bottom daughter vessel.

Further quantitative data on a series of RBC properties such as velocity, circularity, and cell orientation are reported in detail in Appendix C.3. Briefly, no difference in shape was found in the parent vessel between LRBCs and NLRBCs, which agrees well with the capillary number for the RBC flow in the parent vessel:

$$Ca = \frac{\mu \cdot \overline{u}_{\text{RBC},0}}{G_{\text{s}}} = \frac{1.96 \cdot 10^{-3}\,\text{Pa s} \times 0.67 \cdot 10^{-3}\,\text{m/s}}{2.5 \cdot 10^{-6}\,\text{N/m}} \approx 0.55 \tag{3.10}$$

where G_{s} is the surface elastic shear modulus measured in optical tweezer experiments (Hénon et al., 1999).

Instead, a significant shape difference was observed in the daughter vessels, where LRBCs are more elongated than NLRBCs. The LRBCs relax to a rounder shape toward the end of the daughter vessel, but remain still more stretched than the NLRBCs, which agrees with the previous observation that LRBCs remain close to the distal wall also at the outlet of the daughter vessels.

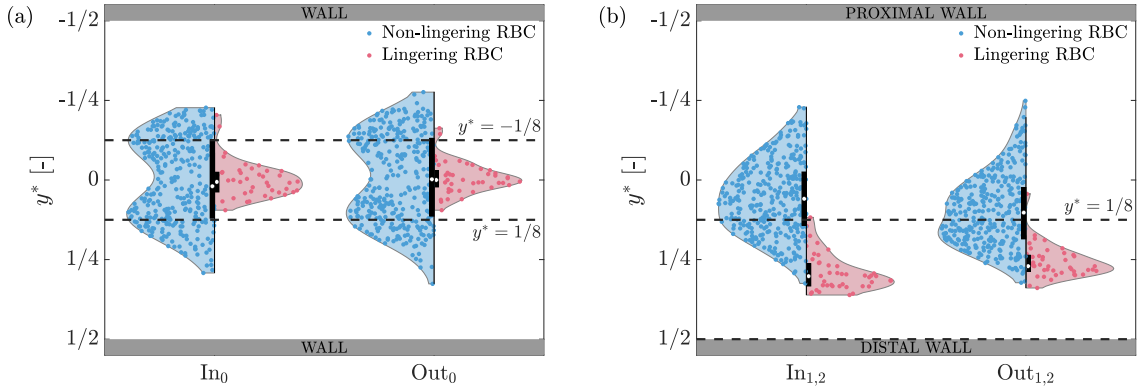

Figure 3.4: Distribution of the lateral RBC position. **a)** Distribution of the lateral RBC position at the inlet (In_0) and outlet (Out_0) of the parent vessel. **b)** Distribution of the lateral RBC position at the inlet ($In_{1,2}$) and outlet ($Out_{1,2}$) of the daughter vessel. Dashed lines indicate $y^* = \pm 1/8$.[4]

3.4.4 Lateral RBC Distribution

If we do not discriminate between NLRBCs and LRBCs, we recover the symmetric lateral RBC distribution in the parent vessel observed by Mantegazza et al. (2020b), where RBCs were distributed symmetrically about the center line of the parent vessel leaving a cell-depleted layer near the wall (Fig. 3.4a, $Sk_{\mathrm{In},0} = 0.009$ and $Sk_{\mathrm{Out},0} = 0.01$). If we observe only NLRBCs at the inlet of the parent vessel, the lateral distribution is bimodal with cell depletion at the center of the channel such that only 52.2% of NLRBCs were found in the interval $-1/8 < y^* < 1/8$. In contrast, LRBCs are distributed in an unimodal fashion and the majority of LRBCs (95.4%) are located close to the centerline of the microchannel ($-1/8 < y^* < 1/8$). At the outlet of the parent vessel, the lateral distribution of RBCs was consistent with the distribution at the inlet: 51.9% NLRBCs and 95.4% LRBCs were located at $-1/8 < y^* < 1/8$. A two-sample K-S test indicated that the lateral distributions of NLRBC and LRBC in the patent vessel come from statistically different continuous distributions ($p = 2.5 \cdot 10^{-5}$ at In_0, $p = 6.8 \cdot 10^{-5}$ at Out_0). These results indicate that RBCs experience lingering almost exclusively if they are flowing close to the centerline of the microchannel.

In contrast, the lateral distributions of RBCs in the daughter vessels is not symmetric with respect to the centerline (Fig. 3.4b), but skewed towards the distal wall ($Sk_{\mathrm{In},1,2} = 0.21$, $Sk_{\mathrm{Out},1,2} = 0.32$). The distributions for the lateral position of LRBCs and NLRBCs are both unimodal. At the entrance of the daughter vessel, the peak of the NLRBC distribution is slightly shifted to the distal wall (only 30.5% of NLRBCs are located at $1/8 < y^* < 1/2$ and $Sk_{\mathrm{NLRBC,In},1,2} = 0.17$). In sharp contrast, 97.7% of LRBCs were found near the distal wall ($Sk_{\mathrm{LRBC,In},1,2} = 0.50$). At the outlet of the daughter vessels, the distributions presented a similar trend: 97.7% of LRBCs and 46.0% of NLRBCs were found at $1/8 < y^* < 1/2$ ($Sk_{\mathrm{LRBC,Out},1,2} = 0.50$ and $Sk_{\mathrm{NLRBC,Out},1,2} = 0.30$). The K-S test confirmed that the NLRBC and LRBC lateral distributions are significantly different ($p = 3.5 \cdot 10^{-24}$ at $In_{1,2}$, $p = 1.1 \cdot 10^{-19}$ at $Out_{1,2}$).

[4]Figure 4 in Bucciarelli et al. (2024). CC BY 4.0.

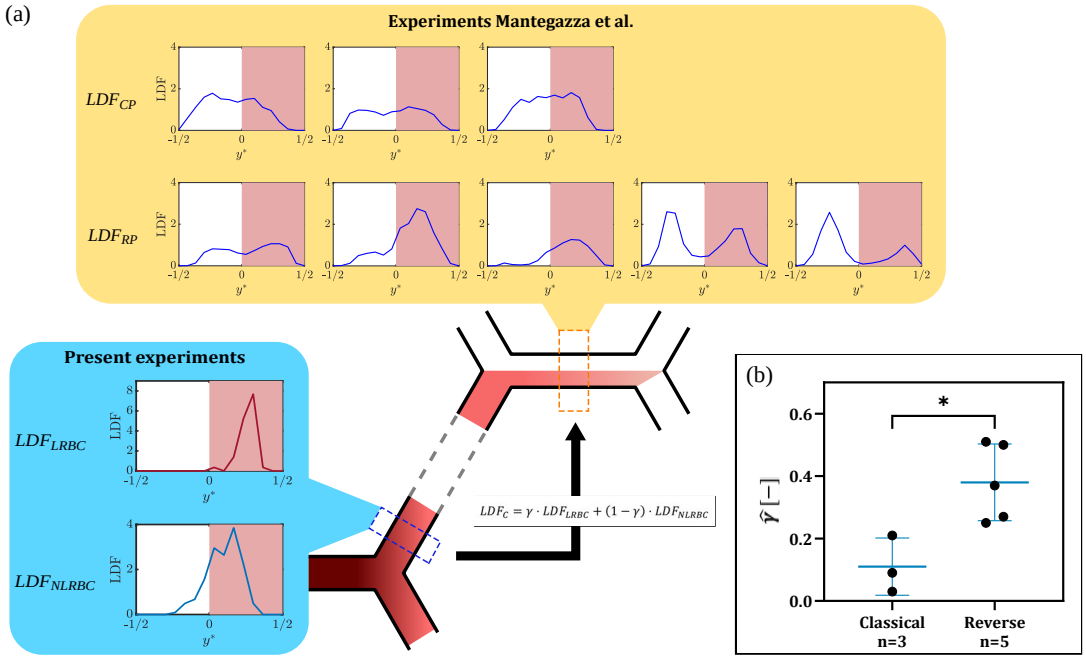

Figure 3.5: Comparison of lateral RBC distributions and optimal lingering frequencies. **a)** Comparison of lateral RBC distributions from Mantegazza et al. (2020b) ($LDF_{\mathrm{RP,CP}}$) measured in the parent vessel of four consecutive diverging bifurcations (*orange dashed box*) with the composite lateral distribution LDF_{C} built from the distributions for lingering and NLRBCs ($LDF_{\mathrm{LRBC,NLRBC}}$) measured in the daughter vessel after a diverging bifurcation (*blue dashed box*). **b)** Optimal lingering frequencies classified for classical and reverse partitioning ($^*p < 0.05$, thin lines indicate the 25th and 75th percentiles and thick lines indicate the median values).[5]

3.4.5 Correlation Between RBC Lingering and Downstream Reverse Partitioning

In Mantegazza et al. (2020b), eight lateral RBC distribution $LDF(y^*)$ were presented. Five of these distributions were connected to reverse partitioning at the following bifurcation and the other three to classical partitioning, they are re-plotted on Fig. 3.5a and are labeled with LDF_{CP} (classical partitioning) and LDF_{RP} (reverse partitioning). It was shown in that study that the skewness of the lateral distributions in the parent vessel was statistically significantly higher for reverse partitioning (mean skewness $\bar{Sk} = 0.21 \pm 0.1$) than for classical partitioning ($\bar{Sk} = 0.11 \pm 0.1$).

In the present study, we observed that the presence of LRBCs in the daughter vessel after lingering can lead to strongly skewed lateral distributions in the daughter vessels, whereas NLRBCs cause much less skewing. To understand whether this effect could explain the skewed distributions observed in Mantegazza et al. (2020b), the composite lateral distribution function $LDF_{\mathrm{C}}(y^*, \gamma)$, equation 3.4, was build from a linear combination of the lateral distributions LDF_{LRBC} and LDF_{NLRBC} (Fig. 3.5a) measured at the end of the daughter vessels for lingering and non-lingering RBCs, respectively. The weighting factor

[5]Figure 5 in Bucciarelli et al. (2024). CC BY 4.0.

Table 3.1: Percentage of RBCs crossing the SA of the parent vessel for different groups of RBCs.[6]

All RBC	4.8%
LRBC	32.6%
NLRBC	1.2%
NLRBC without lingering event	1.2%
NLRBC during lingering event	1.2%

γ can be interpreted as the lingering frequency.

Fig. 3.5b shows the optimal lingering frequencies $\widehat{\gamma}$ which yielded the best fit for the composite distribution LDF_{C} to the respective lateral distributions from Mantegazza et al. (2020b). Note that this fitting was only done in the interval $y^* = [0, 0.5]$ (see shaded areas in Fig. 3.5a), because the data in the interval $y^* = [-0.5, 0]$ of LDF_{RP} and LDF_{CP} were dominated by inflow from another vessel. The optimal lingering frequencies $\widehat{\gamma}$ vary between 0.03 and 0.51, and it appears evident that classical partitioning can be achieved only if a sufficiently small number of LRBCs flow in the daughter vessel. In contrast, a high percentage of LRBCs flowing in the daughter vessel is needed to sufficiently skew the hematocrit profile and, thus, to enable reverse partitioning in the following bifurcation. A Mann-Whitney-U test indicated that $\widehat{\gamma}$ for classical and reverse partitioning are statistically different ($p = 3.6 \cdot 10^{-2}$).

3.4.6 RBC Migration Across the Separation Surface

To assess if LRBCs also influence the hematocrit partitioning at the local bifurcation, it was tested if RBCs departed from their original streamlines and crossed the separation surface before the intersection, i.e., if they crossed the symmetry axis (SA) of the parent vessel. We found that only 4.8% of all RBCs crossed the SA (Table 3.1). For NLRBCs, this percentage (1.2%) did not differ considerably. If only LRBCs were considered, the frequency of SA crossing increased to 32.6%. This may be explained by the fact that LRBCs were more likely to flow in the center of the microchannel such that even a small interaction with a neighboring RBC can push or pull them across the SA.

To further investigate if lingering events influence the RBC distribution in the daughter vessels, the group of NLRBCs was divided into two subgroups: NLRBCs that entered the intersection while there is no lingering event, and NLRBCs that entered the intersection during a lingering event. We found 1.2% SA crossing for NLRBCs without lingering event, and also 1.2% SA crossing for NLRBCs during lingering events. This indicates that lingering events had no effect on NLRBC partitioning at the local bifurcation.

3.5 Discussion

In the present study, we studied RBCs flowing through an *in vitro* model of a microvascular bifurcation to understand if lingering RBCs flowing in the daughter vessel

[6] Table 1 in Bucciarelli et al. (2024). CC BY 4.0.

after lingering may be accountable for skewing the hematocrit profiles after the local bifurcation which may lead to reverse partitioning in the following bifurcation. Despite the measured low tube hematocrit ($\overline{H}_{t,0} \approx 5.2\%$) the findings are physiologically relevant. The tube hematocrit falls within physiologically observed ranges (Lipowsky et al., 1980; Desjardins and Duling, 1987; Pries et al., 1986; Sarelius and Duling, 1982). Moreover, the simulation results by Balogh and Bagchi (2018) were confirmed by our previous *in vitro* experiments (Mantegazza et al., 2020b,a), which used similar tube hematocrit as in this study, thereby reinforcing the validity and physiological relevance of our findings.

3.5.1 Classification of Non-lingering and Lingering RBC

Four criteria for the identification of LRBCs were analyzed: minimal velocity ($u_{\min}$), minimal distance to the apex ($\Delta s_{\min}$), a combination of a threshold for velocity ($u_{\min}$) and distance to the apex (Δs) and relative residence time at the intersection (τ_{RBC}). Using only the minimal distance to the apex or minimal velocity does not effectively classify RBCs (Fig. 3.2a). Combining these two factors improves the classification accuracy, but still lacks the definition of a reference timescale for the RBC lingering. Fig. 3.2a (grey area) shows that using these thresholds alone increases the number of LRBCs but misses RBCs that linger on top of other LRBCs slightly farther from the apex. These lingering RBCs spend a long time in the intersection and, therefore, affect incoming RBCs.

The criterion based on the relative residence time at the intersection yielded the best classification of RBCs. This criterion combines minimal velocity (LRBCs are RBCs stuck at the bifurcation with very low velocity, leading to a longer residence time in the intersection) and distance to the apex (LRBCs have a small minimal distance from the apex, requiring them to travel a longer path through the intersection, which also results in a longer residence time). Additionally, it considers the total amount of time spent in the intersection. A LRBC is not just a slow RBC near the apex; it is a RBC that remains stuck in the intersection for an extended period of time. The relative residence time criterion addresses the definition of a reference timescale for the lingering, which is overlooked by only considering a combination of thresholds for velocity and distance to the apex.

The threshold for lingering was set to $\tau_{\mathrm{RBC}} = 2.0$ which resulted in a lingering frequency of 0.11. This is consistent with *in vivo* experimental data by Kihm et al. (2021), who reported a lingering frequency of $0.1 - 0.2$. In the only other *in vitro* study on RBC lingering, Pskowski et al. (2021) measured a lingering frequency of $0.10 - 0.15$ for 2% and 20% feeding hematocrit, which agrees well with our experimental findings. This study also used a relative residence time criterion to identify LRBCs ($\tau_{\mathrm{RBC}} > 1.25$). However, they did not indicate if the residence time was measured only in the bifurcation region or if it was the whole time from the inlet to the outlet of the microfluidic device. We opted to measure the residence time only at the bifurcation because it is the region where lingering happens. We suspect that the different thresholds for τ_{RBC} between the present study and Pskowski et al. (2021) is simply a consequence of different regions of interest chosen for the data analysis.

3.5.2 Lingering Probability

The lingering probability is strongly related to the lateral position of RBCs in the parent vessel. LRBCs were concentrated around the centerline of the parent vessel, whereas only few NLRBCs were found in that region. The RBCs close to the centerline ($-1/8 < y^* < 1/8$) had a lingering probability of 19.0%, whereas this probability dropped to 1.8% for more marginated RBCs. Additionally, the majority of all lingering events (76.9%) occur during phases where the tube hematocrit is higher than the mean tube hematocrit. These results indicate that the low capillary number in the present experiments ($Ca \approx 0.55$) does not prevent lingering at the bifurcation because the development of lingering mainly depends on cell-cell and cell-wall interactions. For RBCs flowing along the centerline of the parent vessel, the elastic forces developed by the RBC membrane dominate on the viscous forces from the fluid due to the low capillary number. Nevertheless, they are in any case more likely to be lingering RBCs due to the prolonged stagnation that they experience at bifurcations when they interact with the apex. As a result, they need more time than the RBCs flowing close to the parent vessel walls to recover their shape and enter one of the daughter branches.

3.5.3 Effect of Lingering on Hematocrit Partitioning

At the local bifurcation, no effect of RBC lingering on hematocrit partitioning was observed. This is in contrast to the findings of Balogh and Bagchi (2018) who showed that cell-to-cell and cell-wall interactions at the bifurcation influences the RBC distribution. Barber et al. (2011) showed that various types of cell-to-cell interaction exist at a diverging bifurcation, namely trade-off, herding, and following interactions. The trade-off interaction, where the trailing RBC enters the opposite branch to the leading RBC, occurs most frequently for an equal flow rate split between the daughter branches which is the case for the present experiments. Similarly to what we observed, the trade-off interaction results in a more uniform hematocrit partitioning (Barber et al., 2011). Instead, Rashidi et al. (2023) found that lingering may either enhance the Zweifach-Fung effect or induce reverse partitioning. We attribute these conflicting results to the low confinement in our experiments, whereas the simulations reported in Balogh and Bagchi (2018) were performed for highly confined configurations such that LRBCs had a higher impact on the following incoming RBCs.

The present results show, however, that lingering RBCs flowing in the daughter vessel after lingering may influence the RBC distribution at the following bifurcation. We have been able to show that a higher percentage of LRBCs flowing in the daughter vessel after a bifurcation is correlated to reverse partitioning in the following bifurcation, whereas classical partitioning seems to be favored if a smaller percentage of LRBCs are present in the daughter vessel (Fig. 3.5b). This result adds to previous findings (Clavica et al., 2016; Balogh and Bagchi, 2018; Mantegazza et al., 2020b) which connected reverse partitioning to low hematocrit, increased inlet velocity, and a skewed lateral distribution. Furthermore, this result is closely related to the 'history effect' described by Merlo (2018), which refers to the phenomenon that the history of an RBC, i.e., the RBC dynamics in previous bifurcations, affects the RBC behavior at the local bifurcation.

The connection between lingering at a previous bifurcation and the hematocrit distri-

bution at the following bifurcation highlights that RBC transport in the microcirculation is governed by the interplay of all bifurcations in the whole capillary network, rather than just by the RBC behavior at independent bifurcations.

3.5.4 Experiments at Higher Hematocrit

Next to the experiment with a tube hematocrit of $\overline{H}_{t,0} \approx 5.2\%$ ($H_r = 10\%$), two additional experiments were performed with $H_r = 20\%$ and $H_r = 30\%$ to investigate the influence of local hematocrit on RBC lingering. The results of these experiments, which are reported in Appendix C.4, were in qualitative agreement with the findings for $\overline{H}_{t,0} \approx 5.2\%$ ($H_r = 10\%$). The measured tube hematocrit was $\overline{H}_t = 6.3\%$ and $\overline{H}_t = 8.8\%$ for a reservoir hematocrit of $H_r = 20\%$ and $H_r = 30\%$, respectively. Therefore, the tube hematocrit was in the same range for all three experiments despite the larger difference in the feeding hematocrit. We suspect that this is the reason why we did not observe any major difference in the results as a function of the feeding hematocrit. We conclude that small differences in tube hematocrit do not have a noticeable effect on lingering. This is in line with Pskowski et al. (2021), who did not find any change in lingering frequency for reservoir hematocrits of 2% and 20%.

3.6 Conclusion

Flowing lingering RBC in the daughter vessel increases the skewness of the lateral RBC distribution of the vessel. Because a skewed distribution before a bifurcation may promote reverse hematocrit partitioning, our study suggests that flowing lingering RBCs in the daughter vessel after lingering can be connected to reverse hematocrit partitioning in the following bifurcation. A quantitative analysis suggests that reverse partitioning in the following bifurcation occurs if a critical lingering frequency is surpassed in the previous bifurcation. At the same time, we found that lingering had no noticeable influence on the hematocrit partitioning in the local bifurcation, which is probably related to the low-confinement ratio in the present experiment, which prevents LRBCs from temporarily occluding the daughter branches.

Chapter 4

Influence of Pericyte Activation on RBC Flux and Partitioning

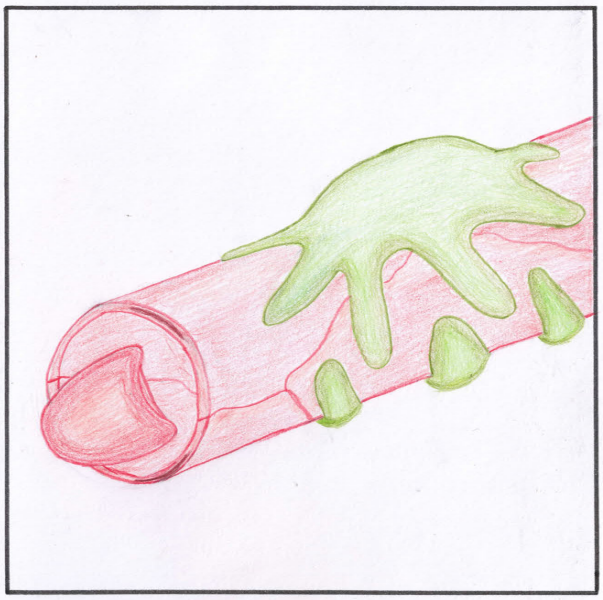

4.1 Introduction

The support of physiological functions in living tissues depends on a constant supply of oxygen and nutrients, as well as the efficient removal of carbon dioxide and metabolic waste. These processes occur within the microcirculation, a highly interconnected network of small capillaries, ranging from 5 to 10 μm in diameter (Pappano and Wier, 2013a). This network is structured in a mesh-like configuration (Wacker et al., 2012), enabling efficient local transport of oxygen by red blood cells (RBCs). Unlike larger vessels, RBCs distribution within the microvasculature is heterogeneous, both spatially and temporally, and is closely influenced by their behavior at microvascular bifurcations (Schulte et al., 2003; Kleinfeld et al., 1998; Mantegazza et al., 2020a,b; Balogh and Bagchi, 2017a).

In the brain, cerebral blood flow (CBF) adjusts to meet metabolic demands during periods of heightened neuronal activity, a process known as neurovascular coupling or functional activation (hyperemia) (Nippert et al., 2018). This essential mechanism ensures that regions of increased neural activity receive adequate oxygen and nutrients, maintaining the functional integrity of the neural network (Iadecola, 2017). Hyperemia is driven by complex interactions between neurons, astrocytes, pericytes (primitive mesenchymal cells), and VSMCs, which coordinate the dilation of arterioles and capillaries, thereby increasing blood flow to specific brain regions (Mishra et al., 2014; Hamilton, 2010; Attwell et al., 2016; Tilton, 1991).

Under healthy conditions, this system functions efficiently, but under pathological conditions like Alzheimer's disease and ischemic stroke, it can be severely compromised. In such cases, impaired blood supply to active brain regions induces neurological damage (Kisler et al., 2017a,b; Berthiaume et al., 2022). VSMCs, which control arteriole diameter, play a key role in modulating blood pressure and flow distribution within downstream capillaries, which is crucial for proper tissue perfusion (Hall et al., 2014; Hill et al., 2015; Mishra et al., 2016). Recent research has expanded the focus beyond arterioles, suggesting that capillaries may also participate in blood flow regulation. Pericytes, contractile cells surrounding capillaries, have been shown to modulate capillary diameter in response to neural activity, enabling more localized blood flow control (Peppiatt et al., 2006; Hall et al., 2014; Hartmann et al., 2021). Hall et al. (2014) found that capillary dilation occurs more rapidly in response to neural activity than arteriole dilation, suggesting that pericytes offer a faster, more precise mechanism for regulating local blood flow. However, studies like Hill et al. (2015) argue that VSMCs primarily regulate CBF, with pericytes playing a secondary role. Consequently, the respective contributions of arterioles and capillaries to neurovascular coupling remain an area of active research.

To better understand blood flow regulation during functional activation, it is essential to study the fluid dynamics of capillary networks, focusing on the distribution of RBCs and their behavior at microvascular bifurcations. Microvascular bifurcations play a crucial role in determining local blood flow and the downstream distribution of RBCs (Bucciarelli et al., 2024). At these bifurcations, RBCs exhibit non-uniform and time-dependent partitioning, preferentially entering daughter vessels with higher flow rates (Balogh and Bagchi, 2018; Clavica et al., 2016; Mantegazza et al., 2020a,b; Shen et al., 2016; Hyakutake et al., 2022), a phenomenon known as the Zweifach-Fung effect or classical partitioning (Pries et al., 1990; Fung, 1973). This effect leads to higher-than-expected hematocrit levels in these branches. However, deviations from this classical behavior have been observed,

particularly in more complex or larger capillary networks, where global RBC dynamics become more intricate (Balogh and Bagchi, 2017b,a; Mantegazza et al., 2020b,a). In certain conditions, reduced or even reverse partitioning has been reported (Shen et al., 2016; Hyakutake et al., 2022; Clavica et al., 2016), highlighting the complexity of RBCs behavior under varying flow regimes.

While *in vivo* and computational models are commonly employed to study neurovascular coupling, *in vitro* systems offer unique advantages by allowing controlled experimental conditions. Artificial microvascular networks have been utilized to investigate blood flow dynamics (Zhou et al., 2021; Hyakutake et al., 2022; Mantegazza et al., 2020b; Kodama et al., 2019; Merlo et al., 2022), but studies focusing on blood flow regulation during hyperemia remain limited. For instance, Mantegazza et al. (2020a) explored the influence of an active pericyte (relaxation) on RBC distribution, velocity, and partitioning in an idealized microvascular network. However, the study did not address the dynamic effects of pericyte activation and deactivation. Hall et al. (2014) demonstrated that pericytes require approximately 5 s to fully modulate vessel diameters in response to neural signals or the cessation thereof.

Building on the study by Mantegazza et al. (2020a), the present study utilizes the same microfluidic device featuring a honeycomb-like network of microchannels with a diameter of 9.6 μm, closely resembling *in vivo* capillary dimensions. This device includes a pneumatic valve system that modulates the cross-sectional area of one channel, effectively simulating pericyte-induced dilation. Additionally, we incorporated a pressure pump, enabling precise and dynamic control of the pressure within the pneumatic valve system, thereby allowing real-time modulation of the channel's cross-sectional area.

The primary objective of this research is to examine how the duration of pericyte activation affects both the spatial extent and magnitude of its impact on RBCs velocity and distribution within the capillary network. By comparing the immediate effects of activation with those resulting from prolonged activation (assumed to represent a steady state), this study aims to offer new insights into the role of pericytes in regulating blood flow during neurovascular coupling in capillary networks.

4.2 Theoretical Analysis of Porosity Variations in Homogeneous Media

To investigate the temporal effects of pericyte activation, we conceptualized the capillary network as a homogeneous porous medium where fluid flow is influenced by localized changes in porosity, which we could think of as pericyte activation. Given that the fluid in the network contains RBCs, which also impact porosity, we hypothesize that during dynamic pericyte activation, RBCs lack sufficient time to rearrange and establish a new "steady state". As a result, the system's response remains localized and exhibits a local dipole-like behavior. However, if the system reaches a steady state (long pericyte activation), the RBCs redistribute to minimize energy, thereby eliminating the dipole effect. In this framework, the medium's porosity reflects the network's overall resistance, which is governed solely by geometry when the fluid is a single phase, such as plasma, but, for blood, a multiphase fluid, resistance also depends on the spatial distribution of RBCs. To distinguish between resistance changes driven by geometric modifications and those

arising from RBC redistribution, we calculate the theoretical effects of a localized porosity change in a homogeneous porous medium. The following derivation examines the velocity and pressure fields for an idealized, homogenized medium with a single point of increased porosity.

We begin by using Darcy's law to describe the flow field $\mathbf{u}$ in a porous medium with permeability $\mathbf{K}$ and a pressure gradient ΔP:

$$\mathbf{u} = \mathbf{K}\nabla P \quad \Rightarrow \quad \nabla \cdot \mathbf{u} = \nabla \cdot (\mathbf{K}\nabla P) = 0\,. \tag{4.1}$$

For our system, we assume the pressure varies only in the x direction, with boundary conditions:

$$P(0, y) = P_{\text{in}}\,, \qquad P(L, y) = 0\,, \tag{4.2}$$

where L is the length of the porous medium. Additionally, the pressure gradient satisfies:

$$\frac{\partial P(x, 0)}{\partial y} = \frac{\partial P(x, L)}{\partial y} = 0\,. \tag{4.3}$$

Initially, the porosity $\mathbf{K}$ is constant throughout the medium, denoted as $\mathbf{k_0}$. To model the effect of pericyte activation, we treat this activation as a perturbation to the system. Specifically, the perturbation introduces a localized increase in permeability, $\mathbf{k_i}$, at $(x, y) = (a, b)$, only in the x direction. We represent the pressure and permeability as sums of their unperturbed (homogeneous) components (P_0 and $\mathbf{k_0}$) and perturbative components (P_1 and $\mathbf{k_i}$), scaled by a small perturbation parameter ϵ:

$$P = P_0 + \epsilon P_1\,, \qquad \mathbf{K} = \mathbf{k_0} + \epsilon \mathbf{k_i} = k_0 \begin{bmatrix} 1 & 0 \\ 0 & 1 \end{bmatrix} + \epsilon k_i(x, y) \begin{bmatrix} 1 & 0 \\ 0 & 0 \end{bmatrix}\,. \tag{4.4}$$

We define $k_i(x, y) = k_1 \delta(x - a)\delta(y - b)$, where δ is the Dirac delta function. This function ensures that the increase in permeability is localized at a single point. Substituting equation (4.4) into equation (4.1), we obtain:

$$\nabla \cdot ((\mathbf{k_0} + \epsilon \mathbf{k_i}) \cdot \nabla (P_0 + \epsilon P_1)) = 0\,. \tag{4.5}$$

This equation can be separated into components based on the order of ϵ:

$$\epsilon^0: \quad \nabla \cdot (\mathbf{k_0} \cdot \nabla P_0) = 0 \qquad \rightarrow \qquad \nabla^2 P_0 = 0\,, \tag{4.6}$$

$$\epsilon^1: \quad \nabla \cdot (\mathbf{k_0} \cdot \nabla P_1 + \mathbf{k_i} \cdot \nabla P_0) = 0 \qquad \rightarrow \qquad \nabla^2 P_1 = -\frac{1}{\mathbf{k_0}} \nabla \cdot (\mathbf{k_i} \cdot \nabla P_0)\,, \tag{4.7}$$

$$\epsilon^2: \quad \nabla \cdot (\mathbf{k_i} \cdot \nabla P_1) = 0\,. \tag{4.8}$$

To solve the system, we first address the zero-order equation (4.6), which determines P_0, the pressure field for the homogeneous porous medium where the permeability is constant. Once P_0 is obtained, it is used in the first-order equation (4.7) to calculate P_1, which represents the pressure perturbation caused by the localized change in permeability. This approach systematically separates the contributions of the base geometry and the localized porosity change, allowing us to analyze their individual effects on the flow field.

4.2.1 Solution for Zeroth-order Equation 4.6

Assuming a separable solution $P_0 = P_x(x)P_y(y)$, we substitute this into the zero-order equation 4.6:

$$\begin{aligned} \frac{\partial^2 P_0}{\partial x^2} + \frac{\partial^2 P_0}{\partial y^2} = 0 \quad &\rightarrow \quad P_y \frac{\partial^2 P_x}{\partial x^2} + P_x \frac{\partial^2 P_y}{\partial y^2} = 0 \\ &\rightarrow \quad \frac{1}{P_x}\frac{\partial^2 P_x}{\partial x^2} + \frac{1}{P_y}\frac{\partial^2 P_y}{\partial y^2} = 0\,. \end{aligned} \tag{4.9}$$

We can then separate the terms for the x- and y-components:

$$\frac{\partial^2 P_x}{\partial x^2} = \lambda P_x\,, \tag{4.10}$$

$$\frac{\partial^2 P_y}{\partial y^2} = -\lambda P_y\,. \tag{4.11}$$

where λ is the separation constant.

Solving for $P_y(y)$

The boundary conditions $\frac{\partial P(x,0)}{\partial y} = \frac{\partial P(x,L)}{\partial y} = 0$ imply that P_y must be constant. Substituting this into the equation $-\lambda P_y = 0$ gives $\lambda = 0$, as this is the only value for which the equation holds. We set $P_y = 1$.

Solving for $P_x(x)$

With $\lambda = 0$, the equation 4.10 becomes:

$$\frac{\partial^2 P_x}{\partial x^2} = 0\,. \tag{4.12}$$

The solution to this equation is:

$$P_x(x) = Ax + B\,, \tag{4.13}$$

where A and B are constants determined by the boundary conditions:

- At $x = 0$, $P(0, y) = P_{\text{in}}$, so $B = P_{\text{in}}$.
- At $x = L$, $P(L, y) = 0$, so $A = -P_{\text{in}}$.

Substituting A and B gives:

$$P_x(x) = P_{\text{in}}\left(1 - \frac{x}{L}\right)\,. \tag{4.14}$$

Since $P_0(x, y) = P_x(x)P_y(y)$ and $P_y = 1$, the final solution is:

$$P_0 = P_{\text{in}}\left(1 - \frac{x}{L}\right)\,. \tag{4.15}$$

4.2.2 Solution for First-order Equation 4.7

Inserting the definitions of P_0, $\mathbf{k_i}$ and $\mathbf{k_i}$ into equation 4.7, we obtain:

$$\nabla^2 P_1 = -\frac{1}{k_0} \cdot \left(\frac{\partial (k_1 \delta(x-a)\delta(y-b))}{\partial x} \cdot \frac{\partial P_0}{\partial x} \right) . \tag{4.16}$$

Substituting $P_0 = P_{\text{in}} \left(1 - \frac{x}{L}\right)$, the equation simplifies to:

$$\nabla^2 P_1 = \frac{P_{\text{in}} k_1 L^2}{L k_0} \cdot \delta'(x-a) \cdot \delta(y-b) = f(x,y) \, . \tag{4.17}$$

Here, L^2 is included to ensure the Dirac delta function operates in a dimensionless system. This equation can be solved using two approaches: Green's functions and the dipole/doublet method.

Solution Using Green's Function

The Green's function for the Poisson equation in an unbounded domain is:

$$G(x,y,\zeta,\eta) = \frac{1}{2\pi} \ln \sqrt{(x-\zeta)^2 + (y-\eta)^2} \, , \tag{4.18}$$

which satisfies:

$$\nabla^2 G(x,y,\zeta,\eta) = \delta(x-\zeta)\delta(y-\eta) \, . \tag{4.19}$$

The solution to $\nabla^2 P_1 = f(x,y)$ is given by:

$$P_1 = \iint G(x,y,\zeta,\eta) f(\zeta,\eta) d\zeta d\eta \, . \tag{4.20}$$

Substituting $f(x,y)$ from equation 4.17:

$$P_1 = \frac{P_{\text{in}} k_1}{L k_0 2\pi} \iint \ln \sqrt{(x-\zeta)^2 + (y-\eta)^2} \cdot \delta'(\zeta - a) \cdot \delta(\eta - b) d\zeta d\eta \, . \tag{4.21}$$

Using the properties of the Dirac delta function:

$$\int g(x)\delta(x-a)dx = g(a) \quad \text{and} \quad \int g(x) \frac{d\delta(x-a)}{dx} dx = -\left. \frac{dg(x)}{dx} \right|_{x=a} , \tag{4.22}$$

we evaluate the integral:

$$P_1 = -\left. \frac{P_{\text{in}} k_1 L^2}{L k_0 2\pi} \frac{\partial}{\partial \zeta} \ln \sqrt{(x-\zeta)^2 + (y-b)^2} \right|_{\zeta=a} . \tag{4.23}$$

Differentiating the logarithmic term, we have the solution for P_1:

$$P_1 = \frac{P_{\text{in}} k_1 L^2}{L k_0 2\pi} \frac{(x-a)}{(x-a)^2 + (y-b)^2} \, . \tag{4.24}$$

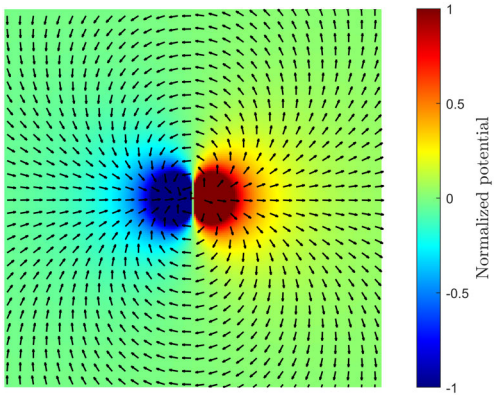

Figure 4.1: Dipole in potential flow. The normalized potential field and flow directions around a dipole are represented by a colormap and normalized velocity vectors.

Solution Using a Dipole/Doublet

We can interpret $\delta'(x-a)\cdot\delta(y-b)$ as a dipole (example in Fig. 4.1). The solution for the velocity potential with a source of strength m located at $(\gamma, 0)$ and a sink of strength $-m$ located at $(-\gamma, 0)$ is given by:

$$\phi = \frac{m}{2\pi}\ln\left((x-\gamma)^2+y^2\right) - \frac{m}{2\pi}\ln\left((x+\gamma)^2+y^2\right). \tag{4.25}$$

For a doublet, where $\gamma \to 0$ and $m \to \infty$, we define the dipole strength vector as $\mathbf{d} = 2m\gamma\mathbf{e}_x$. Expanding $\ln\left((x\pm\gamma)^2+y^2\right)$ for small γ, we use the following approximation:

$$\ln\left((x\pm\gamma)^2+y^2\right) \approx \ln(c) + \ln\sqrt{1\pm\frac{2\gamma x}{c^2}+\frac{\gamma^2}{c^2}}, \tag{4.26}$$

where $c^2 = x^2+y^2$. For small γ, this simplifies further:

$$\ln\left((x\pm\gamma)^2+y^2\right) \approx \ln(c) + \ln\left(1\pm\frac{\gamma x}{c^2}+\ldots\right) \approx \ln(c)\pm\frac{\gamma x}{c^2}, \tag{4.27}$$

Substituting this back into the expression for ϕ, we have:

$$\lim_{\gamma\to 0}\lim_{m\to\infty}\phi \approx \frac{m}{2\pi}\left(\ln c - \frac{\gamma x}{c^2}+\ldots - \ln c - \frac{\gamma x}{c^2}+\ldots\right) = -\frac{m\gamma}{\pi}\frac{x}{c^2}. \tag{4.28}$$

The velocity potential for a dipole is therefore:

$$\phi \approx -\frac{\mathbf{d}\cdot\mathbf{x}}{2\pi c^2}. \tag{4.29}$$

where $c^2 = x^2+y^2$ and $\mathbf{x}$ is the position vector. Since the dipole is positioned at (a,b) rather than the origin, we substitute $x = x-a$, $y = y-b$ and $c^2 = r^2(x,y) = (x-a)^2 + (y-b)^2$. The dipole strength in our case is:

$$\mathbf{d} = -\frac{P_{\text{in}}k_1L^2}{Lk_0}. \tag{4.30}$$

Substituting these values, the resulting pressure perturbation is:

$$P_1 = \frac{P_{\text{in}} k_1}{L k_0 2\pi} \frac{(x-a)}{r^2(x,y)} = \frac{P_{\text{in}} k_1 L^2}{L k_0 2\pi} \frac{(x-a)}{(x-a)^2 + (y-b)^2} \,. \tag{4.31}$$

This result matches the solution obtained using the Green's function method, confirming consistency between the two approaches.

4.2.3 Solution for the Velocity

Using the solutions for the zero-order equation 4.15 and the first-order equation 4.24, the pressure P is given by:

$$P = P_{\text{in}}(1 - \frac{x}{L}) - \frac{P_{\text{in}} k_1}{L 2\pi k_0} \frac{(x-a)}{(r^2(x,y)} \,. \tag{4.32}$$

where $r^2(x,y) = (x-a)^2 + (y-b)^2$. Using the permeability tensor:

$$\mathbf{K}(x,y) = \begin{bmatrix} k_0 + \epsilon k_1 \delta(x-a)\delta(y-b) & 0 \\ 0 & k_0 \end{bmatrix} \,, \tag{4.33}$$

with $k_2 = \epsilon k_1$, and substituting equation 4.32 into Darcy's law, we can extract the velocity components u_x and u_y:

x-Component of Velocity (u_x)

The x-component of the velocity is:

$$u_x = (k_0 + k_2 \delta(x-a)\delta(y-b)) \cdot \left(P_{\text{in}} \frac{\partial}{\partial x}(1 - \frac{x}{L}) + \frac{P_{\text{in}} k_2 L^2}{L 2\pi k_0} \frac{\partial}{\partial x} \frac{(x-a)}{r^2(x,y)} \right) \,. \tag{4.34}$$

Simplifying step-by-step:

$$\begin{aligned} u_x =& \frac{P_{\text{in}}}{L} \left[(k_0 + k_2 \delta(x-a)\delta(y-b)) \cdot \left(-1 + \frac{k_2 L^2}{2\pi k_0} \frac{r^2 \frac{\partial}{\partial x}(x-a) - (x-a)\frac{\partial r^2(x,y)}{\partial x}}{r^4} \right) \right] \\ =& \frac{P_{\text{in}}}{L} \left[(k_0 + k_2 \delta(x-a)\delta(y-b)) \cdot \left(-1 + \frac{k_2 L^2}{2\pi k_0} \frac{r^2 - (x-a)\cdot 2 \cdot (x-a)}{r^4} \right) \right] \\ =& \frac{P_{\text{in}}}{L} \left[(k_0 + k_2 \delta(x-a)\delta(y-b)) \cdot \left(-1 + \frac{k_2 L^2}{2\pi k_0} \frac{(y-b)^2 - (x-a)^2}{r^4} \right) \right] \,. \end{aligned} \tag{4.35}$$

y-Component of Velocity (u_y)

The y-component of the velocity is:

$$u_y = \left(k_0 P_{\text{in}} \cancel{\frac{\partial}{\partial y}(1 - \frac{x}{L})}^{0} - \frac{P_{\text{in}} k_2 k_0 L^2}{L 2\pi k_0} \frac{\partial}{\partial y} \frac{(x-a)}{r^2(x,y)} \right) \,. \tag{4.36}$$

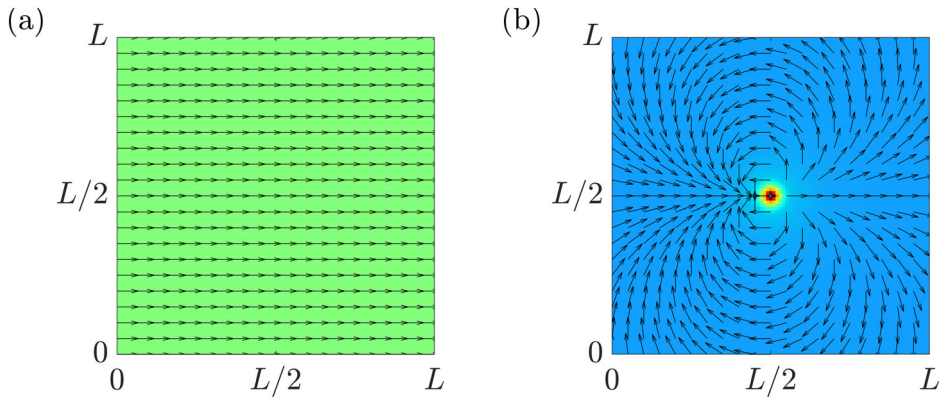

Figure 4.2: Velocity field and perturbation in porous media. **a)** Velocity field in a homogeneous porous medium. **b)** Velocity perturbation due to localized changes in permeability at $(L/2,\, L/2)$.

Simplifying:

$$\begin{aligned} u_y =& -\frac{P_{\text{in}} k_2 L^2}{L2\pi} \left(\frac{r^2 \frac{\partial}{\partial y}\cancelto{0}{(x-a)} - (x-a)\frac{\partial r^2(x,y)}{\partial y}}{r^4} \right) \\ =& -\frac{P_{\text{in}} k_2 L^2}{L2\pi} \frac{-(x-a)\cdot 2\cdot (y-b)}{r^4} = \\ =& \frac{P_{\text{in}} k_2 L^2}{L\pi} \frac{(x-a)(y-b)}{r^4} \,. \end{aligned} \tag{4.37}$$

Final Velocity Field

If the dipole is positioned at $(x, y) = (0, 0)$ and we neglect the Dirac delta function contributions, the velocity components simplify to:

$$u_x = -\frac{P_{\text{in}} k_0}{L} + \frac{P_{\text{in}} k_2 L^2}{2\pi L} \frac{y^2 - x^2}{(x^2+y^2)^2} \,, \tag{4.38}$$

$$v_y = \frac{P_{\text{in}} k_2 L^2}{2\pi L} \frac{2xy}{(x^2+y^2)^2} \,. \tag{4.39}$$

The result of the velocity field in a porous media can be seen in Fig. 4.2.

4.3 Material and Methods

4.3.1 Microfluidic Device, RBC Suspension

The microfluidic chips for this experiment were produced as described in Section 2.1 and we used the honeycombed network microfluidics chip design Fig. 2.4 (Section 2.2.2). For this experiment, we used fresh anonymized human blood and prepared following the protocol outlined in Section 2.3 and used a reservoir hematocrit suspension of $H_r = 10\%$.

4.3.2 Experiments Protocols, Experiments Set-up, Image Analysis and Data Analysis

We performed three different experiments: pericyte activation characterization, a long-time experiment, and a short-time experiment.

Pericyte Activation Characterization Experiment

We followed the experimental protocol outlined in Section 2.5.4 for the pericyte activation characterization experiment. A simple set-up was used, consisting of a microscope and two reservoirs filled with FITC-Dextran in PBS as the fluorescent dye. From the recorded z-stack, we selected a region of the channel unaffected by pericyte activation and determined a fluorescence intensity threshold. This threshold was selected to yield a cross-sectional area of approximately $76.8\,\mu\text{m}^2$, consistent with the dimensions of the channel used ($8\,\mu\text{m} \times 9.6\,\mu\text{m}$). We then applied this threshold to the channel influenced by pericyte activation and fitted polygons to the pixels exceeding the threshold at nine positions along the channel, ensuring the best possible fit.

Long-Time Experiment

For the long-time experiment, we followed the protocol outlined in Section 2.5.2, recording each section of the microfluidic chip for 10000 frames under two conditions: active and inactive pericyte. The experimental setup, described in Section 2.4 and illustrated in Figures 2.5 and 2.6, was used without the flashlight, as synchronization was unnecessary.

The preprocessing of each recorded video involved several steps detailed in Section 2.6.1: defining and retrieving information (Section 2.6.1 IPP-A), grayscale inversion (Section 2.6.1 IPP-C), background detection (Section 2.6.1 IPP-D), LIF and background removal (Section 2.6.1 IPP-E), rotation and binarization (Section 2.6.1 IPP-F), and noise filtering with RBC filling (Section 2.6.1 IPP-G). For *IPP-A*, the main region of interest was defined as a specific channel within each recorded section, as shown in Figure 4.3 (red numbered channels).

After preprocessing, PTV was performed following the procedure described in Section 2.6.2. RBC detection was performed using a combination of the *regionprops* function and a Gaussian kernel mask method (Section 2.6.2 PTV-A). The tracking of detected RBCs was conducted using the open-source software PTVlab (Brevis et al., 2011), with the tracking algorithm detailed in Section 2.6.2 PTV-B.

After calculating the mean velocity ($u_{\text{RBC},ij}$) and hematocrit ($H_{\text{t},ij}$) for each frame and channel using Equations 2.10 and 2.11 (not accounting for repetitions since none were performed in this experiment), we determined the mean velocity for each channel over the entire experiment for the two conditions using the following equations:

$$\overline{u}_{\text{RBC},i} = \frac{1}{10000} \sum_{j=1}^{10000} u_{\text{RBC},ij}\,, \qquad \overline{H}_{\text{t},i} = \frac{1}{10000} \sum_{j=1}^{10000} H_{\text{t},ij}\,, \tag{4.40}$$

where i represents the channel and j denotes the frame number. If the same channel was recorded in multiple sections, the final result was calculated by averaging the means across the sections.

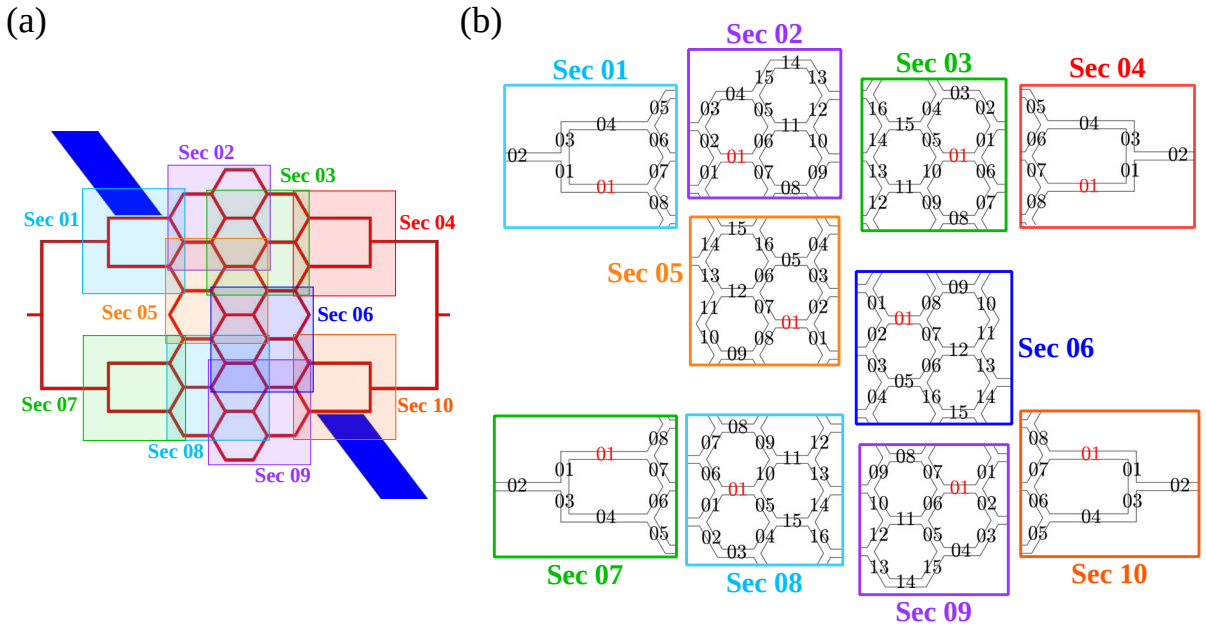

Figure 4.3: Ten sections of the microfluidic chip with the honeycomb network design. **a)** Positions of the ten sections within the microfluidic chip. **b)** Channel numbers in each section, with the main region highlighted in red (01) and the additional regions in black (01-16).

To calculate the RBC flux ($Q_{\mathrm{RBC},i}$) and blood flow rate ($Q_{\mathrm{blood},i}$), the following equations were used:

$$Q_{\mathrm{RBC},i} = \overline{u}_{\mathrm{RBC},i} \cdot \overline{H}_{\mathrm{t},i}(W \cdot H) = \overline{u}_{\mathrm{RBC},i} \cdot \frac{\overline{N}_{\mathrm{RBC},i} \cdot MCV_{\mathrm{RBC}}}{L_{\mathrm{ROI},i}}\,, \tag{4.41}$$

$$Q_{\mathrm{blood},i} = \overline{u}_{\mathrm{blood},i} \cdot (W \cdot H) = \chi \cdot \overline{u}_{\mathrm{RBC},i} \cdot (W \cdot H)\,, \tag{4.42}$$

where H is the channel height, W is the channel width, and $L_{\mathrm{ROI},i}$ is the region of interest length for the specific channel. MCV_{RBC} is the volume of a RBC, $MCV_{\mathrm{RBC}} = 87.4\,\mu\mathrm{m}^3$ (Amin and Sirs, 1985; Lewis, 1996a; Salvioli et al., 1993; Tomaiuolo et al., 2012). The coefficient χ accounts for the velocity difference between plasma and RBCs, and as discussed in Section 2.6.3, we assume $\chi \approx 1$. The term $\overline{N}_{\mathrm{RBC},i}$ is defined as:

$$\overline{N}_{\mathrm{RBC},i} = \frac{1}{10000} \sum_{j=1}^{10000} N_{\mathrm{RBC},ij}\,. \tag{4.43}$$

At the end, we calculated the relative difference between the inactive (inact) and active (act) conditions for velocity and hematocrit in each channel as follows:

$$\Delta u_{\mathrm{RBC},i,\mathrm{rel}} = \frac{\overline{u}_{\mathrm{RBC},i,\mathrm{act}} - \overline{u}_{\mathrm{RBC},i,\mathrm{inact}}}{\overline{u}_{\mathrm{RBC},i,\mathrm{inact}}}\,, \qquad \Delta H_{\mathrm{t},i,\mathrm{rel}} = \frac{\overline{H}_{\mathrm{t},i,\mathrm{act}} - \overline{H}_{\mathrm{t},i,\mathrm{inact}}}{\overline{H}_{\mathrm{t},i,\mathrm{inact}}}\,. \tag{4.44}$$

Short-Time Experiment

For the short-time experiment, we followed the protocol outlined in Section 2.5.3, where we recorded the microfluidic chip during the activation and deactivation of the pericyte. The chip was divided into ten sections, and we performed ten repetitions for each section of the activation and deactivation cycles, as described in Section 2.4.2 and illustrated in Fig. 2.7a.

The experimental setup, including all components, was as detailed in Section 2.4 and illustrated in Fig. 2.5 and 2.6.

The preprocessing procedure involved several steps detailed in Section 2.6.1: defining and retrieving information (Section 2.6.1 IPP-A), synchronization information and translation (Section 2.6.1 IPP-B), grayscale inversion (Section 2.6.1 IPP-C), background detection (Section 2.6.1 IPP-D), LIF and background removal (Section 2.6.1 IPP-E), rotation and binarization (Section 2.6.1 IPP-F), and noise filtering with RBC filling (Section 2.6.1 IPP-G). For *IPP-A*, the main region of interest was defined as a specific channel within each recorded section and repetition, as shown in Figure 4.3.

Following preprocessing, we performed PTV as described in Section 2.6.2. RBC detection was carried out using a combination of the *regionprops* function and the Gaussian kernel mask method (Section 2.6.2 PTV-A). Tracking of detected RBCs was conducted using the open-source software PTVlab (Brevis et al., 2011), with the tracking algorithm detailed in Section 2.6.2 PTV-B.

After calculating the mean velocity ($u_{\mathrm{RBC},ijk}$) and hematocrit ($H_{\mathrm{t},ijk}$) for each repetition, frame, and channel using Equations 2.10 and 2.11, we utilized the flash timing to synchronize all repetitions. We then computed the mean values for each channel and frame, enabling us to observe the system's dynamic response to pericyte activation ($u_{\mathrm{RBC},ij}$, $H_{\mathrm{t},ij}$, Fig. 4.6) as follows:

$$u_{\mathrm{RBC},ij} = \frac{1}{10}\sum_{k=1}^{10} u_{\mathrm{RBC},ijk}\,, \qquad H_{\mathrm{t},ij} = \frac{1}{10}\sum_{k=1}^{10} H_{\mathrm{t},ijk}\,. \tag{4.45}$$

From the synchronization between the pressure pump and the microscope, we identified the frames during which the pericyte was active (j_{act}) and inactive (j_{inact}). Using this information, we calculated the mean velocity and hematocrit as follows:

$$\overline{u}_{\mathrm{RBC},i,\mathrm{act}} = \frac{1}{n_{\mathrm{act}}}\sum_{j\in j_{\mathrm{act}}} u_{\mathrm{RBC},ij}\,, \qquad \overline{u}_{\mathrm{RBC},i,\mathrm{inact}} = \frac{1}{n_{\mathrm{inact}}}\sum_{j\in j_{\mathrm{inact}}} u_{\mathrm{RBC},ij}\,, \tag{4.46}$$

$$\overline{H}_{\mathrm{t},i,\mathrm{act}} = \frac{1}{n_{\mathrm{act}}}\sum_{j\in j_{\mathrm{act}}} H_{\mathrm{t},ij}\,, \qquad \overline{H}_{\mathrm{t},i,\mathrm{inact}} = \frac{1}{n_{\mathrm{inact}}}\sum_{j\in j_{\mathrm{inact}}} H_{\mathrm{t},ij}\,. \tag{4.47}$$

Here, n_{act} and n_{inact} denote the number of frames in the active and inactive conditions, respectively. If the same channel was recorded in multiple sections, the final result was calculated by averaging the means across the sections.

Using the calculated values, the RBC flux ($Q_{\mathrm{RBC},i}$) and blood flow rate ($Q_{\mathrm{blood},i}$) were

determined for both conditions using the following equations:

$$Q_{\mathrm{RBC},i,\mathrm{act}} = \overline{u}_{\mathrm{RBC},i,\mathrm{act}} \cdot \overline{H}_{\mathrm{t},i,\mathrm{act}} \cdot (W \cdot H)\,, \tag{4.48}$$

$$Q_{\mathrm{RBC},i,\mathrm{inact}} = \overline{u}_{\mathrm{RBC},i,\mathrm{inact}} \cdot \overline{H}_{\mathrm{t},i,\mathrm{inact}} \cdot (W \cdot H)\,, \tag{4.49}$$

$$Q_{\mathrm{blood},i,\mathrm{act}} = \chi \cdot \overline{u}_{\mathrm{RBC},i,\mathrm{act}} \cdot (W \cdot H)\,, \tag{4.50}$$

$$Q_{\mathrm{blood},i,\mathrm{act}} = \chi \cdot \overline{u}_{\mathrm{RBC},i,\mathrm{act}} \cdot (W \cdot H)\,. \tag{4.51}$$

Here, H is the channel height, W is the channel width, and χ is the coefficient accounting for the velocity difference between plasma and RBCs. As discussed in Section 2.6.3, $\chi \approx 1$ was assumed. The RBC flux and blood flow rate were corrected to satisfy mass conservation at the bifurcation using the procedure originally developed by Pries et al. (1989), as detailed in Section 2.6.3. This correction was then used to calculate the fractional blood flow rate (Φ) and fractional RBC flux (Ψ) for each diverging bifurcation in the honeycomb network, following equation 2.17.

Finally, the relative differences between the inactive and active conditions for velocity and hematocrit in each channel were calculated as follows:

$$\Delta u_{\mathrm{RBC},i,\mathrm{rel}} = \frac{\overline{u}_{\mathrm{RBC},i,\mathrm{act}} - \overline{u}_{\mathrm{RBC},i,\mathrm{inact}}}{\overline{u}_{\mathrm{RBC},i,\mathrm{inact}}}\,, \qquad \Delta H_{\mathrm{t},i,\mathrm{rel}} = \frac{\overline{H}_{\mathrm{t},i,\mathrm{act}} - \overline{H}_{\mathrm{t},i,\mathrm{inact}}}{\overline{H}_{\mathrm{t},i,\mathrm{inact}}}\,. \tag{4.52}$$

4.3.3 Calculation of the Homogenized Network

To isolate the effects of pericyte activation, we modeled the capillary network as a homogeneous porous medium through which fluid flows. Pericyte activation was interpreted as a localized change in porosity, introducing a dipole-like effect into the system (Section 4.2). Since the fluid contains RBCs, which influence porosity, we aimed to determine whether this dipole effect could still be observed under such conditions.

To do so, we homogenized the system by interpolating the velocity and hematocrit fields using a weighted Gaussian function (WG). The analysis was conducted on the honeycomb network, which was homogenized onto a 21×49 grid in the x and y directions. The weighted Gaussian function was defined as:

$$WG(x_a, y_a, i) = \frac{1}{\sqrt{2 \cdot \pi \cdot m}} \cdot e^{(-d^2/(2 \cdot m))}\,, \tag{4.53}$$

where $m = \sigma^2$ and σ is the channel length (85 μm). The variable d represents the distance between the center of the channel (x_i, y_i) and a point (x_a, y_a) in the homogenized network, calculated as:

$$d = \sqrt{(x_i - x_a)^2 + (y_i - y_a)^2}\,. \tag{4.54}$$

The weighted Gaussian function was normalized to $WG_{\mathrm{norm}}(x_a, y_a, i)$ as follows:

$$WG_{\mathrm{norm}}(x_a, y_a, i) = \frac{WG(x_a, y_a, i)}{\sum_{i=1}^{N_{\mathrm{channels}}} WG(x_a, y_a, i)}\,. \tag{4.55}$$

Using the normalized weighted Gaussian function, the hematocrit at each point (x_a, y_a) in the homogenized grid was computed as:

$$H_{\mathrm{H}}(x_a, y_a) = \sum_{i=1}^{N_{\mathrm{channels}}} WG_{\mathrm{norm}}(x_a, y_a, i) \cdot \overline{H}_{\mathrm{t},i}\,. \tag{4.56}$$

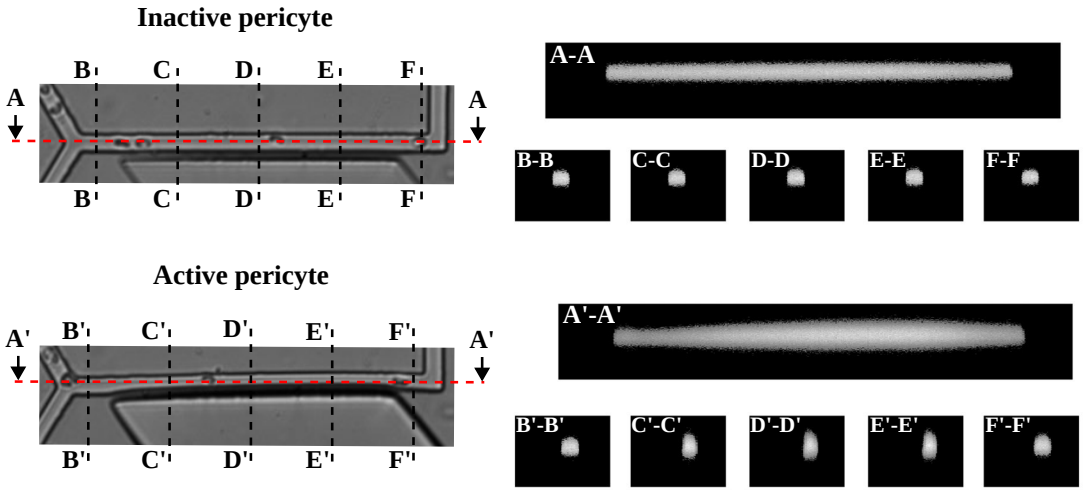

Figure 4.4: Cross-sectional slices of the microchannel in the x-z and y-z planes, illustrating the channel with the pericyte in both inactive and active states. Cross-sectional slices are shown for the x-z planes (A-A and A'-A') and the y-z planes (B-B, B'-B', ..., F-F, F'-F'). These slices were extracted from the z-stack of fluorescent dye within the channel, with a threshold applied to remove background noise. Images were captured using a 20x objective.

This calculation was performed for both the active and inactive conditions in the short-time and long-time experiments, resulting in $H_{\mathrm{H,act}}(x_a, y_a)$ and $H_{\mathrm{H,inact}}(x_a, y_a)$. For the velocity magnitude, the x and y components (depending on the orientation of the specific channel) were separated, and the homogenized velocity components in the x and y directions were computed, resulting in $u_{x,\mathrm{H}}(x_a, y_a)$ and $u_{y,\mathrm{H}}(x_a, y_a)$, respectively:

$$u_{x,\mathrm{H}}(x_a, y_a) = \sum_{i=1}^{N_{\mathrm{channels}}} WG_{\mathrm{norm}}(x_a, y_a, i) \cdot \overline{u}_{x,\mathrm{RBC},i}\,, \tag{4.57}$$

$$u_{y,\mathrm{H}}(x_a, y_a) = \sum_{i=1}^{N_{\mathrm{channels}}} WG_{\mathrm{norm}}(x_a, y_a, i) \cdot \overline{u}_{y,\mathrm{RBC},i}\,. \tag{4.58}$$

These calculations were also performed for both the active and inactive conditions in the short-time and long-time experiments, resulting in $u_{x,\mathrm{H,act}}(x_a, y_a)$, $u_{x,\mathrm{H,inact}}(x_a, y_a)$, $u_{y,\mathrm{H,act}}(x_a, y_a)$ and $u_{y,\mathrm{H,inact}}(x_a, y_a)$.

4.4 Results

4.4.1 Changes in Cross-Sectional Area Induced by Pressure Chamber Activation

As described in Section 2.2.2, applying pressure in the pressure chamber caused the channel near the chamber (Section 10 fourth additional region, Fig. 4.3), viewed in the x-y plane (grayscale images on the left side of Fig. 4.4), to appear smaller rather than

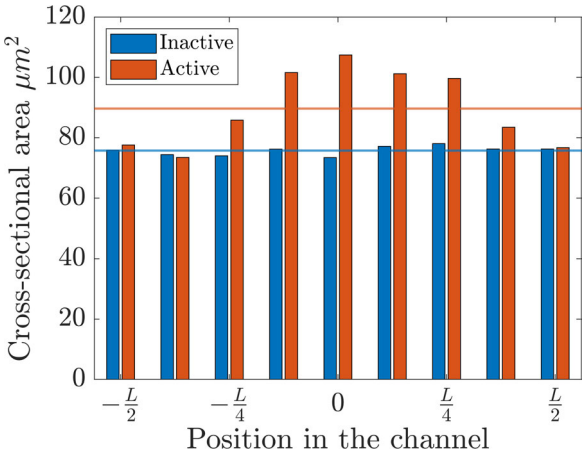

Figure 4.5: Cross-sectional area in y-z direction at various points along the channel, comparing conditions with the pericyte in inactive and active state. The cross-sectional area is plotted along the length (L) of the channel, with the midpoint of the channel indicated as position 0.

larger. This behavior is contrary to the expected effects of pericyte activation (pericyte relaxation). However, examining the x-z cross-sectional slices (A-A for the inactive pericyte and A'-A' for the active pericyte, Fig. 4.4) reveals a vertical increase in the x-z cross-sectional area during the active pericyte state. For A-A, the channel height remains consistent along its length, whereas, for A'-A', there is an increase in height at the center of the channel, with dimensions at the end remaining similar to those in the inactive state.

Observing the y-z cross-sectional slices, which represent the channel cross-sectional area, shows that for the inactive pericyte state (B-B, ..., F-F), the height and width are very consistent. In contrast, for the active pericyte state (B'-B', ..., F'-F'), the first and last slices (B'-B' and F'-F') exhibit z-y cross-sectional areas similar to those of the inactive state, while the middle slices (C'-C', D'-D' and E'-E') show a slightly narrower width but increased height, with the central slice being the tallest.

Polygons were fitted to nine equidistant slices along the channel to quantify the changes in the channel's cross-sectional area. The resulting cross-sectional areas are shown in Fig. 4.5. For the inactive condition, the cross-sectional area remains very consistent along the channel, as observed in Fig. 4.4, with a mean value of $75.72\,\mu\text{m}^2$ and a range of $73.41\,\mu\text{m}^2$ to $78.06\,\mu\text{m}^2$.

In the active condition, the area increases in the center of the channel, indicating that the height changes are bigger than the width changes, leading to a larger channel cross-sectional area. The mean cross-sectional area in the active state is $89.66\,\mu\text{m}^2$, with a range of $73.45\,\mu\text{m}^2$ to $107.42\,\mu\text{m}^2$. This corresponds to a mean increase of 18.54% and a maximum increase of 42.15% in the center of the channel.

4.4.2 Dynamic Response to Pericyte Activation

We initially decided to examine the system's response to dynamic pericyte activation. As outlined in the methods section, the short-time experiment is designed to analyze

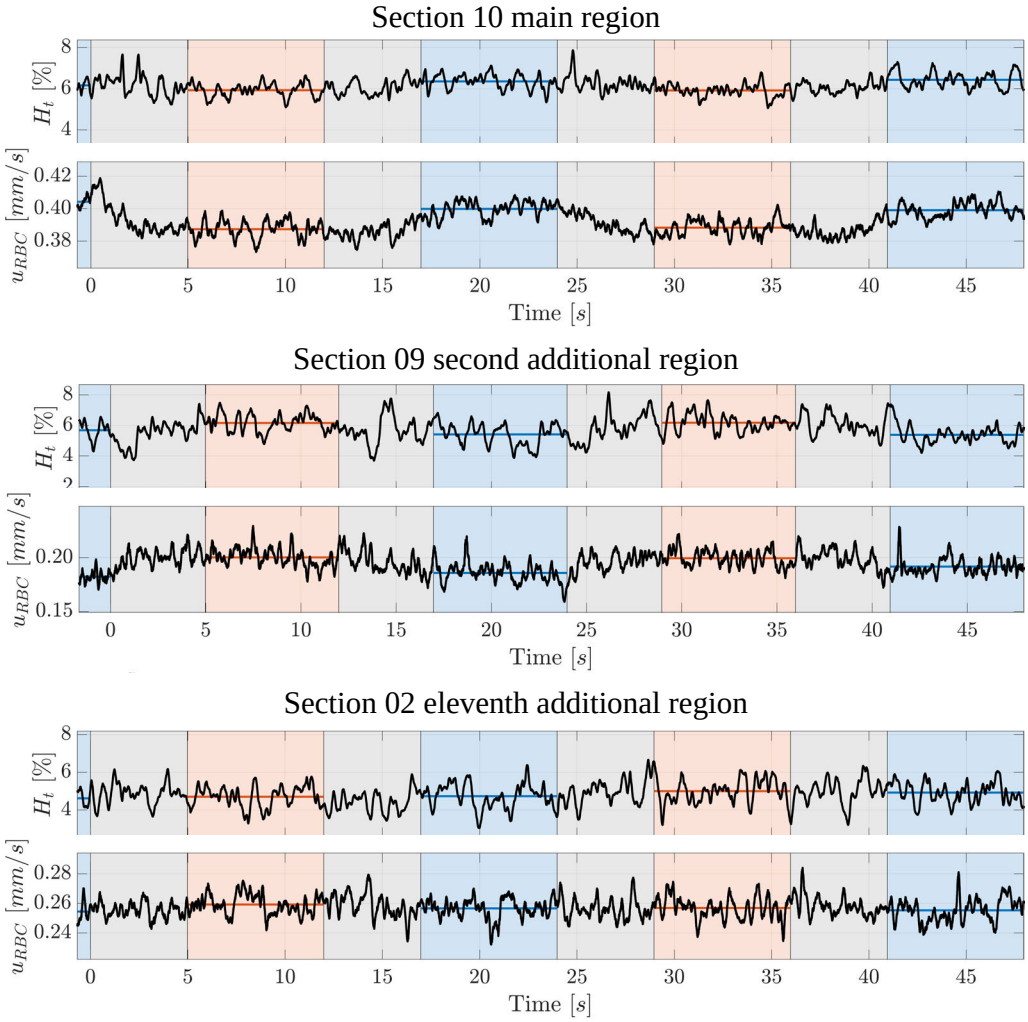

Figure 4.6: Dynamic changes in hematocrit and velocity through pericyte activation and deactivation cycles for three channels: Section 10 main region, Section 09 second additional region and Section 02 eleventh additional region. The data represent the mean results of ten repetitions smoothed using a running mean over 50 frames. The blue-shaded region corresponds to the pericyte's inactive state, with the blue horizontal line indicating the mean value. The orange-shaded region represents the pericyte's active state, with the orange horizontal line denoting the mean value. Grey-shaded regions mark the transitions during the activation and deactivation phases.

temporal fluctuations in velocity and hematocrit during the activation and deactivation phases of the simulated pericyte. Fig. 4.6 illustrates the responses in three channels: Section 10 main region (Sec_10_MR_01), Section 09 second additional region (Sec_09_-AR_02), and Section 02 eleventh additional region (Sec_02_AR_11), as shown in Fig. 4.3. Focusing on the hematocrit and velocity changes in Sec_10_MR_01 and Sec_09_-AR_02, channels located near the pericyte activation site (Section 10 fourth additional region), and analyzing the data using equation 4.3.2, we observe a clear dynamic response which follows the pericyte status. Velocity remains relatively constant when the pericyte

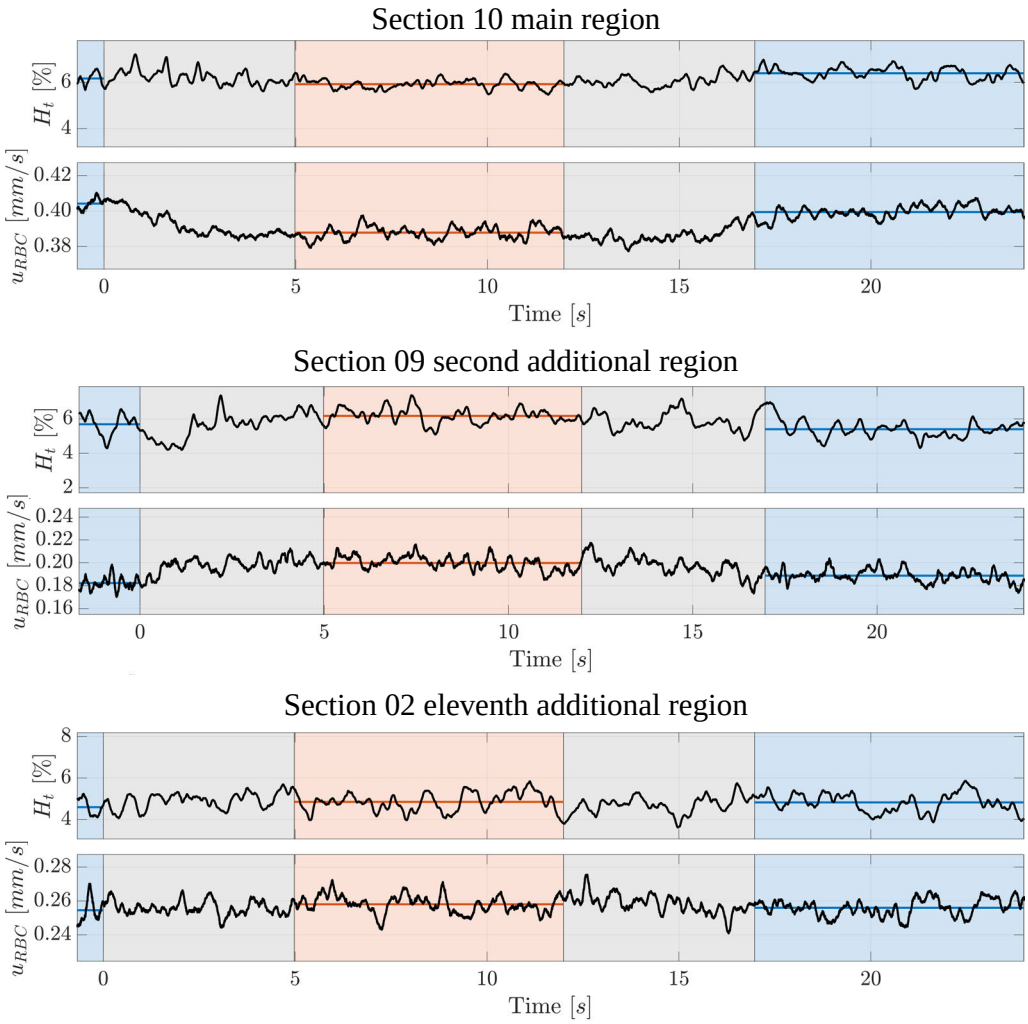

Figure 4.7: Superimposition of the two active-inactive cycles of Fig. 4.6 for three channels: Section 10 main region, Section 09 second additional region and Section 02 eleventh additional region. The data represent the mean results of twenty active-inactive cycles, smoothed using a running mean over 50 frames. The blue-shaded region corresponds to the pericyte's inactive state, with the blue horizontal line indicating the mean value. The orange-shaded region represents the pericyte's active state, with the orange horizontal line denoting the mean value. Grey-shaded regions mark the transitions during the activation and deactivation phases.

is in an active (orange-shaded region) or inactive (blue-shaded region) state, but increases or decreases occur during the transition phases (gray-shaded region).

In contrast, Sec_02_AR_11, which is further away from the pericyte activation site, shows no significant dynamic changes corresponding to the pericyte's state. These plots clearly highlight the system's unsteadiness (lack of a steady state), which is strongly influenced by the heterogeneous distribution of RBCs, constantly evolving over time.

For the channels where differences were observed between active and inactive states, the results of the first and second activation cycles were consistent with each other. To

Table 4.1: Mean velocity and hematocrit values for active and inactive states for the short-time experiment in three channels.

Section	**State**	**Velocity** u_{RBC} [mm/s]	$\Delta u_{\mathrm{RBC,rel}}$ [%]	**Hematocrit** H_{t} [%]	$\Delta H_{\mathrm{t,rel}}$ [%]
Sec_10_MR_01	Inactive	0.400 ± 0.0035	-2.91	6.39 ± 0.26	-7.37
	Active	0.388 ± 0.0035		5.92 ± 0.20	
Sec_09_AR_02	Inactive	0.189 ± 0.0054	5.82	5.40 ± 0.49	12.48
	Active	0.200 ± 0.0059		6.17 ± 0.42	
Sec_02_AR_11	Inactive	0.256 ± 0.0050	0.78	4.83 ± 0.45	0.41
	Active	0.258 ± 0.0050		4.85 ± 0.44	

strengthen the analysis, the two cycles were superimposed, effectively doubling the dataset from ten to twenty repetitions. The resulting graph, shown in Fig. 4.7, indicates no significant deviations from the earlier results (Fig. 4.6).

The mean hematocrit and velocity values for active and inactive states are summarized in Table 4.1. These values reveal distinct trends across the studied regions.

In Sec_10_MR_01, the active-state velocity ($u_{\mathrm{RBC,act}}$) is slightly lower than the inactive-state velocity ($u_{\mathrm{RBC,inact}}$), with a relative velocity decrease of $\Delta u_{\mathrm{RBC,rel}} = -2.91\%$. A similar trend is observed for hematocrit (H_{t}), where the active state exhibits a decrease of $\Delta H_{\mathrm{t,rel}} = -7.37\%$ compared to the inactive state.

In contrast, Sec_09_AR_02 shows a significant increase in both velocity and hematocrit during the active state. The velocity increases by $\Delta u_{\mathrm{RBC,rel}} = 5.82\%$, while the hematocrit increases by $\Delta H_{\mathrm{t,rel}} = 12.48\%$.

Meanwhile, in Sec_02_AR_11, the differences between active and inactive states are negligible. The relative changes are $\Delta u_{\mathrm{RBC,rel}} = 0.78\%$ for velocity and $\Delta H_{\mathrm{t,rel}} = 0.41\%$ for hematocrit, indicating minimal impact of activation in this region.

These findings align with the trends observed in the associated figures, highlighting region-specific differences in the response to activation.

4.4.3 Difference Between Short-Time and Long-Time Experiments

To analyze the effects and differences between short- and long-time pericyte activation, we calculated the mean velocity and hematocrit for both inactive and active pericyte states. Fig. 4.8 illustrates the velocity distribution. In the inactive state (first row), the velocity patterns are similar between the short- and long-time experiments. For the active state (second row), small differences are apparent both between the inactive and active states and between the two experiments. Across all experiments and pericyte states, the mean recorded maximum velocity is $\overline{u}_{\mathrm{RBC,max}} = 0.454 \pm 0.0078\,\mathrm{mm/s}$ while the minimum is $\overline{u}_{\mathrm{RBC,min}} = 0.118 \pm 0.0011\,\mathrm{mm/s}$.

To highlight these differences, the relative difference in velocity between inactive and active states is shown in the third row of Fig. 4.8. In the short-time experiment (third row, first column), significant velocity changes are observed near the pericyte activation site, with a maximum of $\Delta u_{\mathrm{RBC,rel}} = 6.67\%$ and a minimum of $\Delta u_{\mathrm{RBC,rel}} = -12.44\%$. Further

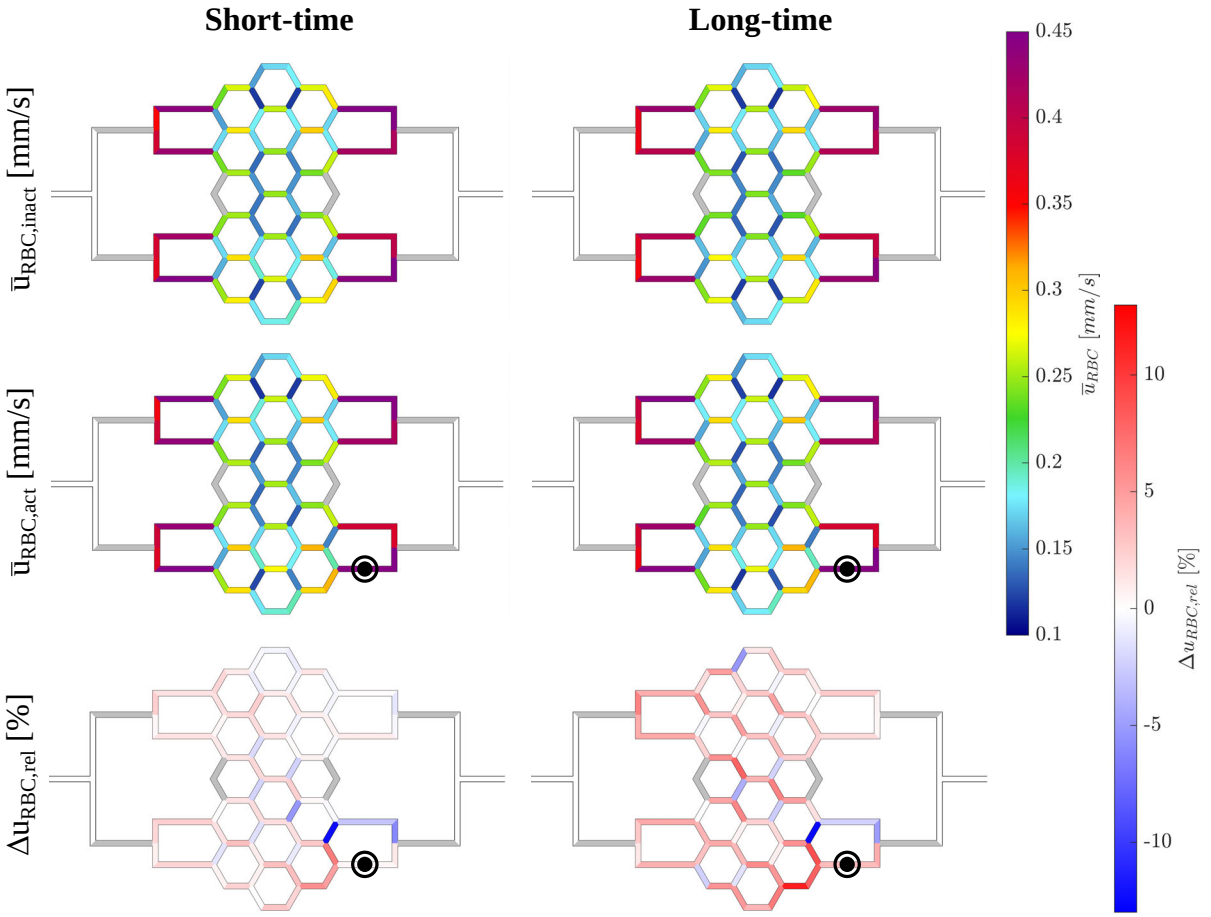

Figure 4.8: Velocity distribution in the microfluidic chip for the short-time and long-time experiments: mean velocity during inactive pericyte $\overline{u}_{\mathrm{RBC,inact}}$, mean velocity during active pericyte $\overline{u}_{\mathrm{RBC,act}}$ and the relative differences between the two ($\Delta u_{\mathrm{RBC,rel}}$). The pericyte activation site is marked with a black circle.

from the activation site, the differences are minimal, ranging between $\Delta u_{\mathrm{RBC,rel}} = -0.95\%$ and $\Delta u_{\mathrm{RBC,rel}} = 2.0\%$, consistent with the observations in Section 4.4.2.

In the long-time experiment (third row, second column), larger and more sustained differences are observed across the microfluidic chip. Near the activation site, the response is similar to the short-time experiment, with a maximum of $\Delta u_{\mathrm{RBC,rel}} = 8.92\%$, and a minimum of $\Delta u_{\mathrm{RBC,rel}} = -12.60\%$. However, further from the activation site, velocity increases are observed, ranging between $\Delta u_{\mathrm{RBC,rel}} = 1.72\%$ and $\Delta u_{\mathrm{RBC,rel}} = 4.84\%$, except for an outlier at $\Delta u_{\mathrm{RBC,rel}} = -5.29\%$. These sustained differences suggest a gradual increase in blood flow rate over time throughout the microfluidic chip.

For the hematocrit distribution (Fig. 4.9), a similar trend emerges. In the inactive state (first row), both short- and long-time experiments display comparable hematocrit patterns. RBCs predominantly follow preferential paths along the top and bottom regions of the chip, symmetrically aligned with the horizontal centerline. In the active state (second row), noticeable differences arise between the inactive and active states and between the two experiments. Across all experiments and pericyte states, the mean recorded max-

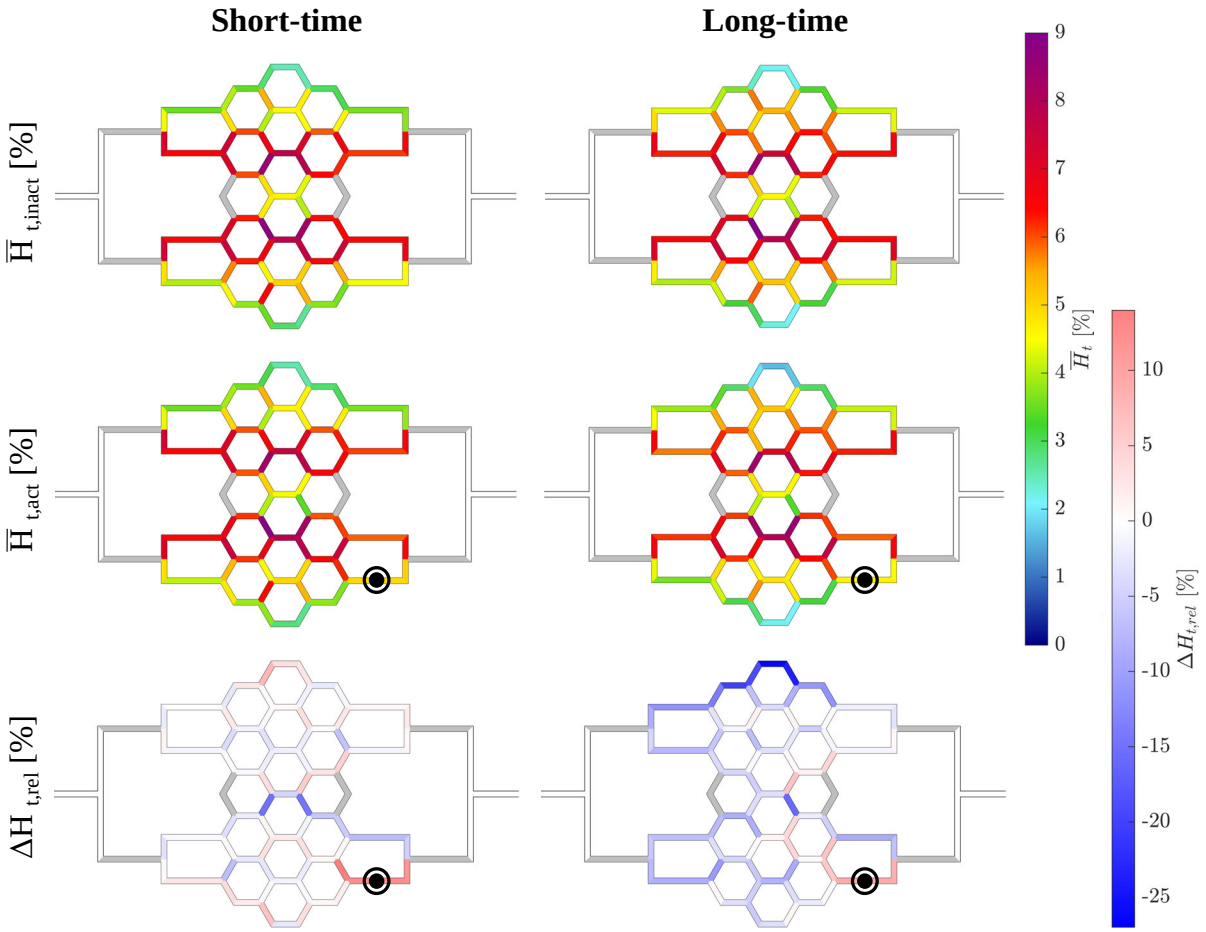

Figure 4.9: Hematocrit distribution in the microfluidic chip for the short-time and long-time experiments: mean hematocrit during inactive pericyte $\overline{H}_{\mathrm{t,inact}}$, mean hematocrit during active pericyte $\overline{H}_{\mathrm{t,act}}$ and the relative differences between the two ($\Delta H_{\mathrm{t,rel}}$). The pericyte activation site is marked with a black circle.

imum hematocrit is $\overline{H}_{\mathrm{t,max}} = 8.78 \pm 0.24\%$ while the minimum is $\overline{H}_{\mathrm{t,min}} = 2.17 \pm 0.44\%$.

The relative hematocrit change between active and inactive states is shown in the third row of Fig. 4.9. In the short-time experiment, the largest differences occur near the pericyte activation site, with a maximum of $\Delta H_{\mathrm{t,rel}} = 13.9\%$ and a minimum of $\Delta H_{\mathrm{t,rel}} = -7.37\%$, as well as at the chip's center. In the long-time experiment, similar differences are observed near the activation site, with a maximum of $\Delta H_{\mathrm{t,rel}} = 6.37\%$ and a minimum of $\Delta H_{\mathrm{t,rel}} = -9.01\%$. However, further from the activation site, a general hematocrit decrease is observed, ranging between $\Delta H_{\mathrm{t,rel}} = -11.68\%$ and $\Delta H_{\mathrm{t,rel}} = -26.32\%$.

For the RBC flux distribution (Fig. 4.10), a similar trend to the hematocrit is observed. In the inactive state (first row), the RBC flux patterns are comparable between short- and long-time experiments. Across all experiments and pericyte states, the mean recorded maximum RBC flux is $\overline{Q}_{\mathrm{RBC,max}} = 2.14 \pm 0.031 \cdot 10^{-6}\,\mathrm{mm}^3/\mathrm{s}$ while the minimum is $\overline{Q}_{\mathrm{RBC,min}} = 2.89 \pm 0.56 \cdot 10^{-7}\,\mathrm{mm}^3/\mathrm{s}$

In the short-time experiment (third row, first column, Fig. 4.10), the most significant

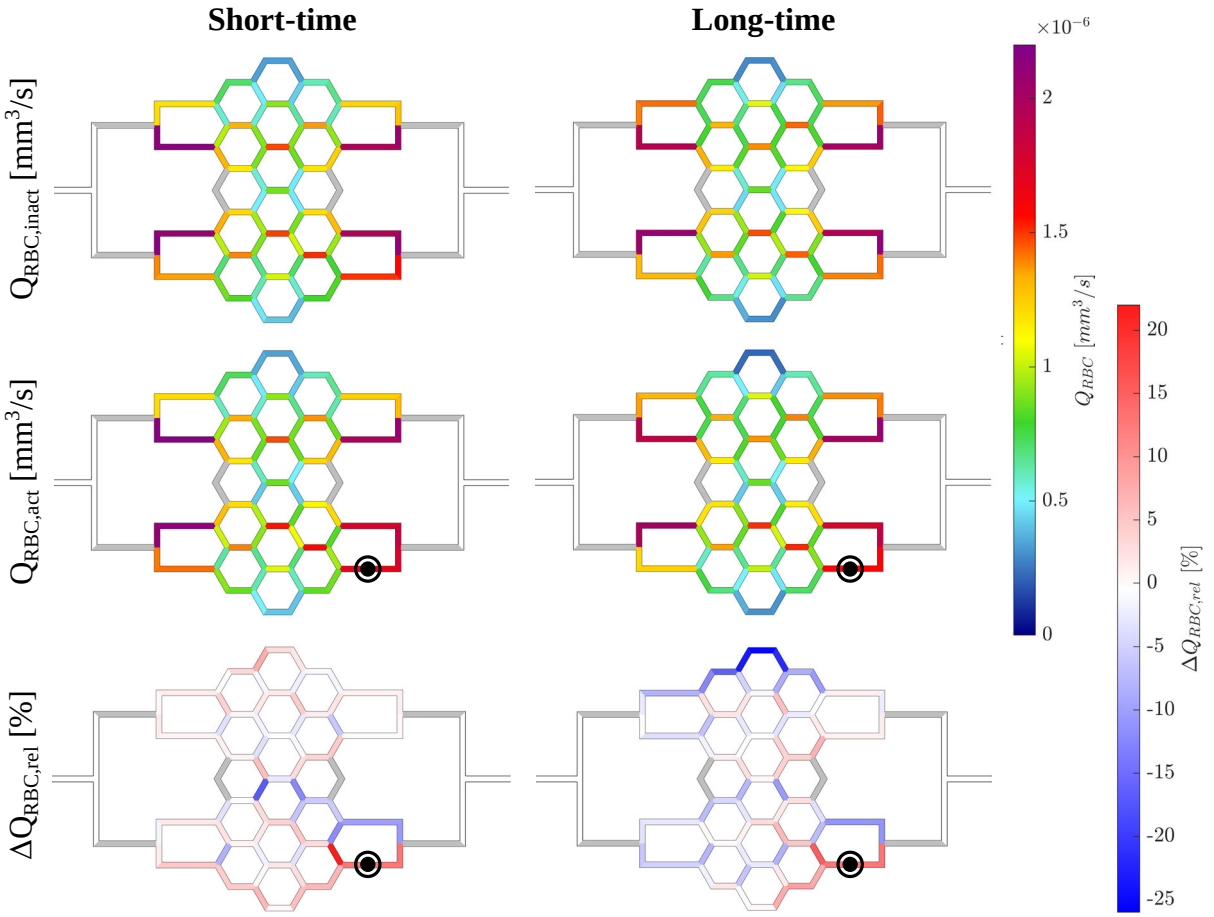

Figure 4.10: RBC flux distribution in the microfluidic chip for the short-time and long-time experiments: RBC flux during inactive pericyte $Q_{\mathrm{RBC,inact}}$, RBC flux during active pericyte $Q_{\mathrm{RBC,act}}$ and the relative differences between the two ($\Delta Q_{\mathrm{RBC,rel}}$). The pericyte activation site is marked with a black circle.

differences occur near the activation site, with a maximum of $\Delta Q_{\mathrm{RBC,rel}} = 21.48\%$ and a minimum of $\Delta Q_{\mathrm{RBC,rel}} = -11.93\%$. Smaller variations further from the activation site range between $\Delta Q_{\mathrm{RBC,rel}} = 7.54\%$ and $\Delta u_{\mathrm{RBC,rel}} = -0.85\%$. In the long-time experiment, significant differences persist near the activation site, with a maximum of $\Delta Q_{\mathrm{RBC,rel}} = 15.19\%$ and a minimum of $\Delta Q_{\mathrm{RBC,rel}} = -7.02\%$. Further away, RBC flux decreases significantly, ranging between $\Delta Q_{\mathrm{RBC,rel}} = -8.11\%$ and $\Delta Q_{\mathrm{RBC,rel}} = -25.39\%$.

To investigate the relationship between these changes and distance from the pericyte activation site, we calculated the travel time for each microchannel in the honeycomb network.

The travel time for a channel is determined as follows. For each channel, we computed the transition time $t_{\mathrm{trans},i} = L_{\mathrm{channel},i}/u_{\mathrm{RBC,inact},i}$, representing the time an RBC takes to flow from the inlet to the outlet of the specific channel under inactive conditions. Using these times, we calculated the shortest path from each channel to the activation site, setting $t_{\mathrm{trav}} = 0$ at the center of section 10 fourth additional region, where the pericyte activation occurs. The total travel time was then used to analyze relative differences.

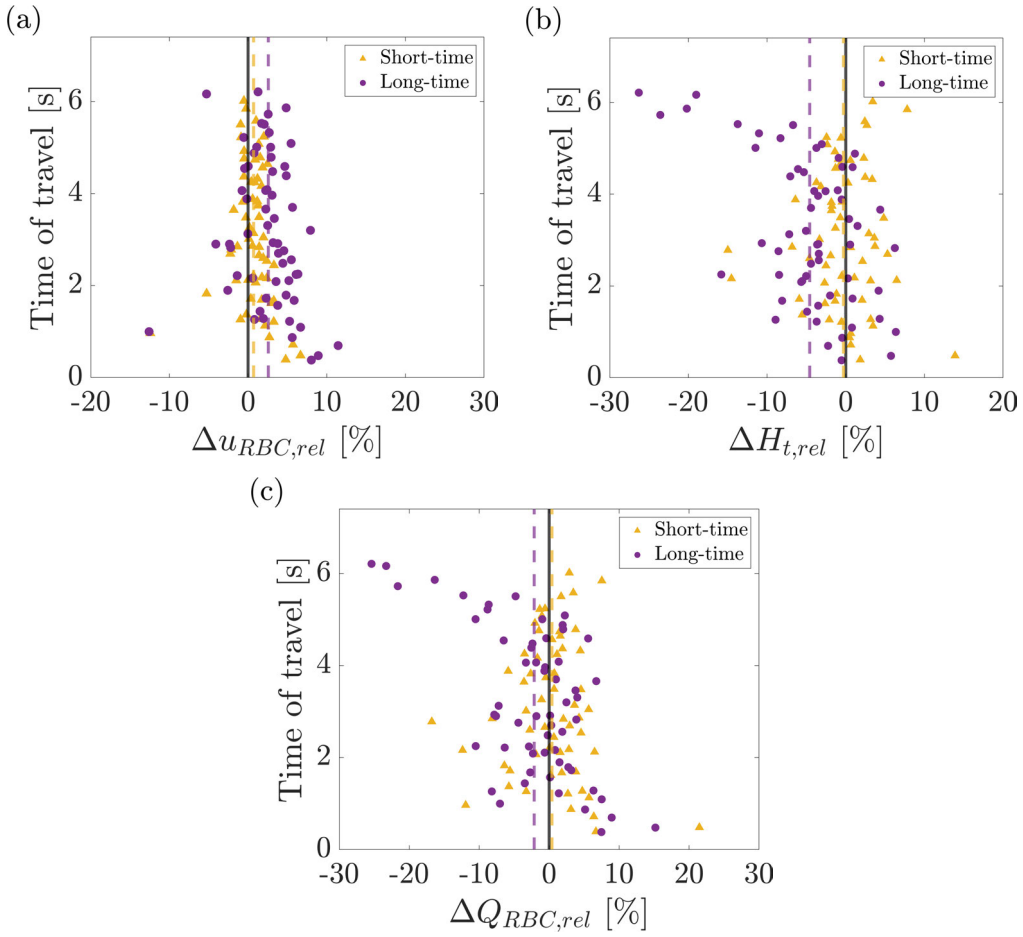

Figure 4.11: Relative difference in velocity hematocrit and RBC flux as a function of travel time. **a)** Relative difference in velocity. **b)** Relative difference in hematocrit. **c)** Relative difference in RBC flux. Data from the short-time experiment is represented by yellow triangles, with the yellow dashed line indicating the respective means. For the long-time experiment, data is represented by violet circles, with the violet dashed line indicating the respective means.

Fig. 4.11a shows the relative velocity difference as a function of travel time. In the short-time experiment (yellow triangles), significant relative differences are observed only at low travel times, with negligible changes at higher travel times, resulting in a mean relative difference of $\overline{\Delta u}_{\mathrm{RBC,rel}} = 0.70\%$. In the long-time experiment (violet circles), high differences persist at both low and high travel times, with a mean relative difference of $\overline{\Delta u}_{\mathrm{RBC,rel}} = 2.57\%$.

Fig. 4.11b shows the relative hematocrit difference. In the short-time experiment (yellow triangles), both positive and negative differences occur regardless of travel time, with a mean relative difference of $\overline{\Delta H}_{\mathrm{t,rel}} = -0.28\%$. In the long-time experiment (violet circles), hematocrit generally decreases with travel time, showing a small decrease at low travel times and a more significant decrease at high travel times, resulting in a mean relative difference of $\overline{\Delta H}_{\mathrm{t,rel}} = -4.58\%$.

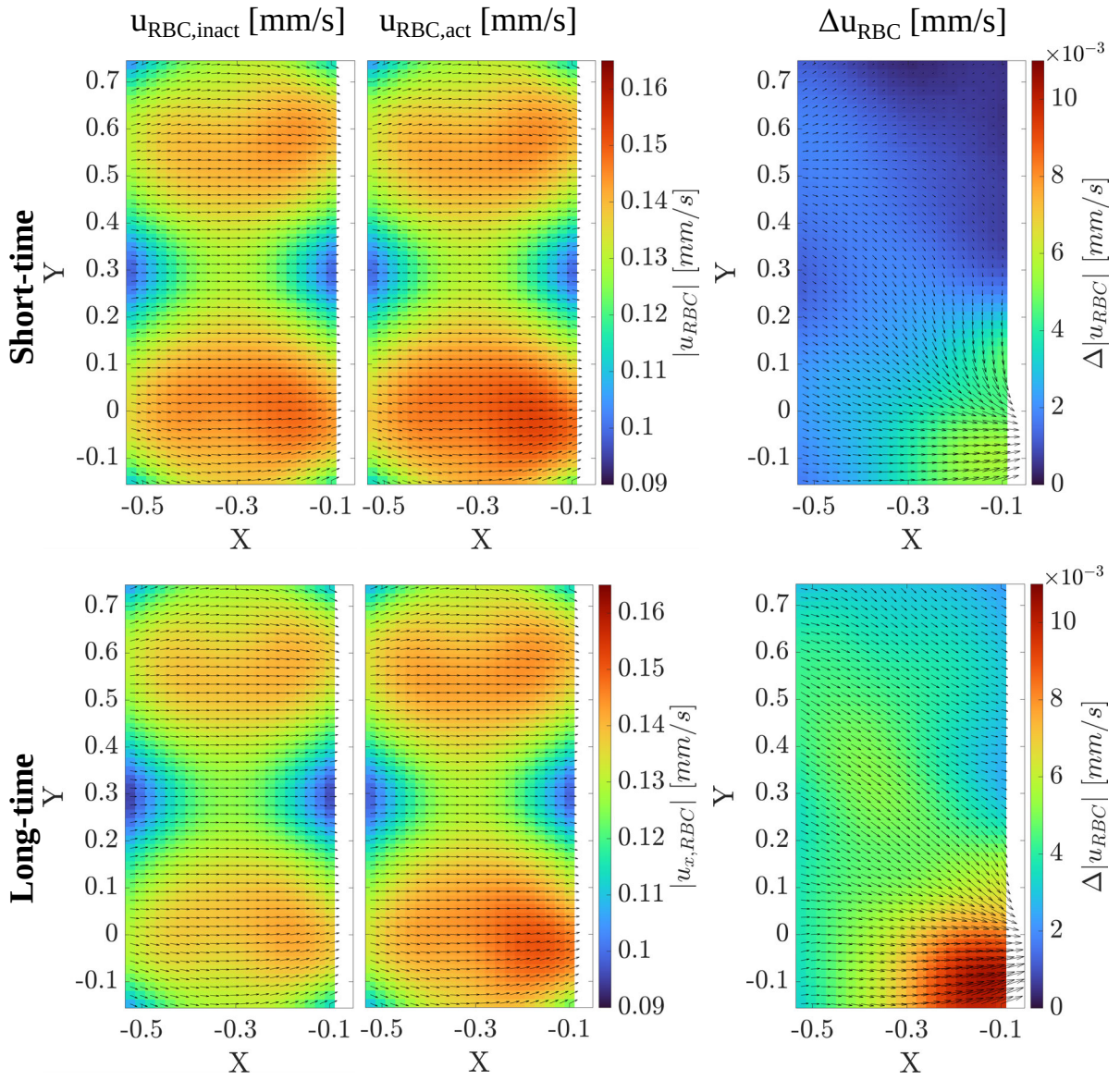

Figure 4.12: Homogenized velocity distribution: A comparison of conditions before and after short-time pericyte activation, before and after long-time pericyte activation, and the difference (Δu_{RBC}) between inactive and active pericyte states. The pericyte activation site is positioned at $(0, 0)$.

Fig. 4.11c shows the relative RBC flux difference. In the short-time experiment (yellow triangles), both positive and negative differences occur independently of travel time, similarly to the hematocrit, with a mean relative difference of $\overline{\Delta Q}_{\mathrm{RBC,rel}} = 0.4\%$. In the long-time experiment (violet circles), positive and negative differences are observed at low travel times, but high travel times show significant decreases, resulting in a mean relative difference of $\overline{\Delta Q}_{\mathrm{RBC,rel}} = -2.14\%$.

4.4.4 Homogenized Network

As detailed in Section 4.2, we modeled the microfluidic chip as a porous medium. To compare theoretical predictions with experimental results, we homogenized the data for each experimental condition following the approach described in Section 4.3.3. Fig. 4.12 illustrates the homogenized velocity fields for both experiments, with the first row corresponding to the short-time experiment and the second row to the long-time experiment. Each column represents a different condition: the first shows the inactive pericyte state, the second displays the active pericyte state, and the third depicts the difference between the two conditions.

In the short-time experiment, minor differences in velocity appear near the pericyte activation site at $(0, 0)$, with a slight increase directed toward the activation site. In contrast, the long-time experiment reveals a broader velocity increase across the homogenized network, peaking near the activation site. This maximum velocity is greater than the peak observed in the short-time experiment.

The homogenized hematocrit distributions, presented in Fig. 4.13, exhibit notable differences between the short-time and long-time experiments. In the short-time experiment, hematocrit increases near the activation site, extending toward the lower region of the network, with a secondary increase near the top. A slight decrease in hematocrit is observed at the network's center. On the other hand, in the long-time experiment, a significant reduction in hematocrit is evident at the top of the network, with only two small regions of increased hematocrit: one near the activation site and another slightly above it.

4.4.5 Phase Separation

To investigate phase separation at diverging bifurcations within the honeycombed network, we plotted the relationship between the blood flow rate fraction (Φ) and the RBC flux fraction (Ψ) (Fig. 4.14). These results were compared to the empirical relationship proposed by Pries et al. (2003) for parent and daughter vessels with a hydraulic diameter of $D_\mathrm{h} = 8.7\,\mu$m, matching the dimensions of our microchannels.

With the exception of two diverging bifurcations, where one daughter vessel carried only plasma, the blood flow rate fraction ranged between 0.3 and 0.7 across both experiments and conditions. For the short-time experiment (Fig. 4.14a), 73.6% of bifurcations were classified as well-balanced under both inactive and active pericyte states, as defined by Schmid et al. (2015) and outlined in equation 2.20. For the long-time experiment (Fig. 4.14b), 78.9% of bifurcations were well-balanced in the inactive pericyte state, compared to 73.6% in the active state.

Comparing the inactive and active pericyte states reveals very similar phase separation behaviors in both experiments, with only slight differences due to the activation (pints connected by black lines). Interestingly, many bifurcations exhibited phase separation close to the identity line, i.e., no phase separation and no bifurcation adhere to Pries's law., and most bifurcations displayed a reverse partitioning behavior. Classical partitioning (Zweifach-Fung effect), as described by Pries's law, occurs when the daughter vessel with a higher blood flow rate fraction also receives a proportionally higher RBC flux fraction. In contrast, reverse partitioning, an inversion of the Zweifach-Fung effect, occurs when

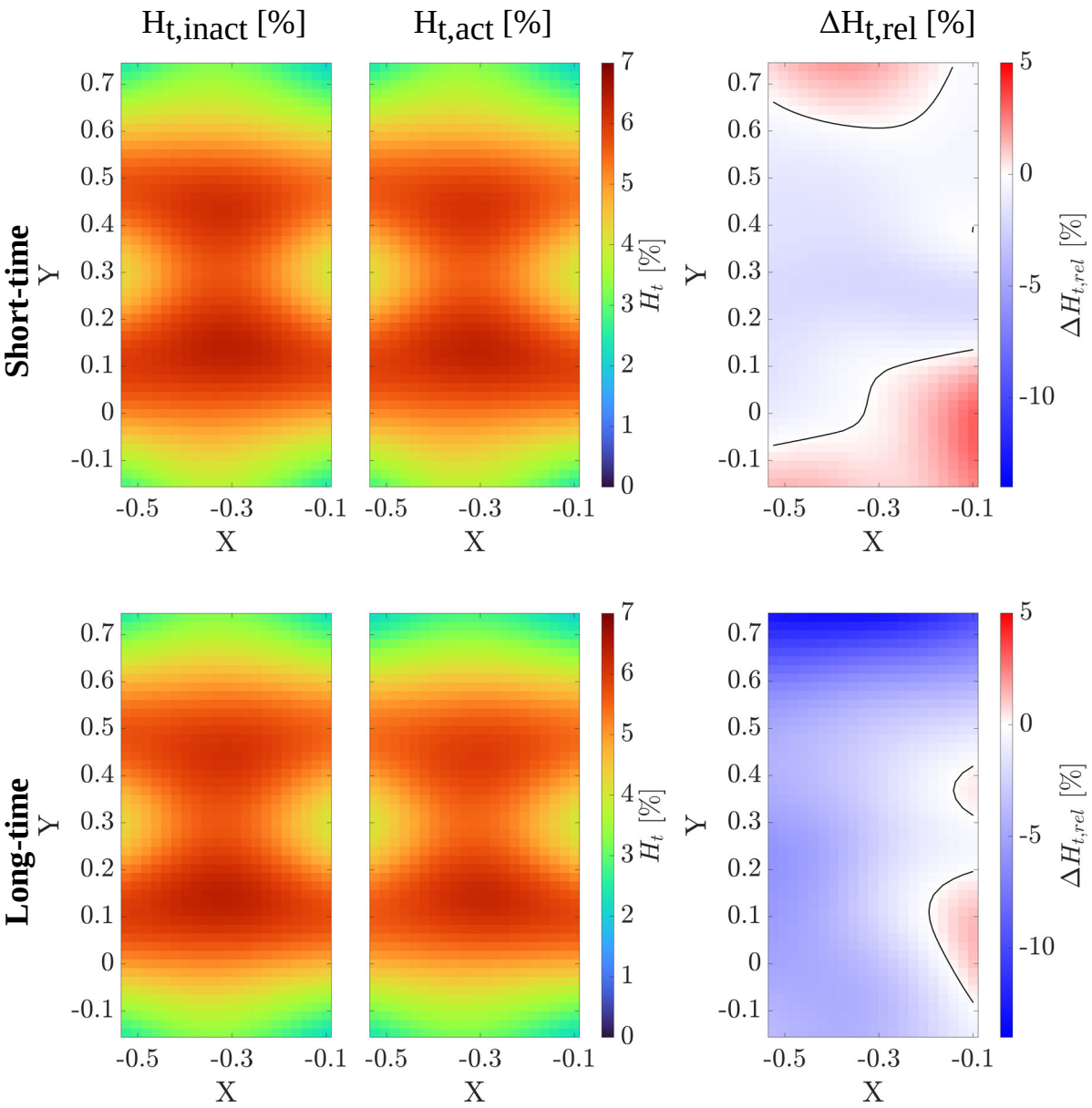

Figure 4.13: Homogenized hematocrit distribution. A comparison of conditions before and after short-time pericyte activation, before and after long-time pericyte activation, and the difference (ΔH_t) between inactive and active pericyte states. The pericyte activation site is positioned at $(0, 0)$.

the daughter vessel with a lower blood flow rate fraction receives a disproportionately higher RBC flux fraction. The gray-shaded regions in Fig. 4.14 indicate areas where reverse partitioning was observed, consistent with findings by Clavica et al. (2016) and Shen et al. (2016).

Additionally, differences in phase separation were noted when bifurcations were grouped based on their horizontal position within the network. Bifurcations sharing the same x-coordinate exhibited similar phase separation behaviors. These findings are detailed

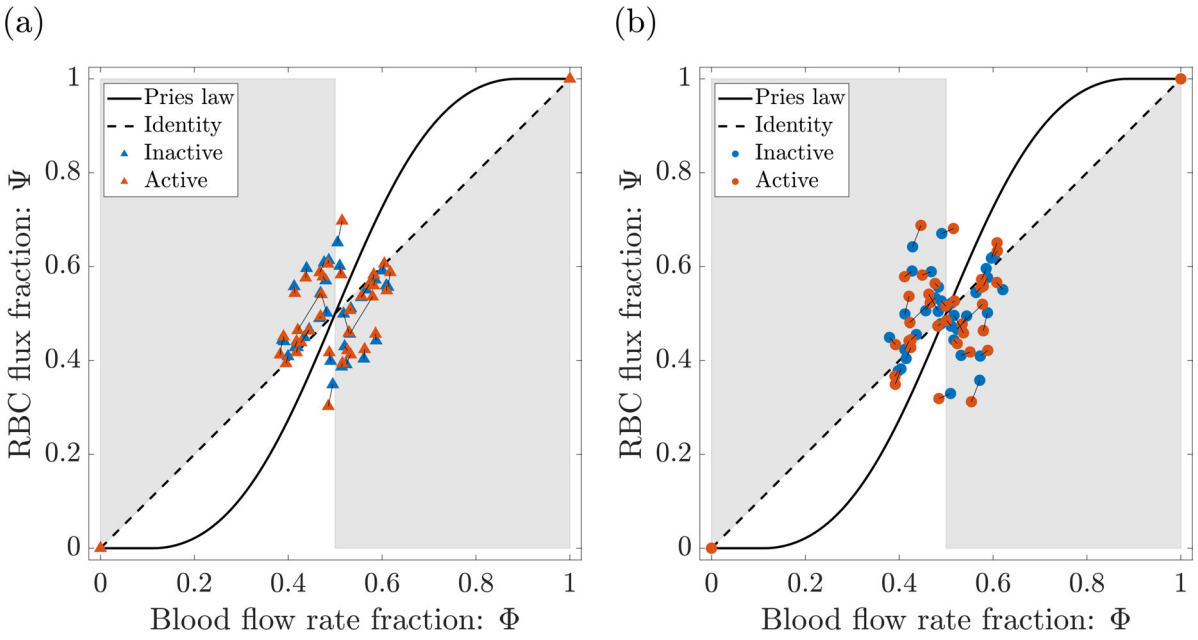

Figure 4.14: Phase separation. **a)** Phase separation for the short-time activation experiment. **b)** Phase separation for the long-time activation experiment. The blue marker indicates the inactive pericyte state, while the orange marker represents the active one. A thin black line connects the same bifurcation in both conditions. The black line represents the empirical relationship proposed by Pries et al. (2003) for parent and daughter vessel diameters of $D_h = 8.7\,\mu$m. The dashed black line indicates the identity line, corresponding to the proportional separation of blood and RBCs (no phase separation). Gray-shaded regions highlight areas where an inversion of the Zweifach-Fung effect is observed, as reported by Clavica et al. (2016) and Shen et al. (2016).

further in Appendix D.1.

4.5 Discussion

In this study, we investigated the effect of pericyte activation duration on RBC velocity and distribution within a microfluidic chip. The microfluidic chip, previously designed in our lab (Mantegazza et al., 2020a), was adapted to simulate dynamic changes in cross-sectional area, representing dynamic pericyte activation. Additionally, new preprocessing steps were introduced to enhance data analysis.

4.5.1 Pericyte Activation and Geometrical Effects

Before starting the experiments, it is essential to analyze the geometrical effects of pericyte activation on our microfluidic chip, as we modified both the experimental setup and the activation method for the pressure chamber representing the pericyte, compared to the approach used by Mantegazza et al. (2020a). In this study, we define pericyte activation as the active relaxation of pericytes, which leads to an increase in the diameter

of the underlying capillary vessel, a phenomenon associated with functional hyperemia in the brain. Hall et al. (2014) reported diameter increases ranging from 5.3% to 17.9%. For a baseline diameter of 9.72 μm (the hydraulic diameter of our channels), this corresponds to an increase in cross-sectional area between 10.08% and 39.0%.

In our experiments, we measured a mean increase in cross-sectional area of 18.54%, which falls within the range observed by Hall et al. (2014). The maximum increase we recorded was 42.15%, slightly exceeding the upper limit reported *in vivo*. However, this value remains comparable to *in vivo* measurements and can still be considered representative of physiological conditions. These findings suggest that our microfluidic model provides a robust platform for simulating the influence of pericyte activation on capillary microchannels.

4.5.2 Short-Time Effects of Pericyte Activation

In the short-time experiments, we observed that RBC velocity and hematocrit near the activation site closely followed the pericyte activation curve (Fig. 4.7). Beyond the activation site, no significant changes occurred, indicating a localized effect of pericyte activation. This supports the hypothesis that capillary networks behave as porous media in a short-time observation, where pericyte activation represents a locally increased porosity. The observed velocity field differences (Fig. 4.12, first row, third column) formed a dipole-like pattern (like Fig. 4.2), indicative of localized porosity changes, but only half of the dipole was visible due to the activation site's location outside the honeycomb network.

4.5.3 Long-Time Effects of Pericyte Activation

In long-time experiments, the dipole-like pattern disappeared (Fig. 4.12, second row, third column), suggesting that RBCs redistributed throughout the network to achieve a minimal resistance configuration. Differences in RBC velocity and distribution between short- and long-time activation (Fig. 4.11) highlight the dynamic impact of pericyte activation. Near the activation site, velocity differences remained similar, but further from the activation site, an increase in velocity was observed in the long-time experiments. These results align with Mantegazza et al. (2020a), who also noted a general increase in velocity across the network during prolonged activation.

However, discrepancies arose between our findings and Mantegazza et al. (2020a), likely due to differences in RBC properties. While Mantegazza et al. (2020a) used pig RBCs, which are smaller, we used human RBCs, which are 1.26 times larger in diameter and have a 1.56 times higher MCV. This difference in size results in varying confinement ratios, 1.2 for human RBCs and 1.5 for pig RBCs (a higher confinement ratio indicates looser confinement). These differences may explain the reduced magnitude of hematocrit and RBC flux changes in our experiments ($-26.32\% < \Delta H_{\mathrm{t,rel}} < 6.37\%$ and $-25.39\% < \Delta Q_{\mathrm{RBC,rel}} < 15.19\%$) compared to $-29\% < \Delta H_{\mathrm{t,rel}} < 19\%$ and $-25\% < \Delta Q_{\mathrm{RBC,rel}} < 45\%$ reported by Mantegazza et al. (2020a).

Our long-time experiments revealed an increase in blood flow rate at the network's entry ($Q_{\mathrm{blood,intact,inlet}} = 1.284 \cdot 10^{-4}\,\mathrm{mm^3/s}$ to $Q_{\mathrm{blood,act,inlet}} = 1.338 \cdot 10^{-4}\,\mathrm{mm^3/s}$) but a decrease in RBC flux ($Q_{\mathrm{RBC,intact,inlet}} = 6.762 \cdot 10^{-6}\,\mathrm{mm^3/s}$ to $Q_{\mathrm{RBC,act,inlet}} = 6.449 \cdot 10^{-6}\,\mathrm{mm^3/s}$). This phenomenon is attributed to the Fåhræus effect, where RBCs flow

faster through the channels, resulting in a decreased concentration within the channels (tube hematocrit). When considering the entire system, we observe a network Fåhræus effect, which leads to a reduction in hematocrit across the network. These results suggest that single pericyte activation is beneficial for immediate responses but may deplete hematocrit over prolonged activation, underscoring the importance of coordinated activation of multiple pericytes and descending arterioles to maintain network perfusion.

4.5.4 RBC Partitioning at Bifurcations

Flow distribution at bifurcations remained well-balanced ($0.4 < \Phi < 0.6$, Fig. 4.14) during all conditions, ensuring robust perfusion. However, unlike the classical RBC partitioning model (Pries et al., 1989), most bifurcations exhibited RBC flux fractions close to blood flow fractions or reversed partitioning (Fig. 4.14, gray-shaded region). This deviation from Mantegazza et al. (2020a) can again be attributed to the higher confinement ratio of human RBCs, leading to increased interactions and lingering at bifurcations (Balogh and Bagchi, 2018; Pskowski et al., 2021). Further analysis of hematocrit skewness in the parent vessel, as performed by Mantegazza et al. (2020a), could provide deeper insights into the reasons for those differences.

4.5.5 Limitations and Future Directions

Although our microfluidic model effectively replicates the fluid dynamics of pericyte activation, it does not capture the full complexity of neurovascular coupling, which involves biological, chemical, and electrical processes (Peppiatt et al., 2006; Hall et al., 2014; Hartmann et al., 2021). Additionally, our channels have rectangular cross-sections due to fabrication constraints, unlike the cylindrical and non-uniform capillaries *in vivo*. Despite these limitations, previous studies (Mantegazza et al., 2020a) confirm that such simplifications have minimal impact on RBC flow investigations. Future work should focus on incorporating more realistic geometries and analyzing hematocrit skewness to better understand RBC partitioning dynamics.

4.6 Conclusion

This study highlights the critical role of pericyte activation dynamics in regulating RBC velocity and distribution within capillary networks, using an *in vitro* microfluidic model. Our findings demonstrate that pericyte activation induces localized increases in RBC velocity and hematocrit, with effects that differ significantly between short-time and long-time activation. In the short-time, activation is beneficial, enhancing local perfusion while maintaining a similar distribution of RBC through the network. However, prolonged activation leads to a decline in hematocrit and RBC flux, which depletes the downstream capillary regions of RBCs. These results suggest that coordinated activation of multiple pericytes and descending arterioles is required to sustain long-time RBC perfusion and prevent systemic imbalances.

The study also emphasizes the impact of confinement effects, showing that RBC size significantly influences partitioning behavior at bifurcations and overall network dynam-

ics. The observed differences between human and pig RBCs highlight the importance of accounting for RBC biophysical properties when interpreting results from *in vitro* studies.

Despite the simplifications inherent in our microfluidic model, the system remains a robust tool for exploring the fluid dynamics of capillary networks. Future work should aim to analyze hematocrit skewness effects and explore the interplay between multiple pericytes to gain deeper insights into the neurovascular coupling.

This work contributes to our understanding of pericyte-mediated capillary regulation of RBC flow and offers a foundation for future investigations into microvascular flow dynamics.

Chapter 5

Conclusion and Outlook

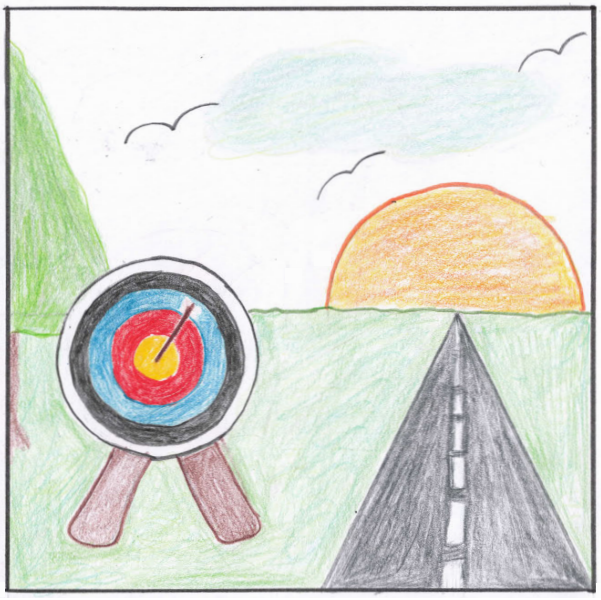

5.1 Conclusion

This doctoral project focuses on understanding the fluid dynamics and partitioning of RBCs in an *in vitro* capillary network and at microvascular bifurcations. To achieve this, three hypotheses were formulated as central questions for analysis, and five objectives were established.

Hypotheses

H1 Lingering RBCs influence the partitioning of RBCs at a bifurcation even in a less confined environment ($\lambda > 1$).

H2 The modulation of blood flow and RBC distribution begins locally near the pericyte if a pericyte is activated (i.e., local capillary dilation) for a short period of time but extends throughout the capillary network with prolonged activation.

H3 The capillary network behaves as a homogeneous porous medium, where pericyte activation can be interpreted as a localized increase in porosity if observed shortly after activation. However, over a prolonged period, the rearrangement of RBCs negates this interpretation.

Objectives

O1 Develop a robust classification method to differentiate lingering and non-lingering RBCs at a bifurcation.

O2 Analyze the influence of lingering and non-lingering RBC dynamics on partitioning at diverging bifurcations.

O3 Adapt and refine the experimental set-up previously established in the lab to enable repeatable dynamic activation of pressure chambers (i.e., channel dilation) as a simulation of pericyte activation.

O4 Investigate the impact of dynamic pericyte activation on capillary network perfusion and RBC distribution.

O5 Compare the effects of pericyte activation with those of a localized increase in porosity within a porous medium.

Across two studies, detailed in individual chapters, the objectives were implemented to evaluate the proposed hypotheses.

In Chapter 3, we investigated hypothesis H1 using an *in vitro* microfluidic chip with a single diverging bifurcation. The microchannel dimensions ($9.6\,\mu\text{m} \times 8\,\mu\text{m}$) were comparable to those in the capillary network but slightly larger than an RBC, resulting in low confinement ($\lambda > 1$). Rabbit RBCs were suspended in a plasma-like solution with three reservoir hematocrit levels (10%, 20%, and 30%). The inflow velocity was set to approximately 0.67 mm/s, and videos of RBC flow through the bifurcation were recorded for 10 s for each hematocrit level. These recordings were then processed to track every RBC.

As stated in hypothesis H1, we focused on the influence of LRBCs. To analyze this, we first developed a robust classification method for LRBCs and NLRBCs, addressing objective O1. Four criteria were compared: minimal velocity, minimal distance to the bifurcation apex, a combination of the two, and relative residence time at the intersection. We found that the first two criteria and their combination failed to capture the time scale aspect of LRBCs, leading to misclassification. The criterion based on relative residence time at the intersection proved to be the most robust for our experimental setup and conditions.

If hypothesis H1 were true, we would expect a significant percentage of NLRBCs to change their original streamline and cross the separation surface to enter the opposite daughter vessel. By analyzing the lateral position of NLRBCs before the bifurcation and the daughter vessel they entered, we found that only a small percentage of NLRBCs crossed the symmetry axis. Furthermore, there was no significant difference in percentage between when an LRBC was present at the apex or not, refuting our initial hypothesis (objective O2).

However, we observed notable differences in the lateral positions of LRBCs and NLRBCs in both the parent and daughter vessels. The presence of LRBCs in a daughter vessel skewed the hematocrit profile. By correlating the number of LRBCs with the hematocrit skewness in the daughter vessel, we demonstrated that achieving a highly skewed hematocrit, previously shown to cause reverse partitioning at diverging bifurcations (Mantegazza et al., 2020a,b), required a high percentage of LRBCs at the preceding bifurcation.

This finding partially supports our initial hypothesis H1, which should be revised as follows: LRBCs do not directly influence RBC partitioning at the diverging bifurcation where they linger but instead have a significant impact at the subsequent bifurcation in a low-confinement environment.

In Chapter 4, we investigated hypotheses H2 and H3, requiring significant adaptations to the existing experimental setup to fulfill objective O3. Before this thesis, an experiment simulating pericyte activation was conducted using an *in vitro* microfluidic chip with an idealized capillary network and a pressure chamber. Pressurizing the chamber altered the cross-sectional area of one channel, enabling two conditions: pericyte inactive (no pressure) and pericyte active (pressurized chamber). However, the manual control of pressurization using a balloon catheter pump limited the precision and reproducibility of the process.

To address these limitations, we developed a system capable of consistently reproducing the gradual activation and deactivation of the pericyte. This was achieved by replacing the manual balloon catheter pump with a programmable pressure pump controlled via a custom-written program. While this modification improved precision, it introduced additional challenges, including the need for reliable synchronization between the pressure pump and the microscope to synchronize the video recordings.

To solve this, we implemented a visual synchronization method by positioning a flashlight near the microfluidic chip. The flashlight illuminated the setup at the end of the pressure pump program, creating a visible intensity increase in the recorded videos. This signal was used to synchronize the videos of the experiment repetitions during analysis. In addition to hardware changes, new preprocessing steps were introduced to enhance the accuracy of image analysis. With these modifications completed, objective O3 was achieved, allowing us to test hypotheses H2 and H3.

To evaluate H2, we addressed objective O4 by conducting two experiments: a short-time experiment and a long-time experiment. If H2 were correct, we would expect localized changes near the pericyte activation during the short-time experiment and network-wide changes during the long-time experiment. The results confirmed that dynamic pericyte activation induced localized increases in RBC velocity and hematocrit near the activation site in the short-time experiments, reflecting enhanced local perfusion due to increased vessel diameter. However, in the long-time experiments, the network exhibited a redistribution of RBCs, leading to a decrease in hematocrit and RBC flux. This behavior aligns with the Fåhræus effect, where RBCs preferentially travel through higher-velocity channels. As RBCs flow faster through the network, the hematocrit within individual channels decreases, leading to an overall reduction in network hematocrit. This suggests the presence of a network Fåhræus effect. These findings highlight the trade-off between localized perfusion benefits during short-term activation and hematocrit depletion in downstream regions during prolonged activation. Additionally, it emphasizes the importance of coordinated activation of multiple pericytes and arterioles to maintain balanced network perfusion over time.

To assess H3, we addressed objective O5 by conceptualizing the capillary network as a homogeneous porous medium and interpreting pericyte activation as a localized increase in porosity. This analogy held true in the short-time experiments, where observed dipole-like velocity patterns near the activation site supported the interpretation. However, in the long-time experiments, RBC redistribution throughout the network invalidated the localized porosity analogy. Unlike a static porous medium, the capillary network dynamically adapts to minimize resistance, driven by RBC redistribution in the network. This distinction underscores the limitations of porous media models for capturing the adaptive and dynamic nature of capillary networks. While localized porosity increases provide a useful framework for understanding short-term effects, they fail to account for the network-wide adjustments observed during prolonged activation.

We also observed deviations in RBC partitioning at bifurcations from classical models. These deviations, not reported in previous experiments with the same microfluidic chip, are likely due to the higher confinement ratio of human RBCs used in our study compared to pig RBCs used previously. The increased confinement ratio may lead to enhanced interactions between RBCs and more pronounced lingering behavior, influencing partitioning dynamics. Further analysis of hematocrit skewness in the parent vessel could provide deeper insights into these deviations and their implications.

In conclusion, our findings underscore the importance of pericyte activation dynamics in regulating capillary flow and RBC distribution, supporting our two initial hypotheses, H2 and H3. This study highlights the dual nature of pericyte activation: its immediate benefits in enhancing local perfusion and its long-term risks of hematocrit depletion without coordinated systemic responses. These insights contribute to our understanding of microcirculatory regulation and provide a foundation for exploring microvascular flow dynamics.

5.2 Outlook

Although the outcomes were positive and the results promising, there is still room for improvement in the microfluidic chip design, experimental set-up, and protocols. Specific recommendations for future work are outlined below.

Modifications of the microfluidic chip design

The microfluidic chip design is effective, but it could benefit from two key improvements. First, currently, the honeycomb section of the chip is divided into two parts: the top (Sec_01 to Sec_04) and the bottom (Sec_07 to Sec_10), with connection channels in between (Sec_05_AD_10, Sec_05_AD_11, Sec_06_AD_10, Sec_06_AD_11, and Sec_05_MD_01, as shown in Fig. 4.3). However, in 4 out of 5 of these connection channels (Sec_05_AD_10, Sec_05_AD_11, Sec_06_AD_10, Sec_06_AD_11), no flow of RBCs or plasma is observed due to their geometrical position within the network. Consequently, the only functional connection enabling communication between the top and bottom parts of the honeycomb section is the Sec_05_MD_01 channel.

In a capillary network, flow pathways are typically interconnected, allowing multiple routes for fluid and cellular exchange. In the current design, movement from the top to the bottom of the honeycomb section is constrained to the single Sec_05_MD_01 channel. To address this, adding an additional column of hexagons to the honeycomb section could provide multiple pathways for the flow and exchange of RBC and plasma, making the network more representative of *in vivo* conditions. This adjustment would enhance the resemblance of the network to biological capillary systems by allowing more points of communication between the top and bottom regions.

Second, the current design includes only two pressure chambers that mimic pericyte activity, positioned opposite each other. However, in the *in vivo* capillary network, multiple pericytes activate sequentially along the direction of descending arterioles (Hillman, 2014). To better replicate this biological behavior, the number of pressure chambers could be expanded and strategically positioned in channels that are sequentially connected to each other.

This modification would not only increase the versatility of the chip but also enable the study of the influence of multiple pericytes and their synchronization. Such an enhancement would provide deeper insights into the collective impact of pericyte activity on capillary flow dynamics and hematocrit partitioning, aligning the chip's functionality more closely with physiological conditions.

Expansion in the experimental set-up

In the dynamic activation of the pericyte, we investigated the effect of pericyte activation alone without considering the activation of the descending arterioles, which occurs approximately 1 s after the pericytes. To address this limitation, we propose using a second pressure pump to drive blood flow through the microfluidic chip, replacing the current method of relying on the height difference between two reservoirs. This setup would enable precise synchronization of pericyte activation with descending arteriole activation.

With this modification, it would be possible to study the individual effects of dynamic pericyte activation and descending arteriole activation, as well as the combined influence

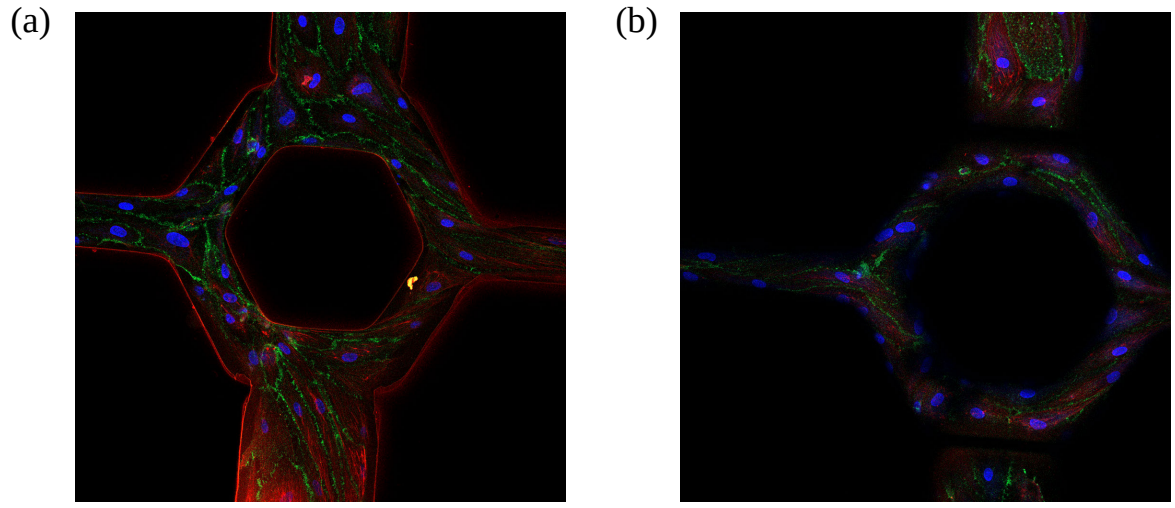

Figure 5.1: Stained endothelial cells covering the microfluidics channel. Red fluorescence (anti-F-Actin) highlights the cytoskeleton of the cells, green fluorescence (Rat anti-pig CD31, Goat anti-Rat AlexaFluor488) highlights cell to cell adhesion and blue fluorescence (DAPI) marks the nuclei. **a)** Ceiling of the microfluidic channels. **b)** Floor of the microfluidic channels.

of varying activation times between the two. This approach would provide a more comprehensive understanding of the interplay between pericytes and descending arterioles in regulating capillary network dynamics.

Microfluidic chip coating

The microfluidic chips used in this thesis were coated exclusively with albumin derived from the plasma-like solution. While this coating minimizes interactions between the channel surfaces and RBCs, it does not accurately mimic the biological environment of real capillaries. *In vivo*, RBCs interact with endothelial cells lining the capillary walls, supported by the glycocalyx, a complex matrix of proteins and carbohydrates essential for vascular function. The absence of these components in the current experimental set-up represents a significant limitation, reducing the physiological relevance of the findings.

A promising solution would be to endothelialize the microfluidic chip, thereby creating a more biologically accurate model. Preliminary tests in this direction have already been conducted and are described in Appendix E, with promising results presented in Fig. 5.1 and Fig. E.1. This improvement would significantly enhance the experimental set-up, enabling a more *in vivo*-like environment with physiological interactions between RBCs and the channel walls, particularly at bifurcations.

Declaration of Originality

The official declaration of originality from the University of Bern is on the next page.

Declaration of Originality

Last name, first name: Bcciarelli, Aurelia Lucilla

Matriculation number: 14-930-978

I hereby declare that this thesis represents my original work and that I have used no other sources except as noted by citations.

All data, tables, figures and text citations which have been reproduced from any other source, including the internet, have been explicitly acknowledged as such.

I am aware that in case of non-compliance, the Senate is entitled to withdraw the doctorate degree awarded to me on the basis of the present thesis, in accordance with the "Statut der Universität Bern (Universitätsstatut; UniSt)", Art. 69, of 7 June 2011.

Place, date

Bern, 08.01.2025

Signature

List of Publications

Journal articles:

A. Bucciarelli, A. Mantegazza, A. Haeberlin, & D. Obrist. *Relation between hematocrit partitioning and red blood cell lingering in a microfluidic network.* Biophysical journal, 2024, 123:3355-3365. 10.1016/j.bpj.2024.07.042 (Data processing was performed by A. Bucciarelli and data analysis was performed by A. Bucciarelli and A. Mantegazza. A. Bucciarelli and A. Mantegazza contributed equally to this work.)

M. Morrison, A. Bucciarelli, A. Korda, L.S. Goetz, M.D. Caversaccio, D. Obrist. & G. Mantokoudis. *Impact of Vibrations and Rapid Decelerations on SemontPLUS Maneuver Efficacy: An In Vitro Study.* Otology & Neurotology, 2024, 10.1097. 10.1097/MAO.0000000000004412 (Software design was performed by A. Bucciarelli and data analysis was performed by A. Bucciarelli and M. Morrison. M. Morrison and A. Bucciarelli contributed equally to this work.)

Conference papers & abstracts:

A. Bucciarelli, A. Mantegazza, D. Obrist. *Dynamics of lingering red blood cells in a diverging microchannel bifurcation.* 9th World Congress of Biomechanics, Taipei, Taiwan, 2022.

A. Bucciarelli, A. Mantegazza, D. Obrist. *In Vitro Characterization of Lingering Red Blood Cells In Capillary Networks.* InterPore2023, Edinburgh, UK, 2023.

A. Bucciarelli, A. Mantegazza, D. Obrist. *On the impact of Lingering RBC on the Reverse Partitioning in capillary networks.* DynaCaps 2023, Compiégne, France, 2023.

A. Bucciarelli, D. Obrist. *Influence of pericyte activation on RBCs flow and partitioning in an in vitro microfluidic network.* BRAIN MICROCIRCULATION Aarhus CTH workshop 2024, Aarhus, Denmark, 2024.

Media Contributions:

Porous Media Tea Time Talks on YouTube, Session 53; a talk on Biomechanics of Red Blood Cells in Capillary Networks 2024.

Curriculum Vitae

Education	
2020-11 – 2025-03	**PhD in Biomedical Engineering**, GCB (Graduate School for Cellular and Biomedical Sciences), University of Bern, Bern, Switzerland

Appendix A

Protocols

In this appendix are all the step-by-step procedures used and developed during this thesis. Below is the detailed protocol for the handle and preparation of the RBCs suspension.

A.1 Protocol for the Silanization of PDMS Molds

SILANIZATION OF PDMS MOLDS

This is the full procedure

Created by Aurelia Bucciarelli (aurelia.bucciarelli@unibe.ch) on Mai 17, 2024
Eddited by Aurelia Bucciarelli (aurelia.bucciarelli@unibe.ch) on July 03, 2024

Printed on the July 3, 2024

CARDIOVASCULAR ENGINEERING

UNIVERSITY OF BERN

ARTORG CENTER BIOMEDICAL ENGINEERING RESEARCH

Protocol purpose:
Mold coating for better peal off of PDMS.

PROTOCOL

Preparation the molds

Step 1 [Time required 15 minutes]

Plasma cleaner

Work with gloves!

1. Start the laminar flow for the flow hood.
2. Clean the surface with isopropanol.
3. Attach the molds with double-sided tape (transparent) to a PMMA plate cut to size.
4. Using the plasma bounding machine:
   - 2.1 Turn on the Plasma Cleaner.
   - 2.2 Open the oxygen bottle
   - 2.3 Do a dry run before one with the chips.
   - 2.4 Take the plastic trade.
   - 2.5 Clean the molds.
   - 2.6 Position the molds on the plastic trade
   - 2.7 Set the following: PDMS-Galss: 65% power, 8 sccm, 1 min
   - 2.8 Start the process and wait until it ends.
   - 2.9 Turn off the plasma cleaner.
   - 2.10 Close the oxygen bottle.

Silanization

Work in the silanization fume hood.

Step 2 [Time required 15 minutes]

Preparetion

Work with gloves!

1. Turn the signaling sheet at the fume hood around such that the warning is visible, and turn the light of the fume hood on.
2. Turn on the hot plate to 60° (last bottom from outside).
3. Prepare glass dish/gas container (normally already done):
   - Attaching glass slide on top to have a small opening when closed.
   - Place a glass slide on the bottom of the container where the mold will be.
   - Place a glass slide around the one for the container to put the saline on.

MATERIAL

Glass container | Backer | Pipette | Pipette tip | Glass slide | PMMA plate | Double sided tape

CHEMICALS

Isopropanol | Silane | dH_2O

EQUIPMENT

Fume hood | Plasma cleaner | Hot plate

DANGERS

Chemicals
Phisical
Environmental

PROTECTIVE GEAR

Gloves

WARNINGS

Chemical
Silane is toxic!

Heat
The oven and the plasma cleaner generate heat and you can burn yourself.

PEOPLE TO CONTACT

Lab responsible from OOC, for any lab question.

NOTES

4. Prepare the pipette with the smallest pipette tip. A volume of 10ul will be needed.
5. Take the silane bottle from the storage and lose the lid inside the fume hood.
6. Place the glass container on the hot plate.
7. ⚠Turn off the Vmax from outside.

Step 3 [Time required 90 minutes]

Silanization

Work with gloves under the fume hood!

1. Transfer the mold from the plasma cleaner to the glass container.
2. Work fast and put 1 to 2 drops of silane on 3 or 4 glass slides around the sample (10ul in total).
3. Distribute the silane with the pipette tip and leave the tip in the glass container.
4. Put the lid on the container with the small opening.
5. Close the silane bottle and put it back in the storage.
6. Close the fume hood but leave the light on and check that Vmax is off, and the warning sign is up.
7. Leave to do the silanization (PDMS 20 min, plastic/resin 1 h and epoxy 2h),
8. Turn off the hot plate with the external switch and turn on the Vmax,
9. Wait a couple of minutes to vent.
10. Open the lid of the glass container and close the fume hood again.
11. Wait a couple of minutes to vent.
12. Rinse the sample with dH_2O inside the fume hood in the glass beaker.
13. Mold is silanized and ready to use for PDMS poring.
14. Empty the water used in the middle container and clean the fume hood.
15. Turn off the light and rotate the warning signal.

A.2 Protocol for the Production of Microfluidic Chip

PRODUCTION OF MICROFLUIDICS CHIPS

This is the full three days procedure

Created by Aurelia Bucciarelli (aurelia.bucciarelli@unibe.ch) **on November 8, 2023**
Eddited by Aurelia Bucciarelli (aurelia.bucciarelli@unibe.ch) on July 03, 2024

Printed on the July 3, 2024

CARDIOVASCULAR ENGINEERING

UNIVERSITY OF BERN

ARTORG CENTER BIOMEDICAL ENGINEERING RESEARCH

Protocol purpose:
Production of Microfluidics chip for the analysis of RBC dynamics in the microcirculation

PROTOCOL

Day 1

Step 1 [Time required 2 minutes]

Preparation

1. Start the laminar flow for the flow hood.
2. Clean the surface with isopropanol.
3. Prepare all the silicon wafers and Petri dish you need.
4. Prepare the PDMS container and spoons.

Step 2 [Time required 35 minutes]

PDMS preparation

Work with gloves!

1. Weight the PDMS liquid part A in the PDMS container (separate per base and channels).
   - For the channel cr. 25g per small Petri dish.
   - For the base cr. 8g per small Petri dish.
   - For the base cr. 20g per big Petri dish.
   - Max 80g pro container.
2. Calculate how much curing agent you need:
   - For the channel 1 to 12 (weight to weight, $m_{CA} = \frac{m_{PDMS}}{12}$).
   - For the base 1 to 10 (weight to weight, $m_{CA} = \frac{m_{PDMS}}{10}$).
3. Add the curing agent with the dedicated pipette all over the PDMS (1 pipette cr. 0.7g).
4. Mix the PDMS for at least 3 min.
   - Needs to have a lot of bubbles, almost white.
   - Don't forget the angels.
5. Put the PDMS in the vacuum chamber.

⚠ It foams a lot at the start! Open the vacuum so as not to make the PDMS overflow.

6. It is done when it is back transparent and no bubble can be seen.

Step 3 [Time required 20 minutes]

Silicon wafer preparation

When the foaming of the PDMS has subsided, you can start preparing the silicon wafer.

1. Cut one aluminum foil for each silicon wafer.

MATERIAL

1st Day

Scale | Silicon wafer | Petri dishes round | Petri dishes insert | Magic tape | Spoons | Tweezers | PDMS Container | Aluminium foil | Aluminium holder | Permanent marker | Pipette for PDMS curing agent

2nd Day

Magic tape | Petri dishes squared | Tweezers | Bistoury | Permanent marker | Biopsy Punch (1.5mm) | Cutting board

3rd Day

Magic tape

CHEMICALS

1st Day

PDMS liquid Part A+B | Isopropanol

2nd and 3rd Day

Isopropanol

EQUIPMENT

1st Day

Vacuum chamber | Oven

2nd Day

2. Place the aluminum holder on the aluminum foil and fold it carefully to the side.
3. Insert the aluminum holder inside the Petri dish.
4. Fold the aluminum carefully to the side of the petri dish.
5. Remove the aluminum holder.
6. Close the Petri dish and carefully remove the excessive aluminum foil.
7. Remove carefully the silicon wafer from the Petri dish where it is stored.
8. Use the pressure air very carefully to ensure it has no dust on it.

⚠ If pressure air is not enough, only use distilled water to clean! No other chemical! You will ruin the photoresist!

9. Attach the silicon wafer to the aluminum foil with three small magic tape pieces.
10. Close the Petri dish and write on the lid of the Petri dish the following:
    - Your name
    - Group
    - Date
    - Silicon wafer name

Step 4 [Time required 50 minutes]

Poring PDMS on silicon wafer and base

1. Put the Petri dish with the silicon wafer on the scale.
2. Pore around 25g of PDMS on it, trying to form as few air bubbles as possible.
3. Close the Petri dish and do the next one; repeat until you have done all of them.
4. Put the Petri dish (open) in the vacuum chamber for cr. 25min.
5. For the base, use a normal Petri dish (no aluminum).
6. On the scale, pore the PDMS into the Petri dish (8g for the small Petri dish and 25g for the big one).
7. Close the Petri dish and label it:
    - Your name
    - Group
    - Date
8. Put the Petri dish (open) in the vacuum chamber for cr. 25min.
9. After checking that there are no bubbles in the PDMS, close them and take them out of the vacuum chamber.
10. Without tiling them, put two pieces of tape to hold them close and place them in the oven at 60° overnight.

Day 2

Step 5 [Time required 2 minutes]

Preparation

1. Start the laminar flow for the flow hood.
2. Clean the surface with isopropanol.
3. Check that you have enough magic tape.
4. Check that the bistoury blade is sharp and, in case, replace it.
5. Prepare all the material you need.

Oven | Plasma cleaner

3rd Day

Microscope

DANGERS

Chemicals
Phisical
Environmental

PROTECTIVE GEAR

Gloves

WARNINGS

Chemical
PDMS is sticky be careful!

Heat
The oven and the plasma cleaner generate heat and you can burn yourself.

PEOPLE TO CONTACT

Severin Müller (OOC) for lab question.
Alexandra Homsy (HES-SO) for the silicon wafer.

NOTES

Step 6 [Time required 20 minutes]

Preparation of the base

Work with gloves!

1. Take the PDMS base out of the oven.
2. Cut with the bistoury around the edge of the Peti dish and go around two times.
3. Peel it off the Petri dish.
4. Quickly cover the part that was in contact with the Petri dish with magic tape.
5. Cut the base into pieces big enough for your chip (4-5 per small Petri dish, 28 for the big one).
6. Clean the edges of each piece and store them into a rectangular Petri dish with tape on the top part.

Step 7 [Time required 40 minutes]

Preparation of the top chip

Do the following for each silicon wafer:

1. Take the PDMS with the silicon wafer out of the oven.
2. Prepare the label for each chip you are cutting onto a piece of tape.
3. Check if PDMS is gone under the aluminum foil.
4. Carefully remove the silicon wafer and aluminum foil from the Petri dish.
5. Mark the boundary and the chip number with the permanent marker on the PDMS.
6. Carefully peel off the aluminum foil from the PDMS and silicon wafer.

⚠ If you put too much pressure on the silicon wafer, it can break.

7. Carefully peel the PDMS of the silicon wafer, do a slight peel of the edge, and go around the silicon wafer.
8. Put the silicon wafer back in the Petri dish and close it.
9. Quickly cover the part that was in contact with the silicon wafer (where the channels are) with magic tape.
10. Cut the chips by doing the following:
    - Cut one chip through the magic tape.
    - Clean the side and back of the chip with tape.
    - Remove the tape from the top of the chip and clean this part with a new tape.
    - Tape the top of the chip.
    - Tape on top of the tape the label of the chip.
    - Store the chip in another rectangular Petri dish.

Step 8 [Time required 40 minutes]

Biopsy punch

Do the following for each chip:

1. Remove the tape and label from the chip.
2. Punch one hole at the end of each channel.

⚠ Make sure that the PDMS came out from the hole; otherwise, you will bind it shut again afterward.

3. Clean the sides, back and top of the chip with tape.
4. Tape the top and bottom of the chip.

5. Tape on top of the tape the label of the chip (on the side of the channels).
6. Store the chip in another rectangular Petri dish.

Step 9 [Time required 40 minutes]

Plasma Bonding

Do the following for 4 to 5 chips at a time:

1. Using the **old** plasma bounding machine:
   - i. Turn on the Plasma Cleaner and Flow meter.
   - ii. Open the oxygen bottle
   - iii. Take the plastic trade.
   - iv. Put a base and a chip with the channel side on the top, on the plastic trade.
   - v. Peal off the tape and place the trade in the plasma cleaner chamber.
   - vi. Check if the valve is at the initial position and turn on the vacuum pump.
   - vii. Wait approx. 3 min ($p < 320$ mtorr, need to be stable).
   - viii. Open the valve.
   - ix. Wait until pressure is stable ($650 < p < 725$ mtorr).
   - x. Set timer to 25 s and turn on the RF-field (start timer).
     - MED for PDMS-PDMS bonding
     - HI for PDMS-Galss bonding
   - xi. After 25s turn off the FR field, Plasma cleaner and vacuum pump.
   - xii. Slowly release the vacuum
   - ⚠ Too fast and your chip will fly around in the chamber!
   - xiii. Take out the chip.
   - xiv. Put the base on a rectangular Petri dish.
   - xv. Carefully bind the chip to the base.
   - xvi. Gently check the edges to see if they are bonded.
   - xvii. With a tweezer, put a piece of tape on the chip.
   - xviii. Put on top of the tape the label.
   - xix. Set the valve to the initial position.
   - xx. Turn on the vacuum chamber to generate a little vacuum.
   - xxi. Turn off the vacuum pump.
   - xxii. Close the oxygen bottle.
2. Using the **new** plasma bounding machine:
   - i. Turn on the Plasma Cleaner.
   - ii. Open the oxygen bottle
   - iii. Do a dry run before one with the chips.
   - iv. Take the plastic trade.
   - v. Put a base and a chip with the channel side on the top, on the plastic trade.
   - vi. Peal off the tape and place the trade in the plasma cleaner chamber.
   - vii. Set the following:
     - PDMS-Galss: 65% power, 8 sccm, 1 min
     - PDMS-PDMS: 50% power, 8 sccm, 1 min
   - viii. Start the process and wait until it ends.
   - ix. Take out the chip.
   - x. Put the base on a rectangular Petri dish.

xi. Carefully bind the chip to the base.
xii. Gently check the edges to see if they are bonded.
xiii. With a tweezer, put a piece of tape on the chip.
xiv. Put on top of the tape the label.
xv. Turn off the plasma cleaner.
xvi. Close the oxygen bottle.

3. Place the Petri dish with the chip in the $60°$ oven overnight.

Day 3

Step 10 [Time required 40 minutes]

Check the usability of the chips

1. Using the microscope ARTORG Zeiss Axio Imager to check each chip for the following:
   - collapsed channels.
   - Damaged separation wall.
   - Centred biopsy punch.

   ⚠ Be careful with the higher magnification that the objective doesn't touch the chip.
2. Discard the ones that are not adequate.

A.3 Protocol for the RBC Sample Preparation

RBC SAMPLE PREPARATION

Preparation of RBC suspended in a plasma like solution

Created by Aurelia Bucciarelli (aurelia.bucciarelli@unibe.ch) **on November 8, 2023**
Eddited by Aurelia Bucciarelli (aurelia.bucciarelli@unibe.ch) on July 03, 2024

Printed on the October 23, 2024

CARDIOVASCULAR ENGINEERING

UNIVERSITY OF BERN

ARTORG CENTER BIOMEDICAL ENGINEERING RESEARCH

Protocol purpose:
Procedure to prepare fresh blood to use for the experiment in microfluidics chips.

PROTOCOL

Day 1

Step 1 [Time required 40 minutes]

Preparation of Solution 0, 1, 2 and 3

Work with gloves and a lab coat!

1. Calculate how much of each Solution you need with the amount of blood you ordered (Normally, for one experiment, 10x10ml Sol. 0 or more).
2. Prepare the following Solutions (quantity for 10 ml):
   Solution 0: 10ml PBS + 100mg BSA
   Solution 1: 10ml PBS + 400mg BSA + 10mg Glucose
   Solution 2: 1ml 10xPBS + 400mg BSA + 10mg Glucose + 9ml Optiprep
   Solution 3: 6.5ml **Solution 1** + 3.5ml **Solution 2**
3. All the volume measurements are done with the pipettes.
4. All the weight measurements are on a precise scale.
5. Store the solution in the fridge ($4°$) with the following label:
   - Your name
   - Date
   - Solution number (on the lid)
   - General information on what is inside (on the side).

Day 2

Step 2 [Time required 120 minutes]

Blood preparation

Work with gloves, a lab coat, and under the chemical flow hood!

1. Filter **all** the Solutions you need and label them with an F (filter of 0.2μm).
2. Prepare all the material under the chemical hood (disinfected with ethanol before putting it in the hood).
3. Take 5 ml of blood and put it in a 15 ml tube (use **our** 1000 ml pipette), mark it as B0.
4. Centrifugate the B0 at 1.8 **RCF** for 10 min.
5. Remove the supernatant.

MATERIALS

1st Day

50 ml Tubes | Permanent Marker | Pipettes | Disposable container | Measuring spoons

2nd Day

15 ml Tubes | 50 ml Tubes | Syringes | Syringes Fitlers ($0.2\,\mu m$) | "Blood" pipette | Permanent Marker

CHEMICALS

1st Day

PBS Sigma P4417 | PBS 10x Sigma P4417 | Glucose Sigma G7021 | Optiprep Sigma D1556

2nd Day

Ethanol 70% | Distilled water | Solution 0 | Solution 3 | Blood

EQUIPMENT

1st Day

Precise scale | $4°C$ Fridge

2nd Day

Chemical flow hood | Centrifuge | $4°C$ Fridge

6. Put 2x0.6 ml of the RBC (taken from the middle) in 9ml Solution 0 (use our 1000ml pipette) and mark it as B1.
7. Mix gently for 10 min.
8. Centrifugate B1 at 2.5 **RCF** for 10 min.
9. Remove the supernatant.
10. Prepare the final hematocrit for the experiment (0.5ml RBCs for each tube, use **our** 1000ml pipette):
    - **Ht=2.5%:** 9.75ml Solution 3 + 0.25ml RBC
    - **Ht=5%:** 9.5ml Solution 3 + 0.5ml RBC
    - **Ht=10%:** 9ml Solution 3 + 1ml RBC
    - **Ht=20%:** 8ml Solution 3 + 2ml RBC
    - **Ht=30%:** 7ml Solution 3 + 3ml RBC
11. Mix gently for 10 min.
12. Store in the fridge (4°) until use.

⚠ You should use it on the same day!

13. Everything that was in contact with the blood is trashed in the Biotrash but before filled with 70% ethanol.
14. Clean the work surface and put on the UV light.

DANGERS

Chemicals
Phisical
Environmental

PROTECTIVE GEAR

Gloves | Lab coat

WARNINGS

Blood
Working with **untested** blood.
You need a **Hepatitis B** vaccination.

PEOPLE TO CONTAT

Sabine Schneider (OOC) for lab question.
Ina Krebber, Interregionale Blutspende SRK AG, for the blood .

NOTES

A.4 Protocol for the Dynamic Pericyte Experiments

PROTOCOL FOR THE DYNAMIC PERICYTE EXPERIMENTS

This is the procedure after the chip production and blood preparation

Created by Aurelia Bucciarelli (aurelia.bucciarelli@unibe.ch) **on November 8, 2023**
Eddited by Aurelia Bucciarelli (aurelia.bucciarelli@unibe.ch) on July 03, 2024

Printed on the October 23, 2024

CARDIOVASCULAR ENGINEERING
UNIVERSITY OF BERN
ARTORG CENTER BIOMEDICAL ENGINEERING RESEARCH

Protocol purpose:
Set up the experiment under the microscope to observe the influence of pericyte on the RBC distribution and velocity.

PROTOCOL

Preparation

Before starting, you need to have printed enough copies of the *Protocol Experiment List* and the section graph.

Step 1 [Time required 20 minutes]

Set-up preparation

1. Take off the Environmental Chamber lid.
⚠ First, detach the cable for the light.
2. Secure the syringes holder to the table.
3. Cover all the surfaces around the sample holder with kitchen paper.
4. Prepare the flashlight on the side of the microscope.
5. Connect the pressure pump (LineUp Flow EZ component) to the compressed air of the building.
6. Connect the pressure pump (LineUp Flow EZ component) to the link component (LineUp LINK).
7. Connect the link component (LineUp LINK) to the electricity.
8. Connect the link component (LineUp LINK) to the microscope TTL signal.
9. Connect the link component (LineUp LINK) to the flashlight through TTL signal.
10. Fill the Falcon tube with H_2O and connect it to the pressure pump with the P-CAP.
11. Connect the lab laptop to the electricity and the pressure pump.
12. Place the reservoir syringes for the blood in the holder
13. Turn on the microscope from the multiport connector.
14. Turn on the microscope computer.
15. Start the microscope program (NIS Element) with the following setting:
    - Your account name
    - Your password
    - Only one camera: Hamamatsu.
16. Connect the external SSD to the microscope computer.

Step 2 [Time required 60 minutes]

Microfluidics chip and microscope preparation

Work with glows!

MATERIAL

Kitchen paper | Power strip | Glass slides | Microfluidics chip | Magic Tape | Syringe reservoir for inlet | CVE pipette | Syringe reservoir for outlet | Section graph | Protocol Experiment List

CHEMICALS

Solution 0 | H_2O | Isopropanol | RBC suspended in plasma-like solution

EQUIPMENT

Inverted microscope with LWD objective | Laptop with Matlab and Fluigent plug-in | Fluigent LineUp Flow EZ™ 0-7000 mbar | Fluigent LineUp™ LINK | Syringe holder | Flashlight activated with TTL signal | External SSD | Vacuum chamber

DANGERS

Chemicals
Phisical
Environmental

PROTECTIVE GEAR

Gloves

1. Place the microfluidics chips on a glass slide.
2. Insert them in the microscope and focus on one inlet hole with an x4 objective.
3. For the microscope:
   - Flash 4.0 for the window in the program.
   - DiaLED for the light.
   - Intensity dial is on the side on the table (CoolLED), between 0.2-1, not more!
   - If it is still too dark, open the condenser on the microscope (on top of your chip).

   ⚠ Needs to be re-positioned to the initial position after the experiment.
   - For the ROI, use the 512x512 px of the program.
   - The frame rate should be near 395 fr/s (framepersec).
   - Check that the norm. auto exposure is set to 1 frame.
4. Check with the 10x objective if the chip is still good.
5. Try to align the chip so that the channels are parallel to the frame.
6. Repeat for all the chips.
7. Take all the chips to a vacuum chamber.
8. Place a big droplet of Solution 0 on top of the chip that covers all the inlets and outlets.
9. Start the vacuum and leave it for approx. 25 min.
10. Insert the most promising chip in the microscope.
11. Cover the other chips so that the droplet doesn't evaporate.
12. Attach the chip to the glass with tape and also to the microscope.
13. Connect the pressure pump to the pericyte intel.
14. Start the pressure pump manually to get a droplet of fluid at the end of the tube and attach it to the inlet of the pericyte channel.
15. Fill the reservoir syringes with solution 0 and Blood.

    ⚠ The end of the tube attached to the syringe should be higher than the reservoir syringe.
16. Slowly higher the syringe to have a small drop at the end of the tube and attach them to the network's inlet and outlet (no bubbles).
17. Place the syringes in the syringes holder.

    ⚠ The outlet reservoir syringe should be placed lower than the inlet reservoir syringe.
18. Remove the water droplet from the chip and focus the chip.
19. Position the flashlight in the flashlight holder and near the microfluidic chip.
20. Set the microscope to 10x.
21. Check that you are still using:
    - For the ROI, use the 512x512 px of the program.
    - The frame rate should be near 395 fr/s.
    - Check that the norm. auto exposure is set to 1 frame.
22. Position the flashlight.
23. To check if the flashlight is positioned correctly:
    - In the Microscope program go to **Aquire** → **fast time laps**.
    - Set the number of frames to max 1000.
    - Set the saving location and name (*Test_Flash*).
    - Save the changes
    - On the laptop with Matlab, run the "initializing set up" part of the script: *preicyte_Au.m*.
    - Run the following: *Link1.triggerTTL(1)*; in the command windows

WARNINGS

Blood
Working with **untested** blood.
You need a **Hepatitis B** vaccination.

PEOPLE TO CONTACT

Fabian Blank (DBMR) for the introduction to the microscope and possible questions.

NOTES

and check visually if the flash worked.
- If so, start the fast time laps and quickly run again *Link1.triggerTTL(1);*.
- Check in the microscope recording if the flash was registered.
- If yes, you are ready for the experiment.
- If no, try to move the flashlight (spatially and change the angle) until you see the flash in the video.

24. You are ready to start the experiment.

Experiment

Step 3 [Time required 300 minutes]

Pericyte activation

1. Focus the RBC on the intel channel #3-5 or #54-56.

⚠ The RBC should be as dark as possible.

2. To check for the right velocity of the RBCs:
   - In the Microscope program go to **Aquire** → **fast time laps**.
   - Set the number of frames to 10 frames (nframes).
   - Set the saving location and name (*Test_Velocity*).
   - Save the changes
   - In the first frame of the resulting video, select a RBC and note the x coordinate in px of the center.
   - On the last frame, do the same for the same RBC.
   - The displacement (Δx) in px should be:

$$\Delta x = \frac{u[\mu m/s]}{\text{cal}[\mu m/px]} \cdot \frac{10[fr]-1}{395[fr/s]}$$

   cal $= 0.65[\mu m/px]$ for 20x objectiv.
   For a $u = 0.4mm/s$, Δx should be $15 - 17px$.
   - Reposition the inlet reservoir syringe to get the wanted velocity.
3. Use the XY position saved for each section to position the ROI of the microscope.
4. Start the experiment by running the Matlab section starting on line 48.
5. Check that all the settings are corrected and press start.
6. Start the Job in the microscope program.
7. After the Job is finished and the frames are saved, check for the following:
   i. The video started before the pressure pump. If not:
      - Increase the delay in the setting of the pressure pump.
   ii. The flash is visible in the video. If not:
      - Add frames if the microscope stops too early.
      - Change the position of the flashlight.
8. Note on the *Protocol Experiment List*: Activation pressure [mbar], Reservoirs height von table [cm], Experiment information (pressure pump file: number, section and repetition) and Microscope file name and Notes.
9. Do the same (points 3 to 8) for the number of wanted repletion for each section:
   i. After 5 repetitions per section.
   ii. Replace the blood with solution 0.
   iii. Let it run until the system is cleaned (to ensure less RBCs sedimentation).
   iv. Replace solution 0 with blood.
   v. Wait a bit and check the velocity (point 2).

vi. Do the next 5 repetitions per section.
vii. Repeat until you are finished with the experiment.

Clean up after experiment

Step 4 [Time required 30 minutes]

Microscope

1. Set the microscope objective to 4x.
2. Shut down the microscope and the microscope computer.
3. Lift the outlet reservoir syringe to a similar height to the inlet syringe.
4. Lower the inlet reservoir syringe to a height lower than the chip and the outlet reservoir syringe.
5. Extract the tube of the inlet reservoir syringe from the chip.
6. Empty the inlet reservoir syringe in the trash.
7. Fill with Solution 0 the inlet reservoir syringe and empty it in the trash (use the plunger to get a strong jet/washout).
8. Fill with H_2O the inlet reservoir syringe and empty it in the trash (use the plunger to get a strong jet/washout).
9. Extract the tube of the outlet reservoir syringe from the chip.
10. Fill with H_2O the outlet reservoir syringe and empty it in the trash (use the plunger to get a strong jet/washout).
11. Store them in the Experiment box.
12. Shut down the laptop.
13. Make sure the pressure of the pressure pump is 0mbar.
14. Extract the tube of the pressure pump from the chip.
15. Empty the pressure pump reservoir using the pressure.
16. Shut down the pressure pump
17. Close the valve from the compressed air hose and detach the pressure pump tube.
18. Pack the pressure pump with the tube where you had H_2O on top to dray.
19. Pack the flashlight and its holder in his box.
20. Remove all the kitchen paper and throw it in the trash.
21. Remove the chip from the microscope and throw it in the trash.
22. Detach the syringes holders.
23. Clean all the surfaces used with isopropanol.
24. Put back on the Environmental Chamber.
25. Throw the non-used chips.
26. Pack all the rest of the material in the corresponding box and trash non-used fluids (if also a blood vial, take it separately to the bio lab).

⚠ Take the trash to the Bio lab in U1 and throw it in the bio bin (blue bin with yellow lid) with the trash bag. If a blood vial is still full, add ethanol 70% and trash it.

27. Replace the trash bag in the microscope room.
28. Transport all the lab material to his respective place.
29. Take back to the office the laptop, *Experiment protocol list* and SSD.

A.5 Protocol for the Endothelial Cell Culture

CELL CULTURE

This is the full procedure

Created by Aurelia Bucciarelli (aurelia.bucciarelli@unibe.ch) **on Mai 17, 2024**
Created by Anastasia Milusev (anastasia.milusev@unibe.ch) **on Mai 27, 2024**
Eddited by Aurelia Bucciarelli (aurelia.bucciarelli@unibe.ch) on July 03, 2024

Printed on the July 3, 2024

CARDIOVASCULAR ENGINEERING

UNIVERSITY OF BERN

ARTORG CENTER BIOMEDICAL ENGINEERING RESEARCH

Protocol purpose:
Culture and expansion of endothelial cells to be used for further experiments

PROTOCOL

Cell culture

In order to seed endothelial cells into a chip, the cells have to be expanded first in standard cell culture flasks for 3-5 days. For porcine arterial endothelial cells (PAEC), you will obtain 3-4 Mio. cells from a confluent T75 flask and 1.5-2 Mio. cells from a confluent T25 flask.

Concerning growth of PAEC: If you seed 0.3-0.4 Mio cells into a T75 flask, the flask will be confluent after 5-6 days. If you seed 1 Mio cells into a T75 flask, the flask will be confluent after 3-4 days. If you seed 0.5 Mio cells into a T25 flask, the flask will be confluent after 3-4 days.

Important: Do not leave cells confluent for too long (more than 1-2 days) as they will start to detach. Ideally, work with 80-90% confluent flasks.

Preparation of cell culture medium

Work in the cell culture lab under a laminar flow hood (Mu24 Room 346)!
Prepare medium in advance, reconstituted medium can be stored at 4°C for up to 1 month.

Step 1 [Time required 15 minutes]

Culture medium

1. Thaw 50 ml of heat-inactivated fetal bovine serum (FBS) and 5 ml of Penicillin/ Streptomycin (Pen/Strep) (-20°C freezer main lab 362 bottom right drawer) at 37°C in a water bath.
2. Start the laminar flow hood and work under the hood for all next steps.
3. Take one bottle of DMEM + Glutamax cell culture medium and remove 50 ml of medium into a falcon tube. Label the tube with initials, date and content.
4. Add 50 ml of thawed FBS and 5 ml of thawed Pen/Strep to the medium bottle. This makes reconstituted medium containing 10% FBS and 1% Pen/Strep which can be used for cell culture.
5. Label the medium bottle with initials, date and added supplements (10% FBS and 1% Pen/Strep).

MATERIAL

- T75 or T25 cell culture flasks
- Pipettes + tips
- Serological pipet + pipet boy
- frozen PAEC

SOLUTIONS

- DMEM Glutamax, Gibco 21885-025
- heat inactivated FBS, Sigma F7542
- Pen/Strep, Gibco 15140-122
- Growth factor, PromoCell C-39216

EQUIPMENT

- Incubator at 37°C
- Laminar flow hood
- Water bath

DANGERS

Chemicals
Physical
Environmental

PROTECTIVE GEAR

- Gloves
- Biolab coat

WARNINGS

Biochemical
PAEC are a primary cell line isolated from real pigs and should be handled with care, but they are not dangerous for humans.

Physical
-150°C material will burn your skin if you maintain contact for too long (more than a couple of seconds). Use protective gloves!

Thawing and plating of endothelial cells

Work in the cell culture lab under a laminar flow hood (Mu24 Room 346)!

Step 2 [Time required 45 minutes]

Seeding cells

1. Start the laminar flow hood.
2. Put reconstituted cell culture medium into the 37°C water bath to warm up (takes 15 min). For a T75 flask you need 10 ml of medium, for a T25 flask you need 5 ml of medium.
3. Label the cell culture flasks with cell type, initials and date.
4. Add the appropriate amount of warm medium to the cell culture flask.
5. Retrieve frozen PAEC from -150°C (freezer 528, tower 4, box labeled with "EC Anastasia"). Immediately thaw the cryovial in the water bath until a small chunk of ice remains.

⚠ Do not leave the cryovial at room temperature as thawing the contents slowly will damage the cells! If you have to wait until you can thaw the cryovial then put it on dry ice.

6. Pipette the contents of the cryovial into the cell culture flask containing medium. Tilt the flask to distribute the cell solution inside the medium.
7. Place the flask in the incubator and leave the cells to attach overnight.
8. The next day, change the medium to remove any leftover DMSO and add 1% growth factor to the fresh medium. (the freezing solution in the cryovial is supplemented with 10% DMSO to keep cells viable, but it's toxic to cells once thawed)
9. **Alternatively:** If you can't change the medium the next day:
   i. Add the contents of the cryovial to a 15 ml falcon tube containing 5 ml of warm medium.
   ii. Spin down the cells using a centrifuge (24°C, 1200rpm, 6 min, acceleration and brake set to 9)
   iii. Remove the medium (take care not to aspire the cell pellet!)
   iv. Resuspend with 1 ml of warm medium
   v. Add to a cell culture flask containing 9 ml of warm medium supplemented with 1% growth factor
   vi. Leave the flask in the incubator and change medium after 2 days as described below.
10. Change medium every second day (you can leave the cells 2 days without changing the medium if it's the weekend) and add fresh growth factor every time you change the medium. Do this until the cells are 80-90% confluent. If the cells are growing faster than expected, you can also change medium without adding growth factor.

PEOPLE TO CONTACT

Lab responsible form OOC for lab question.
Alain Despont from DBMR Rieben Lab for questions about cells and the second lab.

NOTES

A.6 Protocol for the Channel Surface Modification for Cell Coating

CHANNEL SURFACE MODIFICATION FOR CELL COATING

This is the full procedure

Created by Aurelia Bucciarelli (aurelia.bucciarelli@unibe.ch) on Mai 15, 2024
Eddited by Aurelia Bucciarelli (aurelia.bucciarelli@unibe.ch) on July 03, 2024

Printed on the December 15, 2024

CARDIOVASCULAR ENGINEERING

UNIVERSITY OF BERN

ARTORG CENTER BIOMEDICAL ENGINEERING RESEARCH

Protocol purpose:
PDMS surface coating

PROTOCOL

Preparation of chemicals

APTES and Glutaraldehyde can be prepare the day before.

Step 1 [Time required 45 minutes]

Chemicals

Work with gloves under a flow hood!

1. APTES 5% final concentration:
   - Dilute APTES (A3648 Sigma) 1:20 in dH_2O.
2. Glutaraldehyde 0.1% final concentration:
   - Dilute Glutaraldehyde (G-6257 Sigma) 1:250 in dH_2O.
3. Fibronection 50μg/ml final concentration:
   - Dilute Fibronectin (1mg/ml stock solution FC010 Sigma) 1:20 in PBS.
4. Collagen-I 100μg/ml in 0.02M sterile Acetic.

Preparation of channels

Work in the PDMS production Lab until step 3. You need to have the chip produced following the Production of "Microfluidics chips protocol" until Step 8 and the cell culture is ready to be detached ("Cell culture protocol" until confluent cell layer).

Step 2 [Time required 45 minutes]

Plasma cleaner

Work with gloves!

1. Start the laminar flow for the flow hood.
2. Clean the surface with isopropanol.
3. Using the plasma bounding machine:
   i. Turn on the Plasma Cleaner.
   ii. Open the oxygen bottle
   iii. Do a dry run before one with the chips.
   iv. Take the plastic trade.
   v. Clean the microscope coverslip with air and isopropanol and place them on the plastic trade.
   vi. Position the clean chip on the side of the microscope coverslip.
   vii. Peal off the tape and place the trade in the plasma cleaner chamber.

MATERIAL

Petri dish | Pipette + tips | Syringe 3ml | PTFE tube 0.8x1.6mm (IDxOD) | Blunt needles for syringe

CHEMICALS

Isopropanol | MiliQ water | APTES (A3648 Sigma) | Glutaraldehyde 25% stock (G6257 Sigma) | Fibronectin 1mg/ml Stock (FC010 Sigma) | Collagen-I

EQUIPMENT

Oven | Plasma cleaner | Incubator at 37°C | Laminar flow hood

DANGERS

Chemicals
Physical
Environmental

PROTECTIVE GEAR

Gloves | Biolab coat

WARNINGS

Chemical
APTES and Glutaraldehyde are toxic!

Heat
The oven and the plasma cleaner generate heat and you can burn yourself.

viii. Set the following: PDMS-Galss: 65% power, 8 sccm, 1 min
ix. Start the process and wait until it ends.
x. Take out the chip.
xi. Carefully bind the chip to the coverslip.
xii. Gently check the edges to see if they are bonded.
xiii. Move the chip to a Petri dish.
xiv. With a tweezer, put a piece of tape on the chip.
xv. Put on top of the tape the label.
xvi. Turn off the plasma cleaner.
xvii. Close the oxygen bottle.

4. Place the Petri dish with the chip in the $60°$ oven for 30min.

Step 3 [Time required 15 minutes]

APTES coating

Work with gloves under the flow hood! The PTFE tubes and blunt needle should be washed and sterile.

1. Take out the chips from the oven and put them under the hood.
2. Using a syringe with a blunt needle and a PTFE tube, add APTES 5% to the chip channels.
3. Put them in under vacuum for 20 min.
4. Close the Petri dish and bring them to the other lab.

Coating of cahnnels

Work in the Bio lab (room 346) at Mu24 under a laminar flow hood! The PTFE tubes and blunt needle should be washed and sterile.

Step 4 [Time required 45 minutes]

Glutaraldehyde

1. Load MiliQ water in a syringe with a blunt needle and a PTFE tube.
2. Wash the channels and use the aspirator with a 200ul tip to aspirate what comes out the other side.
3. Load Glutaraldehyde in a syringe with a blunt needle and a PTFE tube.
4. Replace the water in the channels with Glutaraldehyde and use the aspirator with a 200ul tip to aspirate what comes out the other side.
5. Leave the Glutaraldehyde for 30 min at RT.

Step 5 [Time required 90 minutes]

Fibronectin

1. Load MiliQ water in a syringe with a blunt needle and a PTFE tube.
2. Wash the channels and use the aspirator with a 200ul tip to aspirate what comes out the other side.
3. Load fibronectin in a syringe with a blunt needle and a PTFE tube.
4. Replace the water in the channels with fibronectin and use the aspirator with a 200ul tip to aspirate what comes out the other side.
5. Leave the fibronectin for 60 min at $37°$ in the incubator. item Load MiliQ water in a syringe with a blunt needle and a PTFE tube.
6. Wash the channels and use the aspirator with a 200ul tip to aspirate what comes out the other side.

PEOPLE TO CONTACT

Lab responsible from OOC for the PDMS lab question.
Alain Despont from DBMR Rieben Lab for questions about cells and the second lab.

NOTES

7. If no collagen is needed, you can change the fibronectin with MillQ water, and the channel can be stored at 4° for up to 7 days.

Step 6 [Time required 120 minutes]

Colagen

This step is optional.

1. Load collagen in a syringe with a blunt needle and a PTFE tube.
2. Replace the fibronectin in the channels with collagen and use the aspirator with a 200ul tip to aspirate what comes out the other side.
3. Leave the collagen for 90 min at 37° in the incubator under laminar flow.
4. You can change the collagen with MillQ water, and the channel can be stored at 4° for up to 7 days.

A.7 Protocol for the Endothelial Cell Seeding in Microfluidics Channels

ENDOTHELIAL CELL SEEDING IN MICROFLUIDICS CHANNELS

CARDIOVASCULAR ENGINEERING

UNIVERSITY OF BERN

ARTORG CENTER BIOMEDICAL ENGINEERING RESEARCH

This is the full procedure

Created by Aurelia Bucciarelli (aurelia.bucciarelli@unibe.ch) on Mai 17, 2024
Created by Anastasia Milusev (anastasia.milusev@unibe.ch) on Mai 28, 2024
Eddited by Aurelia Bucciarelli (aurelia.bucciarelli@unibe.ch) on July 03, 2024

Printed on the July 3, 2024

Protocol purpose:
Culture of endothelial cell in microfluidic channels

PROTOCOL

Seeding of endothelial cells in a microfluidic channel

To start the procedure, you need to have the channel coated with fibronectin following the "Channel coating" protocol as well as a confluent flask of endothelial cells prepared according to the protocol "Cell culture".

Step 1 [Time required 30 minutes]

Detaching endothelial cells

Work in a laminar flow hood with gloves and a bio-lab coat!

1. Start the laminar flow hood.
2. Warm up PBS, reconstituted cell culture medium, and Trypsin in the water bath at 37°C (cr. 15 min).
3. If you have more than one cell culture flask, work sequentially and not with all flasks at once.
4. Remove the medium from the flask by tilting the flask to one corner and using a glass pipette attached to the suction pump to suction off the medium. Make sure not to scratch over the bottom of the flask (where cells are attached) to avoid removing cells.
5. Add 10 ml of PBS to the flask (take care to pipette onto the wall of the flask and not onto the cell layer) to wash off any leftover medium. This is necessary to remove any FBS from the medium left on the cells, which inhibits the activity of trypsin used to detach cells.
6. Remove the PBS and add 2 ml of trypsin (for T75 flask) or 1 ml of trypsin (for T25 flask).
7. Place the flask in the incubator for 3-4 min for the trypsin to detach the cells. After 3-4 min, tap the flask strongly and check that the cells have detached. If many cells are still attached, leave the flask in the incubator for another 1-2 min. **Important:** Do not incubate trypsin for longer than 6-7 min as this will also digest and damage the endothelial cells!
8. Add 8 ml (for T75 flask) or 4 ml (for T25 flask) of warm medium to the flask containing trypsin to inactivate the trypsin.
9. Tilt the flask to one corner and wash the bottom of the flask with the cell suspension to detach all cells.
10. Add the cell suspension to a falcon tube and check the flask to make sure only a few cells are left inside. If there are many cells left, then wash them one more time with a warm medium.
11. Centrifuge at 24°C, 1200 rpm for 6 min with acceleration and brake set to 9. Make sure to balance the centrifuge!

MATERIAL

Petri dish | Falcon tubes, Eppendorf tubes | Pipette + tips | Syringe 3ml | PTFE tube 0.8x1.6mm(IDxOD), sterilized | Blunt needles for syringe, sterilized | Neubauer cell counting chamber

SOLUTIONS

PBS | EDTA-Trypsin 0,5% solution, Gibco 25300-054 | reconst. DMEM Glutamax, Gibco 21885-025 | 0.04% Trypan blue, Sigma T8154-20ML | Dextran 40% solution, Sigma 31390-100G | 37% formaldehyde, Sigma 252549-500ML | BSA, Sigma A7030-100G | PBS-3% BSA solution | Tween 20, AppliChem A4974,0250 | PBS-1% BSA-0.05% Tween 20 solution | Rat anti pig CD31, RD Systems MAB33871 | anti F-Actin, Cytoskeleton PHDH1 | Goat anti Rat AF488, Invitrogen A11006 | DAPI nuclear stain, 1mg stock solution

EQUIPMENT

Water bath | Incubator at 37°C | Light microscope | Centrifuge | Laser scanning microscope | Syringe pump, Harvard Instruments 70-2212

DANGERS

12. In the meantime, prepare medium with 8% dextran used for seeding the cells into the microfluidic chip.
    - Dilute the 40% dextran solution 1:5 in medium (total amount of medium ca. 10 ml).

    ⚠ Dextran is viscous, pipet slowly to prevent it from sticking to the pipette.
    - Vortex the mixture and place it in the water bath to keep it warm.
13. After centrifugation, remove the medium on top of the cell pellet (take care not to aspirate the pellet!) using a glass pipette.
14. Re-suspend the cell pellet with 1 ml of medium containing 8% dextran.

⚠ Make sure to mix the suspension well to avoid cell clumps. The cells can now be counted.

Cells in suspension can be kept in suspension for up to 1h.

Step 2 [Time required 15 minutes]

Counting endothelial cells

Work in a laminar flow hood with gloves and a bio-lab coat!

1. Take a Neubauer cell counting chamber and place it inside the flow hood.
2. Pipette 90 μl of trypan blue into a 0.5 ml sterile Eppendorf tube.
3. Add 10 μl of the cell suspension from Step 1.14 to the trypan blue.

⚠ Make sure to mix the cell suspension very well to avoid clumps and uneven cell distribution. Mix the trypan blue-cell suspension by pipetting up and down 5 times.

4. Add 10 μl of this suspension to the Neubauer chamber.
5. Using the light microscope, count all the cells in two random 4x4 squares (use a hand counter).

⚠ Cells that appear blue have been stained by trypan blue and are dead; don't count these cells!

6. Calculate the cell concentration (CC):
   $CC = NC/2 \cdot 10^5 \cdot DF$
   NC is the number of cells counted in both squares, DF is the dilution factor (if you re-suspended the cell pellet in 1 ml of medium $DF = 1$)

Step 3 [Time required 45 minutes]

Seeding cells into microfluidic chip

Work in a laminar flow hood with gloves and a bio-lab coat!

1. Using a 3 ml syringe with a blunt needle and a PTFE tube, fill the chip with medium containing 8% dextran and put it in the incubator for 15 min before loading cells.
2. Adjust the cell suspension to 4 Mio/ml using medium with 8% dextran.
3. Using a 3 ml syringe with a blunt needle and a PTFE tube inject the cell suspension into the microfluidic chip. Check under the light microscope to see if some cells are in the channel.
4. Place chips into a petri dish and submerge the chips in warm medium (without dextran) to ensure sufficient nutrient exchange. Put the chips in the incubator and leave them overnight for the endothelial cells to attach.
5. **Alternatively:** Seed the cells under flow using a syringe pump
   i. Inject the cell suspension into the chip as described above.
   ii. Prepare a syringe filled with warm medium (without dextran) and attach 50 cm of sterile PTFE tubing to the syringe.

Chemicals
Physical
Environmental

PROTECTIVE GEAR

Gloves | Biolab coat

WARNINGS

Chemical
Trypsin and Trypan blue can damage skin, if you were directly exposed wash the area immediately with water.

Chemical
Formaldehyde is toxic, work under a chemical fume hood when using the undiluted stock solution. Formaldehyde is also toxic for skin, if you were directly exposed wash the area immediately with water. Diluted 4% formaldehyde is more harmless, you can work on a normal bench.

PEOPLE TO CONTACT

Alain Despont from DBMR Rieben Lab for questions about cells and the second lab.

NOTES

iii. Aspirate 0.3 μl of cell suspension into the tube; this will only fill the tubing with cell suspension, leaving a normal medium in the syringe.

⚠ Make sure to avoid bubbles!

iv. Place the syringe pup beside the incubator.

v. Set the syringe pump to 1.25 μl/min flow and secure the syringe to the pump using tape.

vi. Place the chip into the incubator.

vii. Start the pump, and as soon as a small drop of medium accumulates at the tip of the tubing, connect the tubing to the inlet of the chip.

⚠ Make sure that the biggest part of the tubing is inside the incubator to maintain the temperature.

viii. Run the pump overnight.

6. The next day check the chips under the light microscope, there should be one layer of attached endothelial cells along the entire channel.

Visualizing endothelial cells

To look at the endothelial cells inside the microfluidic chip, they need to be stained by immunofluorescence and visualized with a laser scanning microscope.

Step 4 [Time required 30 minutes]

Fixing endothelial cells

1. Using a 1 ml syringe with a blunt needle and a PTFE tube mounted into a syringe pump set to 1.25 μl/min flow, wash the channels with room temperature PBS for 5 min.

⚠ For all next steps, flush the chip only with the syringe pump and not by hand; high flow will detach the cells!

2. Prepare a 4% formaldehyde solution from the 37% stock solution. Dilute the stock solution 1:9.25 in PBS. Around 3-5 ml is enough to fix 10 channels.
3. Empty the PBS from the 1 ml syringe and fill it with 4% formaldehyde solution.
4. Connect the syringe with a blunt needle and a PTFE tube mounted into a syringe pump set to 1.25 μl/min flow and perfuse the channel for 15 min.

⚠ Do not fix the cells for more than 15 min, as this will damage them.

5. Empty the formaldehyde solution from the 1 ml syringe, wash it with some PBS, and fill it with PBS.
6. Connect the syringe with a blunt needle and a PTFE tube mounted into a syringe pump set to 1.25 μl/min flow and wash the channel for 10 min with PBS.
7. At this point, if you can't continue with the staining immediately, the chip can be stored submerged in PBS at 4°C for up to 3 days. Do not store the chip longer, as cells will start to detach after more than 3 days.
8. If you want to continue with the staining, go to the next section.

Step 5 [Time required 90 minutes]

Staining endothelial cells, primary antibodies

You need to perform both steps 5 and 6 together (2 days of work). Staining can be performed on the bench, it does not have to be in a

laminar flow hood.
⚠The PBS-3%BSA and PBS-1%BSA-0.05%Tween solution should be prepared in advance (the day before) to gain time on the day of staining.

1. Prepare PBS-3%BSA (block the fixed endothelial cells): For 10 ml of PBS weigh out 300 mg BSA (kept at 4°C in lab 361) into a falcon tube using a scale. Add 10 ml of PBS and mix well to dissolve the BSA.
2. Prepare PBS-1%BSA-0.05%Tween 20: From the PBS-3%BSA take one 1 ml and add it to 2 ml of PBS. To this, add 0.05%Tween 20 (chemical cabinet next to chemical hood in lab 362) and vortex to mix. Keep both solutions at 4°C; they can be stored for up to 1 month.
3. Load 200 μl PBS-3%BSA in a 1 ml syringe connected to a blunt needle and a PTFE tube.
4. Mount the syringe into a syringe pump set to 1.25 μl/min
5. Wash the chip for 15 min.
6. Disconnect the tubing and leave a drop of PBS-3%BSA on the chip.
7. Incubate static for another 45 min (total blocking time = 1h).
8. Prepare the primary antibody solution, per chip you need 250 μl primary antibody solution:
   i. Pipette an appropriate amount of PBS-1%BSA-0.05%Tween into an Eppendorf tube on ice.
   ii. Add Rat anti-pig CD31 (diluted 1:100, stored at -20°C in lab 362) and anti-F-Actin (diluted 1:200, stored at -20°C in lab 362) to the solution,
   iii. vortex briefly to mix.
   ⚠ Turn off the light in the lab while working with this antibody! F-Actin is directly labeled; don't expose the antibody solution to direct light to avoid bleaching the fluorophore.
9. Load the primary antibody solution into a 1 ml syringe connected to a blunt needle and a PTFE tube.
10. Mount the syringe into a syringe pump set to 1.25 μl/min.
11. Perfuse the chips for 15 min.
12. Disconnect the tubing and leave a drop of primary antibody solution on the chip.
13. Incubate the chips overnight at 4°C in the dark.

Step 6 [Time required 120 minutes]

Staining endothelial cells, secondary antibodies

Staining can be performed on the bench, it does not have to be in a laminar flow hood.

1. Wash the chips for 10 min with PBS using a 1 ml syringe connected to a blunt needle and a PTFE tube mounted into a syringe pump set to 1.25 μl/min (this removes any unbound primary antibody).
2. Prepare the secondary antibody solution, per chip you need 250 μl secondary antibody solution:
   i. Pipette an appropriate amount of PBS-1%BSA-0.05%Tween into an Eppendorf tube on ice.
   ii. Add Goat anti-Rat AlexaFluor488 (diluted 1:500, stored at 4°C in lab 361) and DAPI (diluted 1:1000, nuclear stain, stored at 4°C in lab 361).
   iii. Vortex briefly to mix.
   ⚠ Turn off the light in the lab while working with this antibody! Secondary antibodies are labeled with a fluorophore; don't ex-

pose the antibody solution to direct light to avoid bleaching the fluorophore.

3. Load the secondary antibody solution into a 1 ml syringe connected to a blunt needle and a PTFE tube.
4. Mount the syringe into a syringe pump set to 1.25 μl/min.
5. Perfuse the chips for 15 min.
6. Disconnect the tubing and leave a drop of secondary antibody solution on the chip.
7. Incubate the chip for another 75 min in the dark at room temperature (total incubation time = 90 min, use alu to protect the chips).
8. Wash the chips for 10 min with PBS using a 1 ml syringe connected to a blunt needle and a PTFE tube mounted into a syringe pump set to 1.25 μl/min (this removes any unbound secondary antibody).
9. Leave a drop of PBS on the chips to avoid drying out.
10. You are ready to image the chips with a laser scanning microscope.

Step 7 [Time required 60-90 minutes]

Imaging endothelial cells

Book the LSM980 Zeiss microscope (located in Mu24) on the online booking tool. Depending on the amount of channels imaging will take 60-120 min.

1. Set the channels you need for imaging:
   i. F488 (for CD31)
   ii. F555 (for F-Actin)
   iii. DAPI
2. Choose the option "best signal".
3. Set the following acquisition parameters:
   i. resolution: 1024x1024
   ii. scanning speed: 7
   iii. averaging: 2
   iv. laser power: 0.2-0.8% (depending on the strength of your signal)
   v. gain: 500-650
4. Acquire images of both the top and the bottom of the channel, both should be covered in a layer of endothelial cells.
5. Save images as .czi.
6. Acquire a z-stack:
   i. resolution 1024x1024
   ii. scanning speed: 9
   iii. choose the first and last slice (should span 30-50μm)
7. Start the acquisition (10-20 min).
8. Save images as .czi.
9. Shout down the microscope and fill the manual.
10. Images and the z-stack can be visualized with Fiji.

Appendix B

3D Printing of Circular Networks

B.1 Introduction

At the beginning of the project described in Chapter 4, we also wanted to evaluate the feasibility of fabricating capillary networks with round channels at dimensions below 10 μm. To this end, we employed a high-resolution 3D printer utilizing two-photon polymerization, an advanced additive manufacturing technique capable of achieving resolutions below 1 μm^3 and producing circular microchannels. This method involves patterning the desired design into IP photoresists, which are negative-tone cross-linking polymers developed by Nanoscribe GmbH. These photoresists can be tailored to meet specific requirements, such as submicron feature resolution, overhanging structures, optical-quality surfaces, high-speed mesoscale fabrication, biocompatibility, or high refractive index.

The 3D printing process is conducted in direct immersion mode, with the objective tip in constant contact with the IP photoresist. While the objective remains stationary, the positioning of the base with the photoresist is controlled by a piezoelectric unit. Galvanometric MEMS mirrors scan the xy-plane, enabling movement within a 200 μm radius that defines the printing area, which can be printed without moving the stage. For our setup, which used a 25x objective and a writing speed of 50 m/s, the spatial resolution achieved was approximately $0.3 \times 0.3 \times 2\,\mu m^3$. If the object exceeds the printing area, it must be divided into multiple blocks. Each block is sequentially printed: the piezoelectric stage moves to the designated xy position, and the galvanometric mirrors, combined with the piezoelectric z stage, print the first corresponding block. After one block is complete, the stage shifts to the next position and the process repeats. Due to the system's high sensitivity, printing must be performed in a clean room, free from UV light.

This technique theoretically allows for the production of round microchannels with extremely small dimensions. However, as it will be discussed in Section B.3, despite numerous attempts, we were unable to fabricate the desired channels successfully.

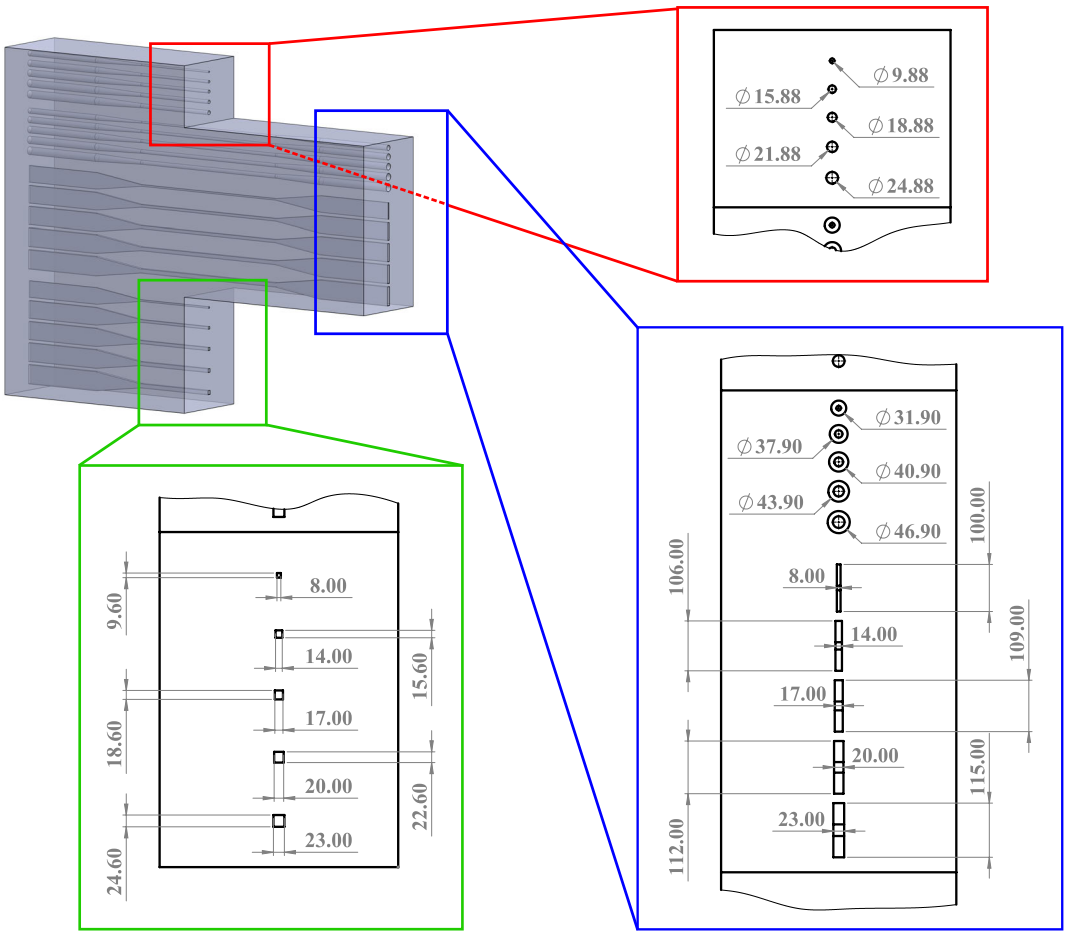

Figure B.1: Design of the 3D printed part with the corresponding dimensions.

B.2 Material and Methods

B.2.1 Design

We designed a microfluidic chip to evaluate the feasibility and the limitations of the 3D printer. The chip, shown in Fig. B.1, is divided into two sections: one with rectangular channels and another with round channels. The primary goal was to print round channels to create a more *in vivo*-like structure while simultaneously assessing whether there were differences in performance between rectangular and round channels. This dual design allowed us to compare the two geometries directly.

Each channel comprises a larger inlet/outlet section and a smaller central section. To ensure that the smallest features could be printed accurately, we doubled the number of channels and cut half of them vertically in the center for easy inspection.

The rectangular channels feature inlet/outlet dimensions of $100\times8\,\mu m^2$, $106\times14\,\mu m^2$, $109\times17\,\mu m^2$, $112\times20\,\mu m^2$, and $115\times23\,\mu m^2$ (Fig. B.1, bottom blue square). Their central sections measure $9.6\times8\,\mu m^2$, $15.6\times14\,\mu m^2$, $18.6\times17\,\mu m^2$, $22.6\times20\,\mu m^2$, and $24.6\times23\,\mu m^2$ respectively (Fig. B.1, green square).

The circular channels have inlet/outlet diameters of $31.90\,\mu m$, $37.90\,\mu m$, $40.90\,\mu m$, $43.90\,\mu m$, and $46.90\,\mu m$ (Fig. B.1, top blue square). Their central sections have diame-

ters of 9.88 μm, 15.88 μm, 18.88 μm, 21.88 μm, and 24.88 μm respectively (Fig. B.1, red square).

The length of the inlet/outlet channels is 500 μm, the length of the central section is 1000 μm, and these are connected by a linear tapering of length 334 μm.

B.2.2 Production

The fabrication process comprises two main steps: 3D printing using a two-photon polymerization technique with a high-resolution 3D printer (Photonic Professional GT, Nanoscribe GmbH, Germany) and a development process to finalize the structure.

3D Printing Process

For the printing, an indium tin oxide (ITO)-coated glass slide is used as the base. The IP-S photoresist (Nanoscribe GmbH, Germany) was selected due to its biocompatibility, non-cytotoxic nature, smooth surface finish, and optical-quality surface roughness and shape accuracy. A droplet of IP-S is placed on the ITO-coated glass slide, which is then mounted onto the holder of the Nanoscribe printer, equipped with a 25x objective (LCI Plan-Neofluar 25/0.8 Imm Korr DIC M27, Zeiss, Germany). The interface between the glass slide and the IP-S is then located based on the refractive index difference.

The printing settings are configured using the Describe software (Nanoscribe GmbH, Germany). The STL file of the design is loaded into the software. Since the design exceeds the printable area, it is divided into smaller blocks. Two block shapes were tested: hexagonal blocks (fitted within $200 \times 190 \times 250\,\mu m^3$) and square blocks ($200 \times 200 \times 140\,\mu m^3$), with the square blocks yielding better results.

To minimize shadowing effects at block edges, a shear angle of 13° in the z-direction is applied. Additionally, a block overlap of 2 μm is set to reinforce adhesion at the block boundaries. A scaffolding technique is employed within the bulk of the structure to reduce writing time, with the shell set to a wall thickness of 18 μm. A triangular support structure with a 20 μm spacing between planes and a scaffolding wall thickness of 3 μm is used.

The laser (65 mW) power settings are tailored for different structure parts: shell 50% or 70% power and internal scaffolding 42% or 70%. The total writing time for a single microfluidic structure is approximately 29 hours.

Development Process

After printing, the gals slide with the 3D printed object is carefully removed from the holder to be developed. The development process involves the following steps:

PGMEA Treatment The substrate is immersed in a beaker filled with PGMEA (Sigma-Aldrich, 484431) and placed on a stirring plate. Channels are oriented to face the flow direction to enhance residue removal. Gentle stirring is performed for 4, 8 or 12 hours to remove undeveloped photoresist. A test with also heating the PGMEA to 40° C and to 70° C to increase the solubility of the PI-s was tested.

Isopropanol Immersion: The developed structure is immersed in isopropanol for 2 hours in the same stirring configuration.

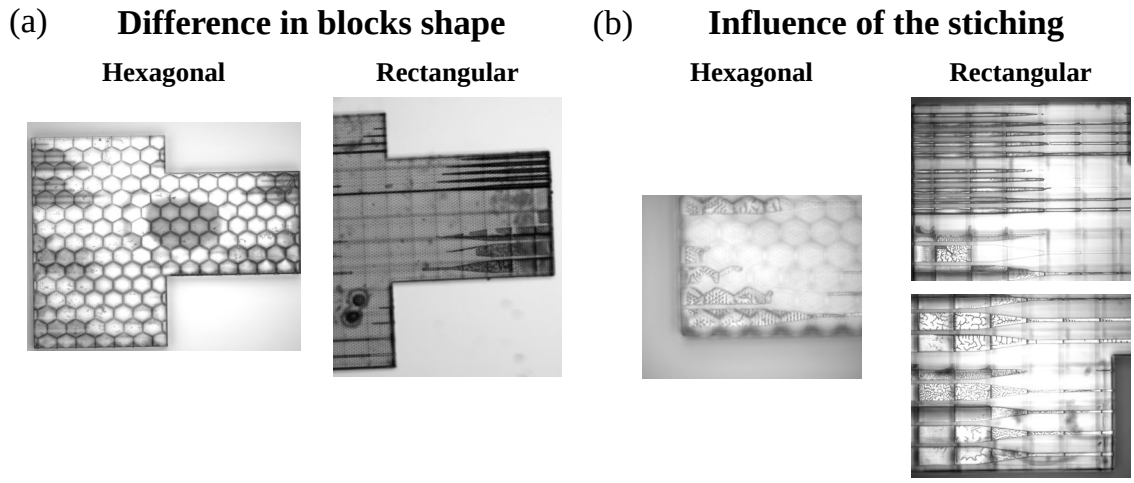

Figure B.2: Building blocks shape and influence of stitching. **a)** Bottom view of the chip showing the shapes of hexagonal and rectangular building blocks. **b)** Stitching effects are visible in the horizontal channels, where the edges of the building blocks are observable for both hexagonal and rectangular designs.

Drying: The substrate is dried naturally in a vertical position to prevent distortion.

To prevent premature hardening, the entire development process is conducted without exposing the photoresist to UV light. Finally, to harden the photoresist within the shell, the printed object is exposed to UV light for 15 minutes.

B.3 Results

The initial tests were conducted using the parameters outlined by Montinaro et al. (2018) as a reference. The building blocks utilized for the chip fabrication were hexagonal in shape, and the development process involved immersing the structures in PGMEA for 4 hours at room temperature, followed by 2 hours in isopropanol. As shown in Fig. B.2a, the hexagonal shapes are clearly visible on the bottom side of the chip and the interfaces between adjacent building blocks can also be observed within the channels (Fig. B.2b). Notably, the channels are not empty; they are still filled with hardened IP-S resin (Fig. B.2b).

To address this issue, we modified the building block shape to a rectangular configuration and increased the development time in PGMEA to 8 hours. As illustrated in Fig. B.2a, the rectangular building blocks are less visible than the hexagonal ones but are still visible as horizontal lines in Fig. B.2b. Additionally, the larger round channel in Fig. B.2a is entirely empty, indicating that the extended development time improved channel clearing. However, in the smaller channels still retained some material, demonstrating that these changes were insufficient to fully empty all channels. Despite further adjustments to development time and temperature, no significant improvement in channel production quality was observed.

Fig. B.3 provides a side view of the channels produced under four different fabrication conditions. The second setting (Fig. B.3b) looks different because no IP-S resin remained

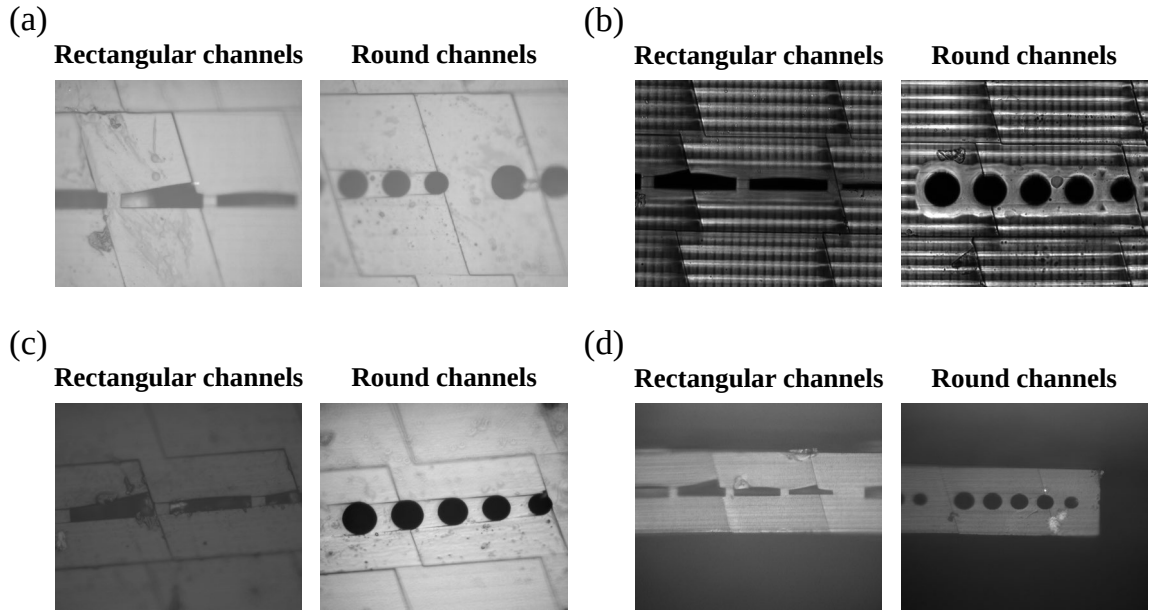

Figure B.3: Side view of the rectangular and round channels under different production settings. **a)** Hexagonal building block developed in PGMEA for 4 hours at room temperature and 2 hours in isopropanol. **b)** Rectangular building block developed in PGMEA for 8 hours at room temperature and 2 hours in isopropanol. **c)** Rectangular building block developed in PGMEA for 8 hours at 40° C and 2 hours in isopropanol. **d)** Rectangular building block developed in PGMEA for 12 hours at 70° C and 2 hours in isopropanol.

inside the shell due to the presence of a small crack in the shell. However, across all settings, issues with printing rectangular channels persisted. Channels positioned along stitching interfaces exhibited non-horizontal top walls, and even in channels not located on stitching lines, the top walls were not perfectly flat (Fig. B.3a). Although round channels displayed fewer imperfections, small irregularities were still apparent.

B.4 Discussion and Conclusion

Despite testing multiple fabrication settings, none yielded satisfactory results. In addition to the stitching-related issues, an alignment problem with the Nanoscribe machine was identified, further complicating the fabrication process. The time required to optimize the settings and produce an acceptable microfluidic chip far exceeded the initial expectations for this secondary project. Consequently, we decided to stop this line of research and refocus our efforts on the primary objective of the project.

Appendix C

Supplementary Material for Chapter 3 on Lingering RBCs

C.1 Supplementary Videos

The supplementary video in .avi format can be retrieved `https://doi.org/10.1016/j.bpj.2024.07.042`. All the videos are slowed down 5 times, at 79 frames per second (original recording at 395 fps).

Supplemental video S1: Recorded video of the RBC flowing through the bifurcation for a feeding hematocrit $H_r = 10\%$.

Supplemental video S2: Recorded video of the RBC flowing through the bifurcation for a feeding hematocrit $H_r = 20\%$.

Supplemental video S3: Recorded video of the RBC flowing through the bifurcation for a feeding hematocrit $H_r = 30\%$.

C.2 Sensitivity Analysis of $\tau_{RBC,t}$

We conducted a sensitivity analysis to assess the impact of the threshold $\tau_{RBC,t}$ by selecting three values: $\tau_{RBC,t} = 1.7$, 2.0, and 2.3. To evaluate the influence of $\tau_{RBC,t}$, we calculated the mean values for the various RBC properties for both LRBC and NLRBC groups and compared the resulting p-values for $H_r = 10\%$. Table C.1 presents all data relative to $\tau_{RBC,t} = 2.0$, with differences in p-values highlighted in red. We observed one change in the velocity at the end of the parent vessel, where a threshold of $\tau_{RBC,t} = 2.3$ removes the statistical difference between LRBC and NLRBC; however, this does not impact our overall conclusions. The remaining differences are in the orientation p-values. As discussed in Section C.3.3, orientation is challenging to measure, leading to high variability across $\tau_{RBC,t}$ values. Thus, we conclude that the main results and conclusions of this study remain qualitatively unaffected by the choice of $\tau_{RBC,t}$ within the tested range.

Table C.1: Sensitivity analysis of $\tau_{\mathrm{RBC,t}}$ for $H_{\mathrm{r}} = 10\%$. Percentage of RBCs, median velocity ($\tilde{u}$), median circularity ($\tilde{\epsilon}$) and median orientation ($\tilde{\beta}$), in the parent vessel (0) and daughter vessels (1,2). The percentage of RBCs that are located between $-1/8 < y^* < 1/8$ in the parent vessel (0) and $1/8 < y^* < 1/2$ in the daughter vessels (1,2). $\epsilon = 1$ represents a perfect circle. $\beta = 0°$ indicates that an RBC is aligned with the centerline of the respective ROI (i.e., the RBC follows the main flow direction). A two-sample Kolmogorov-Smirnov test was performed to evaluate statistical differences between the LRBC and NLRBC distributions. Differences in p-values relative to $\tau_{\mathrm{RBC,t}} = 2.0$ are highlighted in red.

		$\tau_{\mathrm{RBC,t}} = 1.7$				$\tau_{\mathrm{RBC,t}} = 2.0$				$\tau_{\mathrm{RBC,t}} = 2.3$			
		In_0	Out_0	$\mathrm{In}_{1,2}$	$\mathrm{Out}_{1,2}$	In_0	Out_0	$\mathrm{In}_{1,2}$	$\mathrm{Out}_{1,2}$	In_0	Out_0	$\mathrm{In}_{1,2}$	$\mathrm{Out}_{1,2}$
LRBC	[%]	97.1	95.7	95.7	94.2	95.4	95.4	97.7	97.7	97.2	97.2	97.2	97.2
NLRBC	[%]	48.2	48.2	25.2	42.4	52.2	51.9	30.5	46.0	53.1	52.8	32.1	47.2
p-value		$3.2{\cdot}10^{-7}$	$1.4{\cdot}10^{-7}$	$5.5{\cdot}10^{-32}$	$1.6{\cdot}10^{-25}$	$2.5{\cdot}10^{-5}$	$6.8{\cdot}10^{-5}$	$3.5{\cdot}10^{-24}$	$1.1{\cdot}10^{-19}$	$3.2{\cdot}10^{-4}$	$1.9{\cdot}10^{-4}$	$5.5{\cdot}10^{-21}$	$6.5{\cdot}10^{-16}$
$\tilde{u}_{\mathrm{LRBC}}$	[mm/s]	0.72	0.67	0.18	0.26	0.72	0.68	0.13	0.24	0.73	0.67	0.12	0.23
$\tilde{u}_{\mathrm{NLRBC}}$	[mm/s]	0.68	0.64	0.33	0.34	0.67	0.64	0.33	0.33	0.69	0.64	0.33	0.33
p-value		$3.3{\cdot}10^{-6}$	$5.2{\cdot}10^{-3}$	$1.5{\cdot}10^{-25}$	$3.0{\cdot}10^{-23}$	$1.2{\cdot}10^{-4}$	$7.4{\cdot}10^{-3}$	$3.4{\cdot}10^{-20}$	$4.4{\cdot}10^{-15}$	$8.1{\cdot}10^{-5}$	$6.7{\cdot}10^{-2}$	$7.7{\cdot}10^{-17}$	$3.3{\cdot}10^{-12}$
$\tilde{\epsilon}_{\mathrm{LRBC}}$		0.75	0.77	0.56	0.67	0.73	0.77	0.51	0.65	0.73	0.77	0.50	0.65
$\tilde{\epsilon}_{\mathrm{NLRBC}}$		0.77	0.78	0.78	0.78	0.77	0.78	0.76	0.78	0.77	0.78	0.76	0.76
p-value		0.27	0.57	$8.7{\cdot}10^{-21}$	$2.5{\cdot}10^{-13}$	$4.4{\cdot}10^{-2}$	0.71	$2.9{\cdot}10^{-21}$	$3.9{\cdot}10^{-10}$	$1.4{\cdot}10^{-2}$	0.77	$6.6{\cdot}10^{-21}$	$6.4{\cdot}10^{-10}$
$\tilde{\beta}_{\mathrm{LRBC}}$	[°]	9.3	18.7	12.0	4.5	4.8	11.4	10.8	4.6	6.4	18.7	10.7	4.2
$\tilde{\beta}_{\mathrm{NLRBC}}$	[°]	4.6	4.3	1.1	5.3	5.0	5.0	4.2	5.0	4.6	4.6	5.4	5.
p-value		$2.3{\cdot}10^{-3}$	$1.3{\cdot}10^{-4}$	$6.6{\cdot}10^{-10}$	$2.2{\cdot}10^{-3}$	0.20	$9.4{\cdot}10^{-2}$	$2.3{\cdot}10^{-7}$	$1.4{\cdot}10^{-2}$	$8.8{\cdot}10^{-2}$	$1.3{\cdot}10^{-2}$	$5.8{\cdot}10^{-6}$	$5.2{\cdot}10^{-2}$

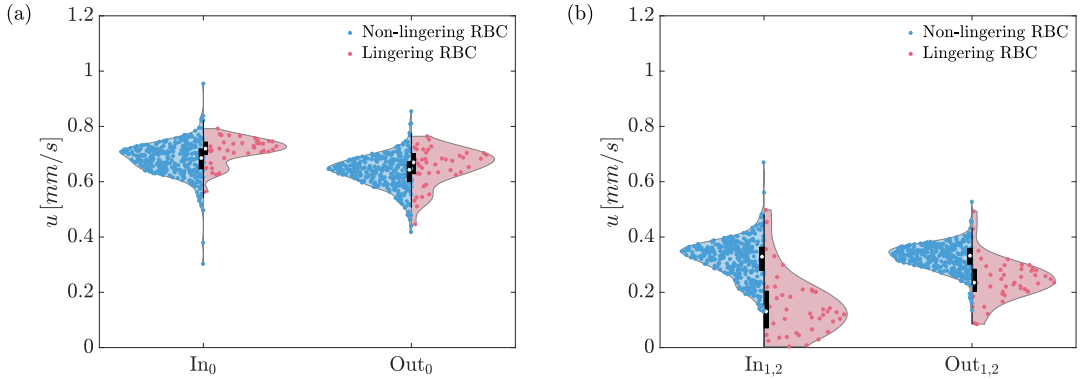

Figure C.1: RBC velocity distribution in the parent and daughter vessels. **a)** RBC velocity at the inlet (In_0) and outlet (Out_0) of the parent vessel. **b)** RBC velocity at the inlet ($In_{1,2}$) and outlet ($Out_{1,2}$) of the daughter vessel.[1]

C.3 Additional Analysis for Experiment with $H_r = 10\%$

In addition to the lateral RBC distributions presented in Chapter 3, we report here an analysis on other properties for NLRBCs and LRBCs such as RBC velocity, circularity and orientation.

C.3.1 Velocity

Fig. C.1a shows that LRBCs are statistically significantly faster than NLRBCs in the parent vessel (K-S test: p-value of $1.2 \cdot 10^{-4}$ at In_0 and $7.4 \cdot 10^{-3}$ at Out_0). This is related to the observation that LRBCs are mostly located close to the centerline of the channel at the inlet of the parent vessel where the flow velocity was the highest (Fig. 3.4).

At the outlet of the daughter vessels, the NLRBC velocity remained similar to the inlet ($\tilde{u}_{\mathrm{NLRBC}} = 0.33\,\mathrm{mm/s}$). The LRBC velocity increased, but it remained statistically lower than the NLRBC velocity: $\tilde{u}_{\mathrm{LRBC}} = 0.24\,\mathrm{mm/s}$ (K-S test: $p = 4.4 \cdot 10^{-15}$ at $Out_{1,2}$). This velocity difference is probably connected to the lateral position of the LRBCs, which remained very close to the microchannel distal wall when flowing in the daughter vessels.

C.3.2 Circularity

As illustrated in Fig. 3.3 RBCs may undergo large deformations when they flow through the microchannel, especially if they linger at the apex of the bifurcation. To quantify this phenomenon, we measured the circularity ϵ, which is a measure of the roundness of an object ($\epsilon = 1$ is a perfect circle). In the parent vessel, the circularity distribution for NLRBCs and LRBCs was unimodal with peaks at $\tilde{\epsilon}_{\mathrm{NLRBC,In_0}} = 0.77$, $\tilde{\epsilon}_{\mathrm{NLRBC,Out_0}} = 0.78$, $\tilde{\epsilon}_{\mathrm{LRBC,In_0}} = 0.73$ and $\tilde{\epsilon}_{\mathrm{LRBC,Out_0}} = 0.77$ (Fig. C.2a). These distributions are statistically different at the inlet but not at the outlet of the ROI_0 ($p = 4.4 \cdot 10^{-2}$ at In_0, $p = 0.71$ at Out_0, respectively). Generally, all RBCs were highly circular and not

[1]Figure S1 in Bucciarelli et al. (2024). CC BY 4.0.

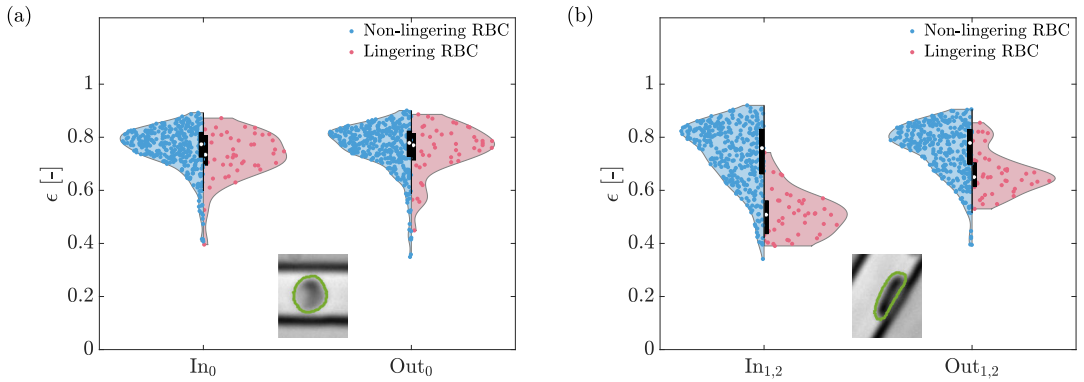

Figure C.2: RBC circularity (ϵ) distribution. $\epsilon = 1$ represents a perfect circle. **a)** Circularity at the inlet (In_0) and outlet (Out_0) of the parent vessel. In the inset is depicted an RBC with $\epsilon = 0.83$. **b)** Circularity at the inlet ($In_{1,2}$) and outlet ($Out_{1,2}$) of the daughter vessels. In the inset is depicted an RBC with $\epsilon = 0.57$.[2]

subjected to a significant state of deformation as they approached the bifurcation. An example of a physiological discocyte is depicted in Fig. C.2a ($\epsilon = 0.83$).

In the daughter vessels, NLRBCs had a broader circularity distribution than LRBCs, but the medians were similar ($\tilde{\epsilon}_{\mathrm{NLRBC,In_{1,2}}} = 0.76$ and $\tilde{\epsilon}_{\mathrm{NLRBC,Out_{1,2}}} = 0.78$). In contrast, LRBCs were highly deformed at the inlet of the daughter vessels (Fig. C.2b) with a median circularity of $\tilde{\epsilon}_{\mathrm{LRBC,In_{1,2}}} = 0.51$. This is confirmed visually by the example in Fig. 3.3, which shows a LRBC that elongates at the intersection ($\overline{\epsilon}_I = 0.63$) and holds its deformed shape when it leaves the bifurcation region. In the daughter vessels, the LRBCs partially relaxed, but they did not recover their initial discoid shape ($\tilde{\epsilon}_{\mathrm{LRBC,Out_{1,2}}} = 0.65$). The difference in circularity distribution between NLRBCs and LRBCs in the daughter vessels is statistically significant ($p = 2.9 \cdot 10^{-21}$ at $In_{1,2}$, $p = 3.9 \cdot 10^{-10}$ at $Out_{1,2}$). This implies that the lingering has an influence on the shape of the RBCs after the bifurcation.

C.3.3 Orientation

The orientation β was defined as the angle between the major axis of the ellipse fitted to each individual RBC and the axis of each vessel. Because the RBCs typically featured a circular discocyte shape in the parent vessel, the orientation was difficult to measure in that region. Even a minor variation in the cell aspect ratio resulted in a significant orientation change. As a result, we found that both NLRBCs and LRBCs had a broad orientation distribution in the parent vessel (Fig. C.3a). It seemed that NLRBCs aligned more with the main flow direction than the LRBCs ($p = 2.0 \cdot 10^{-1}$ at In_0, $p = 9.4 \cdot 10^{-4}$ at Out_0). However, NLRBCs lost their preferential orientation at the entrance of the daughter vessel (Fig. C.3b). In contrast, LRBCs were aligned with the main flow direction and just slightly tilted upwards towards the center of the vessel. This is represented by a narrow orientation distribution and is related to the fact that LBRCs in the daughter vessels were leaning on the distal wall (Fig. C.2b).

[2]Figure S2 in Bucciarelli et al. (2024). CC BY 4.0.

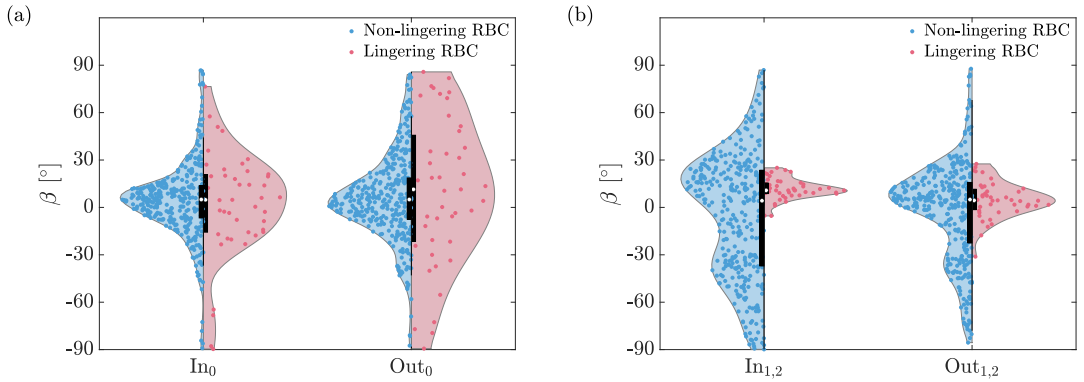

Figure C.3: RBC orientation (β) distribution. $\beta = 0°$ indicates that an RBC is aligned with the centerline of the respective ROI (i.e. the RBC follows the main flow direction). **a)** Orientation at the inlet (In_0) and outlet (Out_0) of the parent vessel. **b)** Orientation at the inlet ($\text{In}_{1,2}$) and outlet ($\text{Out}_{1,2}$) of the daughter vessels.[3]

C.4 Results for $H_\text{r} = 20\%$ and $H_\text{r} = 30\%$

For the experiment at $H_\text{r} = 20\%$ a total of 522 RBCs were tracked, thereof 50 LRBCs and 472 NLRBCs resulting in a lingering frequency of 9.6%. For the experiment at $H_\text{r} = 30\%$ a total of 776 RBCs were tracked, thereof 80 LRBCs and 696 NLRBCs resulting in a similar lingering frequency of 10.3%.

C.4.1 Hematocrit Lateral Distribution Measurements

Detailed information on the RBC hematocrit distribution (i.e. RBC lateral distribution for LRBCs and NLRBCs) are reported in Table C.2. Fig. C.4 shows the distribution of the RBC lateral position in the parent and daughter vessels for $H_\text{r} = 20\%$ and $H_\text{r} = 30\%$. The shape of the lateral position distribution is similar to the results for $H_\text{r} = 10\%$ (Fig. 3.3). This reinforces our conclusion that LRBCs are concentrated in the center of the parent vessel and that they flow near the distal wall in the daughter vessels, whereas NLRBCs are shifted to the side in the parent vessel and flow closer to the centerline of the daughters vessels.

C.4.2 Correlation Between RBC Lingering and Downstream Reverse Partitioning

Similarly to the results reported for $H_\text{r} = 10\%$, we calculated the best-fitting $\hat{\gamma}$ for the composite lateral distribution functions measured in this study LDF_C (for $H_\text{r} = 20\%$ and $H_\text{r} = 30\%$) to each lateral distribution function LDF reported by Mantegazza et al. (2020b). We found $0 \leq \hat{\gamma} \leq 0.45$ and $0 \leq \hat{\gamma} \leq 0.43$ for $H_\text{r} = 20\%$ and $H_\text{r} = 30\%$, respectively. Fig. C.5 shows that a statistically significantly higher percentage of LRBCs is needed to obtain a skewed hematocrit distribution that leads to reverse partitioning

[3]Figure S3 in Bucciarelli et al. (2024). CC BY 4.0.
[4]Summary of Table S1, S3, S4 and S5 in Bucciarelli et al. (2024). CC BY 4.0.

Table C.2: Percentage of RBCs, median velocity ($\tilde{u}$), median circularity ($\tilde{\epsilon}$) and median orientation ($\tilde{\beta}$), in the parent vessel (0) and daughter vessels (1,2). The percentage of RBCs that are located between $-1/8 < y^* < 1/8$ in the parent vessel (0) and $1/8 < y^* < 1/2$ in the daughter vessels (1,2). $\epsilon = 1$ represents a perfect circle. $\beta = 0°$ indicates that an RBC is aligned with the centerline of the respective ROI (i.e., the RBC follows the main flow direction). A two-sample Kolmogorov-Smirnov test was performed to evaluate statistical differences between the LRBC and NLRBC distributions. Differences in p-values relative to $H_r = 10\%$ are highlighted in red.[4]

		$H_r = 10\%$				$H_r = 20\%$				$H_r = 30\%$			
		In_0	Out_0	$In_{1,2}$	$Out_{1,2}$	In_0	Out_0	$In_{1,2}$	$Out_{1,2}$	In_0	Out_0	$In_{1,2}$	$Out_{1,2}$
LRBC	[%]	95.4	95.4	97.7	97.7	88.0	92.0	94.0	94.0	85.0	93.8	98.8	97.5
NLRBC	[%]	52.2	51.9	30.5	46.0	52.1	51.1	30.7	48.7	50.7	48.3	27.9	43.0
p-value		$2.5{\cdot}10^{-5}$	$6.8{\cdot}10^{-5}$	$3.5{\cdot}10^{-24}$	$1.1{\cdot}10^{-19}$	$8.2{\cdot}10^{-4}$	$1.2{\cdot}10^{-5}$	$4.4{\cdot}10^{-36}$	$3.7{\cdot}10^{-21}$	$5.3{\cdot}10^{-4}$	$5.0{\cdot}10^{-6}$	$1.8{\cdot}10^{-45}$	$8.8{\cdot}10^{-29}$
$\tilde{u}_{\text{LRBC}}$	[mm/s]	0.72	0.68	0.13	0.24	0.81	0.74	0.18	0.29	0.74	0.68	0.19	0.25
$\tilde{u}_{\text{NLRBC}}$	[mm/s]	0.67	0.64	0.33	0.33	0.78	0.72	0.38	0.38	0.72	0.66	0.34	0.35
p-value		$1.2{\cdot}10^{-4}$	$7.4{\cdot}10^{-3}$	$3.4{\cdot}10^{-20}$	$4.4{\cdot}10^{-15}$	$3.8{\cdot}10^{-3}$	$1.4{\cdot}10^{-1}$	$3.5{\cdot}10^{-20}$	$1.1{\cdot}10^{-14}$	$5.1{\cdot}10^{-4}$	$1.0{\cdot}10^{-1}$	$1.9{\cdot}10^{-21}$	$3.9{\cdot}10^{-25}$
$\tilde{\epsilon}_{\text{LRBC}}$		0.73	0.77	0.51	0.65	0.75	0.73	0.54	0.65	0.74	0.73	0.52	0.64
$\tilde{\epsilon}_{\text{NLRBC}}$		0.77	0.78	0.76	0.78	0.75	0.75	0.76	0.76	0.75	0.75	0.74	0.74
p-value		$4.4{\cdot}10^{-2}$	0.71	$2.9{\cdot}10^{-21}$	$3.9{\cdot}10^{-10}$	$2.4{\cdot}10^{-1}$	$2.1{\cdot}10^{-2}$	$2.4{\cdot}10^{-24}$	$7.0{\cdot}10^{-15}$	$5.4{\cdot}10^{-1}$	$1.5{\cdot}10^{-1}$	$6.8{\cdot}10^{-31}$	$5.7{\cdot}10^{-19}$
$\tilde{\beta}_{\text{LRBC}}$	[°]	4.8	11.4	10.8	4.6	8.5	5.3	11.1	3.7	1.9	-1.2	11.4	4.0
$\tilde{\beta}_{\text{NLRBC}}$	[°]	5.0	5.0	4.2	5.0	5.7	5.2	4.2	5.2	3.3	1.6	1.1	5.9
p-value		$2.0{\cdot}10^{-1}$	$9.4{\cdot}10^{-2}$	$2.3{\cdot}10^{-7}$	$1.4{\cdot}10^{-2}$	$8.1{\cdot}10^{-2}$	$1.2{\cdot}10^{-2}$	$7.0{\cdot}10^{-8}$	$2.3{\cdot}10^{-2}$	$1.6{\cdot}10^{-1}$	$7.0{\cdot}10^{-2}$	$2.1{\cdot}10^{-13}$	$9.9{\cdot}10^{-4}$

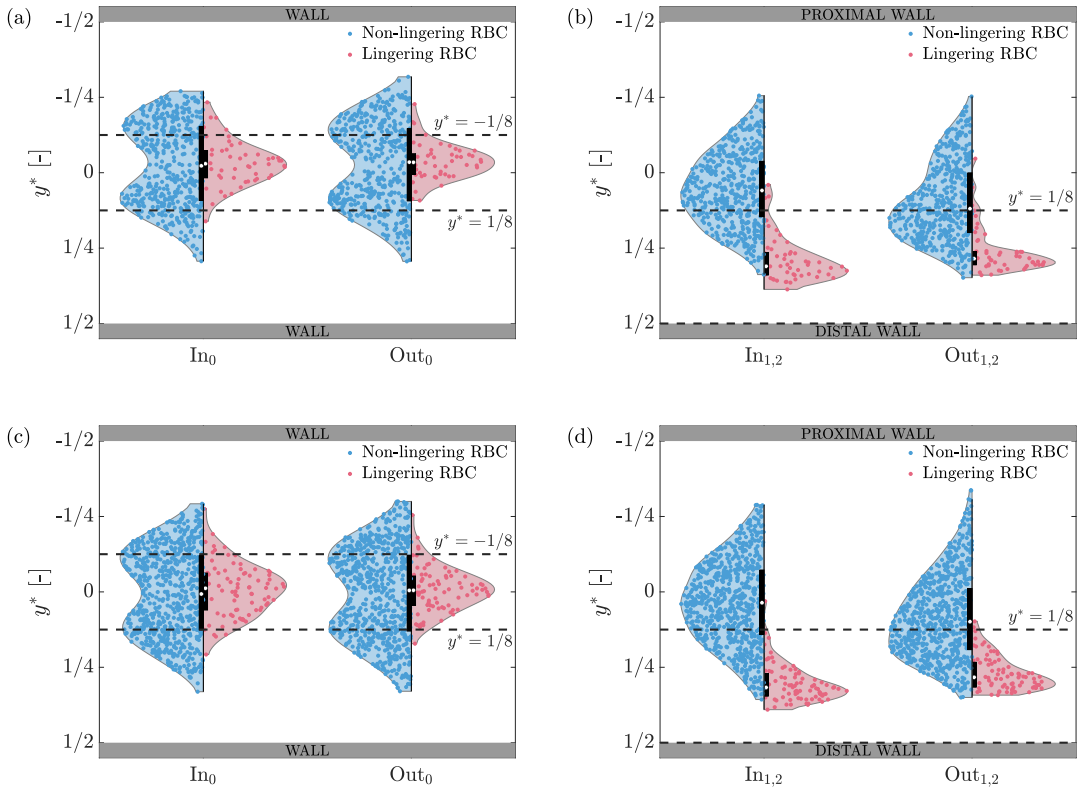

Figure C.4: Distribution of the RBC lateral position in the parent and daughter vessels for $H_r = 20\%$ and $H_r = 30\%$. The position of the RBC centroid is normalized with respect to the channel width ($y^* = y/W$). $y^* = 0$ is the centerline of the microchannel, whereas $y^* = 1/2$ and $y^* = -1/2$ are the distal and proximal wall of the microchannel, respectively. **a)** Distribution of the RBC lateral position at the inlet (In_0) and outlet (Out_0) of the parent vessel for $H_r = 20\%$. **b)** Distribution of the RBC lateral position at the inlet ($In_{1,2}$) and outlet ($Out_{1,2}$) of the daughter vessels for $H_r = 20\%$. **c)** Distribution of the RBC lateral position at the inlet (In_0) and outlet (Out_0) of the parent vessel for $H_r = 30\%$. **d)** Distribution of the RBC lateral position at the inlet ($In_{1,2}$) and outlet ($Out_{1,2}$) of the daughter vessels for $H_r = 30\%$.[5]

(M-W-U test: $p = 3.6 \cdot 10^{-2}$ and $p = 3.6 \cdot 10^{-2}$ for $H_r = 20\%$ and $H_r = 30\%$, respectively.)

C.4.3 RBC Migration Across the Separation Surface

We analyzed the influence of LRBCs on the RBC distribution at the bifurcation. Similarly to the experiments at $H_r = 10\%$, RBCs generally did not migrate across the separation surface (Table C.3, "All RBC") even at the higher hematocrits. However, if only LRBCs are considered, we observed that the percentage of RBCs crossing the symmetry axis increases. The percentage of NLRBCs crossing the symmetry axis does not differ considerably from "All RBCs" (Table C.3, "All NLRBC" vs. "All NLRBC"). For the

[5]Figure S4 in Bucciarelli et al. (2024). CC BY 4.0.

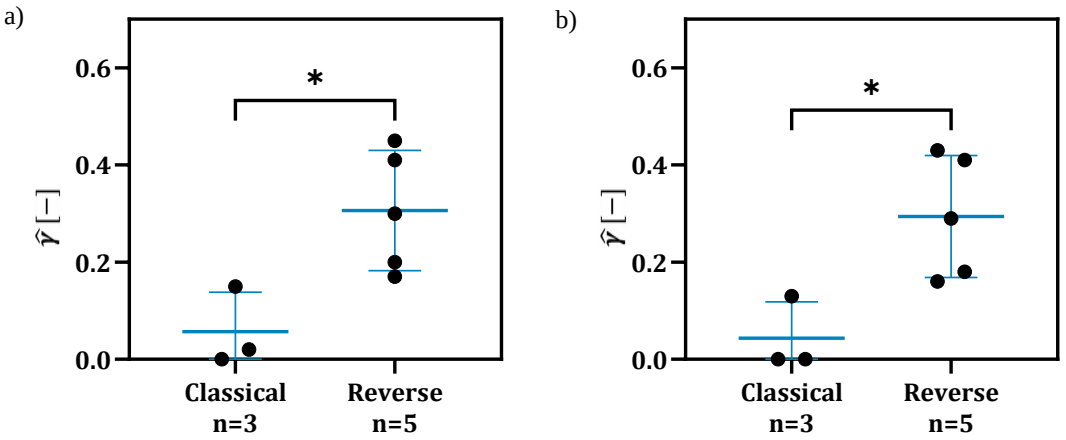

Figure C.5: Lingering frequency $\hat{\gamma}$ which yields the best fit to the previously reported distributions LDF from Mantegazza et al. (2020b) classified by the resulting type of partitioning. The lingering frequency for the reverse partitioning group is statistically different from the classical partitioning group for both hematocrits: **a)** $H_r = 20\%$ ($p = 3.6 \cdot 10^{-2}$) and **b)** $H_r = 30\%$ ($p = 3.6 \cdot 10^{-2}$).[6]

Table C.3: Statistics on all RBCs that were able to cross the SA while approaching the bifurcation. The RBC population was divided into subgroups: All RBC, LRBC, All NLRBC, NLRBC when there is no lingering event (LE) and NLRBC when there is a lingering event.[7]

	$H_r = 20\%$	$H_r = 30\%$
All RBC	6.7%	8.1%
LRBC	36.0%	41.2%
All NLRBC	3.6%	4.3%
NLRBC without LE	4.3%	4.7%
NLRBC during LE	1.6%	3.6%

subgroups of NLRBCs without any lingering event and NLRBCs during lingering event (LE), no major difference can be observed (Table C.3 "NLRBC no LE" vs. "NLRBC during LE"). Overall, our data suggest that LRBCs do not have a direct influence on NLRBCs partitioning for the present configuration of our microfluidic network.

C.4.4 Velocity

Results reported in Table C.2, Fig. C.6a, Fig. C.6c show that LRBCs are statistically significantly faster than NLRBCs at the inlet of the parent vessel for both hematocrits that we tested, but this difference disappears at the outlet. In the daughter vessels (Fig. C.6b and Fig. C.6d), the LRBCs have a statistically significantly lower velocity than the NLRBCs either at the inlet and at the outlet for both hematocrits.

[6]Figure S5 in Bucciarelli et al. (2024). CC BY 4.0.
[7]Table S2 in Bucciarelli et al. (2024). CC BY 4.0.

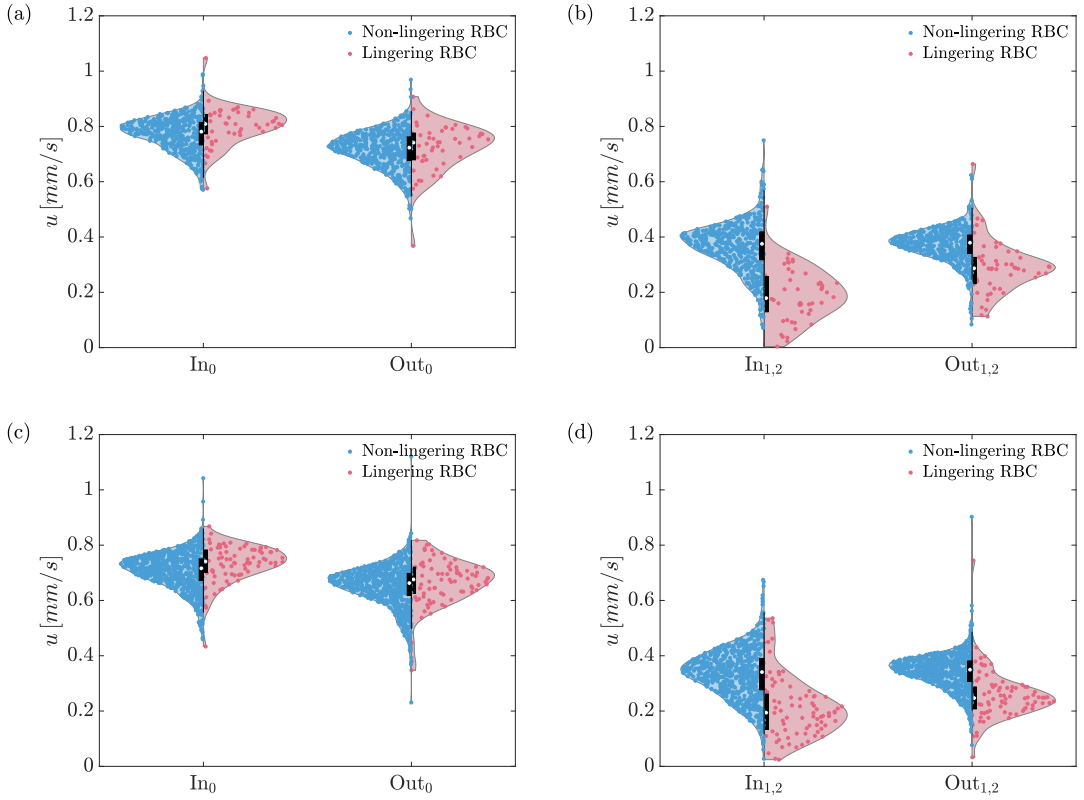

Figure C.6: RBC velocity distribution in the parent and daughter vessels for $H_r = 20\%$ and $H_r = 30\%$. **a)** RBC velocity at the inlet (In_0) and outlet (Out_0) of the parent vessel for $H_r = 20\%$. **b)** RBC velocity at the inlet ($In_{1,2}$) and outlet ($Out_{1,2}$) of the daughter vessels for $H_r = 20\%$. **c)** RBC velocity at the inlet (In_0) and outlet (Out_0) of the parent vessel for $H_r = 30\%$. **d)** RBC velocity at the inlet ($In_{1,2}$) and outlet ($Out_{1,2}$) of the daughter vessels for $H_r = 30\%$.[8]

C.4.5 Circularity

Similar to what we found for $H_r = 10\%$ (Appendix C.3.2), all RBCs in the parent vessel have a round shape for $H_r = 20\%$ and $H_r = 30\%$ (Table C.2, Fig. C.7a, Fig. C.7c). In the daughter vessels, the NLRBC eccentricity distribution is similar to what we found in the parent vessel, whereas LRBCs have a lower circularity (Fig. C.7b and Fig. C.7d).

C.4.6 Orientation

The RBC orientation from the experiments at $H_r = 20\%$ and $H_r = 30\%$ is broadly distributed in the parent vessel (Table C.2, Fig. C.8a and Fig. C.8c) and it seems that the NLRBCs align more with the flow direction (similarly to $H_r = 10\%$). As explained in Appendix Section C.3.3, this broad distribution may be related to the uncertainty of determining the orientation of an object with a discoid-like shape. In the daughter vessels, we observed quite the opposite situation where the LRBCs align with the flow direction

[8]Figure S6 in Bucciarelli et al. (2024). CC BY 4.0.

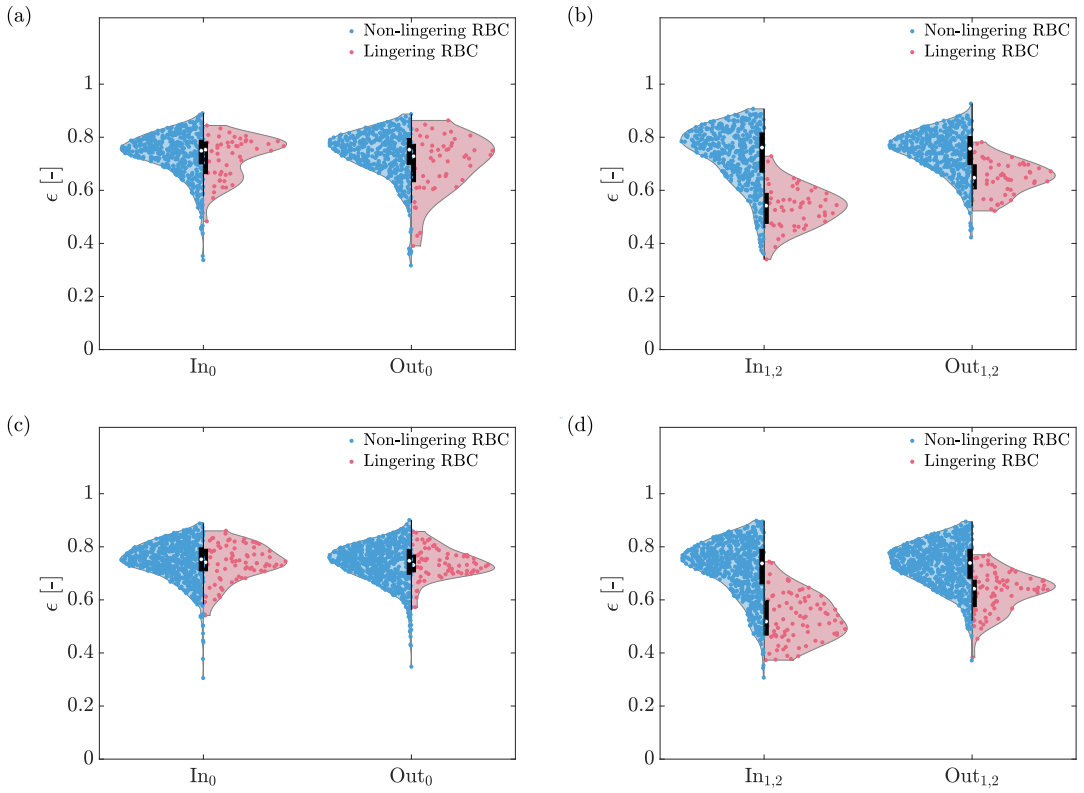

Figure C.7: RBC circularity (ϵ) distributions for $H_r = 20\%$ and $H_r = 30\%$, where $\epsilon = 1$ represents a perfect circle. **a)** Circularity at the inlet (In_0) and outlet (Out_0) of the parent vessel $H_r = 20\%$. **b)** Circularity at the inlet ($In_{1,2}$) and outlet ($Out_{1,2}$) of the daughter vessels $H_r = 20\%$. **c)** Circularity at the inlet (In_0) and outlet (Out_0) of the parent vessel $H_r = 30\%$. **d)** Circularity at the inlet ($In_{1,2}$) and outlet ($Out_{1,2}$) of the daughter vessels $H_r = 30\%$.[9]

and the NLRBCs do not seem to have a preferential orientation (Fig. C.8b and Fig. C.8d).

[9]Figure S7 in Bucciarelli et al. (2024). CC BY 4.0.
[10]Figure S8 in Bucciarelli et al. (2024). CC BY 4.0.

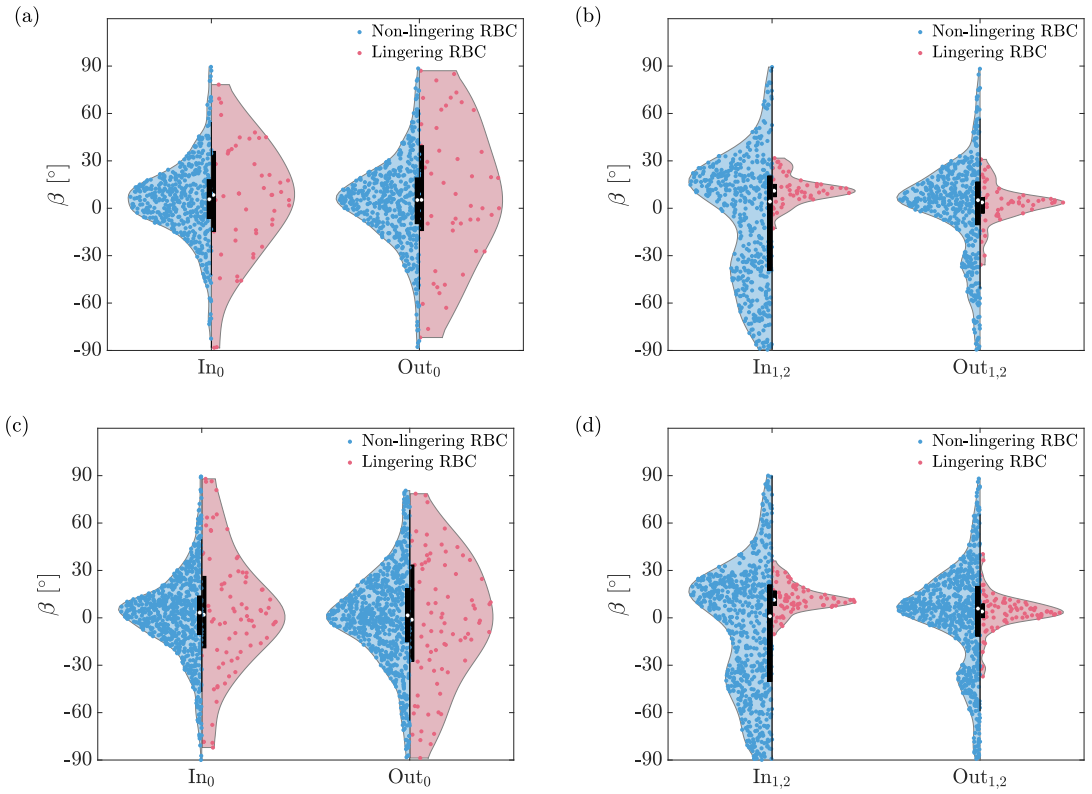

Figure C.8: RBC orientation (β) distributions for $H_\mathrm{r} = 20\%$ and $H_\mathrm{r} = 30\%$. $\beta = 0°$ indicates that an RBC is aligned with the centerline of the respective ROI (i.e. the RBC follows the main flow direction). **a)** Orientation at the inlet (In_0) and outlet (Out_0) of the parent vessel for $H_\mathrm{r} = 20\%$. **b)** Orientation at the inlet ($\mathrm{In}_{1,2}$) and outlet ($\mathrm{Out}_{1,2}$) of the daughter vessels for $H_\mathrm{r} = 20\%$. **c)** Orientation at the inlet (In_0) and outlet (Out_0) of the parent vessel for $H_\mathrm{r} = 30\%$. **d)** Orientation at the inlet ($\mathrm{In}_{1,2}$) and outlet ($\mathrm{Out}_{1,2}$) of the daughter vessels for $H_\mathrm{r} = 30\%$.[10]

Appendix D

Supplementary Material for Chapter 4 on Dynamic Pericyte Activation

D.1 Spatial Variations in Phase Separation

As discussed in Section 4.4.5, we analyzed the phase separation behavior at diverging bifurcations within the honeycombed network, dividing the bifurcations into four groups based on their horizontal position relative to the pericyte activation site.

For the bifurcations furthest from the pericyte activation site, the phase separation behavior aligned closely with the identity line in both the short-time (Fig. D.1a) and long-time experiments (Fig. D.2a). These bifurcations exhibited blood flow rate fractions of approximately $\Phi \approx 0.4$ with $\Psi \approx 0.4$ or $\Phi \approx 0.6$ with $\Psi \approx 0.6$.

The bifurcations located second furthest from the pericyte activation site deviated from both the identity line and Pries's law in both experiments (Fig. D.1b and Fig. D.2b). These bifurcations typically had a blood flow rate fraction of $\Phi \approx 0.5$ with RBC flux fractions ranging between $0.5 < \Psi < 0.7$ or $0.3 < \Psi < 0.5$. Where for the long-time experiment has more bifurcation whit phase separation near $\Phi = 0.5$ and $\Psi = 0.5$.

The bifurcations second closest to the pericyte activation site (Fig. D.1c and Fig. D.2c) generally followed the identity line, with blood flow rate fractions in the range $0.4 < \Phi < 0.6$ and RBC flux fractions in the range $0.4 < \Psi < 0.6$. In contrast, the bifurcations nearest to the pericyte (Fig. D.1d and Fig. D.2d) were similar to those second furthest, except for two bifurcations where one daughter vessel carried only plasma, resulting in $\Phi = 0$ and $\Psi = 0$ or $\Phi = 1$ and $\Psi = 1$.

These differences, depending on the bifurcations' topological positions, highlight the importance of flow history in determining RBC distribution at individual bifurcations and across the entire network.

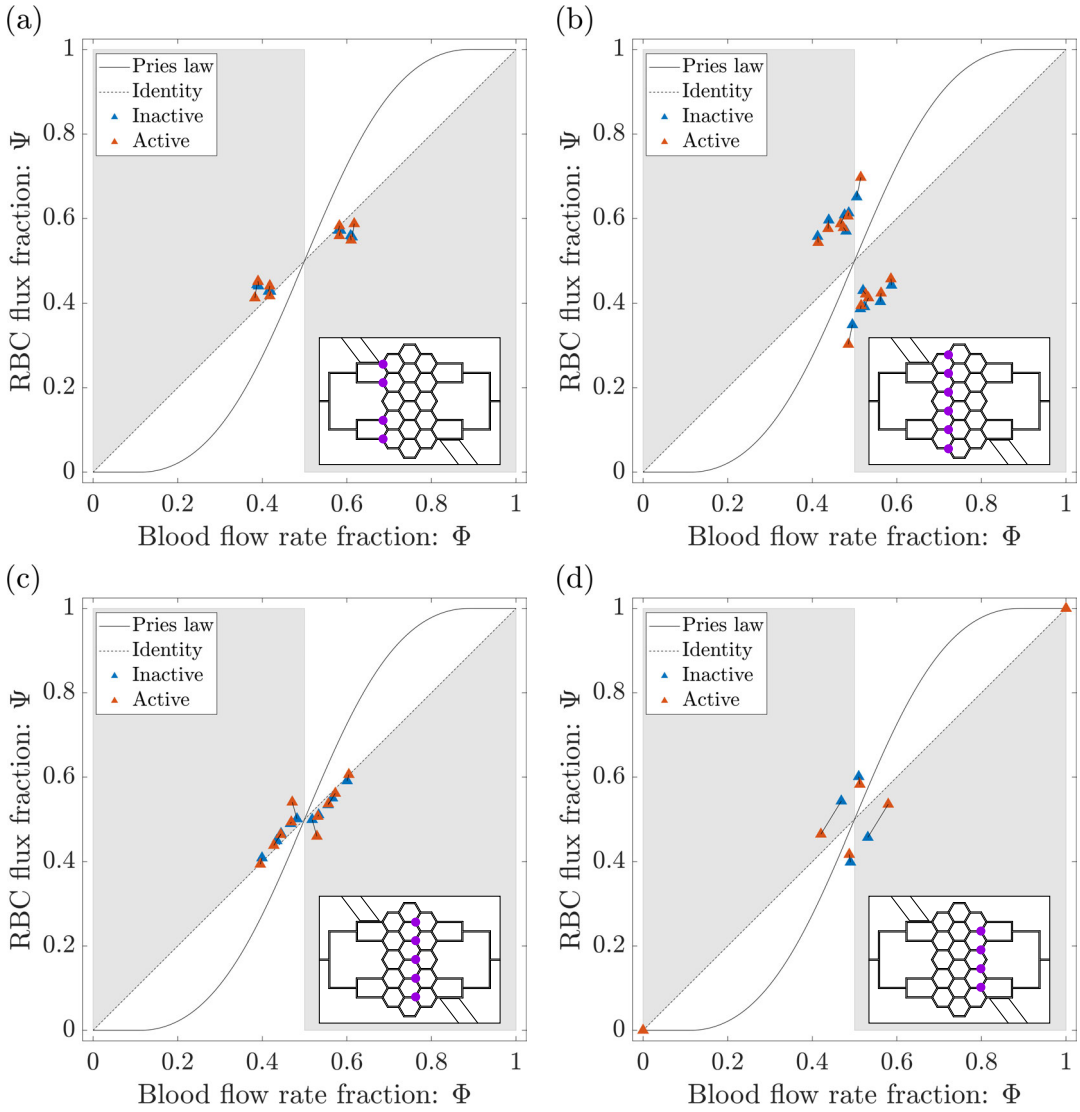

Figure D.1: Phase separation results for short-time activation experiment grouped by the diverging bifurcation horizontal location (indicated by the violet points in the microfluidic chip schematic shown in the bottom-right corner). **a)** Phase separation at the bifurcations located furthest from the pericyte activation site along the x-axis. **b)** Phase separation at the bifurcations located second furthest from the pericyte activation site along the x-axis. **c)** Phase separation at the bifurcations located second closest to the pericyte activation site along the x-axis. **d)** Phase separation at the bifurcations located closest to the pericyte activation site along the x-axis. The blue marker indicates the inactive pericyte state, while the orange marker represents the active one. A thin black line connects the same bifurcation in both conditions. The black line represents the empirical relationship proposed by Pries et al. (2003) for parent and daughter vessel diameters of $D_\mathrm{h} = 8.7\,\mu\mathrm{m}$. The dashed black line indicates the identity line, corresponding to the proportional separation of blood and RBCs (no phase separation). Gray-shaded regions highlight areas where an inversion of the Zweifach-Fung effect is observed, as reported by Clavica et al. (2016) and Shen et al. (2016).

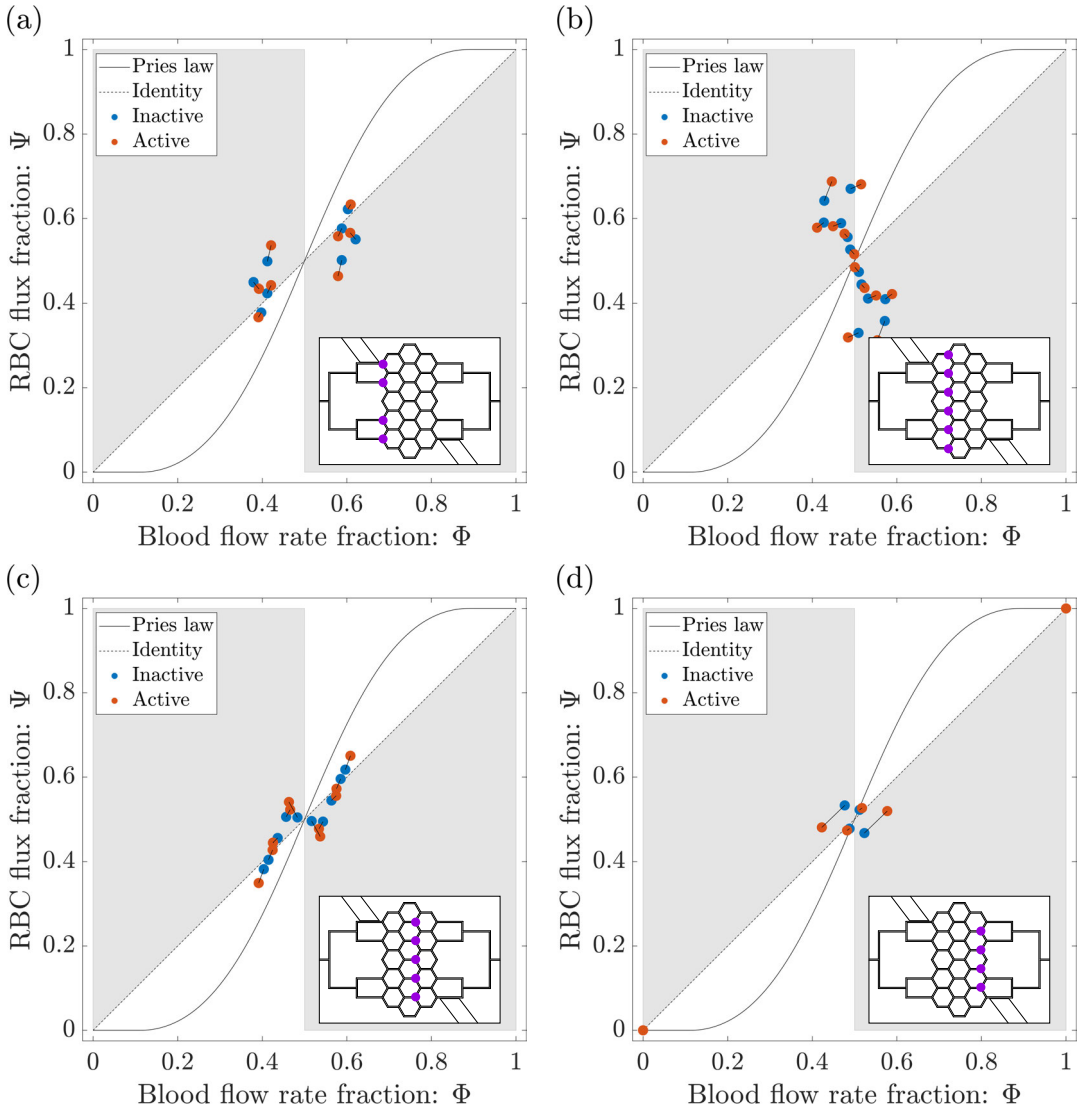

Figure D.2: Phase separation results for long-time activation experiment grouped by the diverging bifurcation horizontal location (indicated by the violet points in the microfluidic chip schematic shown in the bottom-right corner). **a)** Phase separation at the bifurcations located furthest from the pericyte activation site along the x-axis. **b)** Phase separation at the bifurcations located second furthest from the pericyte activation site along the x-axis. **c)** Phase separation at the bifurcations located second closest to the pericyte activation site along the x-axis. **d)** Phase separation at the bifurcations located closest to the pericyte activation site along the x-axis. The blue marker indicates the inactive pericyte state, while the orange marker represents the active one. A thin black line connects the same bifurcation in both conditions. The black line represents the empirical relationship proposed by Pries et al. (2003) for parent and daughter vessel diameters of $D_\mathrm{h} = 8.7\,\mu\mathrm{m}$. The dashed black line indicates the identity line, corresponding to the proportional separation of blood and RBCs (no phase separation). Gray-shaded regions highlight areas where an inversion of the Zweifach-Fung effect is observed, as reported by Clavica et al. (2016) and Shen et al. (2016).

Appendix E

Endothelialization of Microfluidics Channels

E.1 Introduction

The microfluidic chips utilized throughout this thesis were coated solely with albumin derived from the plasma-like solution. While this coating provides a minimal level of interaction between the channels and the RBCs, it does not accurately replicate the biological environment found in real capillaries. *In vivo*, RBCs interact with endothelial cells that line the capillary walls and are further supported by the glycocalyx, a complex layer of proteins and carbohydrates that plays a critical role in vascular function. This discrepancy highlights a significant limitation in the experimental setup, as the absence of these components affects the physiological relevance of the findings.

To address this limitation, a key area of interest is to explore whether endothelial cells can be successfully cultured within the microfluidic channels. This involves determining if these cells can adhere to the channel walls, grow to fully cover the inner surfaces, and maintain their viability over time under experimental conditions. Achieving such a setup would not only enhance the biological fidelity of the model but also provide a platform for investigating more realistic interactions between RBCs, endothelial cells, and the glycocalyx.

E.2 Material and Methods

To achieve this, we designed and fabricated a new microfluidic chip with channels of larger dimensions to accommodate endothelial cell culture (we used $50\,\mu$m $\times$ $50\,\mu$m instead of $9.6\,\mu$m $\times$ $8\,\mu$m). Unlike the standard procedure outlined in Section 2.1.1, the mold for this chip was produced using a 3D printer (microArch, BMF Boston Micro Fabrication, Maynard, MA, USA) and photosensitive resin (HTL-5, BMF Boston Micro Fabrication, Maynard, MA, USA). This fabrication method allowed for faster fabrication time and faster prototyping. The entire process was carried out in collaboration with the Acoustofluidics group at the Department of Biomedical Engineering, Lund University, whose expertise and resources significantly contributed to the success of the production of the microfluidic chip. After the mold was printed, the microfluidic chips were sub-

jected to a silanization process to prepare the surface for subsequent fabrication steps. The silanization procedure was conducted according to the protocol outlined in Appendix A.1. Once silanized, the microfluidic chips were produced using the same replica molding technique described in Section 2.1.2, maintaining uniformity with the established fabrication workflow.

Before endothelializing the microfluidic channels, two crucial steps are required: the preparation of the endothelial cells and the functionalization of the microfluidic channel walls to promote cell attachment.

To seed endothelial cells into the microfluidic chips, the cells must first be expanded in standard cell culture flasks over 3 to 5 days. During this expansion phase, it is critical to achieve a sufficient cell concentration to ensure successful seeding. Specifically, a concentration of $4 \cdot 10^6$ cells/mL with a minimum volume of 1 mL is necessary, which typically provides enough cells to seed 3 to 4 microfluidic chips. The detailed protocol for expanding and culturing endothelial cells can be found in Appendix A.5.

The functionalization of the microfluidic channel walls is performed immediately after the production of the chips, following the plasma bonding step (Appendix A.2). After plasma bonding, the chips are cured in an oven for 30 minutes to prepare them for surface modifications. Only 30 minutes to ensure a strong bond while retaining some free silanol groups ($Si-OH$) for subsequent functionalization. The functionalization process involves a series of surface coatings designed to enhance endothelial cell adhesion. First, an APTES coating is applied to introduce amino groups to the surface, creating a foundation for subsequent modifications. This is followed by a glutaraldehyde coating, which serves as a cross-linker and provides reactive sites for protein attachment. Next, a fibronectin coating is added to offer a protein-based surface that facilitates endothelial cell adhesion. Optionally, a collagen coating can also be applied to further improve cell attachment and better mimic the extracellular matrix. The specific steps for this functionalization process are detailed in Appendix A.6.

With the functionalization complete, the microfluidic channels are ready for endothelialization. We adapted a method originally described by Tsai et al. (2011) and Qiu et al. (2018) and modified it to suit our setup, leveraging the expertise of the Cardiovascular Disease Group (Rieben Lab) at the Department for BioMedical Research, University of Bern. The detailed protocol for this process can be found in Appendix A.7.

For this experiment, we used pig endothelial cells, although human endothelial cells can also be utilized. The cells were prepared at the desired concentration, suspended in culture medium supplemented with 8% dextran. The addition of dextran is crucial for facilitating the effective transport of cells into the microfluidic channels. By increasing the medium's viscosity and reducing the cells' velocity upon entry, dextran enhances the likelihood of the cells attaching to the channel walls. The microfluidic chip, pre-filled with culture medium containing 8% dextran and maintained at 37° C, was seeded with the endothelial cells using a syringe connected to the chip via a PTFE tube.

Two different methods were employed to promote cell attachment during seeding: static and underflow conditions. In the static method, the seeded microfluidic chip was placed in a Petri dish, submerged in culture medium, and incubated overnight. Alternatively, in the underflow method, the microfluidic chip was connected to a syringe pump and maintained inside the incubator while a flow rate of 1.25 μL/min of culture medium was imposed overnight. Both approaches ensured that by the next day, the microfluidic

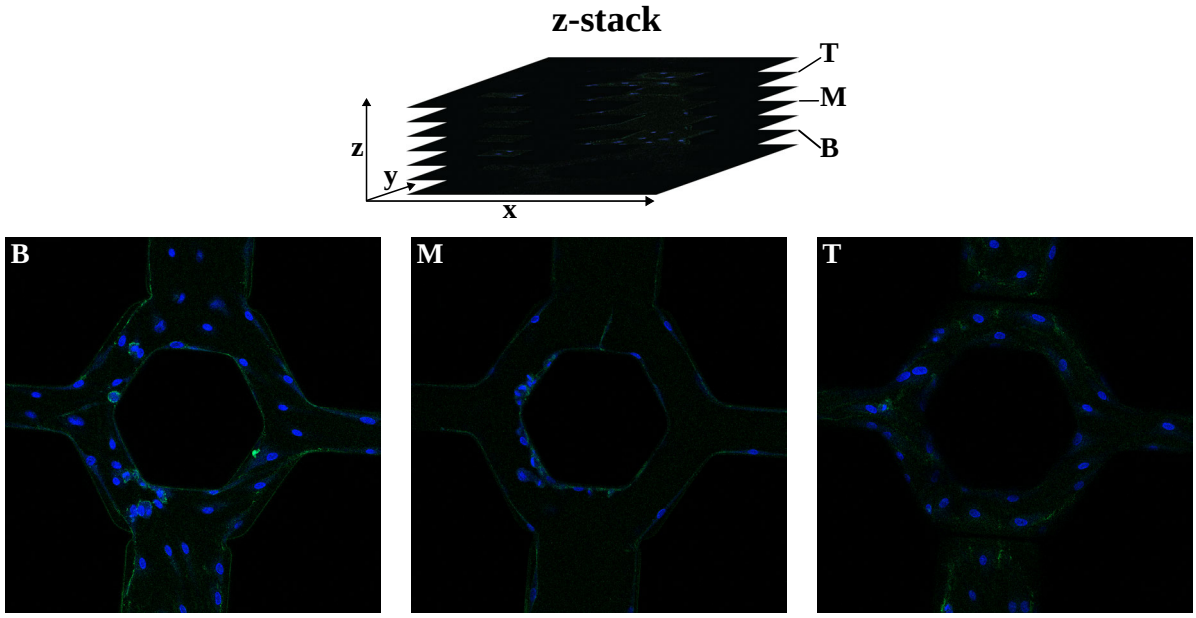

Figure E.1: Z-stack of the endothelialized microfluidic chip with stained cells. Green fluorescence (Rat anti-pig CD31 and Goat anti-Rat AlexaFluor488) highlights cell-cell adhesion, while blue fluorescence (DAPI) marks the nuclei. Three slices from the Z-stack are shown: at the floor of the microchannel (B), at the center of the channel where nuclei along the walls are visible (M), and at the ceiling of the microchannel (T).

channels were fully endothelialized.

To verify the success of the endothelialization protocol, we fixed the endothelial cells and performed staining to visualize their adhesion and morphology. Cell to cell adhesion was assessed using Rat anti-pig CD31 antibodies, followed by secondary staining with Goat anti-Rat AlexaFluor488. The nuclei were stained with DAPI, and the cytoskeleton was visualized with anti-F-Actin.

E.3 Results

As shown in both Fig. E.1 and Fig. 5.1, we can observe a monolayer of endothelial cells on all walls of the microfluidic channels. In Fig. E.1B and Fig. 5.1a, the floor of the microfluidic chip is covered with endothelial cells exhibiting strong cell to cell connections and a well-defined cytoskeleton. Similarly, Fig. E.1M highlights nuclei (blue) along the walls of the channels, confirming endothelial cell attachment and coverage in these regions. Finally, in Fig. E.1T and Fig. 5.1b, endothelial cells are visible on the ceiling of the microfluidic channels, also demonstrating clear cell to cell connections and cytoskeletal integrity.

E.4 Conclusion

These results demonstrate that our protocol effectively produces endothelialized microchannels, with cells forming a continuous monolayer along the channels' walls, ceiling, and floor. The current microfluidic channel dimensions of $50\,\mu$m $\times$ $50\,\mu$m provide adequate space for endothelialization, even accounting for the reduction in effective channel size due to the endothelial layer. Despite this, future experiments should explore smaller channels to better mimic capillary dimensions. It is important to note that these promising results were achieved after only two test runs, serving as a proof of concept. Further optimization and testing could refine this protocol to achieve endothelialization on smaller channels.

List of Figures

List of Tables

Bibliography

Abkarian, M., and A. Viallat, 2008. Vesicles and red blood cells in shear flow. *Soft Matter* 4:653–657. DOI: 10.1039/B716612E.

Abkarian, M., M. Faivre, and A. Viallat, 2007. Swinging of Red Blood Cells under Shear Flow. *Physical Review Letters* 98:188302. DOI: 10.1103/PhysRevLett.98.188302.

Alberts, B., 2017. 22 - Stem Cells and Tissue Renewal. In: Molecular Biology of the Cell, 6th edition, Garland Science. https://books.google.ch/books?id=jK6UBQAAQBAJ.

Amin, T. M., and J. A. Sirs, 1985. The Blood Rheology of Man and Various Animal Species. *Quarterly Journal of Experimental Physiology* 70:37–49. DOI: 10.1113/expphysiol.1985.sp002895.

Attwell, D., and C. Iadecola, 2002. The neural basis of functional brain imaging signals. *Trends in Neurosciences* 25:621–625. DOI: 10.1016/S0166-2236(02)02264-6.

Attwell, D., A. M. Buchan, S. Charpak, M. Lauritzen, B. A. MacVicar, and E. A. Newman, 2010. Glial and neuronal control of brain blood flow. *Nature* 468:232–243. DOI: 10.1038/nature09613.

Attwell, D., A. Mishra, C. N. Hall, F. M. O'Farrell, and T. Dalkara, 2016. What is a pericyte? *Journal of Cerebral Blood Flow & Metabolism* 36:451–455. DOI: 10.1177/0271678X15610340.

Balogh, P., and P. Bagchi, 2017. A computational approach to modeling cellular-scale blood flow in complex geometry. *Journal of Computational Physics* 334:280–307. DOI: 10.1016/j.jcp.2017.01.007.

Balogh, P., and P. Bagchi, 2017. Direct numerical simulation of cellular-scale blood flow in 3D microvascular networks. *Biophysical journal* 113:2815–2826. DOI: 10.1016/j.bpj.2017.10.020.

Balogh, P., and P. Bagchi, 2018. Analysis of red blood cell partitioning at bifurcations in simulated microvascular networks. *Physics of Fluids* 30:51902. DOI: 10.1063/1.5024783.

Bandopadhyay, R., C. Orte, J. Lawrenson, A. Reid, S. De Silva, and G. Allt, 2001. Contractile proteins in pericytes at the blood-brain and blood-retinal barriers. *Journal of Neurocytology* 30:35–44. DOI: 10.1023/A:1011965307612.

Barber, J. O., J. M. Restrepo, and T. W. Secomb, 2011. Simulated Red Blood Cell Motion in Microvessel Bifurcations: Effects of Cell-Cell Interactions on Cell Partitioning. *Cardiovascular Engineering and Technology* 2:349–360. DOI: 10.1007/s13239-011-0064-4.

Basu, H., A. K. Dharmadhikari, J. A. Dharmadhikari, S. Sharma, and D. Mathur, 2011. Tank Treading of Optically Trapped Red Blood Cells in Shear Flow. *Biophysical Journal* 101:1604–1612. DOI: 10.1016/j.bpj.2011.08.043.

Bélanger, M., and Y. Marois, 2001. Hemocompatibility, biocompatibility, inflammatory and in vivo studies of primary reference materials low-density polyethylene and polydimethylsiloxane: A review. *Journal of Biomedical Materials Research* 58:467–477. DOI: 10.1002/jbm.1043.

Berthiaume, A.-A., F. Schmid, S. Stamenkovic, V. Coelho-Santos, C. D. Nielson, B. Weber, M. W. Majesky, and A. Y. Shih, 2022. Pericyte remodeling is deficient in the aged brain and contributes to impaired capillary flow and structure. *Nature Communications* 13:5912. DOI: 10.1038/s41467-022-33464-w.

Brevis, W. A., Y. Niño, and G. H. Jirka, 2011. Integrating cross-correlation and relaxation algorithms for particle tracking velocimetry. *Experiments in Fluids* 50:135–147. DOI: 10.1007/s00348-010-0907-z.

Brust, M., O. Aouane, M. Thiébaud, D. Flormann, C. Verdier, L. Kaestner, M. W. Laschke, H. Selmi, A. Benyoussef, T. Podgorski, G. Coupier, C. Misbah, and C. Wagner, 2014. The plasma protein fibrinogen stabilizes clusters of red blood cells in microcapillary flows. *Scientific Reports* 4:4348. DOI: 10.1038/srep04348.

Bucciarelli, A., A. Mantegazza, A. Haeberlin, and D. Obrist, 2024. Relation between hematocrit partitioning and red blood cell lingering in a microfluidic network. *Biophysical Journal* 123:3355–3365. DOI: 10.1016/j.bpj.2024.07.042.

Clavica, F., A. Homsy, L. Jeandupeux, and D. Obrist, 2016. Red blood cell phase separation in symmetric and asymmetric microchannel networks: effect of capillary dilation and inflow velocity. *Scientific reports* 6:1–12. DOI: 10.1038/srep36763.

Corrons, J. V., L. B. Casafont, and E. F. Frasnedo, 2021. Concise review: how do red blood cells born, live, and die? *Annals of Hematology* 100:2425–2433. DOI: 10.1007/s00277-021-04575-z.

Coupier, G., B. Kaoui, T. Podgorski, and C. Misbah, 2008. Noninertial lateral migration of vesicles in bounded Poiseuille flow. *Physics of Fluids* 20:111702. DOI: 10.1063/1.3023159.

Dalal, S. M., O. Nano, and M. Vulfovich, 2024. Red Blood Cell Membrane Disorders. In: L. Sokol, and L. Zhang, editors, Non-Neoplastic Hematologic Disorders, Springer. https://doi.org/10.1007/978-3-031-62373-8_14.

Desjardins, C., and B. R. Duling, 1987. Microvessel hematocrit: measurement and implications for capillary oxygen transport. *American Journal of Physiology-Heart and Circulatory Physiology* 252:H494–H503. DOI: 10.1152/ajpheart.1987.252.3.H494.

Doddi, S. K., and P. Bagchi, 2009. Three-dimensional computational modeling of multiple deformable cells flowing in microvessels. *Physical Review E* 79:046318. DOI: 10.1103/PhysRevE.79.046318.

Dupire, J., M. Socol, and A. Viallat, 2012. Full dynamics of a red blood cell in shear flow. *Proceedings of the National Academy of Sciences* 109:20808–20813. DOI: 10.1073/pnas.1210236109.

Eberth, C., 1871. Handbuch der Lehre von den Geweben des Menschen und der Tiere, volume Vol 1. Leipzig : Engelmann, http://archive.org/details/b21273418.

Fåhræus, R., and T. Lindqvist, 1931. The viscosity of the blood in narrow capillary tubes. *American Journal of Physiology-Legacy Content* 96:562–568. DOI: 10.1152/ajplegacy.1931.96.3.562.

Fåhraeus, R., 1929. The suspension stability of the blood. *Physiological reviews* 9:241–274. DOI: 10.1152/physrev.1929.9.2.241.

Fenech, M., V. Girod, V. Claveria, S. Meance, M. Abkarian, and B. Charlot, 2019. Microfluidic blood vasculature replicas using backside lithography. *Lab on a Chip* 19:2096–2106. DOI: 10.1039/C9LC00254E.

Fenton, B. M., R. T. Carr, and G. R. Cokelet, 1985. Nonuniform red cell distribution in 20 to 100 μm bifurcations. *Microvascular Research* 29:103–126. DOI: 10.1016/0026-2862(85)90010-X.

Frey, S., 2018. Hemodynamics in peripheral arterio-venous malformations. PhD Thesis, University of Bern.

Fung, Y.-C., 1973. Stochastic flow in capillary blood vessels. *Microvascular research* 5:34–48. DOI: 10.1016/S0026-2862(73)80005-6.

Geekiyanage, N. M., M. A. Balanant, E. Sauret, S. Saha, R. Flower, C. T. Lim, and Y. Gu, 2019. A coarse-grained red blood cell membrane model to study stomatocyte-discocyte-echinocyte morphologies. *PLOS ONE* 14:e0215447. DOI: 10.1371/journal.pone.0215447.

Grandchamp, X., G. Coupier, A. Srivastav, C. Minetti, and T. Podgorski, 2013. Lift and Down-Gradient Shear-Induced Diffusion in Red Blood Cell Suspensions. *Physical Review Letters* 110:108101. DOI: 10.1103/PhysRevLett.110.108101.

Hall, C. N., C. Reynell, B. Gesslein, N. B. Hamilton, A. Mishra, B. A. Sutherland, F. M. O'Farrell, A. M. Buchan, M. Lauritzen, and D. Attwell, 2014. Capillary pericytes regulate cerebral blood flow in health and disease. *Nature* 508:55–60. DOI: 10.1038/nature13165.

Hall, J., 2015. 14 - Overview of the Circulation; Biophysics of Pressure, Flow, and Resistance. In: Guyton and Hall Textbook of Medical Physiology, Elsevier Health Sciences. https://shop.elsevier.com/books/guyton-and-hall-textbook-of-medical-physiology/hall/978-1-4557-7005-2.

Hall, J., 2015. 25 - The Body Fluid Compartments: Extracellular and Intracellular Fluids; Edema. In: Guyton and Hall Textbook of Medical Physiology, Elsevier Health Sciences. https://shop.elsevier.com/books/guyton-and-hall-textbook-of-medical-physiology/hall/978-1-4557-7005-2.

Hall, J., 2015. 70 - Protein Metabolism. In: Guyton and Hall Textbook of Medical Physiology, Elsevier Health Sciences. https://shop.elsevier.com/books/guyton-and-hall-textbook-of-medical-physiology/hall/978-1-4557-7005-2.

Hamilton, N. B., 2010. Pericyte-mediated regulation of capillary diameter: a component of neurovascular coupling in health and disease. *Frontiers in Neuroenergetics* 2. DOI: 10.3389/fnene.2010.00005.

Hartmann, D. A., R. G. Underly, R. I. Grant, A. N. Watson, V. Lindner, and A. Y. Shih, 2015. Pericyte structure and distribution in the cerebral cortex revealed by high-resolution imaging of transgenic mice. *Neurophotonics* 2:041402. DOI: 10.1117/1.NPh.2.4.041402.

Hartmann, D. A., A.-A. Berthiaume, R. I. Grant, S. A. Harrill, T. Koski, T. Tieu, K. P. McDowell, A. V. Faino, A. L. Kelly, and A. Y. Shih, 2021. Brain capillary pericytes exert a substantial but slow influence on blood flow. *Nature Neuroscience* 24:633–645. DOI: 10.1038/s41593-020-00793-2.

Hassan, Y. A., T. K. Blanchat, and C. H. S. Jr, 1992. PIV flow visualisation using particle tracking techniques. *Measurement Science and Technology* 3:633. DOI: 10.1088/0957-0233/3/7/001.

Hénon, S., G. Lenormand, A. Richert, and F. Gallet, 1999. A New Determination of the Shear Modulus of the Human Erythrocyte Membrane Using Optical Tweezers. *Biophysical Journal* 76:1145–1151. DOI: 10.1016/S0006-3495(99)77279-6.

Hill, R. A., L. Tong, P. Yuan, S. Murikinati, S. Gupta, and J. Grutzendler, 2015. Regional Blood Flow in the Normal and Ischemic Brain Is Controlled by Arteriolar Smooth Muscle Cell Contractility and Not by Capillary Pericytes. *Neuron* 87:95–110. DOI: 10.1016/j.neuron.2015.06.001.

Hillman, E. M. C., 2014. Coupling Mechanism and Significance of the BOLD Signal: A Status Report. *Annual Review of Neuroscience* 37:161–181. DOI: 10.1146/annurev-neuro-071013-014111.

Huang, Z., X. Li, M. Martins-Green, and Y. Liu, 2012. Microfabrication of cylindrical microfluidic channel networks for microvascular research. *Biomedical Microdevices* 14:873–883. DOI: 10.1007/s10544-012-9667-2.

Hudetz, A. G., 1997. Blood flow in the cerebral capillary network: a review emphasizing observations with intravital microscopy. *Microcirculation* 4:233–252. DOI: 10.1111/aor.13941.

Hyakutake, T., H. Abe, Y. Miyoshi, M. Yasui, R. Suzuki, S. Tsurumaki, and Y. Tsutsumi, 2022. In vitro study on the partitioning of red blood cells using a microchannel network. *Microvascular Research* 140:104281. DOI: 10.1016/j.mvr.2021.104281.

Iadecola, C., 2017. The Neurovascular Unit Coming of Age: A Journey through Neurovascular Coupling in Health and Disease. *Neuron* 96:17–42. DOI: 10.1016/j.neuron.2017.07.030.

Ishikawa, M., Y. Murai, A. Wada, M. Iguchi, K. Okamoto, and F. Yamamoto, 2000. A novel algorithm for particle tracking velocimetry using the velocity gradient tensor. *Experiments in Fluids* 29:519–531. DOI: 10.1007/s003480000120.

Johnston, I. D., D. K. McCluskey, C. K. L. Tan, and M. C. Tracey, 2014. Mechanical characterization of bulk Sylgard 184 for microfluidics and microengineering. *Journal of Micromechanics and Microengineering* 24:035017. DOI: 10.1088/0960-1317/24/3/035017.

Karimi, K., A. Fardoost, N. Mhatre, J. Rajan, D. Boisvert, and M. Javanmard, 2024. A Thorough Review of Emerging Technologies in Micro- and Nanochannel Fabrication: Limitations, Applications, and Comparison. *Micromachines* 15:1274. DOI: 10.3390/mi15101274.

Khanafer, K., A. Duprey, M. Schlicht, and R. Berguer, 2009. Effects of strain rate, mixing ratio, and stress–strain definition on the mechanical behavior of the polydimethylsiloxane (PDMS) material as related to its biological applications. *Biomedical Microdevices* 11:503–508. DOI: 10.1007/s10544-008-9256-6.

Kihm, A., S. Quint, M. W. Laschke, M. D. Menger, T. John, L. Kaestner, and C. Wagner, 2021. Lingering dynamics in microvascular blood flow. *Biophysical journal* 120:432–439. DOI: 10.1016/j.bpj.2020.12.012.

Kim, J.-C., H.-I. Yun, S.-W. Cha, K.-H. Kim, W. S. Koh, and M.-K. Chung, 2002. Haematological changes during normal pregnancy in New Zealand White rabbits: a longitudinal study. *Comparative Clinical Pathology* 11:98–106. DOI: 10.1007/s005800200006.

Kim, Y., J. Park, and M. Kim, 2017. Diagnostic approaches for inherited hemolytic anemia in the genetic era. *Blood research* 52:84–94. DOI: 10.5045/br.2017.52.2.84.

Kisler, K., A. R. Nelson, A. Montagne, and B. V. Zlokovic, 2017. Cerebral blood flow regulation and neurovascular dysfunction in Alzheimer disease. *Nature Reviews Neuroscience* 18:419–434. DOI: 10.1038/nrn.2017.48.

Kisler, K., A. R. Nelson, S. V. Rege, A. Ramanathan, Y. Wang, A. Ahuja, D. Lazic, P. S. Tsai, Z. Zhao, Y. Zhou, D. A. Boas, S. Sakadžić, and B. V. Zlokovic, 2017. Pericyte degeneration leads to neurovascular uncoupling and limits oxygen supply to brain. *Nature Neuroscience* 20:406–416. DOI: 10.1038/nn.4489.

Kleinfeld, D., P. P. Mitra, F. Helmchen, and W. Denk, 1998. Fluctuations and stimulus-induced changes in blood flow observed in individual capillaries in layers 2 through 4 of rat neocortex. *Proceedings of the National Academy of Sciences* 95:15741–15746. DOI: 10.1073/pnas.95.26.15741.

Kodama, Y., H. Aoki, Y. Yamagata, and K. Tsubota, 2019. *In vitro* analysis of blood flow in a microvascular network with realistic geometry. *Journal of Biomechanics* 88:88–94. DOI: 10.1016/j.jbiomech.2019.03.022.

Krogh, A., 1921. Studies on the physiology of capillaries. *The Journal of Physiology* 55:412–422. DOI: 10.1113/jphysiol.1921.sp001985.

Lacolley, P., V. Regnault, A. Nicoletti, Z. Li, and J.-B. Michel, 2012. The vascular smooth muscle cell in arterial pathology: a cell that can take on multiple roles. *Cardiovascular Research* 95:194–204. DOI: 10.1093/cvr/cvs135.

Lewis, J. H., 1996. 2 - Laboratory Methods and Test Parameters. In: Comparative Hemostasis in Vertebrates, Springer US, Boston, MA. https://link.springer.com/chapter/10.1007/978-1-4757-9768-8_2.

Lewis, J. H., 1996. 28 - Comparative Hematology. In: Comparative Hemostasis in Vertebrates, Springer US, Boston, MA. https://link.springer.com/chapter/10.1007/978-1-4757-9768-8_28.

Lewis, J. H., 1996. 16 - Rabbits. In: Comparative Hemostasis in Vertebrates, Springer US, Boston, MA. https://link.springer.com/chapter/10.1007/978-1-4757-9768-8_16.

Lindauer, U., C. Leithner, H. Kaasch, B. Rohrer, M. Foddis, M. Füchtemeier, N. Offenhauser, J. Steinbrink, G. Royl, M. Kohl-Bareis, and U. Dirnagl, 2010. Neurovascular Coupling in Rat Brain Operates Independent of Hemoglobin Deoxygenation. *Journal of Cerebral Blood Flow & Metabolism* 30:757–768. DOI: 10.1038/jcbfm.2009.259.

Lipowsky, H. H., S. Usami, and S. Chien, 1980. In vivo measurements of "apparent viscosity" and microvessel hematocrit in the mesentery of the cat. *Microvascular research* 19:297–319. DOI: 10.1016/0026-2862(80)90050-3.

Mantegazza, A., M. Ungari, F. Clavica, and D. Obrist, 2020. Local vs. Global Blood Flow Modulation in Artificial Microvascular Networks: Effects on Red Blood Cell Distribution and Partitioning. *Frontiers in Physiology* 11:566273. DOI: 10.3389/fphys.2020.566273.

Mantegazza, A., F. Clavica, and D. Obrist, 2020. In vitro investigations of red blood cell phase separation in a complex microchannel network. *Biomicrofluidics* 14:14101. DOI: 10.1063/1.5127840.

Mantegazza, A., D. De Marinis, and M. D. de Tullio, 2024. Red blood cell transport in bounded shear flow: On the effects of cell viscoelastic properties. *Computer Methods in Applied Mechanics and Engineering* 428:117088. DOI: 10.1016/j.cma.2024.117088.

Merlo, A., M. Berg, P. Duru, F. Risso, Y. Davit, and S. Lorthois, 2022. A few upstream bifurcations drive the spatial distribution of red blood cells in model microfluidic networks. *Soft Matter* 18:1463–1478. DOI: 10.1039/D1SM01141C.

Merlo, A., 2018. Écoulement de suspensions de globules rouges dans des réseaux de micro-canaux: hétérogénéités et effets de réseaux. PhD Thesis, Institut de Mécanique des Fluides, CNRS, INPT, UPS.

Mishra, A., F. M. O'Farrell, C. Reynell, N. B. Hamilton, C. N. Hall, and D. Attwell, 2014. Imaging pericytes and capillary diameter in brain slices and isolated retinae. *Nature Protocols* 9:323–336. DOI: 10.1038/nprot.2014.019.

Mishra, A., J. P. Reynolds, Y. Chen, A. V. Gourine, D. A. Rusakov, and D. Attwell, 2016. Astrocytes mediate neurovascular signaling to capillary pericytes but not to arterioles. *Nature Neuroscience* 19:1619–1627. DOI: 10.1038/nn.4428.

Montinaro, E., M. Grisi, M. C. Letizia, L. Pethö, M. a. M. Gijs, R. Guidetti, J. Michler, J. Brugger, and G. Boero, 2018. 3D printed microchannels for sub-nL NMR spectroscopy. *PLOS ONE* 13:e0192780. DOI: 10.1371/journal.pone.0192780.

Neu, B., and H. J. Meiselman, 2002. Depletion-Mediated Red Blood Cell Aggregation in Polymer Solutions. *Biophysical Journal* 83:2482–2490. DOI: 10.1016/S0006-3495(02)75259-4.

Nippert, A. R., K. R. Biesecker, and E. A. Newman, 2018. Mechanisms Mediating Functional Hyperemia in the Brain. *The Neuroscientist* 24:73–83. DOI: 10.1177/1073858417703033.

Oosterbroek, R. E., 1999. Modeling, design and realization of microfluidic components. PhD Thesis, University of Twente.

Pappano, A. J., and W. G. Wier, 2013. 8 - The Microcirculation and Lymphatics. In: Cardiovascular Physiology (Tenth edition), Elsevier, Philadelphia. https://doi.org/10.1016/B978-0-323-08697-4.00008-3.

Pappano, A. J., and W. G. Wier, 2013. 1 - Overview of the Circulation and Blood. In: Cardiovascular Physiology (Tenth edition), Elsevier, Philadelphia. https://doi.org/10.1016/B978-0-323-08697-4.00001-0.

Peppiatt, C. M., C. Howarth, P. Mobbs, and D. Attwell, 2006. Bidirectional control of CNS capillary diameter by pericytes. *Nature* 443:700–704. DOI: 10.1038/nature05193.

Peter Klinken, S., 2002. Red blood cells. *The International Journal of Biochemistry & Cell Biology* 34:1513–1518. DOI: 10.1016/S1357-2725(02)00087-0.

Pries, A. R., and T. W. Secomb, 2008. Chapter 1 - Blood Flow in Microvascular Networks. In: Microcirculation (Second Edition), Academic Press, San Diego. https://doi.org/10.1016/B978-0-12-374530-9.00001-2.

Pries, A. R., K. Ley, and P. Gaehtgens, 1986. Generalization of the Fahraeus principle for microvessel networks. *American Journal of Physiology-Heart and Circulatory Physiology* 251:H1324–H1332. DOI: 10.1152/ajpheart.1986.251.6.H1324.

Pries, A. R., K. Ley, M. Claassen, and P. Gaehtgens, 1989. Red cell distribution at microvascular bifurcations. *Microvascular Research* 38:81–101. DOI: 10.1016/0026-2862(89)90018-6.

Pries, A. R., T. W. Secomb, P. Gaehtgens, and J. F. Gross, 1990. Blood flow in microvascular networks. Experiments and simulation. *Circulation Research* 67:826–834. DOI: 10.1161/01.RES.67.4.826.

Pries, A. R., B. Reglin, and T. W. Secomb, 2003. Structural response of microcirculatory networks to changes in demand: Information transfer by shear stress. *American Journal of Physiology - Heart and Circulatory Physiology* 284:H2204–H2212. DOI: 10.1152/ajpheart.00757.2002.

Pskowski, A., P. Bagchi, and J. D. Zahn, 2021. Investigation of red blood cell partitioning in an in vitro microvascular bifurcation. *Artificial organs* 45:1083–1096. DOI: 10.1111/aor.13941.

Qiu, Y., B. Ahn, Y. Sakurai, C. E. Hansen, R. Tran, P. N. Mimche, R. G. Mannino, J. C. Ciciliano, T. J. Lamb, C. H. Joiner, S. F. Ofori-Acquah, and W. A. Lam, 2018. Microvasculature-on-a-chip for the long-term study of endothelial barrier dysfunction and microvascular obstruction in disease. *Nature Biomedical Engineering* 2:453–463. DOI: 10.1038/s41551-018-0224-z.

Rand, P. W., E. Lacombe, H. E. Hunt, and W. H. Austin, 1964. Viscosity of normal human blood under normothermic and hypothermic conditions. *Journal of Applied Physiology* 19:117–122. DOI: 10.1152/jappl.1964.19.1.117.

Randaelli, A., and F. Montevecchi, 2012. Biomeccanica. Analisi multiscala di tessuti biologici. Pàtron editore, https://www.patroneditore.eu/volumi/9788855531764/biomeccanica-analisi-multiscala-di-tessuti-biologici.

Rashidi, Y., G. Simionato, Q. Zhou, T. John, A. Kihm, M. Bendaoud, T. Krüger, M. O. Bernabeu, L. Kaestner, M. W. Laschke, M. D. Menger, C. Wagner, and A. Darras, 2023. Red blood cell lingering modulates hematocrit distribution in the microcirculation. *Biophysical Journal* DOI: 10.1016/j.bpj.2023.03.020.

Reinhart, W. H., N. Z. Piety, J. W. Deuel, A. Makhro, T. Schulzki, N. Bogdanov, J. S. Goede, A. Bogdanova, R. Abidi, and S. S. Shevkoplyas, 2015. Washing stored red blood cells in an albumin solution improves their morphologic and hemorheologic properties. *Transfusion* 55:1872–1881. DOI: 10.1111/trf.13052.

Roman, S., S. Lorthois, P. Duru, and F. Risso, 2012. Velocimetry of red blood cells in microvessels by the dual-slit method: Effect of velocity gradients. *Microvascular Research* 84:249–261. DOI: 10.1016/j.mvr.2012.08.006.

Roman, S., A. Merlo, P. Duru, F. Risso, and S. Lorthois, 2016. Going beyond 20 μm-sized channels for studying red blood cell phase separation in microfluidic bifurcations. *Biomicrofluidics* 10:34103. DOI: 10.1063/1.4948955.

Rouget, C., 1873. Mémoire sur le développement, la structure et les propriétés physiologique des cappilaires sanguins et lymphatiques, volume 5. Archives de physiologie normale et pathologique, http://publikationen.ub.uni-frankfurt.de/frontdoor/index/index/docId/17190.

Ruhnau, P., C. Guetter, T. Putze, and C. Schnörr, 2005. A variational approach for particle tracking velocimetry. *Measurement Science and Technology* 16:1449. DOI: 10.1088/0957-0233/16/7/007.

Salvioli, G., E. Gaetti, R. Panini, R. Lugli, and J. M. Pradelli, 1993. Different resistance of mammalian red blood cells to hemolysis by bile salts. *Lipids* 28:999–1003. DOI: 10.1007/BF02537121.

Sarelius, I. H., and B. R. Duling, 1982. Direct measurement of microvessel hematocrit, red cell flux, velocity, and transit time. *American Journal of Physiology-Heart and Circulatory Physiology* 243:H1018–H1026. DOI: 10.1152/ajpheart.1982.243.6.H1018.

Schindelin, J., I. Arganda-Carreras, E. Frise, V. Kaynig, M. Longair, T. Pietzsch, S. Preibisch, C. Rueden, S. Saalfeld, B. Schmid, and others, 2012. Fiji: an open-source platform for biological-image analysis. *Nature methods* 9:676–682. DOI: 10.1038/nmeth.2019.

Schirinzi, D., 2018. In vitro investigation of red blood cell rheology and phase separation in micro uidic networks mimicking the cerebral microvasculature. Master's thesis, ETH Zürich.

Schmid, F., J. Reichold, B. Weber, and P. Jenny, 2015. The impact of capillary dilation on the distribution of red blood cells in artificial networks. *American Journal of Physiology-Heart and Circulatory Physiology* 308:H733–H742. DOI: 10.1152/ajpheart.00335.2014.

Schmid, F., M. J. P. Barrett, P. Jenny, and B. Weber, 2019. Vascular density and distribution in neocortex. *NeuroImage* 197:792–805. DOI: 10.1016/j.neuroimage.2017.06.046.

Schmid, F., M. J. P. Barrett, D. Obrist, B. Weber, and P. Jenny, 2019. Red blood cells stabilize flow in brain microvascular networks. *PLoS computational biology* 15:e1007231. DOI: 10.1371/journal.pcbi.1007231.

Schmid-Schönbein, G. W., R. Skalak, S. Usami, and S. Chien, 1980. Cell distribution in capillary networks. *Microvascular Research* 19:18–44. DOI: 10.1016/0026-2862(80)90082-5.

Schulte, M. L., J. D. Wood, and A. G. Hudetz, 2003. Cortical electrical stimulation alters erythrocyte perfusion pattern in the cerebral capillary network of the rat. *Brain research* 963:81–92. DOI: 10.1016/S0006-8993(02)03848-9.

Scott, S. M., and Z. Ali, 2021. Fabrication Methods for Microfluidic Devices: An Overview. *Micromachines* 12:319. DOI: 10.3390/mi12030319.

Secomb, T. W., and C. Pozrikidis, 2003. Mechanics of red blood cells and blood flow in narrow tubes. In: Modeling and Simulation of Capsules and Biological Cells, Chapman and Hall/CRC, New York. https://doi.org/10.1201/9780203503959.

Secomb, T. W., R. Skalak, N. Özkaya, and J. F. Gross, 1986. Flow of axisymmetric red blood cells in narrow capillaries. *Journal of Fluid Mechanics* 163:405–423. DOI: 10.1017/S0022112086002355.

Secomb, T. W., 2017. Blood Flow in the Microcirculation. *Annual Review of Fluid Mechanics* 49:443–461. DOI: 10.1146/annurev-fluid-010816-060302.

Shen, Z., G. Coupier, B. Kaoui, B. Polack, J. Harting, C. Misbah, and T. Podgorski, 2016. Inversion of hematocrit partition at microfluidic bifurcations. *Microvascular research* 105:40–46. DOI: 10.1016/j.mvr.2015.12.009.

Sherwood, J. M., D. Holmes, E. Kaliviotis, and S. Balabani, 2014. Spatial distributions of red blood cells significantly alter local haemodynamics. *PloS one* 9:e100473. DOI: 10.1371/journal.pone.0100473.

Smith, J. E., 1987. Erythrocyte Membrane: Structure, Function, and Pathophysiology. *Veterinary Pathology* 24:471–476. DOI: 10.1177/030098588702400601.

Spiga, M., and G. L. Morino, 1994. A symmetric solution for velocity profile in laminar flow through rectangular ducts. *International Communications in Heat and Mass Transfer* 21:469–475. DOI: 10.1016/0735-1933(94)90046-9.

Svanes, K., and B. W. Zweifach, 1968. Variations in small blood vessel hematocrits produced in hypothermic rats by micro-occlusion. *Microvascular Research* 1:210–220. DOI: 10.1016/0026-2862(68)90019-8.

Sweeney, M. D., S. Ayyadurai, and B. V. Zlokovic, 2016. Pericytes of the neurovascular unit: Key functions and signaling pathways. *Nature neuroscience* 19:771–783. DOI: 10.1038/nn.4288.

Takehara, K., and T. Etoh, 1998. A Study on Particle Identification in PTV Particle Mask Correlation Method, volume 1. Journal of Vision, https://content.iospress.com/articles/journal-of-visualization/jov1-3-10.

Tilton, R. G., 1991. Capillary pericytes: Perspectives and future trends. *Journal of Electron Microscopy Technique* 19:327–344. DOI: 10.1002/jemt.1060190308.

Tomaiuolo, G., and S. Guido, 2011. Start-up shape dynamics of red blood cells in microcapillary flow. *Microvascular Research* 82:35–41. DOI: 10.1016/j.mvr.2011.03.004.

Tomaiuolo, G., D. Rossi, S. Caserta, M. Cesarelli, and S. Guido, 2012. Comparison of two flow-based imaging methods to measure individual red blood cell area and volume. *Cytometry Part A* 81A:1040–1047. DOI: 10.1002/cyto.a.22215.

Tomaiuolo, G., L. Lanotte, R. D'Apolito, A. Cassinese, and S. Guido, 2016. Microconfined flow behavior of red blood cells. *Medical Engineering & Physics* 38:11–16. DOI: 10.1016/j.medengphy.2015.05.007.

Tsai, M., A. Kita, J. Leach, R. Rounsevell, J. N. Huang, J. Moake, R. E. Ware, D. A. Fletcher, and W. A. Lam, 2011. In vitro modeling of the microvascular occlusion and thrombosis that occur in hematologic diseases using microfluidic technology. *The Journal of Clinical Investigation* 122. DOI: 10.1172/JCI58753.

Vand, V., 1948. Viscosity of Solutions and Suspensions. I. Theory. *The Journal of Physical and Colloid Chemistry* 52:277–299. DOI: 10.1021/j150458a001.

Viallat, A., and M. Abkarian, 2014. Red blood cell: from its mechanics to its motion in shear flow. *International Journal of Laboratory Hematology* 36:237–243. DOI: 10.1111/ijlh.12233.

Wacker, B. K., A. B. Freie, J. L. Perfater, and J. M. Gidday, 2012. Junctional Protein Regulation by Sphingosine Kinase 2 Contributes to Blood–Brain Barrier Protection in Hypoxic Preconditioning-Induced Cerebral Ischemic Tolerance. *Journal of Cerebral Blood Flow & Metabolism* 32:1014–1023. DOI: 10.1038/jcbfm.2012.3.

Wagner, C., P. Steffen, and S. Svetina, 2013. Aggregation of red blood cells: From rouleaux to clot formation. *Comptes Rendus. Physique* 14:459–469. DOI: 10.1016/j.crhy.2013.04.004.

Windberger, U., A. Bartholovitsch, R. Plasenzotti, K. J. Korak, and G. Heinze, 2003. Whole blood viscosity, plasma viscosity and erythrocyte aggregation in nine mammalian species: reference values and comparison of data. *Experimental physiology* 88:431–440. DOI: 10.1113/eph8802496.

Wolf, T., U. Lindauer, A. Villringer, and U. Dirnagl, 1997. Excessive oxygen or glucose supply does not alter the blood flow response to somatosensory stimulation or spreading depression in rats. *Brain Research* 761:290–299. DOI: 10.1016/S0006-8993(97)00354-5.

Xia, Y., and G. M. Whitesides, 1998. SOFT LITHOGRAPHY. *Annual Review of Materials Research* 28:153–184. DOI: 10.1146/annurev.matsci.28.1.153.

Zhou, Q., J. Fidalgo, M. O. Bernabeu, M. S. N. Oliveira, and T. Krüger, 2021. Emergent cell-free layer asymmetry and biased haematocrit partition in a biomimetic vascular network of successive bifurcations. *Soft Matter* 17:3619–3633. DOI: 10.1039/D0SM01845G.

Zimmermann, K. W., 1923. Der feinere Bau der Blutcapillaren. *Zeitschrift für Anatomie und Entwicklungsgeschichte* 68:29–109. DOI: 10.1007/BF02593544.